

University of Warwick institutional repository: <http://go.warwick.ac.uk/wrap>

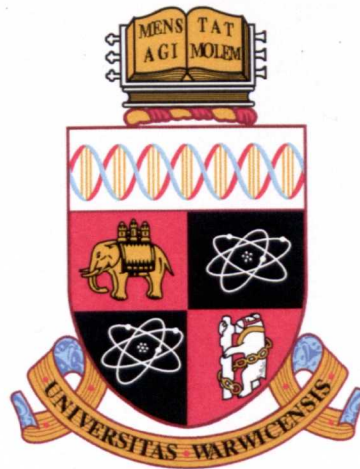
A Thesis Submitted for the Degree of PhD at the University of Warwick

<http://go.warwick.ac.uk/wrap/49964>

This thesis is made available online and is protected by original copyright.

Please scroll down to view the document itself.

Please refer to the repository record for this item for information to help you to cite it. Our policy information is available from the repository home page.



**A Direct Numerical Simulation of Dielectric Barrier
Discharge (DBD) Plasma Actuators for Turbulent
Skin-Friction Control**

by

Dana Elam

Thesis

Submitted to the University of Warwick

for the degree of

Doctor of Philosophy

School of Engineering

June 2012

THE UNIVERSITY OF
WARWICK

NO CD/DVD

ATTACHED

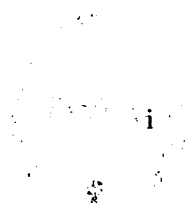
PLEASE APPLY

TO

UNIVERSITY

Contents

List of Tables	v
List of Figures	vi
Acknowledgments	xii
Declarations	xiii
Abstract	xiv
Abbreviations	xv
Chapter 1 Introduction	1
1.1 Introduction	1
Chapter 2 Literature review	4
2.1 Flow Control	6
2.2 Spanwise motions	8
2.2.1 Longitudinal standing wave	13
2.2.2 Travelling waves	14
2.3 Dielectric barrier discharge plasma	16
2.3.1 DBD models	22
2.3.2 DBD flow control	23



Chapter 3	DNS and DBD Plasma Model	26
3.1	Direct numerical simulation (DNS)	26
3.2	Plasma model	27
3.2.1	Shyy et al. model	28
3.2.2	Integration into the DNS code	31
3.2.3	Smoothing Function	32
3.3	Actuator pairs	35
3.4	Multiple actuator configurations	36
3.4.1	Uniform plasma	36
3.5	Initial simulations	36
3.5.1	Time step	38
3.6	Summary	40
Chapter 4	Quiescent fluid DBD simulations	41
4.1	Introduction	41
4.2	Method	42
4.3	Single DBD actuator	42
4.4	Profile parameters	49
4.4.1	Effect of strength, D_c	49
4.4.2	Effect of profile angle, θ_p	50
4.4.3	Effect of profile width, b	52
4.4.4	Conclusion	52
4.5	Scaling	54
4.6	Multiple DBD actuators	57
4.7	Discussion	61
4.8	Chapter Summary	64
Chapter 5	Temporal oscillating plasma	65
5.1	Introduction	65

5.2	Method	66
5.2.1	Numerical procedure	68
5.3	Results	69
5.3.1	Stokes layer	78
5.3.2	Velocity and turbulence statistics	91
5.3.3	$Y - Z$ plane data	107
5.3.4	Flow visualisation	108
5.4	Discussion	116
5.5	Summary	121
Chapter 6 Spatial oscillating plasma		122
6.1	Introduction	122
6.2	Method	123
6.3	Results	125
6.3.1	Stokes layer	129
6.3.2	Velocity and turbulence statistics	134
6.4	Discussion	141
6.5	Chapter Summary	145
Chapter 7 Conclusions		147
7.1	Conclusions	147
7.2	Recommendations	150
Appendix A Helmholtz resonators		151
A.1	Introduction	151
A.2	Resonator model	154
A.2.1	Pressure term	156
A.3	Resonator optimisation	157
A.4	Method	159

A.5 Results	160
A.5.1 Wall-normal velocity and wall-pressure correlation	160
A.5.2 Offline optimisation	162
A.5.3 Controlled channel flows	163
A.5.4 Mean properties	165
A.6 Discussion	170
A.7 Summary	172
Appendix B Temporal oscillating plasma results	173
Appendix C Spatial oscillating plasma results	179

List of Tables

4.1	Actuator configurations.	57
5.1	DBD actuator configurations for simulations.	67
5.2	Data for different periods of oscillation and actuator configurations, $W_m^+ = 12$	71
5.3	Data for spanwise wall oscillations for different periods of oscillation, $W_m^+ = 12$	72
5.4	Data for one period of oscillation $T^+ = 100$, for uniform plasma configuration for various values of W_m^+	73
5.5	Data for one period of oscillation $T^+ = 100$, for discrete plasma configurations for various values of W_m^+	74
6.1	Data for different wavelengths of oscillation and actuator configurations.	126
6.2	Data for spanwise wall oscillation for different wavelengths of oscilla- tion, $W_m^+ = 12$	127
A.1	Simulation parameters, $T_o^+ = 800$	164

List of Figures

2.1	Three-dimensional plot of $DR\%$ versus T^+ and W_m^+	10
2.2	Map of DR in the $\omega - \kappa_x$ plane for $W_m^+ = 12$ and $Re = 4760$	16
2.3	Schematic illustration of DBD plasma actuator.	17
2.4	Illustration of electron drift that dictates portions of ac period where air ionises in DBD process.	19
2.5	Schematic representation of the surface-discharge.	19
2.6	Velocity profiles of the wall jets created by DDBD actuator.	21
2.7	Smoke wire flow-visualisation images around a DDBD actuator.	22
2.8	Schematic illustration of a triode plasma actuator.	22
3.1	Illustration of the signal supplied to a DBD actuator.	28
3.2	Schematic of the plasma profile.	29
3.3	Illustration of the smoothing profile.	33
3.4	Vorticity ω^+ vorticity contours for: a) the original profile b) after smoothing (Quisecent flow, u_τ based on $Re_\tau = 200$). Purple rectangle indicate z -location of plasma.	34
3.5	Sketch of an actuator pair.	35
3.6	Illustration of the effect to the electric field lines, if the actuator s_p is less the plasma width, b	37
3.7	Illustration of the electric field distribution of spatially uniform plasma.	

3.8	Spanwise velocity contours for a DBD actuator for different grid spacings.	39
3.9	Time history for Reynolds shear stress $\overline{u'v'}$, for simulation case 44 (see chapter 5).	39
4.1	Vorticity contours ω around a single DBD plasma actuator in initial quiescent flow.	43
4.2	Z-direction velocity contours w around a single DBD plasma actuator in initial quiescent flow.	44
4.3	Wall-normal velocity contours v around a single DBD plasma actuator in initial quiescent flow.	45
4.4	Starting vortex location.	46
4.5	Velocity profiles at various z locations, at $t^+ = 150$	46
4.6	Sketch based on previous diagram by Whalley (2011) of the evolution of the flow created by a solitary DBD plasma actuator.	48
4.7	Velocity profiles for various strengths, D_c	49
4.8	Velocity profiles for various plasma profile widths	50
4.9	Velocity profiles for various profile angles, θ_p	50
4.10	Wall-normal velocity per unit length for various values of $\theta_p = 10$. .	51
4.11	Vortex trajectory for various profile angles, θ_p	52
4.12	Velocity profiles for various plasma profile widths.	53
4.13	Vortex trajectory for plasma profile widths.	53
4.14	Normalised maximum z-direction velocity.	54
4.15	Starting vortex scalings: a) z_s vs. t^s , b) y_s vs. t^s , c) y_c vs. x_c	56
4.16	Vorticity contours, ω^+ , around a DBD plasma actuator, $s_p^+ = 20$. .	58
4.17	z-direction velocity contours, w^+ , around a DBD plasma actuator, $s_p^+ = 20$	59

4.18	Wall-normal velocity contours, v^+ , around a DBD plasma actuator, $s_p^+ = 20$	60
4.19	Sketch of the evolution of the flow created by multiple DBD plasma actuators.	62
4.20	Vortex trajectory for various strengths D_c	63
4.21	Time for vortex to disperse for different actuator configurations and strengths, d_c	64
5.1	Schematic of the system for a turbulent channel flow with temporal oscillation.	66
5.2	Schematic of the actuator sets and their activation in accordance with $a(t)$	67
5.3	Time averaged coefficient of friction for different periods of oscillation T^+ for different plasma actuator configurations and spanwise wall oscillation (SWO) for $W_m^+ = 12$	70
5.4	Time averaged coefficient of friction against maximum spanwise ve- locity W_m^+ for different plasma actuator configurations for $T^+ = 100$	75
5.5	Skin-friction behaviour for different actuator configurations over one period of oscillation for $W_m^+ = 12$	77
5.6	Contour of spanwise velocity w^+ , for spanwise wall oscillations for one period of oscillation, $T^+ = 100$	78
5.7	Spanwise velocity profile at various points in time for one period of oscillation, $T^+ = 100$	79
5.8	Maximum spanwise velocity over one cycle for uniform plasma and spanwise wall oscillation.	80
5.9	Stokes layer penetration depth for uniform plasma, spanwise wall oscillation and analytical result.	81

5.10 Stokes layer penetration depth difference between spanwise wall oscillation and uniform plasma simulations.	81
5.11 Contours of spanwise velocity for the minimum PSLs and uniform plasma Stokes layer over one period of oscillation, $T^+ = 30$	83
5.12 Contours of spanwise velocity for the minimum PSLs and uniform plasma Stokes layer over one period of oscillation, $T^+ = 100$	84
5.13 Contours of spanwise velocity for the minimum PSLs and uniform plasma Stokes layer over one period of oscillation, $T^+ = 200$	85
5.14 Contours of spanwise velocity for the minimum PSLs and uniform plasma Stokes layer over one period of oscillation, $T^+ = 500$	86
5.15 Correlation $r_{w,w}(t)$ for the discrete plasma actuator configurations. .	89
5.16 Correlation $r_{w,w}$ for the discrete plasma actuator configurations. . .	90
5.17 u_{rms} , normalised by the actual wall-shear velocity, u_{τ_m}	93
5.18 v_{rms} , normalised by the actual wall-shear velocity, u_{τ_m}	94
5.19 w_{rms} , normalised by the actual wall-shear velocity, u_{τ_m}	95
5.20 Phase averaged u_{rms} contour plot for $T^+ = 100$	96
5.21 Phase averaged v_{rms} contour plot for $T^+ = 100$	97
5.22 Phase averaged w_{rms} contour plot for $T^+ = 100$	98
5.23 Phase averaged $\omega'_{x_{rms}}$ contour plot for $T^+ = 100$	99
5.24 Phase averaged $\omega'_{y_{rms}}$ contour plot for $T^+ = 100$	100
5.25 Phase averaged $\omega'_{z_{rms}}$ contour plot for $T^+ = 100$	101
5.26 Mean velocity profiles normalised by actual wall-shear velocities, u_{τ_m} . .	102
5.27 Reynolds shear stress, normalised by u_{τ_0} for $T^+ = 100$	103
5.27 Reynolds shear stress from each quadrant.	106
5.28 Phase averaged $y - z$ plane data, $s_p^+ = 10$	110
5.29 Phase averaged $y - z$ plane data, $s_p^+ = 12.5$	112
5.30 Phase averaged $y - z$ plane data, $s_p^+ = 20$	114
5.31 λ_2 visualisation for the no-control case $x = 0 - 9$, $\lambda_2^+ = -0.0125$. . .	115

5.32	λ_2 visualisation for the uniform plasma.	116
5.33	λ_2 visualisation for the $s_p^+ = 10$ configuration.	117
5.34	λ_2 visualisation for the $s_p^+ = 12.5$ configuration.	117
5.35	λ_2 visualisation for the $s_p^+ = 20$ configuration.	118
6.1	Schematic of the system for a turbulent channel flow with streamwise oscillation.	123
6.2	Schematic of the actuator sets and their activation in accordance with $a(x)$	124
6.3	Time-averaged coefficient of friction for different wavelengths of oscillation λ_x^+ for different plasma actuator configurations and spanwise wall oscillation.	127
6.4	skin-friction behaviour for different actuator configurations over one wavelength of oscillation.	128
6.5	skin-friction behaviour for different actuator configurations over one period of oscillation for $T^+ = 125$	129
6.6	Spanwise velocity profile at various longitudinal locations for one period of oscillation, $\lambda_x^+ = 1200$: a) spanwise wall oscillation, b) uniform plasma.	130
6.7	Maximum spanwise velocity over one cycle for uniform plasma and spanwise wall oscillation.	131
6.8	Correlation $r_{w,w}(x)$ for the discrete plasma actuator configurations. .	133
6.9	Correlation $r_{w,w}(t)$ for the discrete plasma actuator configurations. .	134
6.10	<i>rms</i> velocity fluctuations, normalised by the actual wall-shear velocity, u_{τ_m}	136
6.11	Mean velocity profiles normalised by actual wall-shear velocities, u_{τ_m} . .	137
6.12	Reynolds shear stress, normalised by u_{τ_0} for $\lambda_x^+ = 1200$	137
6.13	Reynolds shear stress from each quadrant.	140

6.14 Reynolds shear stress from each quadrant.	142
6.15 $r_{u,w}$ contour plots	143
A.1 Schematic diagram of opposition control.	153
A.2 Sketch of a cavity.	154
A.3 Surface plot of r_{pv}	161
A.4 Joint probability density of the wall-pressure fluctuations and the wall-normal velocities at $y^+ \approx 10$	162
A.5 Correlation of wall-normal velocity with the resonator output, R_{vv_j} , .	163
A.6 Time history of the skin-friction coefficient.	165
A.7 Joint probability density of resonator output v_j and the wall-normal velocities at $y^+ \approx 10$	166
A.8 Mean velocity profiles.	166
A.9 Root-mean-square fluctuations normalised by the wall-shear velocity in global coordinates.	167
A.10 Root-mean-square pressure fluctuations	168
A.11 Reynolds shear stress and total shear stress.	169
A.12 Reynolds shear stress from each quadrant.	169
A.13 Root-mean square vorticity fluctuations	170
B.1 Time history of the skin-friction coefficient	174
B.2 u_{rms} , normalised by the wall-shear velocity, u_{τ_0}	175
B.3 v_{rms} , normalised by the wall-shear velocity, u_{τ_0}	176
B.4 w_{rms} , normalised by the wall-shear velocity, u_{τ_0}	177
B.5 Mean-velocity profiles normalised by u_{τ_0}	178
C.1 rms velocity fluctuations, normalised by u_{τ_0}	180

Acknowledgments

I would like to extend my thanks to my tutor, Dr. Yongmann Chung, for his guidance, supervision and advice during my studies. I would also like to extend my gratitude to Prof. George Rowlands, Prof. Rudolph Roemer and Dr. David Quigley for their kind interest and advice throughout my time at Warwick University. Prof. Rowlands has been exceptional in his most welcome attention and encouragement that has helped me through my postgraduate studies.

I must also take the opportunity to thank my fellow Ph.D. students, Tariq Talha and Edward Hurst, in the Centre for Scientific Computing for their collegial support and our many useful discussions. My gratitude also goes to Ms. Christine Jarvis, the CSC. Secretary, for her kind help and administrative assistance throughout the years. Dr. Matthew Ismail for his administration of the HPC systems. I also thank other Ph.D. colleagues both past and present, Robert Chin, Andrew Ferguson, Ahmed Al-Makky, Dr. Jason Laurie and Dr. Paul Clifford for their friendship and help.

Finally, and most importantly, I thank all my family for their support. My deep gratitude goes to my parents for their continued financial support and encouragement throughout all my years at university, while my grandmother, sister and brother-in-law have given their moral support and endeavoured to keep my spirits up.

Declarations

This thesis, and its contents is my own work unless otherwise referenced. It has not been submitted for a degree at any other university.

Abstract

Turbulent skin-friction control is the subject of much research and the use of transverse (spanwise) oscillating motions offers the means of obtaining a significant reduction in skin-friction. Dielectric barrier discharge (DBD) actuators can be used to generate spanwise oscillating waves but the difficulty in placing a sensor in the area of plasma gives rise to problems in recording near-wall velocities. A modified version of the Shyy et al. (2002) DBD model was integrated into a direct numerical simulation (DNS). This numerical model was used in a series of two-dimensional simulations, in initially quiescent flow, and the results were compared to results reported from experimental investigations. A close affinity was found confirming that the DBD model is satisfactory.

Both a temporal and a spatial, spanwise oscillating flow were investigated. Only one plasma profile was investigated. Three actuator spacings were investigated. Only the largest actuator spacing resulted in a gap between each plasma profile that was larger than the plasma profile width itself. A spatially uniform plasma configuration produced larger $DR\%$ than spanwise wall oscillation for both spatial and temporal waves, maximum $DR = 51\%$ compared to a $DR = 47\%$ for a spanwise wall oscillation. Increased skin-friction reductions originated from the displacement of the Stokes layer.

The spatial wave produced lower skin-friction values than temporal waves for all the configurations. For both spatial and temporal waves the performance of the discrete configurations in producing an overall skin-friction reduction decreased with increasing actuator spacing. Using both temporal and spatial waves, the configuration with the largest spacing, which is relatively small, did not produce a drag reduction for any case that was tested.

Abbreviations

APW	Actuator pair width
CFD	Computational fluid dynamics
DBD	Dielectric barrier discharge
DDBD	Dual dielectric barrier discharge
DNS	Direct numerical simulation
FSM	Fractional step method
GSL	Generalised Stokes layer
MEMS	Microelectricalmechanical devices
PED	Pulse envelope duration
PEF	Pulse envelope frequency
PRF	Pulse repetition frequency
PTSL	Pseudo-temporal Stokes layer
PSSL	Pseudo-spatial Stokes layer
QSV	Quasi-streamwise vortex
RF	Radio frequency
SDBD	Single dielectric barrier discharge
SSL	Spatial Stokes layer
SWO	Spanwise wall oscillation
TSL	Temporal stokes layer

Nomenclature

Δ	Stokes layer thickness
δ	Stokes layer thickness
$\delta_{1/2}$	Wall jet half width
D_m^+	Maximum displacement of oscillation
λ	Wavelength of oscillation
μ	Absolute viscosity
ν	Kinematic viscosity
ω	Vorticity
ϕ	Phase
ψ	Duty cycle, ratio of plasma per unit time
ρ	Density
θ_p	Plasma profile angle
u_{τ_m}	Controlled flow wall-shear velocity
u_{τ_0}	No-control flow wall-shear velocity
a_m	Maximum spanwise acceleration

b	Plasma profile width
c	Phase speed of oscillation
C_f	Skin-friction co-efficient
C_w	Turbulence convection velocity
D_c	Force strength
E	Electric field strength
E_b	Electric breakdown strength
E_o	Maximum electric field strength
F	Force
h	Channel half-height
I	Force intensity
l_s	Stokes layer penetration depth
L_x	Streamwise (longitudinal) length of domain
L_y	Height of domain
L_z	Spanwise (transverse) width of domain
n	Number of actuator pairs
p	Pressure
Q	Wall-normal velocity per unit length
q_c	Electron charge density (C/m^3)
r	Correlation

Re	Reynolds number based on bulk mean velocity, $Re = U_m h / \nu$
Re_τ	Reynolds number based on skin-friction velocity, $Re_\tau = u_\tau h / \nu$
S	Scaling parameter
S_c	Smoothing function constant
S_f	Smoothing function
s_p	Actuator spacing
T	Period of oscillation
t	Time
T_G	Time scale of a generalised Stokes layer
t_i	Point in time where skin-friction averaging starts
T_{opt}	Optimum period of oscillation
u	Streamwise velocity
U_m	Bulk mean velocity
u_s	Velocity of vortex
v	Wall-normal velocity
w	Spanwise velocity
w_j	Maximum steady wall jet velocity
W_m	Maximum spanwise velocity of oscillation
w_{max}	Maximum instantaneous wall jet velocity
W_{min}	Minimum spanwise velocity of oscillation

x Streamwise distance

y Wall-normal distance

y_s Y -location of vortex

z Spanwise distance

z_s Z -location of vortex

Superscript $*$ Dimensional variable

Superscript s Indicates starting vortex scaling by w_j

Superscript $+$ Indicates viscous scaling (based on $u_{\tau,0}$ unless stated otherwise)

$$t^+ = \frac{tu_{\tau}^2}{\nu}, y^+ = \frac{yu_{\tau}}{\nu}, u^+ = \frac{u}{u_{\tau}}$$

Subscript x Indicates in the x -direction

Subscript y Indicates in the y -direction

Subscript z Indicates in the z -direction

Subscript ref Reference variable

Subscript 0 No-control simulation value

Subscript m Controlled simulation value

Subscript w Wall value

Chapter 1

Introduction

1.1 Introduction

Flow control is a broad classification of several different engineering goals including laminar-to-turbulent transition control, flow separation control, mixing enhancement, noise attenuation and turbulent skin-friction control. Near-wall turbulence of a flat-plate consists of coherent structures (Robinson, 1991) such as low-speed streaks and quasi-streamwise vortices (QSV) that form an autonomous cycle (Jimenez and Pinelli, 1999). A result of the near-wall turbulence is 'sweep events' where high momentum fluid is drawn towards the wall increasing the skin-friction (Kravchenko et al., 1993). Control or suppression of near-wall structures or events may result in a reduction in skin-friction drag.

The quest to reduce turbulent skin-friction has been a topic of research for several decades. Turbulent boundary layers and the consequential drag they generate have financial implications in many areas of industry ranging from the movement of oil through pipelines to the fuel consumption of aircraft, shipping and road transport vehicles. The global reliance and ever increasing demand on the world's finite energy resources has not only led to an escalation in energy costs but also increased pressure for the development of energy saving technology such as flow control.

The fuel consumption of the global aviation industry was 155 million tonnes in 2002 and has been estimated to rise to 400 million tonnes by 2030 (Leschziner et al., 2011). Almost 60% of the total drag on an airliner is the result of skin-friction and the development of a viable means of reducing skin-friction would offer the potential for lower fuel consumption and financial benefits. In addition there is increasing environmental concern for economy in fuel use, as the air, sea and road transport industries are responsible for around 30% of the global CO₂ emissions. Achieving just a 1% reduction in the drag on an airliner at cruise conditions would result in a 0.75% drop in fuel consumption and this suggests that there is the potential to achieve a reduction of 9 million tonnes of CO₂ emissions per 1% of drag reduction (Leschziner et al., 2011). From a financial perspective, the airline industry uses 1.5 billion barrels of oil a year, a reduction of 30% would result in a saving of \$45 billion per year based on the current price of oil (Kim, 2011). The Advisory Council for Aeronautics Research in Europe (ACARE, 2001) set targets for 2020 that included a 50% reduction in CO₂ emissions and noise and an 80% reduction in NO_x. The continued demand for global transport, coupled with increasing environmental concerns, enforce the need to improve flow control technology and access the potential environmental and financial benefits that are associated with it.

There are currently several different avenues of investigation of turbulent skin-friction control. One area of particular interest is transverse (spanwise) motions as the result of the movement of the boundary wall or the introduction of a force. Oscillation of the wall or force results in significant skin-friction reductions. One proposed method of producing oscillating spanwise motions is by the use of dielectric barrier discharge (DBD) actuators. Over the past decade the use of these actuators have been investigated for a variety of flow control topics such as separation control (Moreau, 2007).

This current research focuses on the use of DBD actuators for skin-friction control by the generation of oscillating spanwise motions. A model for a DBD

actuator is integrated into direct numerical simulation (DNS) and the effect of actuator spacing and the period of oscillation are investigated for both temporal and longitudinal spanwise oscillating flows.

Chapter 2 presents a brief review of turbulent skin-friction control research with particular regard given to spanwise oscillating flows. DBD actuators and their use in flow control and models of DBD actuators are also reviewed. The DBD model used in this work is outlined in Chapter 3 and descriptions of modifications are given together with the findings from initial simulations. A series of two dimensional simulations are presented in Chapter 4 and a comparison of the flow from a solitary DBD actuator to experimental results is made. This is followed by a parametric study to provide insight on the values to be used for turbulent skin-friction control simulations while the descriptions of the flow generated by a single actuator and a series of actuators are provided.

Chapter 5 presents a large parametric study of DBD actuators to create a temporally oscillating spanwise flow for a large range of periods of oscillation, actuator spacing and maximum velocity. This is followed in Chapter 6 by a study into the use of DBD actuators to create a longitudinally oscillating (spatial) spanwise flow for a range of wavelengths and actuator spacings.

The thesis is brought to a close with a review of the results and recommendations for further research. Appendix A is a self-contained investigation into the use of Helmholtz resonators for turbulent skin-friction control, this was one of the topics of research before focus was placed on DBD actuators.

Chapter 2

Literature review

The effect of the transition of a laminar flow to a turbulent one is to flatten the velocity profile from that of the parabolic (pipe and channel flow) or Blasius profile (zero-pressure gradient) for a laminar boundary layer. The total shear stress τ is the sum of the Reynolds shear stress $-\rho\overline{uv}$ and the viscous stress $\mu(dU/dy)$. For non-accelerating channel and pipe flow, the shear stress decreases linearly from a maximum at the wall ($\tau_w = \mu(dU/dy)_w$) to zero at the centreline. The linear variation of the shear stress, results in a relationship between the Reynolds shear stress and the wall shear stress, where an increase in the Reynolds stress results in an increase in the wall shear stress (Adrian, 2007).

Therefore the motions that cause the u and v components to be anti-correlated are of most importance, and the suppression of these motions would lead to skin-friction reductions, and the benefits this produces. Although there is no standard definition, such motions and other organised motions that are persistent in time and space and contribute to the transport of heat, mass and momentum are regarded as coherent structures (Adrian, 2007). Close to the wall, in the buffer layer, the two structures of most importance are the quasi-streamwise vortices (QSV) and the corresponding low speed streaks where the QSVs lift lower speed fluid upwards from the wall, the two structures together form an autonomous cycle (Robinson,

1991; Jimenez and Pinelli, 1999; Adrian, 2007). As a QSV draws higher momentum fluid towards the wall i.e., sweep on one side, and low-speed fluid drawn away from region near the wall i.e., ejection, they are responsible for large skin-friction increases (Kravchenko et al., 1993). Such vortices have been observed to be up to 200 wall units in length, but can overlap in their streamwise extent to produce streaks of low and high speed fluid > 1000 wall units length. These streaks and QSVs are predominant in the buffer region and are also observed in the logarithmic region. The scale of the coherent structures growing with increasing distance from the wall (Adrian, 2007).

The QSVs are the basis of the legs of hairpin vortices (also known as horse-shoe eddies, hairpin vortices and hairpin eddies), which are present in the logarithmic layer and wake region but become less frequent with increasing distance from the wall. They can occur singly or in streamwise orientated packets. These structures are believed to be a mechanism for the transport of vorticity, low momentum fluid and turbulent kinetic energy away from the wall but are not the exclusive mechanism for such transport (Adrian, 2007; Marusic et al.). Control or suppression of near-wall structures may result in a reduction in skin-friction drag (Kim, 2011).

Within this thesis the term drag reduction is frequently used, the term drag reduction can imply a reduction in any of the resistible forces that act on an object that interacts with a fluid, but in this work it applies to a skin-friction reduction only.

A brief review of turbulent skin-friction control is presented in Section 2.1, followed by a more in-depth review of skin-friction control by spanwise motions in Section 2.2. In Section 2.3, DBD actuators, DBD models and their use in flow-control research, in particular for turbulent skin-friction control is examined.

2.1 Flow Control

Turbulence skin-friction control strategies are usually grouped into two categories. The first set are defined as 'active' and require an external energy source during operation while the second set are referred to as 'passive' and require no energy to operate (Gad-el Hak, 2000; Joslin et al., 2005; Gad-el Hak, 1996).

An initial measurement of the success of a turbulent flow control system is the amount of skin-friction reduction achieved and the gross resultant energy saving that this produces (Joslin et al., 2005). However as active systems expend energy to obtain a skin-friction reduction this energy expenditure has to be taken into consideration and the net energy saving is calculated to determine if an energy saving in addition to a skin-friction reduction has been achieved (Baron and Quadrio, 1996; Choi and Moin, 1994). In the case of industrial application of a system, several other factors have to be considered including the ease and cost of implementation, the survivability of the system e.g., tolerance to dirt, the maintenance requirements and in some circumstances the weight.

Several examples of passive strategies have been utilised with varying degrees of success. The injection of polymer solutions in the order of only a few (weight-part-per-million) into liquid pipe flows has resulted in drag reductions (DR) of more than 50% and for many years has been a commercial product utilised in industrial piping e.g., oil pipelines (Joslin et al., 2005).

Nature has also provided inspiration when scientists became intrigued by the ability of dolphins to maintain high speeds in water and this lead to research in compliant surfaces, which are believed to delay laminar to turbulent transition (Carpenter et al., 2000; Joslin et al., 2005). Other aquatic animals e.g., sharks and seals, have inspired research into riblets (Garcia-Mayoral and Jimenez, 2011), which are believed to act as longitudinal fences that affect the evolution and disposition of quasi-streamwise vortices (QSV) (Choi et al., 1993; Karniadakis and Choi,

2003). Riblets have produced a skin-friction reduction in the order of a 10% and a 2% drag reduction on an Airbus A320 which had 70% of its surfaces covered in riblets, but unfortunately there were reliability/maintenance issues caused by dirt and temperature effects. (Joslin et al., 2005; Garcia-Mayoral and Jimenez, 2011). Riblets have also been used with success on the hulls of competition sailing vessels, olympic rowing boats and swimsuits (Karniadakis and Choi, 2003). The impact of riblets in these competitive sports resulted in their use being actively suppressed in some sports by regulations.

Active strategies can be divided into two sub-categories dependent on their control mechanism and are either 'open-loop' or 'closed-loop' controlled strategies. The former acts broadly, manipulating the flow to a predetermined routine set for the particular flow conditions. The latter contain not only an actuation system, but a sensory and feed-back control element, that analyses the flow situation and manipulates certain structures or events e.g., a sweep event (Gad-el Hak, 2000).

Microelectricalmechanical systems (MEMS) technology has provided the potential to sense and manipulate near-wall turbulence (Jeon and Blackwater, 2000; Cattafesta and Sheplak, 2011). A closed-loop strategy that has been the subject of much interest is the opposition control envisaged by Choi et al. (1994). Numerically this control strategy has been found to produce a 25% reduction in skin-friction, with a large net power saving (Choi et al., 1994; Chung and Talha, 2011). However this strategy ideally requires velocity information within the flow and there has been much research into control algorithms using wall data alone. In addition the manufacture of sensors and actuators for such a strategy is not without difficulties (Cattafesta and Sheplak, 2011). Opposition control is covered in more detail in Appendix A.

There are many examples of 'open-loop' strategies within the field of flow control, but for turbulent skin-friction control the open-loop strategy of most interest is active spanwise motions. These have been found to produce skin-friction

reductions of over 40% and are discussed in detail in the next section. A comprehensive review of flow control strategies is given by Gad-el Hak (2000) and a review of flow control and noise control strategies and the relationships between them is provided by Joslin et al. (2005).

2.2 Spanwise motions

Jung et al. (1992), were the first to suggest from use of DNS that a drag reduction could be obtained by oscillating the wall of a bounded flow in a spanwise direction to provide a sustained reduction in skin-friction. This work was inspired by earlier observations, as for example example that of Moin et al. (1990), that when a boundary layer is subjected to a constant spanwise pressure gradient the production of turbulence is temporarily suppressed in a transient state, however this transient state is followed by a new steady state with a higher Reynolds stress than that of the original flow.

Jung et al. (1992) oscillated the wall at a prescribed spanwise velocity:

$$w(t) = W_m \sin \frac{2\pi}{T}t. \quad (2.1)$$

Where T , is the period of oscillation and W_m , is the maximum spanwise velocity or amplitude of oscillation. They found that the skin-friction reduction was strongly dependent on the period of oscillation with the largest reduction $DR=40\%$, obtained at $T^+ = 100$. Observations on the mechanism for the drag reduction revealed that there was an upward shifting of the logarithmic layer suggesting a thickening of the viscous sub-layer and a reduction in the intensities of velocity fluctuations by up to 35%.

Laadhari et al. (1994), carried out an experimental investigation into the effect of spanwise oscillation on a turbulent boundary layer, and found a reduction in the near-wall velocity gradient with a reduction in the velocity fluctuations. This

supported the results of the numerical investigation by Jung et al. (1992). Laadhari et al. (1994) suggested that the drag reduction was a result of modification in the displacement between quasi-streamwise vortices (QSV) and their associated low speed streaks. An experimental investigation by Choi et al. (1998) found a maximum skin-friction reduction of 45% occurred downstream of the leading edge of the oscillating wall and a gradual return to normal, downstream from the trailing edge of the oscillating plate. Choi and Graham (1998) also experimentally achieved a 25% skin-friction reduction in pipe flow using spanwise wall oscillation.

As spanwise wall oscillation is an active flow control strategy, its viability was not assessed until Baron and Quadrio (1996) found by use of DNS that with low amplitudes of oscillation, $W_m^+ = 4.5$ and $T^+ = 100$, a net energy saving of 7% could be obtained. However at higher amplitudes there they found a larger rise in the energy expended to saved, so that there was a net energy cost. They suggested that the turbulence reduction was the result of a disruption in the spatial coherence between the QSVs and the low speed streaks. The oscillation creating a Stokes layer, and its thickness was dependent on the period of oscillation.

Choi et al. (1998) proposed that the Stokes layer interacted with the viscous sublayer to reduce the skin-friction. The Stokes layer contains a sheet of positive or negative streamwise vorticity depending on the direction of forcing. This vorticity sheet is tilted in the positive or negative spanwise direction depending, on the direction of the wall movement and thus always produces an increase in the positive spanwise vorticity in the near-wall region. This consequently leads to a reduction in the streamwise velocity gradient, and a reduction in the length of QSVs and thereby weakening sweep events. Choi and Clayton (2001) concluded that the thickness of the viscous sub-layer was of comparable size to that of a laminar Stokes layer that would be produced by the oscillating surface.

Dhanak and Si (2000) suggested that spanwise wall oscillations lead to rapid decay in QSVs and a corresponding weakening of slow speed streaks, attenuating

the self sustaining mechanism between them, consequently reducing the sweep and ejection events.

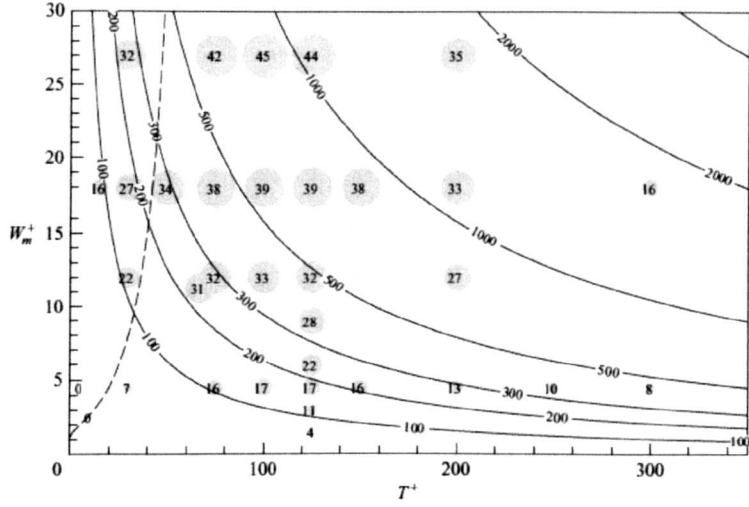


Figure 2.1: Three-dimensional plot of $DR\%$ versus T^+ and W_m^+ . The size of the circles is proportional to $DR\%$. Hyperbolae are curves of constant maximum displacement D_m^+ . Taken from Quadrio and Ricco (2004).

Spanwise wall oscillations are defined by two parameters, the period of oscillation, T_p and spanwise velocity, W_m . A third parameter D_m^+ the maximum displacement of the wall during an oscillation, can be defined from the the first two parameters:

$$D_m^+ = \frac{W_m^+ T^+}{\pi}. \quad (2.2)$$

Optimisation based on W_m^+ and T^+ would result in an alteration to D_m^+ , however for many experimental investigations D_m^+ is fixed (Quadrio, 2011). Quadrio and Ricco (2004) undertook a large numerical study to find two optimal periods of oscillation, one for a fixed displacement, D_m^+ and one for a fixed amplitude, W_m^+ . Figure 2.1 is a plot of the drag-reduction data given and illustrates the dependency of the percentage drag reduction on the two parameters, W_m^+ and T^+ . The percentage skin-friction reduction is displayed within the circles. Lines with constant maximum displacement of the wall, D_m^+ , are hyperbolae in this plane. Quadrio and Ricco

(2004) showed that for all amplitudes tested the optimum period of oscillation $T_{opt}^+ = 100 \sim 125$. The skin-friction reduction increases with W_m^+ , for a fixed period of oscillation, but the rate at which the skin-friction reduction increases with W_m^+ keeps decreasing.

Realising the similarity of the spanwise mean velocity field created by turbulent DNS simulations to that of the laminar Stokes boundary layer Choi et al. (2002), produced a scaling parameter for skin-friction reduction based on the oscillation parameters. They started with the laminar solution of the Stokes second problem:

$$w^+(y^+, t^+) = W_m^+ \exp(-y^+ \sqrt{\pi/T^+}) \sin\left(\frac{2\pi}{T^+} t^+ - y^+ \sqrt{\pi T^+}\right), \quad (2.3)$$

and then derived a wall-normal length scale related to the depth the Stokes layer has influence into the turbulent flow:

$$l_s^+ = \sqrt{\frac{T^+}{\pi}} \ln\left(\frac{W_m^+}{W_{th}^+}\right). \quad (2.4)$$

The length scale being the furthest distance from the wall where the maximum oscillating velocity has a magnitude higher than a threshold velocity W_{th} , representing a typical value of the spanwise turbulent fluctuations ($w_{rms} \approx 1.0$) (Choi et al., 2002). This is different to the Stokes layer thickness:

$$\delta^+ = \sqrt{\frac{4\pi}{T^+}}, \quad (2.5)$$

where the amplitude of oscillation, W_m^+ , has no bearing. From here the length-scale, l_s^+ , is referred to as the Stokes layer penetration depth. A second variable, a_m^+ , the maximum spanwise acceleration at a given distance, \bar{y}^+ , from the wall is calculated by:

$$a_m^+ = \frac{2\pi}{T^+} W_m^+ \exp(-\bar{y}^+ \sqrt{\pi/T^+}). \quad (2.6)$$

Choi et al. (2002) combined the two parameters to produce a scaling parameter, S^+ , which gave a good correlation with skin-friction reductions obtained both experimentally and numerically.

$$S^+ = \frac{a_m^+ l^+}{W_m^+}. \quad (2.7)$$

Quadrio and Ricco (2004) found excellent correlation between S^+ and the drag reduction with the values $\bar{y}^+ = 6.3$ and $W_{th}^+ = 1.2$. However the correlation deteriorated as the periods of oscillation increased to $T^+ > 150$. Quadrio and Ricco suggested that with increasing T^+ and/or W_m^+ the Stokes layer penetration depth increases suppressing more near-wall turbulence and increasing DR . However, $T_{opt}^+ = 100 \sim 125$ and the deterioration of the correlation between S^+ and DR is because the time scale which represents the life time of the longest lived, and statistically important near-wall turbulent structures becomes greater than the half period of oscillation. The scaling parameter, S^+ , is linearly related to the drag reduction until the period of oscillation is too long and the turbulence has time to redevelop between successive oscillations.

Ricco and Quadrio (2008) further investigated the scaling parameter S^+ and found it correlated well for $W_m^+ < 40$ and $30 < T^+ < 150$, they also found that a minimum spanwise wall velocity W_{min} is required for a drag reduction, with W_{min} increasing as the period of oscillation decreases as the reduction in the penetration depth of the Stokes layer require a stronger forcing to affect the turbulence. For higher periods of oscillation $t^+ > 30$, W_{min} becomes constant, $W_{min}^+ \approx 1.8$. Ricco and Quadrio (2008) also found that the drag reduction decreases slightly as the Reynolds number increases with the effect increasing, with increasing period of oscillation.

2.2.1 Longitudinal standing wave

Spanwise wall oscillations have a spatial counterpart and it is possible to remove the unsteadiness of spanwise wall oscillations and utilise the convective nature of the flow. Although there is no-slip at the wall, the convection velocity of turbulence close to the wall $y^+ < 15$, is essentially independent of the wall distance and remains constant at the value $C_w^+ = 10$ (Kim and Hussain, 1993). This near-wall value of the convection velocity allows the translation of the temporal oscillating wall displacement into a spatially oscillating displacement. Berger et al. (2000) used a modelled temporal oscillating spanwise Lorentz force within DNS:

$$F_z(y, t) = I e^{-y/\Delta} \sin\left(\frac{2\pi}{T}t\right), \quad (2.8)$$

where I , is the intensity, which exponentially decays away from the wall on a length scale or penetration depth Δ . Equation 2.8 was then converted into a longitudinal oscillation equivalent:

$$F_z(y, x) = I e^{-y/\Delta} \sin\left(\frac{2\pi}{\lambda_x}x\right), \quad (2.9)$$

where λ_x denotes the forcing wavelength rather than the period of oscillation. Berger et al. (2000) with longitudinal oscillation produced a skin-friction reduction comparable to temporal oscillation with an improvement in the energy balance. Viotti et al. (2009) recently undertook a large DNS parametric study at $Re_\tau = 200$, using longitudinal wall oscillation. The velocity of the wall defined by:

$$w(x) = W_m^+ \sin\left(\frac{2\pi}{\lambda_x}x\right). \quad (2.10)$$

Once spatially averaged the Stokes layer from the turbulent simulations was found to be laminar like its temporal oscillating counterpart. Both Berger et al. (2000) and Viotti et al. (2009) observed a parallel between longitudinal and temporally oscillating waves through the convection velocity, $\lambda_x^+ = C_w^+ T^+$. The optimum wave-

length, $\lambda_{x_{opt}}^+ = 1000 \sim 1250$ compared well with the optimum oscillation period, $T_{opt}^+ = 100 \sim 125$. However Viotti et al. (2009) stated that the longitudinal oscillation produced larger skin-friction reductions than did temporal oscillation for a given amplitude of oscillation and its oscillation period equivalent. A maximum skin-friction reduction of $DR = 52\%$ was achieved for a wavelength of $\lambda_x^+ = 1250$ and amplitude $W_m^+ = 20$.

2.2.2 Travelling waves

Du and Karniadakis (2000) and Du et al. (2002) proposed a spanwise force that resembles a travelling wave along the spanwise direction:

$$F_z(z, t) = Ie^{-y/\Delta} \sin\left(\frac{2\pi}{\lambda_z}z - \frac{2\pi}{T}t\right). \quad (2.11)$$

Du et al. (2002) reported a $DR = 30\%$ at $Re_\tau = 150$ using DNS, with the low speed streaks attenuated and replaced in turn by large straight ribbons of low speed fluid. Zhao et al. converted the spanwise travelling body force wave into a space and time dependent spanwise wall velocity:

$$w(z, t) = W_m^+ \sin\left(k_z z - \frac{2\pi}{T}t\right), \quad (2.12)$$

Quadrio et al. (2009), converted the wall velocity in Equation 2.12 into a spanwise modulated travelling wave:

$$w(x, t) = W_m^+ \sin\left(\frac{2\pi}{\lambda_x}x - \frac{2\pi}{T}t\right), \quad (2.13)$$

Where the phase speed is:

$$c = \frac{\lambda_x}{T} \quad (2.14)$$

Quadrio et al. (2009) undertook a large DNS parametric study for spanwise modulated wall travelling waves (Equation 2.13) at $Re_\tau = 200$ for a maximum velocity

of $W_m^+ = 12$. The obtained DR values plotted against the angular frequency of oscillation $\omega = \frac{2\pi}{T}$ and the longitudinal wavenumber $\kappa = \frac{2\pi}{\lambda_x}$ are presented in Figure 2.2. The x -axis line represents spatially uniform temporal oscillations (Equation 2.1), while the y -axis line represents longitudinal oscillations (Equation 2.10). The blue triangular region indicates parameters that cause an increase in skin-friction as the phase speed of the oscillation is similar to the speed of the near-wall turbulence, $c = C_w$. The largest drag reduction resides on a red crest line close to the y -axis, and indicates the near optimum performance of streamwise standing waves.

Ricco and Quadrio (2010) went further to find an analytical expression for the transverse boundary layer of a laminar Poiseuille flow for travelling waves, called the generalised Stokes layer (GSL). Defining a time scale for the forcing :

$$T_G^+ = \frac{\lambda_x^+}{c^+ - C_w^+} \quad (2.15)$$

where T_G is the period of oscillation imposed on a turbulent structure as it moves with the speed C_w and reduces to conventional T for space-uniform spanwise wall oscillation. Providing the phase speed of the waves, c , is sufficiently different from the near-wall convection velocity C_w , the skin-friction reduction obtained increases with increasing thickness of the Stokes layer until $T_G \geq 120$. As with space uniform oscillations the trend is that the thicker the Stokes layer the more effective is its interaction in suppressing the near-wall turbulence until the forcing time scale becomes larger than the typical lifetime of the near-wall turbulence.

Spanwise flow control is a simple technique, that has the potential to offer a physical energy saving, and it requires no feedback loops or small scale sensors. Karniadakis and Choi (2003) reviews riblets, spanwise wall oscillations and spanwise travelling waves. Quadrio (2011) has recently provided a review of recent developments on transverse motions for turbulent skin-friction control. Transverse motions have been investigated through wall displacement or a body force such as Lorentz

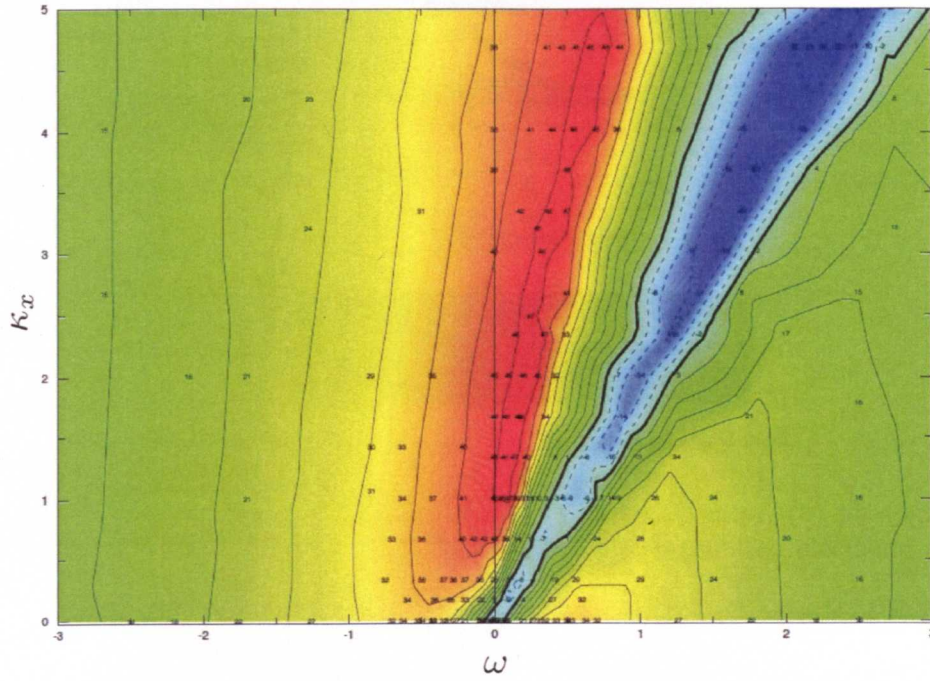


Figure 2.2: Map of DR in the $\omega - \kappa_x$ ($\omega = \frac{2\pi}{T}$ and $\kappa_x = \frac{2\pi}{\lambda_x}$) plane for $W_m^+ = 12$ and $Re = 4760$. Loci of zero DR are indicated by thick lines and negative values are represented by dashed lines. The numbers indicate percentage drag reduction at measured points. Taken from Quadrio et al. (2009).

forcing and Quadrio (2011) suggests that if the penetration depth of the body forcing is small then the spanwise velocity profile induced resembles that produced by an oscillating wall Stokes layer. DBD plasma actuators provide a method of applying a body force on the wall of a turbulent flow and are discussed in the next section.

2.3 Dielectric barrier discharge plasma

Plasma actuators refer to a broad class of devices that use high voltage electrical discharges to provide an induced momentum on fluid. They can be used in active air control to manipulate a flow to provide a desired change in its characteristics. The advantages of plasma actuators are that they are fully electrical with no moving parts, have response times in the order of micro seconds, are cheap to manufacture,

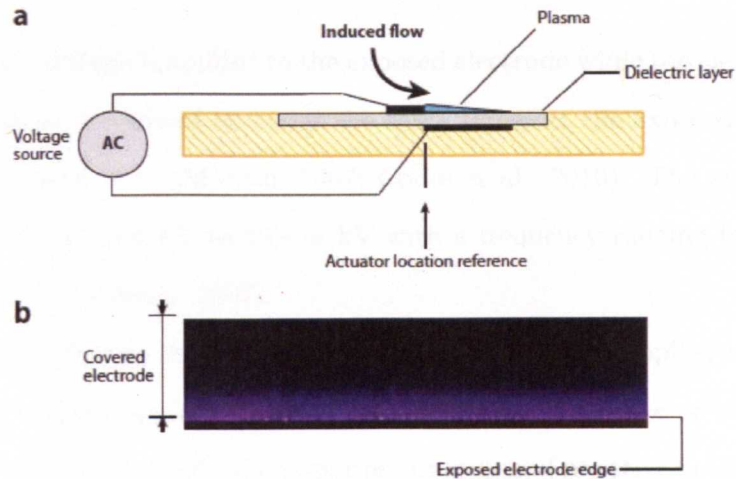


Figure 2.3: (a) Schematic illustration of DBD plasma actuator, (b) photograph of ionized air at 1 atm. pressure that forms over an encapsulated electrode. Taken from Corke et al. (2010).

are of very low mass and can be attached to a pre-existing surface without extensive modifications to the underlying structure. (Jukes et al., 2006a; Moreau, 2007). Moreau (2007) offers a comprehensive review of these actuators.

The most commonly used actuator for flow control, and the subject of this thesis, is a surface Dielectric Barrier Discharge plasma (DBD) actuator. These DBD actuators consist of two electrodes in an asymmetric configuration with one electrode exposed on the surface (wall) and the other encapsulated by a dielectric material (Roth et al., 2000). An example configuration is shown in Figure 2.3(a).

The DBD actuator illustrated in Figure 2.3(a) is termed a single DBD actuator (SDBD) as there is an encapsulated electrode on only one side so a net force is generated in one direction (uni-directional). Double DBD actuators (DDBD) have two grounded electrodes either side of the exposed electrode resulting in the generation of two forces in opposite horizontal directions on both sides of the exposed electrode (bi-directional). Only single DBD actuators are used in this research and when the term DBD actuator is used it is in reference to SDBDs unless otherwise

stated.

An AC voltage is applied to the exposed electrode while the electrode covered by the dielectric is earthed or under the same signal at the exposed electrode but out of phase by $\phi = \pi$, (Moreau, 2007; Corke et al., 2010). The applied voltages can range from several kV to 10's of kV with a frequency ranging from 100 Hz to several 10's kHz (Moreau, 2007).

Figure 2.4 is an illustration of a sinusoidal voltage supplied to the exposed electrode of a DBD actuator but it can also be a square wave or triangular wave (Corke et al., 2010). Initially the potential difference of negative polarity and therefore the electric field strength increases, this first half-cycle is referred as the forward stroke. As the electric field strength reaches the electric breakdown strength, indicated by the point (a) in Figure 2.4, electrons are emitted from the exposed electrode and deposited on the dielectric surface above the encapsulated electrode. This discharge of electrons causes the air to weakly ionise, and this ionised air is referred to as a 'plasma'. Figure 2.3(b) is a photograph of the ionised air that forms over the dielectric surface above the encapsulated electrode. The deposited electrons cause a charge build up on the dielectric surface reducing the potential difference between the electrodes to the point that the discharge ceases at point (b) in Figure 2.4. The discharge is therefore a self-limiting process and in order for it to continue the voltage supplied to the exposed electrode would need to continue to increase, in order to overcome the charge build-up (Corke et al., 2007).

The DBD plasma discharge is thought to be neutral with the discharge containing equal numbers of positive and negative charges which each respond to the applied electric field. The negative charges that are present in the plasma move towards the positively charged electrode while the positive charges move towards the negatively charged electrode. During the other half-cycle, referred to as the backstroke, the polarity of the AC signal is positive and when the potential difference is large enough the electrons that were deposited on the dielectric surface move

back to the now positive exposed electrode (Enloe et al., 2004a; Corke et al., 2007), illustrated by points (c) to (d) in Figure 2.4.

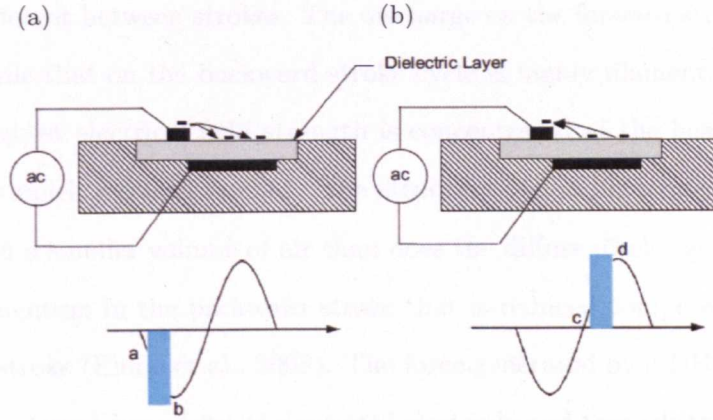


Figure 2.4: Illustration of electron drift that dictates portions of ac period where air ionises in DBD process, (a) forward stroke, (b) backstroke. Taken from Corke et al. (2007)

The plasma appears uniform to the naked eye (Corke et al., 2007) but in reality it consists of a series of individual filaments and discharges. Analysis of the current has shown that during the forward stroke the discharges are frequent and a low charge is transferred between the electrodes by each one, while for the backstroke there is relatively small number of more intense discharges (Enloe et al., 2004a; Pons et al., 2005; Orlov, 2006).

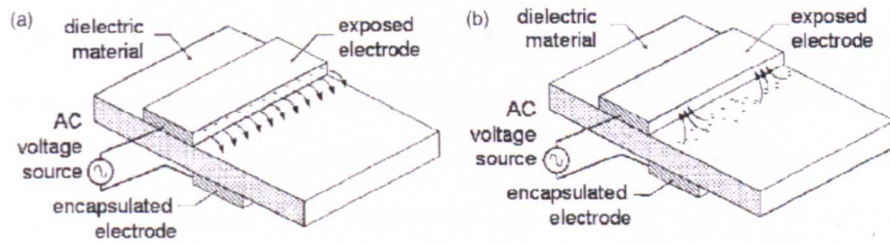


Figure 2.5: Schematic representation of the surface-discharge, (a) forward stroke, (b) backstroke. Taken from Enloe et al. (2008)

The momentum coupling and the way in which the asymmetry between the

half cycles results in a body force is an area of discussion. Enloe et al. (2004a) undertook optical measurements and found that the structure of the plasma is substantially different between strokes. The discharge on the forward stroke is a diffuse discharge while that on the backward stroke cycle is highly filamentary (see Figure 2.5). The highest electrical field strength is concentrated at the head of these filaments and is much reduced behind. The structure of the filaments is such that it interacts with a smaller volume of air than does the diffuse discharge, suggesting an induced momentum in the backward stroke that is reduced compared to that from the forward stroke (Enloe et al., 2008). The force generated by a DBD actuator has been shown to travel away from the exposed electrode and towards the encapsulated electrode (Enloe et al., 2004a; Corke et al., 2007).

One contradictory point is that the momentum inducing positive ions within the forward stroke are attracted in the opposite direction and would therefore create a force going towards the exposed electrode. However studies using different techniques have shown that the oxygen present in air forms negative ions that are responsible for the resultant direction of force (Kim et al., 2007; Enloe et al., 2008). Enloe et al. (2008) reported a 97% to 3% momentum split between the forward and backward stroke respectively, while Kim et al. (2007) concluded that the force generated is always towards the encapsulated electrode, although it is stronger during the forward stroke.

Enloe et al. (2004b) and more recently Forte et al. (2007) and Thomas et al. (2009) explored the optimisation of DBD actuators, the performance of the which depends on several factors including the potential difference and frequency of the signal and the thickness of the electrodes and dielectric.

The flow created by DBD actuators is likened to that of a tangential wall jet (Jukes et al., 2006a; Corke et al., 2007; Forte et al., 2007). The velocity profile broadening and weakening with the y -location of maximum velocity increasing downstream of the actuator (Jukes et al., 2006a; Forte et al., 2007). Figure 2.6 is

an example of the velocity profile of two wall jets created either side of a DDBD actuator. The wall jet creates a starting vortex as it initiates that travels away from the actuator and the wall (Jukes et al., 2006a; Corke et al., 2007), an example is presented in Figure 2.7. Jukes et al. (2008) has also taken temperature measurements and found that the air was heated to approximately 4°C above the ambient temperature and concluded that the flow generated by a DBD actuator is not thermally driven.

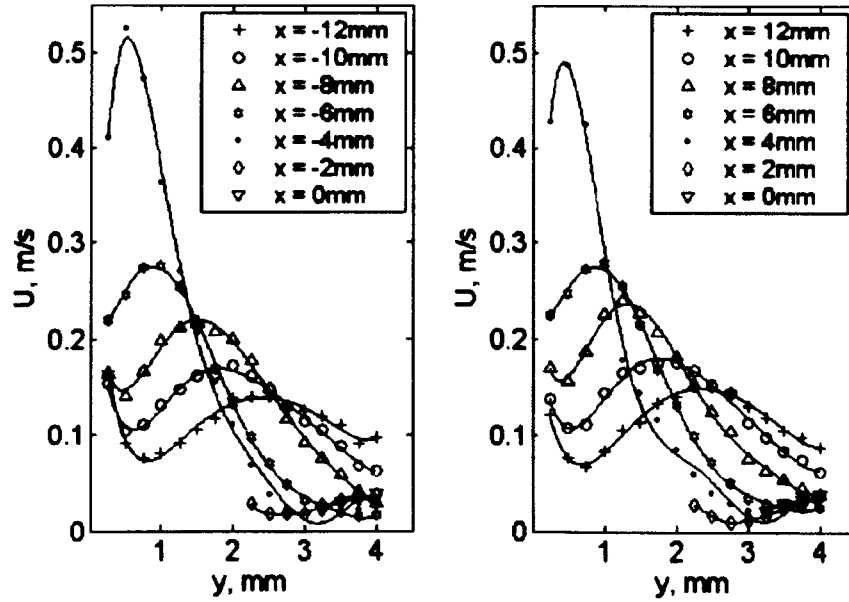


Figure 2.6: Velocity profiles of the wall jets created by DDBD actuator. Taken from Jukes et al. (2006a).

A new type of plasma actuator has been developed in recent years, the sliding discharge actuator consists of three electrodes (Moreau et al., 2007; Corke et al., 2010). Figure 2.8(a) is a schematic diagram of a triode plasma actuator which is a particular type of plasma actuator (Corke et al., 2010). When the triode actuator is operating with only an AC input, it acts like a DBD actuator. Figure 2.8(b) shows that the visible plasma is located only near the edges of the two exposed electrodes, with the addition of a DC current between the two exposed electrodes, causes the

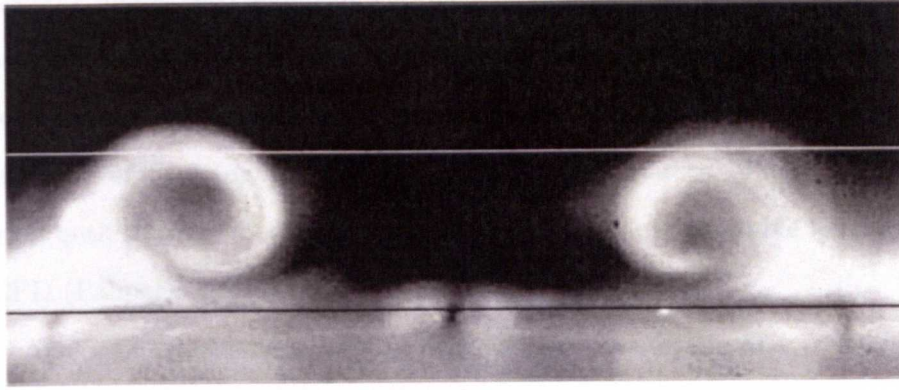


Figure 2.7: Smoke wire flow-visualisation images around a DDBD actuator, the plasma electrode is in the centre of the image. Taken from Jukes et al. (2006a).

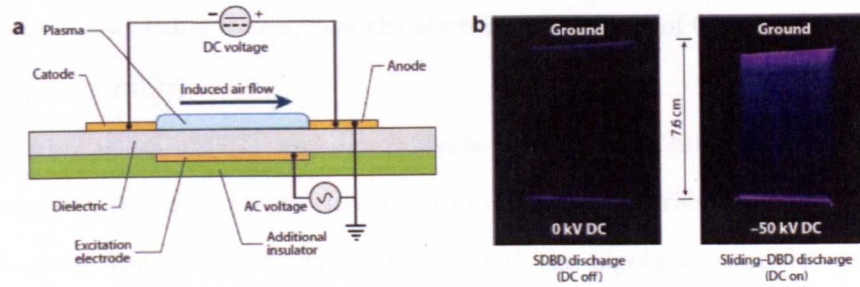


Figure 2.8: (a) Schematic illustration of a triode sliding plasma actuator, (b) photograph of ionised air. Taken from Corke et al. (2010)

plasma to completely fill the gap. The improvement in the plasma coverage from only a few mm to a few cm coupled with the increased maximum obtainable velocity from that of a DBD actuator suggests that sliding actuators offer potential for flow control usage in the future.

2.3.1 DBD models

Numerical models for DBD actuators can be generally split into two categories; algebraic and chemistry based models. There are several examples of chemistry based models (Boeuf and Pitchford, 2005; Singh et al., 2006; Boeuf et al., 2007) and

they usually model the chemical components in the plasma i.e., the ions, electrons and neutral particles and the collisions between them. These models provide a high degree of accuracy in modelling a DBD actuator and are usually developed with the intention of studying the morphology of DBD actuators. These are complex, requiring both small grid spacings and time steps and are unsuitable for integration into CFD (Palmeiro and Lavoie, 2011).

Algebraic models have been utilised more extensively in flow control simulations (Palmeiro and Lavoie, 2011). Shyy et al. (2002) developed one of the earliest and most commonly used models because of its ease of implementation (Corke et al., 2010). The model approximates an electric field linearly decaying from a specified maximum value and assumes a spatially constant charge density. Suzen et al. (2007) developed a model that determines the electric field by use of Gauss Law rather than assuming uniformity.

Orlov et al. (2007) and later Mertz and Corke (2011) proposed a model that emulates the actuator by an electrical circuit of a series of virtual electrodes. Palmeiro and Lavoie (2011) recently reviewed the algebraic models summarising the assumptions required by each model, and the need for empirical calibration to a specific actuator. The Shyy et al. and Suzen et al. models are both reliant on the definition of a charge density, Shyy et al. also requiring a defined profile for the electric field which is linear. While the resistor models, require information on the plasma height and resistivity.

2.3.2 DBD flow control

Since the inception and publication of the first DBD actuator developed by Roth et al. (2000) DBD actuators have been utilised in a considerable range of applications within aerodynamic flow control (Corke et al., 2010). Moreau (2007) provides a review of the airflows manipulated by DBD actuators some examples are: flow separation control on wing sections (Gaitonde et al., 2005; Orlov et al., 2007; Nelson

et al., 2007; Corke et al., 2011), turbine blades (Huang, 2005; Suzen et al., 2007), cavity noise control (Huang and Zhang, 2008) and bluff body wake control (Thomas et al., 2008; Jukes and Choi, 2009a,b; Li et al., 2009; Rizetta and Visbal, 2009).

Wilkinson (2003) developed an experimental concept for creating spanwise oscillations with DBD plasma actuators but, because of difficulties encountered with the signal generation to the actuators, never tested the concept in turbulent flow. Jukes et al. (2006b), conducted a series of experimental investigations into using opposing sets of DBD actuators to create oscillating spanwise wall motions in order to achieve a drag reduction on a turbulent boundary layer, $Re_\tau = 380$. They used a series of actuator pairs orchestrated into two sets and orientated in a spanwise direction running for 1800 wall units downstream. Spanwise alternating wall jets were created by each actuator producing alternating co-rotating vortices in the inner layer of the boundary layer. Several different actuator spacings were used with a maximum spanwise velocity of $W_m^+ = 15$. Near-wall velocity and skin-friction measurements proved difficult however to measure because of the difficulty in placing a sensor in the area of plasma and the heat generated by the actuators (Jukes et al., 2006b; Jukes, 2007).

Choi et al. (2011) recently reported on methods to create travelling waves and temporal spanwise oscillations, suggesting that the DBD actuators create streamwise vortices because the forcing is applied to discrete locations. These vortices reduce the mean velocity in the buffer layer and lower log-law region, but their contribution on the skin-friction was unclear because of difficulty in measuring.

Spanwise motions offer the potential for large skin-friction reductions, methods of actuation are required to introduce a near-wall spanwise forcing into a turbulent boundary layer and plasma actuators offer the potential to do this. Plasma actuators are the subject of current research because of their light weight, simplicity and reliability. A numerical investigation offers the possibility of providing further insight into near-wall flow, which is difficult to achieve experimentally because of

the difficulty in placing a sensor in the area of the plasma actuators.

Chapter 3

DNS and DBD Plasma Model

This chapter briefly outlines the DNS that is used to simulate fluid flow, and also describes the DBD plasma actuator model, based on the model by Shyy et al. (2002) with some modifications, that is integrated as a body force term into the DNS. Further details of the modelling of DBD, in particular actuator pairings, spacings and the signals that the numerical DBD actuators receive. These topics are also frequently discussed in the results chapters. Finally the preliminary simulations, are explained along with their findings.

3.1 Direct numerical simulation (DNS)

Direct numerical simulation (DNS) is the most accurate method of turbulence simulation, allowing the Navier-Stokes equations to be solved directly with no averaging or approximation and DNS is free from errors other than spatial and temporal discretisation errors (Kim et al., 2002b). DNS allows the smallest scales of motion in time and space to be resolved.

The incompressible Navier-Stokes equations can be used as the density changes caused by DBD plasma actuators is considered to be negligible (Enloe et al., 2004a) while the temperature changes caused by DBD actuators is considered to be slight

allowing the temperature to be considered as constant (Jukes et al., 2006a, 2008).

The nondimensional governing equations used are:

$$\frac{\partial u_i}{\partial t} + \frac{\partial}{\partial x_j} u_i u_j = -\frac{\partial p}{\partial x_i} + \frac{1}{Re} \frac{\partial^2 u_i}{\partial x_j^2} + F_i, \quad (3.1)$$

$$\frac{\partial u_i}{\partial x_i} = 0. \quad (3.2)$$

where x_i are the Cartesian coordinates and u_i are the corresponding velocity components in each direction. Re is the Reynolds number and all variables are non-dimensionalised by a characteristic length and velocity scale, which in the case of these simulations is; h the half channel height, U_m the bulk mean velocity of the channel flow, and ρ_{ref} a referenced fluid density.

The numerical procedure used is a fully implicit fractional step method (FSM), proposed by (Kim et al., 2002b), in which both the convective and viscous terms are temporarily discretised by a second-order-implicit Crank-Nicolson method. Finite volume discretisation is used and the momentum equations are integrated on a staggered grid, where the pressure is defined at the cubic cell centre while each velocity component is defined at the centre of the orthogonal planes at the cell faces. A thorough description and proving of the DNS code can be found in Talha (2011).

3.2 Plasma model

An example of a high voltage AC signal supplied to the exposed electrode taken from Jukes et al. (2006a) is illustrated in Figure 3.1, and there are several components to the signal. When the actuator is engaged it is fed a high frequency signal or pulse repetition frequency (PRF) that produces the backstroke and forward stroke discussed in Section 2.3, this signal is normally in the order of 10^4 Hz. The PRF is an oscillating square wave signal (but can be a triangular wave or a sinusoidal

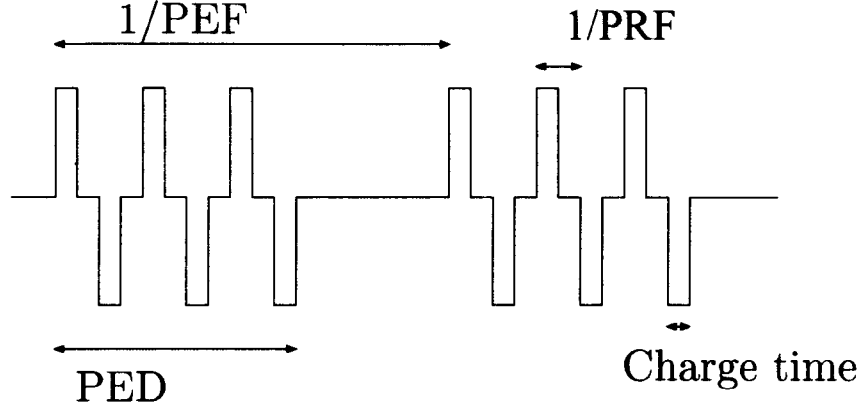


Figure 3.1: Illustration of the signal supplied to a DBD actuator.

wave as the example in Figure 2.4), with the duration of each pulse or charge time in the order of μs . As the charge time duration is so short, and the plasma can only exist in this period, the actual time that the plasma exists in relation to the period of time that the actuator is said to be on is also short (Shyy et al., 2002). The pulse envelope duration, PED , is the period of time that the actuator is engaged, while the pulse envelope frequency, PEF , is the frequency of each pulse envelope. Depending on the design, some DBD actuators can be kept on continually with no envelopes of operation and then they are referred to as running at 100% duty cycle (Whalley, 2011). All the simulations presented in this work use a 100% duty cycle.

3.2.1 Shyy et al. model

The plasma model used in the investigation to calculate the body force term used, is the Shyy et al. (2002) referred to in Section 2.3. This is one of the more commonly used models because of its simplicity and previous use in turbulent simulations (Corke et al., 2010). A concern with the model is that it assumes that the electric field strength, E , decreases linearly from the edge of the exposed electrode toward the surface of the dielectric covered electrode while experiments have alluded to an exponential decrement and, as a result, over-predicts the actuator strength (Corke et al., 2010). The issues of over-prediction are not a concern as the force strength

parameter of the model is tailored to provide a desired spanwise velocity e.g $w^+ = 12$, rather than the model being used to calculate a spanwise velocity for a given physical input signal, based on potential difference and PRF.

Figure 3.2 is a schematic diagram of the plasma profile used by Shyy et al. (2002). The model is two-dimensional in that it creates forces in only two directions, referred to as x and y direction in the original paper. As all the simulations undertaken in this research utilised actuators that were spanwise orientated the forces generated are now in the wall-normal, y , and spanwise, z , direction, so in the following equations x , has been replaced by the spanwise term z to avoid confusion. Also the equations have been further altered from the original by the removal of the height of the profile, (a) , and its replacement with an angle θ_p so that the height is now, $a = b \tan \theta_p$, where b is the width of the profile.

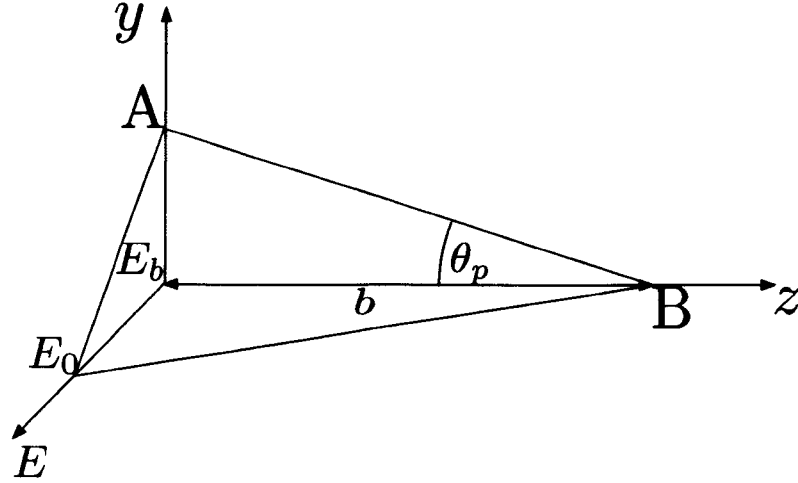


Figure 3.2: Schematic of the plasma profile the line $A - B$ representing the plasma boundary where the electric field strength outside the line is not strong enough to ionise the air. E_0 represents the point of minimum distance between the electrodes and hence maximum electric field strength.

The variation of the vector, E , the electric field strength generated by a

plasma actuator can be written as:

$$E(y, z) = E_0 - \frac{E_0 - E_b}{b}z - \frac{E_0 - E_b}{b \tan \theta_p}y. \quad (3.3)$$

E_0 is the maximum electric field strength and can be represented as the line of shortest distance between the two electrodes, d , and the potential difference of the supplied signal, V so that the dimensionalised maximum electric field strength E_0^* :

$$E_0^* = \frac{V^*}{d^*}, \quad (3.4)$$

where the $*$ represents a dimensionalised term. E_b , the electric breakdown strength, is the electric field strength where plasma ceases and is represented by the line $A - B$ in Figure 3.2. Electric breakdown strength in air is in the order of $E_b = 3 \times 10^6 V/m$.

The electric field strength vector, $|E|$, can be broken down into its components by the following equations:

$$E_z(y, z) = E(y, z) \frac{1}{\tan \theta_p} \left(\frac{1}{\tan^2 \theta_p} + 1 \right)^{-\frac{1}{2}}, \quad (3.5)$$

$$E_y(y, z) = -E(y, z) \left(\frac{1}{\tan^2 \theta_p} + 1 \right)^{-\frac{1}{2}}. \quad (3.6)$$

Which can be simplified as $\theta_p < 90^\circ$ to:

$$E_z(y, z) = E(y, z) \cos \theta_p, \quad (3.7)$$

$$E_y(y, z) = -E(y, z) \sin \theta_p. \quad (3.8)$$

A modification has been made with a minus sign included on the RHS of Equation 3.6, as the original model by Shyy et al. (2002) produces a wall-normal force component going away from the dielectric surface, which is contradictory to experimental findings and a criticism of the original model (Corke et al., 2010).

As the PRF is high while the plasma duration is short, the charge time is

much shorter than the times scale of the fluid flow and the force acting on the fluid when an actuator is engaged can be safely regarded as constant and can be time averaged.

The time-averaged force in the z and y directions are calculated from the following equations:

$$F_i^* = \psi q_c^* E_i^*, \quad (3.9)$$

where q_c , is the electron charge density (C/m^3), ψ is the decimal of the percentage duty cycle.

3.2.2 Integration into the DNS code

Before integration into the momentum equations of the incompressible Navier-Stokes equations, F_i is non-dimensionalised by the addition of the term D_c :

$$F_i = D_c E_i, \quad (3.10)$$

so that Equation 3.1 becomes:

$$\frac{\partial u_i}{\partial t} + \frac{\partial}{\partial x_j} u_i u_j = -\frac{\partial p}{\partial x_i} + \frac{1}{Re} \frac{\partial^2 u_i}{\partial x_j^2} + D_c E_i. \quad (3.11)$$

The term D_c represents the scaling of the electrical to inertial forces, the reference terms and the coefficients of the F_i^* term excluding E_i^* :

$$D_c = \frac{\psi q_c^* q_{c,ref} E_{ref} L_{ref}}{\rho_{ref} U_{ref}^2}, \quad (3.12)$$

where E_{ref} is equal to E_0^* . Therefore all the terms that prescribe the strength of the force as a result of the electric field are amalgamated into the term D_c , while the electric field, E , is defined by the profile width, b , the profile angle θ_p , the maximum electric field strength E_0 and the electric breakdown strength, E_b . In all the simulations undertaken in these studies, $E_0 = E_0^*/E_{ref} = 1.0$ while $E_b = 0.1$.

The effects of altering b and θ_p are investigated and discussed in Chapter 4.

For ease, D_c is prescribed a value rather than one calculated from physical values for its constituent parts. The force created by the actuator can be tailored by altering D_c .

3.2.3 Smoothing Function

It was noted from initial simulations that the plasma profile discretised on to a grid, resulted in one cell on the $y - z$ plane closest to the wall, having the maximum electric field strength, E_0 , while the adjacent cell in the z direction has no forcing. This large disparity between adjacent cells causes large gradients in velocities etc, resulting in rapid and unrealistic fluctuations. A function was added to the plasma model to smooth the profile and reduce numerical instability.

Firstly the centre of the smoothing profile was placed at half the width of the plasma profile, $z = b/2$. For this section of work only Δz is considered to be the non-dimensional spanwise displacement from the centre of the profile normalised by the profile width, b , so that $\Delta z = (b/2 - z)/b$. The function is then defined as:

$$S_f(\Delta z) = \frac{1}{2} \left(1 + \tanh \left(\frac{\frac{1}{2} - |\Delta z|}{s_c} \right) \right), \quad (3.13)$$

where $s_c = 0.25$, an arbitrary value set as such from observation. The value for s_c and consequently the size of the additional area added to the plasma profile is affected by the spanwise grid resolution (see Section 3.5), with higher resolutions reducing the required area of smoothing. F_s is calculated from $\Delta z = -1.0$ to 0 . Once calculated F_s is used in conjunction with the old values of E to calculate a new plasma profile, that for this section only is called E_{new} to differentiate it from the pre-smoothed profile:

$$E_{new}(y, z) = \begin{cases} S_f(\Delta z)E(y, 0) & \text{if } -1.0 < \Delta Z < -0.5, \\ S_f(\Delta z)E(y, z) & \text{if } -0.5 < \Delta Z < 0, \\ E(y, z) & \text{if } 0 < \Delta Z < 0.5, \\ 0 & \text{if } E_{new}(y, z) < E_b. \end{cases} \quad (3.14)$$

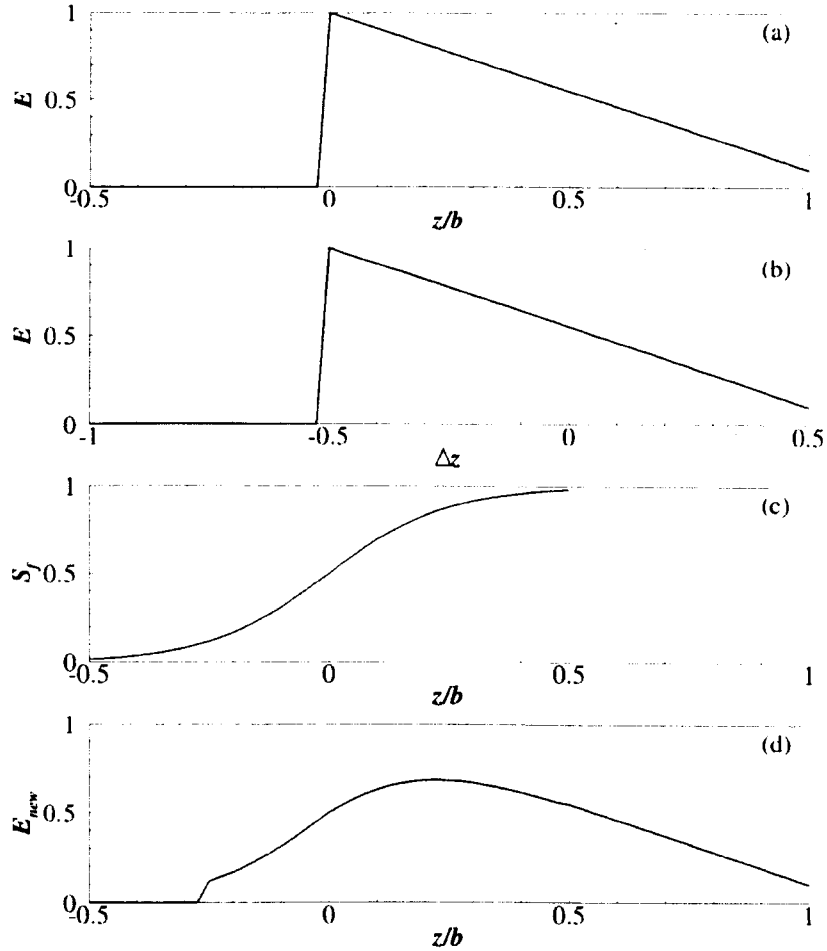


Figure 3.3: Illustration of the smoothing profile: a) original profile generated by the model. b) original profile generated by the model plotted against Δz , ($\Delta z = 0$ at $z/b = 0.5$), c) the smoothing function F_s , d) the smoothed profile.

Figure 3.3. illustrates the smoothing function. Figure 3.3(a) displays the original profile generated by the model with the spanwise displacement normalised

by the width of the profile, b , while Figure 3.3(b) displays the same profile but the displacement represented by Δz as used in the Equation 3.14. Figure 3.3(c) displays F_s as calculated and the new profile as a result of the smoothing is shown in Figure 3.3(d). Figure 3.4 shows the effect of the smoothing profile, note the removal of the local minima close to the wall at $z = -0.25$.

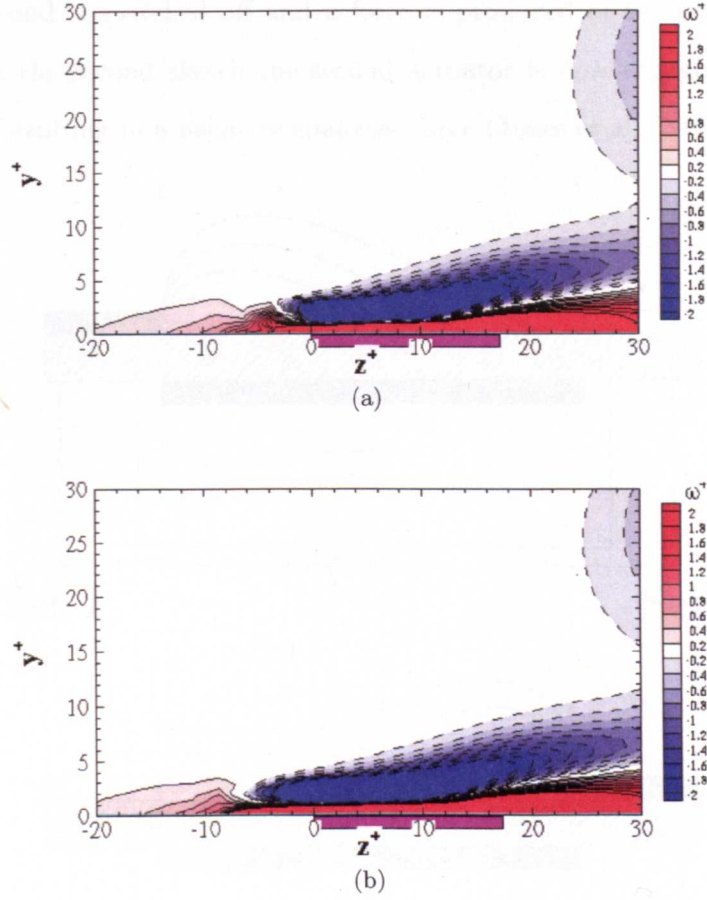


Figure 3.4: Vorticity ω^+ vorticity contours for: a) the original profile b) after smoothing (Quiscent flow, u_τ based on $Re_\tau = 200$). Purple rectangle indicate z -location of plasma.

3.3 Actuator pairs

DBD actuators can be grouped into opposing pairs sharing a common dielectric covered electrode and alternating the signal between each actuator results in the pair of actuators producing a force in alternate directions. Figure 3.5 provides an illustration of such an arrangement. In the first sketch the first actuator is engaged while the second is switched off and a force is produced in the positive spanwise direction. In the second sketch the second actuator is now engaged and the first is switched off resulting in a negative spanwise force (Jukes et al., 2006b).

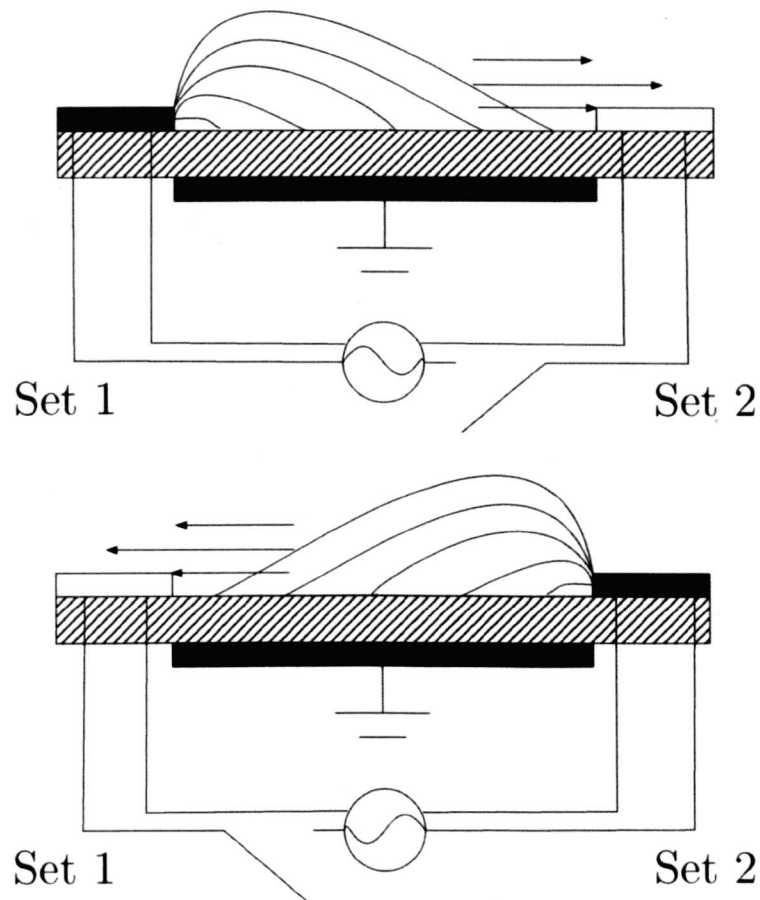


Figure 3.5: Sketch of an actuator pair.

3.4 Multiple actuator configurations

Several plasma configurations are used in the simulations undertaken, where the concentration of pairs of actuators in the spanwise direction is altered. When describing actuator configurations, the plasma actuator concentration is described by the parameter, s_p , which defines the distance between the opposing electrodes on the basis of the number of actuators pairs that would be evenly distributed across the spanwise width of the domain Jukes et al. (2006b). The equation for s_p which is referred to as the actuator spacing is:

$$s_p = \frac{1}{2} \frac{L_z}{n}, \quad (3.15)$$

where n , is the number of actuators pairs.

3.4.1 Uniform plasma

DBD plasma actuators provide a discrete forcing because the generated force from the perspective of a spanwise force along the wall is distributed into individual elements. One of the configurations used in Chapters 5 and 6 is non-discrete uniform plasma. This entails removing the spanwise decrement in the electric field strength, $|E|$ so that:

$$E(y) = E_0 - \frac{E_0 - E_b}{b \tan \theta_p} y, \quad (3.16)$$

and now the electric field, $|E|$, decays linearly in the wall-normal direction only while it is uniform in the spanwise direction as illustrated in Figure 3.7.

3.5 Initial simulations

Before simulations could be commenced to obtain results for evaluation, the spatial resolutions of the grid had to be determined. Grid spacing, used previously for uncontrolled low Reynolds number DNS flows and in flow-control procedures such

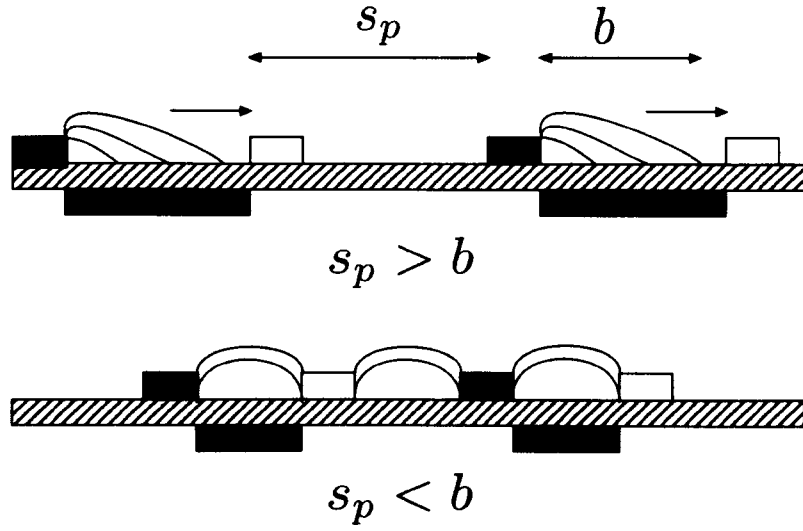


Figure 3.6: Illustration of the effect to the electric field lines, if the actuator s_p is less the plasma width, b .

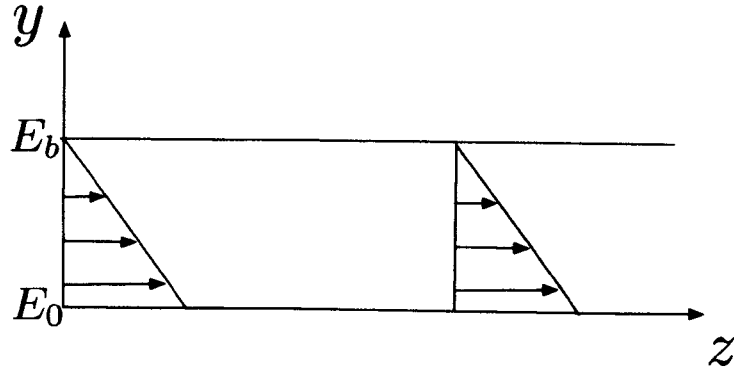


Figure 3.7: Illustration of the electric field distribution of spatially uniform plasma.

as spanwise wall oscillation, are well documented (Kim et al., 1987; Choi et al., 1994; Baron and Quadrio, 1996). However DBD actuators required an evaluation as the plasma profiles are discrete and the force they produce is in-homogenous in the spanwise and wall-normal directions and requires an analysis of the wall-normal (Δy) and spanwise grid spacing (Δz).

Observation of the discretised plasma profiles on the grid alone, led to the

conclusion that the wall-normal grid spacing near the wall needed to be less than that normally used for conventional uncontrolled turbulent DNS channel flow, in order to obtain an acceptably discretised profile.

A series of simulations were run with in which Δz was altered to determine a suitable grid size. Figure 3.8(a) is the spanwise velocity contours from a grid with $\Delta z^+ = 5.0$, which is a suitable grid space for spanwise wall oscillation simulations. However discretising a profile over such a grid spacing would result in the entire profile being conveyed in a 3-4 cell width and the information of much interest, i.e the skin-friction profile in the spanwise direction, would have a limited number of points to exposit the profile. It is evident from Figure 3.8 that increasing the resolution alters the velocity contours which become less irregular as $\Delta z^+ \leq 2.5$. A compromise had to be made between resolution and computational expense and therefore $\Delta z^+ = 2.5$ for the plasma simulations was chosen.

3.5.1 Time step

As the DNS code is fully implicit a time step size, Δt , must be prescribed. Therefore before a set of simulations is run, a time step trial is undertaken using the parameters that would result in the highest value of Re_τ and most likely to produce the highest velocity perturbations and stresses. In the test, simulations are run using a range of time step sizes, the time history of the velocity fluctuations, Reynolds stress and skin-friction velocity from the range of time-steps are then compared. Figure 3.9 is an example of such a profile and it is evident in this case that the profile for the largest time step, $\Delta t^+ = 0.2$ shows increased dependancy on the time step, that was not demonstrated in the lower time steps and is therefore unsuitable.

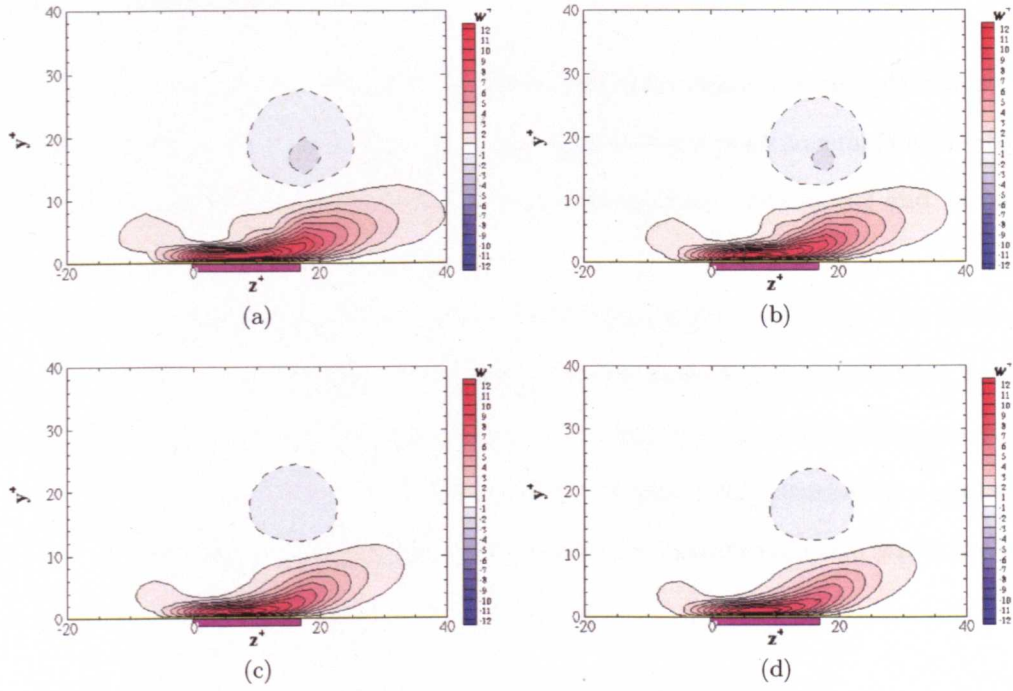


Figure 3.8: Spanwise velocity contours ($Re_\tau = 200$) for a DBD actuator a) $\Delta z^+ = 5.0$, b) $\Delta z^+ = 4.0$ c) $\Delta z^+ = 2.5$ d) $\Delta z^+ = 2.0$. Purple rectangle indicates z -location of plasma.

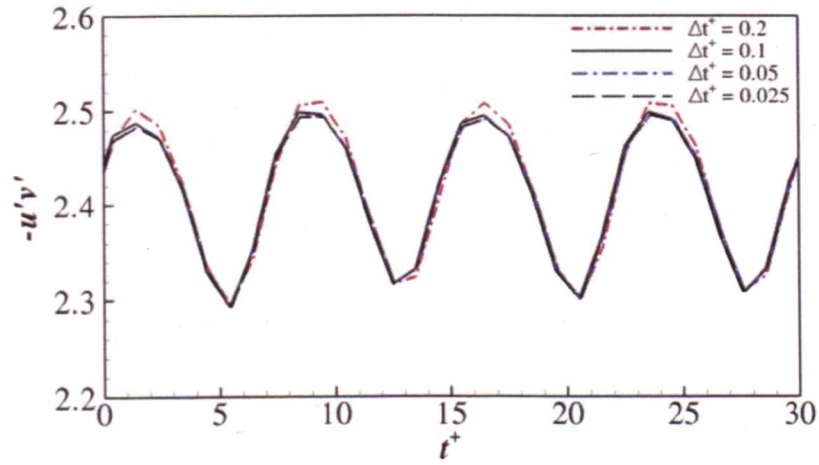


Figure 3.9: Time history for Reynolds shear stress $\overline{u'v'}$, for simulation case 44 (see chapter 5).

3.6 Summary

This chapter has briefly outlined the DNS and then described the plasma model used to calculate the force body term in the spanwise and wall-normal Navier-Stokes equations used by the DNS. Modifications to the original DBD model and variables that defined the model are explained.

The strength of the forcing is altered by changing the value D_c . The intention of this research is to evaluate the changes to the turbulent flow resulting from a prescribed velocity from a plasma actuator and not from a prescribed physical input to an actuator e.g., the potential difference V . Plasma configurations are explained because of the frequent need to discuss these in the results chapters while the grid resolution and time step size are also discussed.

Chapter 4

Quiescent fluid DBD simulations

4.1 Introduction

The plasma model described in Chapter 3 is a modified version of the Shyy et al. (2002) model a prerequisite of which is that parameters that define the profile have to be designated (Palmeiro and Lavoie, 2011). The model parameters that define the strength, D_c , the length of the forcing profile, b , and its angle, θ_p , are altered to investigate the effects of each parameter in order to provide a conclusion as to what parameters need to be used for the turbulent flow simulations. In this Chapter the plasma model is investigated using two-dimensional simulations with initially static fluid i.e., quiescent, in order that the flow generated by a solitary DBD plasma actuator can be investigated. The flow structures and velocity profiles that are generated, in particular the formation and evolution of the starting vortex, may have influence on the turbulent flow simulations. A comparison is then made with various DBD actuator configurations, in order to evaluate the alterations made to the flow characteristics by the presence of several actuators rather than one.

In this chapter the use of the term 'upstream' implies a negative z location

from the actuator reference point, while 'downstream', implies a positive z location from the reference point. The reference point being the point of maximum electric field strength E_o in Figure 3.2 and equates to $z = 0$ in the figures presented in this chapter. In the turbulent simulations in the following chapters, the uncontrolled simulations have a Reynolds number of $Re_\tau = 200$, and for ease of comparison length and velocity scales based on $Re_\tau = 200$ are used in this chapter.

4.2 Method

The results presented here have been computed using the implicit scheme and plasma model described in Chapter 3. The simulations are two dimensional in initially quiescent fluid with the computational domain, $L_y = 2$ and $L_z = 4$. A 129×320 grid was used and the corresponding grid spacings were $\Delta y_{min}^+ = 0.1$, $\Delta y_{max}^+ = 9.0$ and $\Delta z^+ = 2.5$. The time step used was $\Delta t^+ (= \Delta t u_\tau^2 / \nu) = 0.1$. Actuators were prescribed to the top and bottom wall. Periodic boundary conditions were applied in the spanwise direction while no-slip was applied to the top and bottom walls.

4.3 Single DBD actuator

Figures 4.1, 4.2 and 4.3 present the vorticity (ω), z -direction velocity (w), and wall-normal velocity (v), at $t^+ = 10, 20, 40, 60, 90$ and 120 (based on $Re_\tau = 200$) respectively for a single DBD actuator as an example. It is evident that a starting vortex is created as previously observed in experiments (Corke et al., 2007; Jukes et al., 2008), by the formation of a plasma wall jet which causes a vortex roll-up.

As the plasma is initially engaged, at $t^+ = 10$, a wall jet of positive z -direction fluid motion is produced close to the wall at the location of the plasma forcing. There is an area of positive vorticity, but not a vortex, located at the wall (see Figure 4.1(a)), and a negative vortex above that, at the location of the actuator. Upstream of the plasma actuator there is an entrainment of fluid (negative

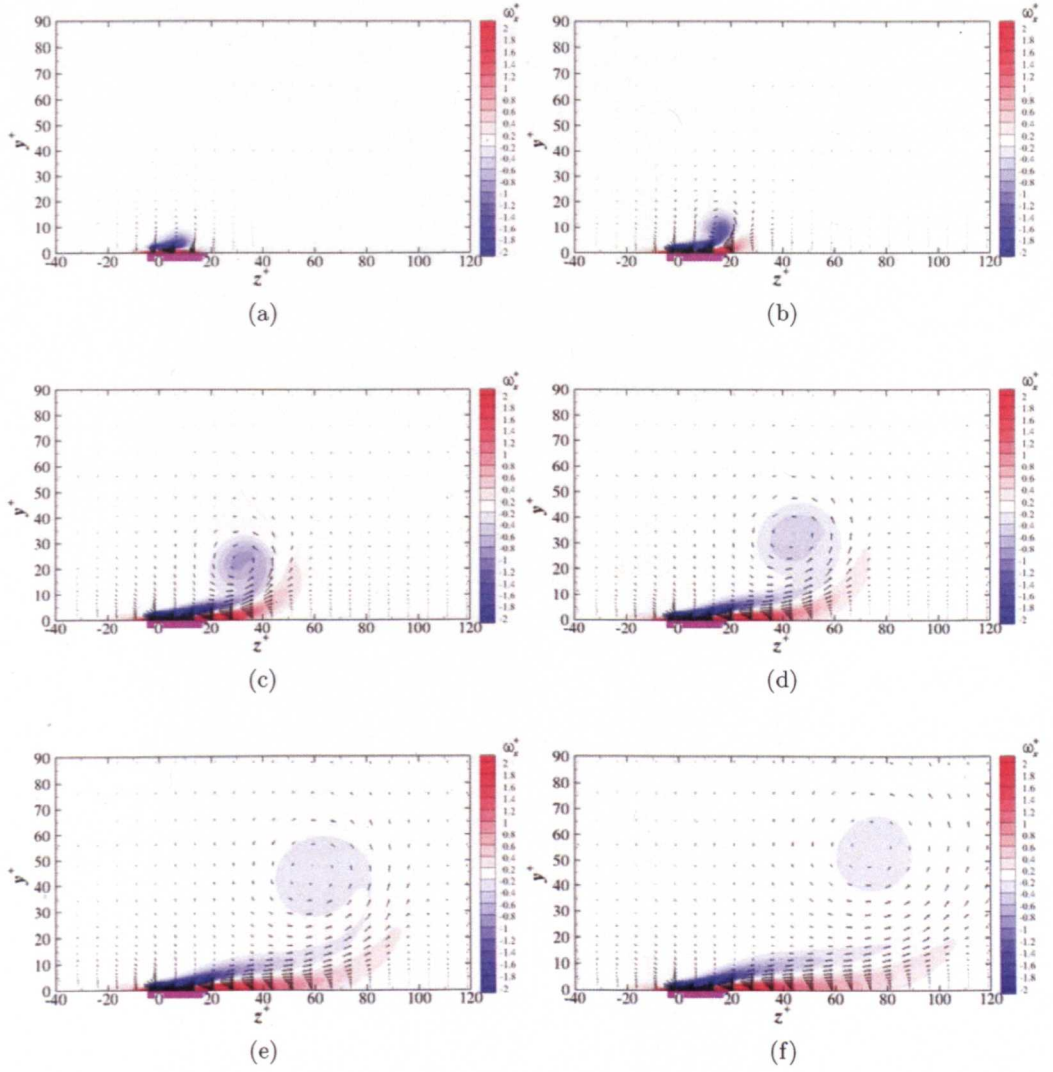


Figure 4.1: vorticity contours ω around a single DBD plasma actuator in initial quiescent flow. Purple rectangle indicates location of actuator strength, $D_c = 40.0$, width of the forcing profile, $b^+ = 17.5$, forcing profile angle, $\theta_p = 10^\circ$: a) $t^+ = 10$, b) $t^+ = 20$, c) $t^+ = 40$, d) $t^+ = 60$, e) $t^+ = 90$ and f) $t^+ = 120$.

wall-normal velocity) towards the wall and downstream of the actuator an expulsion of fluid away from the wall (see Figure 4.3(a)).

At $t^+ = 20$, the wall jet has propagated further in the spanwise direction and has started to roll upwards resulting in the formation of a vortex of negative vorticity. By $t^+ = 30$ a starting vortex, generated by the initial roll-up of the

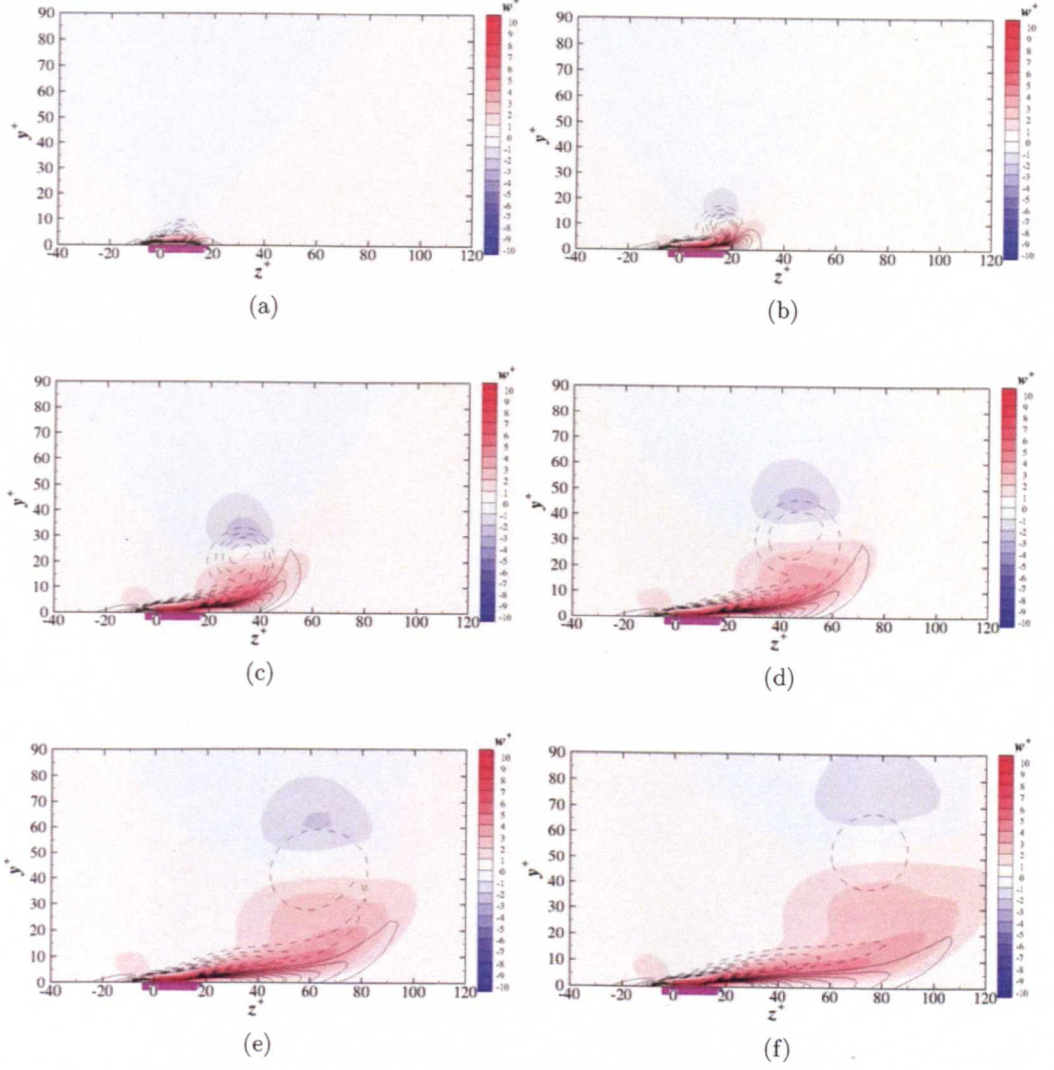


Figure 4.2: Z-direction velocity contours w around a single DBD plasma actuator in initial quiescent flow. Purple rectangle indicates location of actuator, strength, $D_c = 40.0$, width of the forcing profile, $b^+ = 17.5$, forcing profile angle, $\theta_p = 10^\circ$: a) $t^+ = 10$, b) $t^+ = 20$, c) $t^+ = 40$, d) $t^+ = 60$, e) $t^+ = 90$ and f) $t^+ = 120$.

spanwise wall jet, has begun to separate from the area of vorticity situated above the plasma actuator. The starting vortex is travelling at approximately 32° to the horizontal in a positive z -direction, however it is at a much slower speed than that of the wall jet velocity at approximately $u_s^+ = 0.5$. Figures 4.2(c) and 4.3(c) show the previously observed wall jet still producing entrainment of fluid upstream and

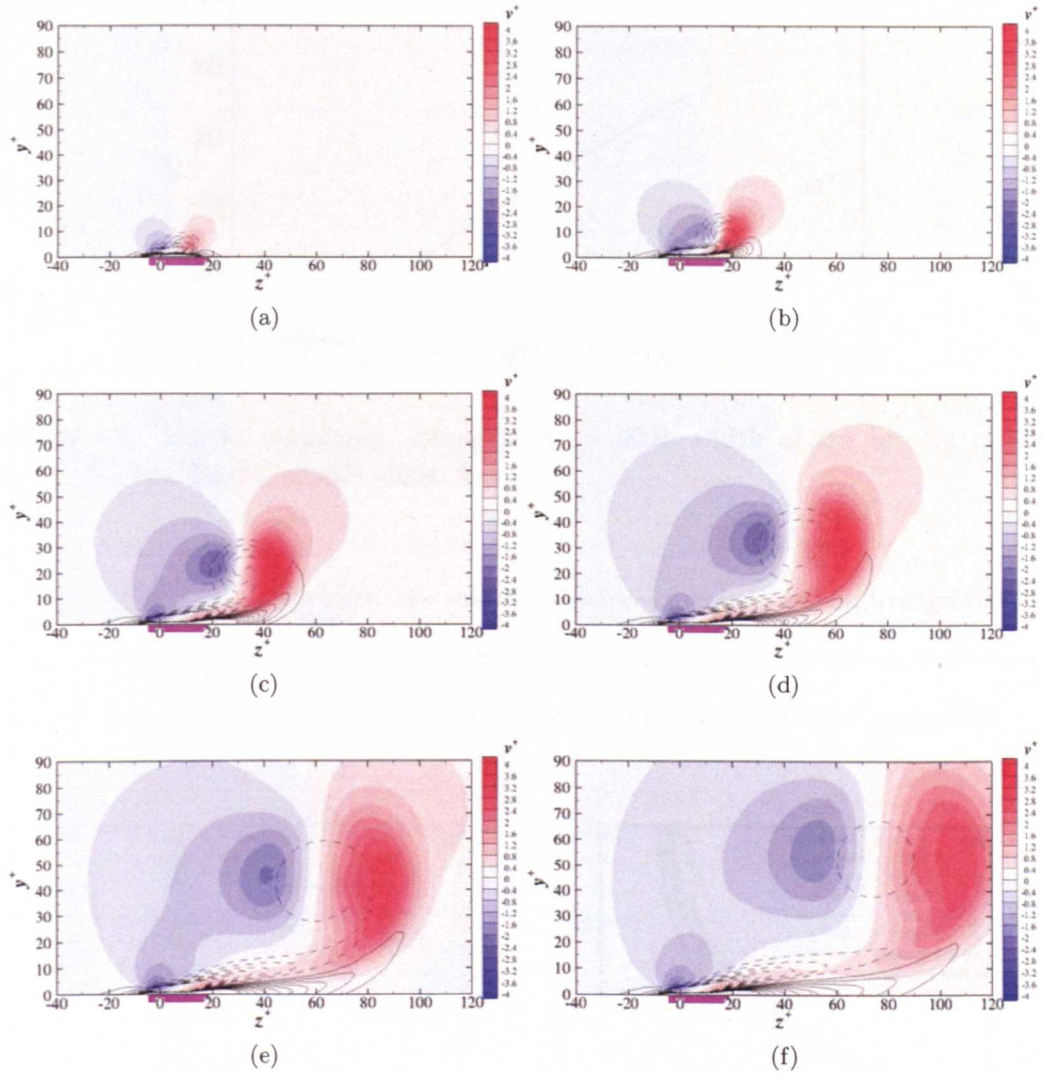


Figure 4.3: Wall-normal velocity contours v around a single DBD plasma actuator in initial quiescent flow. Purple rectangle indicates location of actuator, strength, $D_c = 40.0$, width of the forcing profile, $b^+ = 17.5$, forcing profile angle, $\theta_p = 10^\circ$: a) $t^+ = 10$, b) $t^+ = 20$, c) $t^+ = 40$, d) $t^+ = 60$, e) $t^+ = 90$ and f) $t^+ = 120$.

ejection of fluid downstream of the actuator and with large fluid motions caused by the starting vortex.

Consequently in time the flow structure evolves, with the wall jet propagating further downstream of the actuator, and producing an area of positive vorticity close to the wall with a corresponding area of negative vorticity above it. Figure 4.4 is the

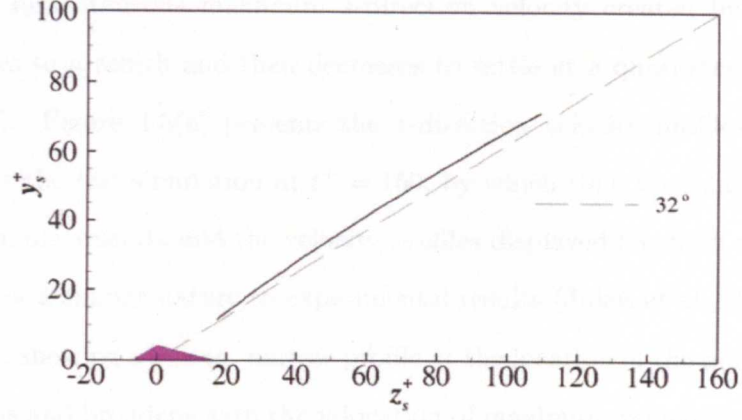


Figure 4.4: Vortex trajectory, strength $D_c = 40.0$, width of the forcing profile, $b^+ = 17.5$ and forcing profile angle, $\theta_p = 10^\circ$.

vortex location (y_s, z_s) in time, the velocity field was interpolated on to a grid of five fold increase in resolution, and the core was defined as a local minimum in vorticity. The starting vortex continues to travel at approximately 32° to the horizontal.

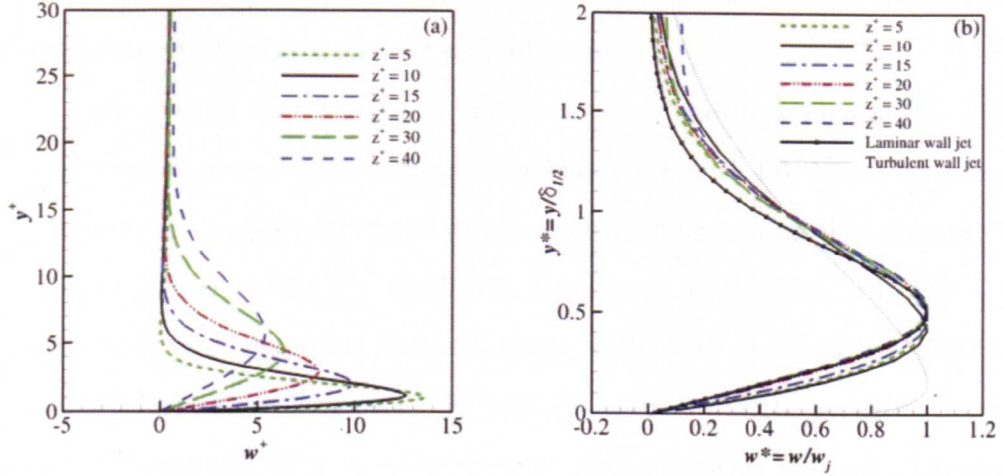


Figure 4.5: Velocity profiles at various z locations, at $t^+ = 150$: a) original data, b) velocity profiles normalised with the maximum velocity, W_m^+ , and the jet half-width, $\delta_{1/2}$. (Laminar and turbulent jet profile from Glauert (1956)).

The instantaneous maximum z -direction velocity created by the actuator initially rises to a zenith and then decreases to settle at a quasi-steady value, (see Section 4.5). Figure 4.5(a) presents the z -direction velocity profiles at various z locations for the test simulation at $t^+ = 150$, by which time the quasi-steady state in the maximum velocity and the velocity profiles displayed has been achieved. The profiles are of a similar nature to experimental results (Jukes et al., 2006a; Moreau et al., 2007), showing a strong, narrow profile at the location of the plasma actuator, that weakens and broadens with the y -location of maximum velocity moving further away from the wall with increasing distance from the plasma actuator. Figure 4.5(b) is the nondimensional profiles of the same data, where the velocity for each profile has been normalised by the maximum spanwise velocity for that profile, w_j , and the jet half-width, $\delta_{1/2}$, which is the y -location where the velocity had reduced to $w_j/2$. The theoretical profile of a laminar and turbulent wall jet, derived by Glauert (1956) are also plotted, and it is evident that as reported in experimental results for DBD actuators (Jukes et al., 2006a) the velocity profile created by the plasma model is close to that of a laminar wall jet profile.

The general observations of the evolution of the flow created by a DBD actuator during several simulations are presented in Figure 4.6. When the actuator is switched on, a wall jet is created which expels fluid away from the actuator. This jet creates a large shear, $\frac{dw}{dy}$, which is a component of vorticity, $\omega = \left(\frac{dw}{dy} - \frac{dv}{dz} \right)$, leading to areas of opposing vorticity above and below the wall jet. The large spatial z -direction acceleration of the wall jet upstream of the actuator results in continuity entraining fluid, from behind and above, towards the wall. The spatial development of the wall jet is initially short, and results in a large $-\frac{dw}{dz}$ component and wall-normal expulsion of fluid at the front of the jet profile, as represented by the arrowhead in Figure 4.6, leading to the jet 'rolling up'. The roll-up produces a $\frac{dv}{dz}$ gradient, as does the entrainment upstream of the actuator and, coupled with the shear, a vortex is formed. This 'starting vortex' then travels at approximately 32° to

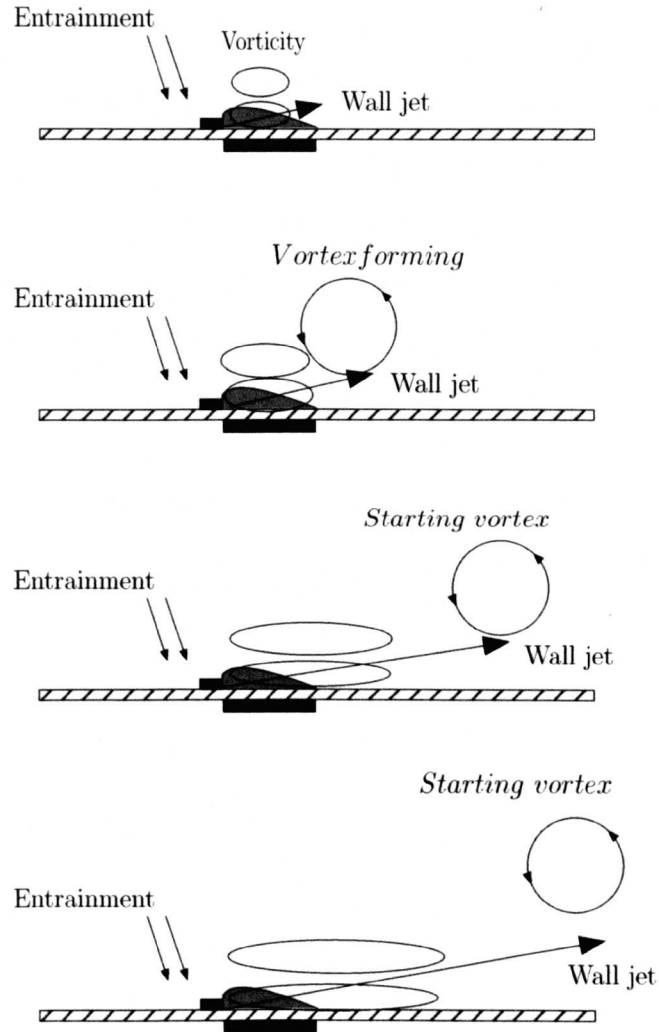


Figure 4.6: Sketch based on previous diagram by Whalley (2011) of the evolution of the flow created by a solitary DBD plasma actuator.

the horizontal, reducing in strength while broadening in size and moving at a much slower speed to the wall jet velocity. The wall jet itself, and the shear it produces, both slowly propagate spatially in the z direction. This results in a reduction in the $-\frac{dw}{dz}$ component so reducing the intensity of the expulsion. However the $+\frac{dw}{dz}$ component upstream of the actuator remains strong and consequently there is a strong entrainment of fluid.

4.4 Profile parameters

As mentioned in the introduction to this chapter, the variables that mainly define the plasma forcing profile; the strength, D_c , the length of the forcing profile, b , and its angle, θ_p , are varied individually to investigate the consequent effects, and to provide a guidance on the parameters to be used for the turbulent flow simulations. Baseline values of $D_c = 40$, $b^+ = 17.5$ and $\theta_p = 10^\circ$ are used, and for each parameter study, one value is alternated while the other two values remain at the baseline value.

4.4.1 Effect of strength, D_c

The result of altering the strength, D_c , from $D_c = 30 - 70$ on the wall jet velocity profile, is shown in Figure 4.7. The jet profile at $z^+ = 10$, a location within the actuator where the highest velocity normally occurs, is shown in Figure 4.7(a) while Figure 4.7(b) shows the profile at $z^+ = 30$ a location downstream of the actuator, the wall jet velocity increases with increasing D_c .

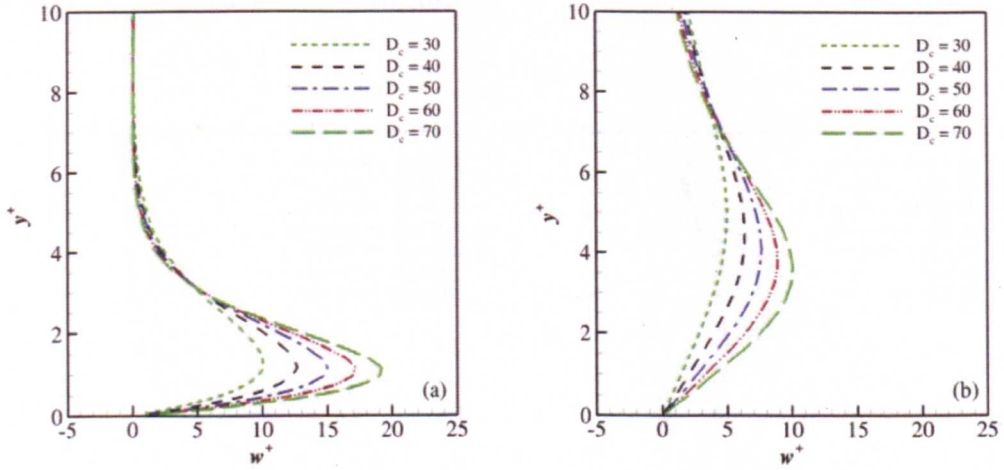


Figure 4.7: Velocity profiles for various strengths, D_c at $t^+ = 150$: a) $z^+ = 10$, b) $z^+ = 30$.

In Figure 4.8 the location of the starting vortex cores against time for the

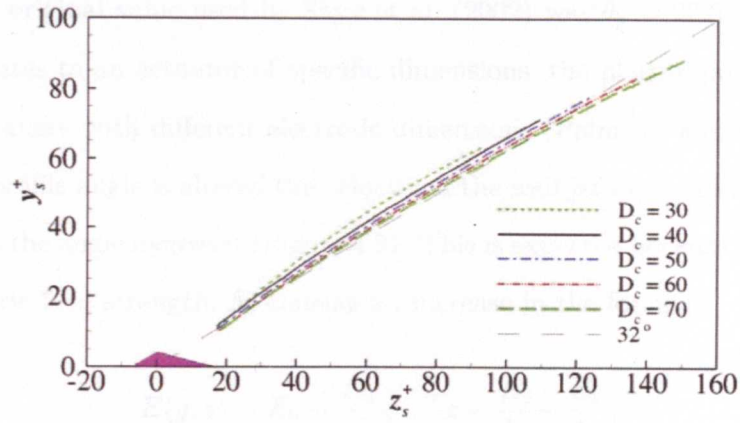


Figure 4.8: Vortex trajectory for various strengths, D_C . Purple triangle indicates location of plasma.

various D_c strengths are shown. The trajectories of the vortices are very similar for the different strengths and have a similar angle to the horizontal in the range of 32° . The total displacements, and consequently velocity of the vortex increases with increasing strength.

4.4.2 Effect of profile angle, θ_p

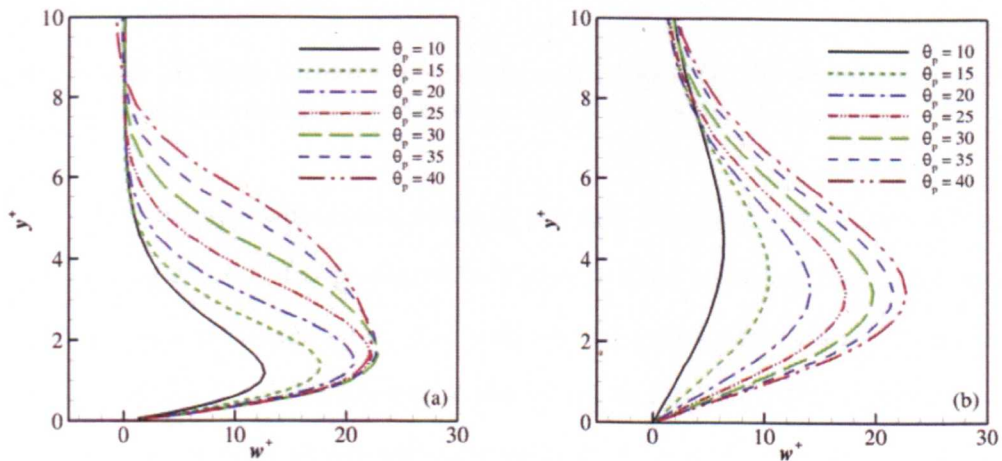


Figure 4.9: Velocity profiles for various profile angles, θ_p at $t^+ = 150$: a) $z^+ = 10$, b) $z^+ = 30$.

The original value used by Shyy et al. (2002) was $\theta_p = 22.5^\circ$, however this value is relates to an actuator of specific dimensions, the plasma profile of a DBD actuator changes with different electrode dimensions (Palmeiro and Lavoie, 2011). When the profile angle is altered the velocity of the wall jet increases and the profile broadens as the angle increases (Figure 4.9). This is expected because of the increase in the electric field strength, E , causing an increase in the forcing:

$$E(y, z) = E_0 - \frac{E_0 - E_b}{b}z - \frac{E_0 - E_b}{b \tan \theta_p}y. \quad (3.3)$$

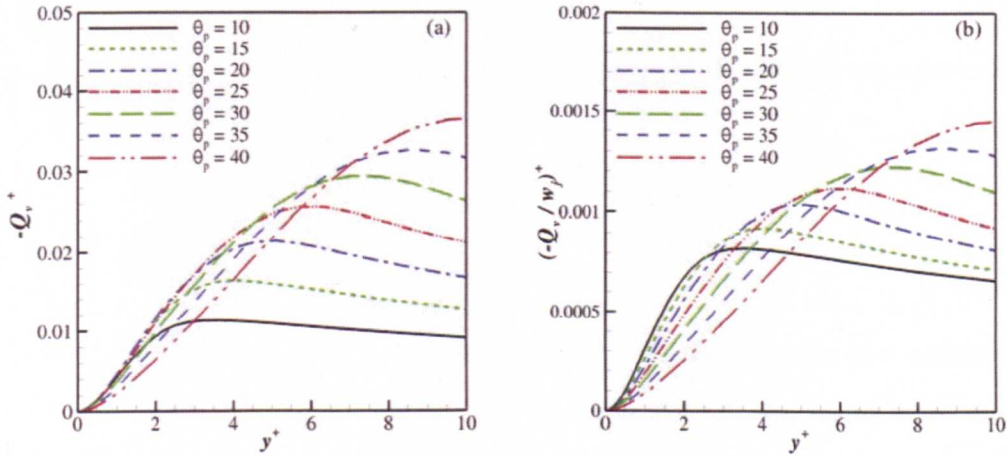


Figure 4.10: a) Wall-normal velocity per unit length, Q , b) Wall-normal velocity per unit length normalised by maximum wall jet velocity, Q/w_j .

The average wall-normal velocity per unit length $Q = \bar{v}/l_z$ from $z^+ = -10$ to $z^+ = 0$ at $t^+ = 150$ is presented in Figure 4.10(a) to access the entrainment of fluid upstream of the actuator. The wall-normal velocity increases with increasing θ_p . Normalising Q by the velocity of the jet w_j in Figure 4.10(b) still resulted in a large increase in entrainment with increasing θ_p .

Figure 4.11 shows that there is very little change in the trajectory of the starting vortex when the plasma profile angle is changed, with the vortex travelling

at approximately 32° to the horizontal. As the angle is increased there is an increase in the displacement, and therefore velocity of the vortex, this is due to the increased strength of the wall jet produced.

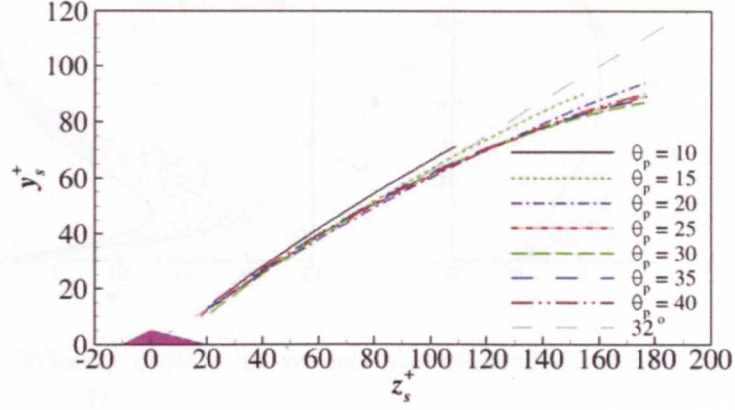


Figure 4.11: Vortex trajectory for various profile angles, θ_p . Purple triangle indicates location of plasma.

4.4.3 Effect of profile width, b

Alteration of the width of the plasma profile, b , would, as in the case of alteration of θ_p , lead to an increase in the electric field strength, E , and result in an increase in the velocity of the jet. Figure 4.12 shows that the maximum velocity of the jet profile increases with increasing actuator width. Again Figure 4.13 shows the angle of travel of the starting vortex is very similar to those in previous results for all the configurations tested.

4.4.4 Conclusion

Alteration of the strength and width of the plasma profile has very little effect apart from altering the velocity of the wall jet that is produced. The results suggest that in the case of the drag reduction simulations a low angle, $\theta_p = 10^\circ$, is the most suitable. The desired spanwise wall motion would be achieved for the minimum

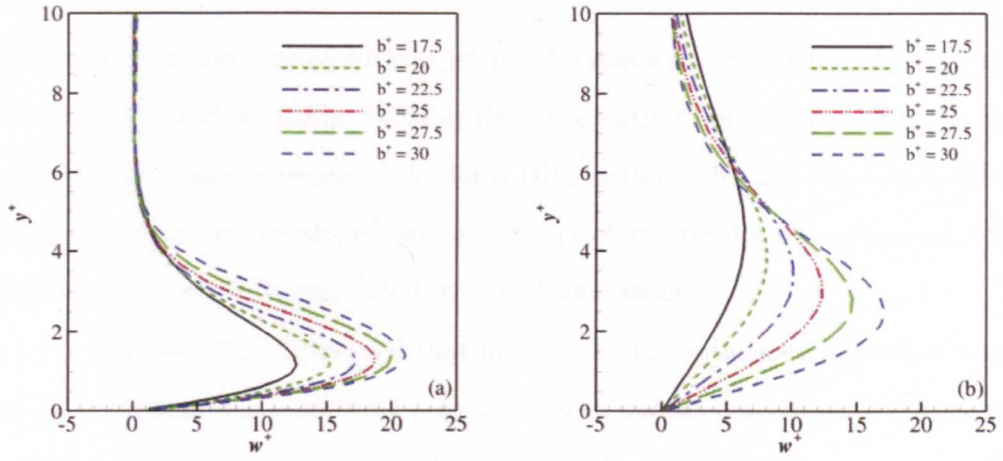


Figure 4.12: Velocity profiles for various plasma profile widths, b , at $t^+ = 150$: a) $z^+ = 10$, b) $z^+ = 30$.

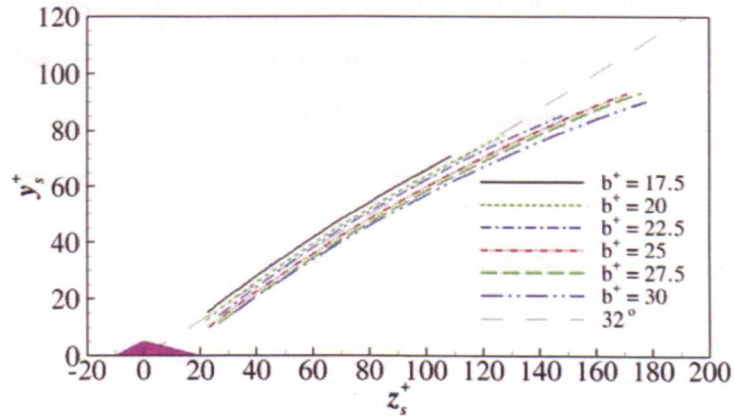


Figure 4.13: Vortex trajectory for plasma profile widths, b . Purple triangle indicates location of plasma.

entrainment of fluid that would draw high speed fluid towards the wall upstream of the actuator. The width of the plasma profile was chosen to be $b^+ = 17.5$ as this is of a similar order to the experimental actuators used by Jukes et al. (2006b). A small value for b thus reducing the minimum value of the actuator spacing, s_p , facilitates the condition $b < s_p$.

4.5 Scaling

Different configurations and hence jet profiles require a scaling in order to compare velocity and vorticity fields. Whalley (2011) recently investigated scaling the results that were obtained experimentally for a DBD actuator by non-dimensionalising by the velocity of the developed jet w_j . Some of his results are compared here to similarly scaled results generated by the plasma model.

Whalley (2011) observed that in tests the instantaneous maximum velocity, w_{max} , with time, increases from zero to a zenith and then decreases to the constant value w_j . The constant velocity defines the velocity scale $w^s = w_{max}/w_j$ and the time scale which is defined as $t^s = \frac{tw_j^2}{\nu}$. In the cases that Whalley (2011) tested the velocity becomes constant at $t^s = 5000$. The velocity fields generated from the D_c parametric study (see section 4.4.1) were normalised and an overshoot in the velocity is observed for all cases, Figure 4.14. In addition the velocity returns to a constant in the region of $t^s = 4000$ and thus suggesting some similarity between both the experimental and simulated results.

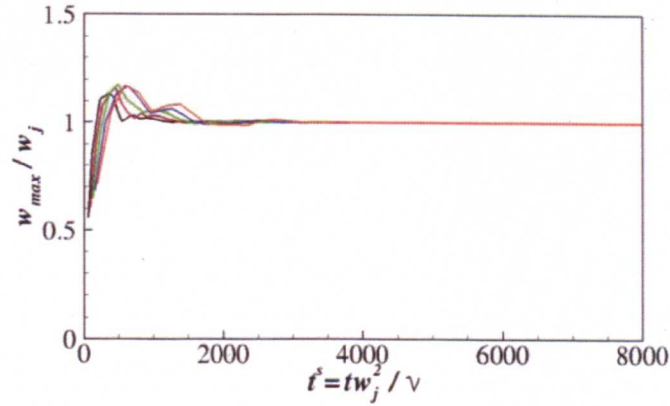


Figure 4.14: Normalised maximum z -direction velocity, w_{max}/w_j against normalised time, t^s for plasma strengths, D_c .

The vortex core location, (y_c, z_c) can be fitted to a general power law:

$$\frac{w_j(y_c, z_c)}{\nu} = k \left(\frac{tw_j^2}{\nu} \right)^2. \quad (4.1)$$

Figure 4.15(a) and 4.15(b) show that the vortex core location scales very well to the power law and moves in the both the horizontal and vertical directions with a scaling rate of $t^{0.67}$ and $t^{0.68}$ respectively. This is in very close agreement with the $t^{0.71}$ observed for experimental results by Whalley (2011). Figure 4.15(c) is a plot of y_c against z_c and the line of best fit indicates that the average angle of the vortex is 32° to the horizontal which is in excellent agreement with the 31° Whalley (2011) observed experimentally.

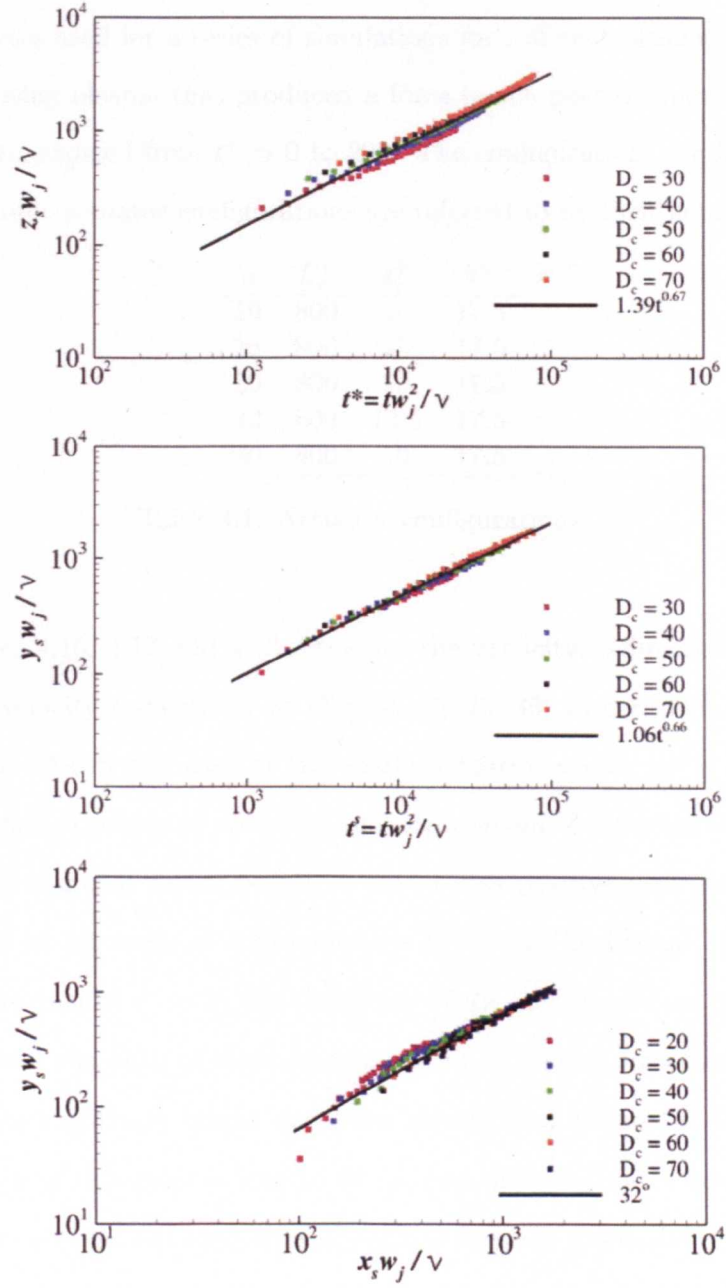


Figure 4.15: Starting vortex scalings: a) z_s vs. t^s , b) y_s vs. t^s , c) y_c vs. x_c .

4.6 Multiple DBD actuators

The plasma profile parameters used for the turbulent simulations $\theta_p = 10^\circ$ and $b^+ = 17.5$, were used for a series of simulations for different plasma configurations of non-oscillating plasma that produced a force in the positive spanwise direction. The actuators engaged from $t^+ = 0$ to 200. The configurations are listed in Table 4.1, the different actuator configurations are referred to by their actuator spacing.

n	L_z^+	s_p^+	b^+
10	800	40	17.5
16	800	25	17.5
20	800	20	17.5
32	800	12.5	17.5
40	800	10	17.5

Table 4.1: Actuator configurations.

Figures 4.16, 4.17 and 4.18 represent the vorticity, z-direction velocity and wall-normal velocity respectively at $t^+ = 10, 20, 25, 30, 40$ and 60 for the $s_p^+ = 20$ configuration. As in the case of the single actuator a wall jet is created, with entrainment and expulsion of upstream and downstream of the actuator respectively. An associated starting vortex begins to travel in a positive z direction and away from the wall at an angle of approximately 32° to the horizontal. Figure 4.16(c) shows however that at $t^+ = 25$ the trajectory of the starting vortex begins to differ noticeably from the path of that generated from a solitary actuator. The vortex centre reduces slightly in height and then travels in a horizontal direction. The starting vortex at this point is located to the rear of the actuator downstream, and the entrainment of fluid (Figure 4.18(c)) at this location interacts with the starting vortex and may cause the reduction in height of the vortex. By $t^+ = 30$ (Figure 4.17(d)), an undulating sheet of significant spanwise velocity has evolved from the individual jets, and is responsible for the horizontal trajectory of the vortex.

Further at $t^+ = 40$ the starting vortex has disappeared as it amalgamates

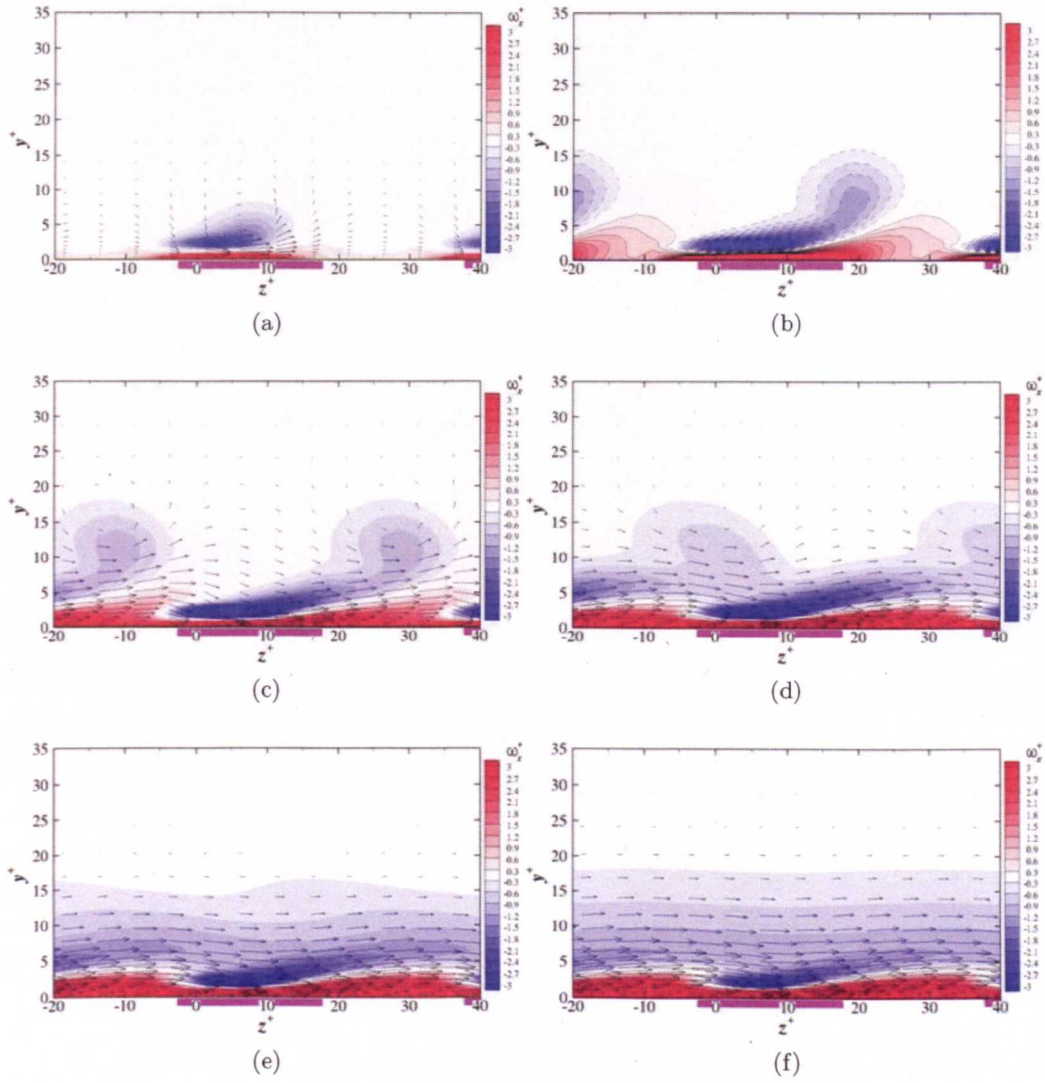


Figure 4.16: Vorticity contours, ω^+ , around a DBD plasma actuator in initially quiescent flow. Purple rectangle indicates location of actuator, strength, $D_c = 40.0$, width of the forcing profile, $b^+ = 17.5$, forcing profile angle, $\theta_p = 10^\circ$, $n = 20$: a) $t^+ = 10$, b) $t^+ = 20$, c) $t^+ = 25$, d) $t^+ = 30$, e) $t^+ = 40$ and f) $t^+ = 60$.

with the sheet of negative vorticity, caused by the negative $\frac{dw}{dy}$ gradient produced by the now relatively uniform sheet of w velocity. Further in time at $t^+ = 60$ the w velocity sheet has increased in uniformity and height, resulting in a similar alteration to the sheet of negative vorticity. However, areas of high negative vorticity at the locations of the plasma remain with the areas of entrainment and expulsion,

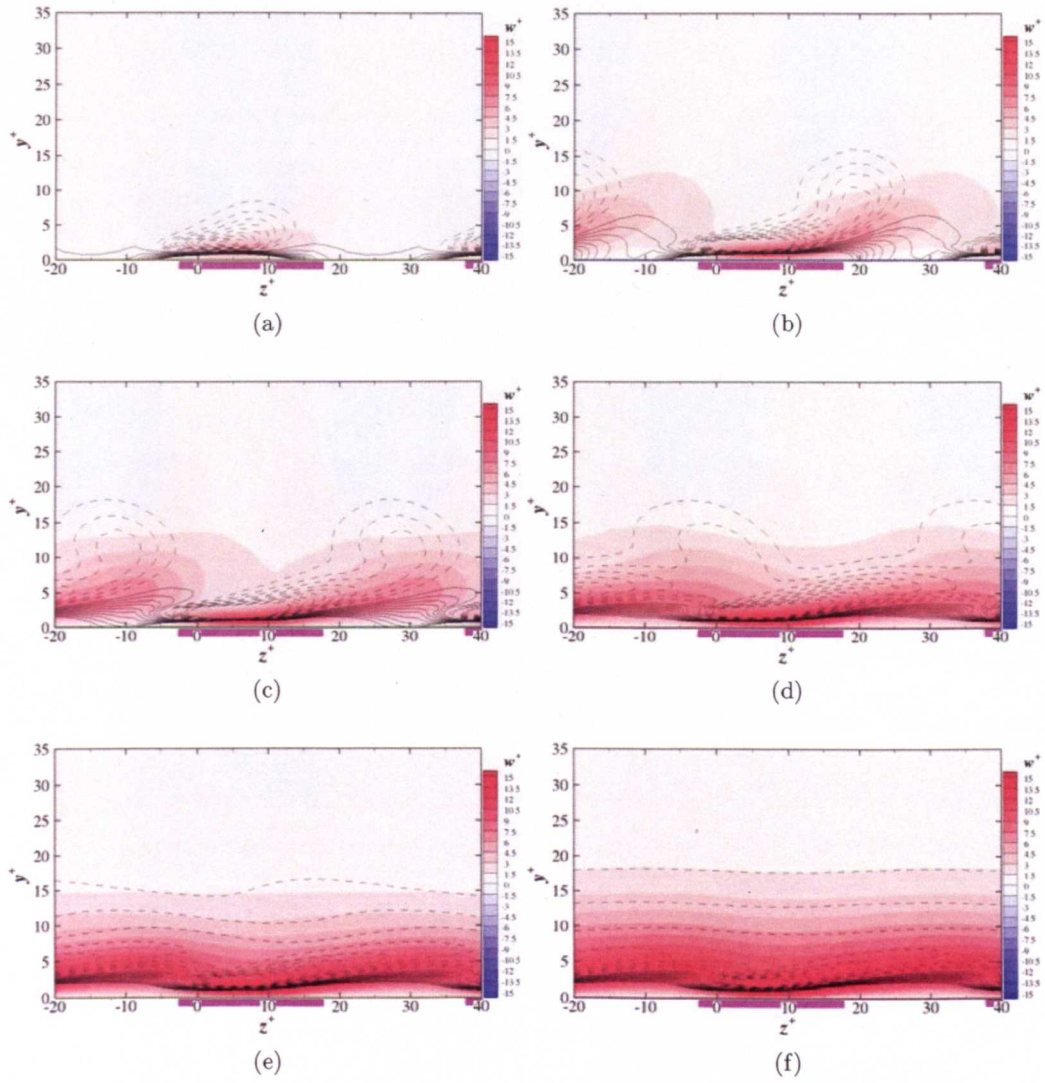


Figure 4.17: z -direction velocity contours, w^+ , around a DBD plasma actuator in initially quiescent flow. Purple rectangle indicates location of actuator, strength, $D_c = 40.0$, width of the forcing profile, $b^+ = 17.5$, forcing profile angle, $\theta_p = 10^\circ$, $n = 20$: a) $t^+ = 10$, b) $t^+ = 20$, c) $t^+ = 25$, d) $t^+ = 30$, e) $t^+ = 40$ and f) $t^+ = 60$.

upstream and downstream of each actuator, still present, Figure 4.18(f).

Figure 4.20 illustrates the changes made to the trajectory of the vortex cores by the effect of multiple actuators. In the cases presented the eventual horizontal velocity, and the slight decrease from a maximum y -location from the wall for the starting vortices, are highlighted. It is evident that with decreasing actuator spacing

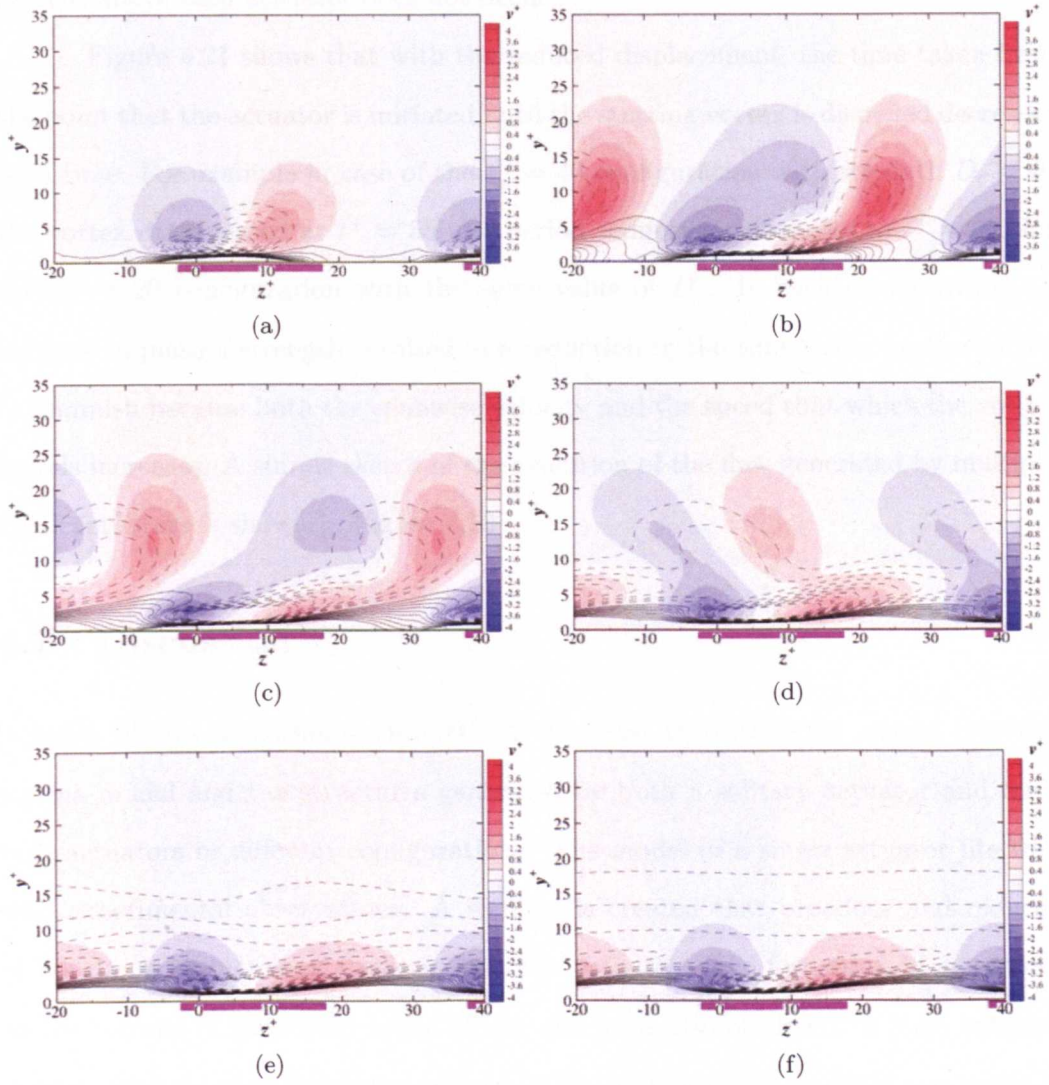


Figure 4.18: Wall-normal velocity contours, v^+ , around a DBD plasma actuator in initially quiescent flow. Purple rectangle indicates location of actuator, strength, $D_c = 40.0$, width of the forcing profile, $b^+ = 17.5$, forcing profile angle, $\theta_p = 10^\circ$, $n = 20$: a) $t^+ = 10$, b) $t^+ = 20$, c) $t^+ = 25$, d) $t^+ = 30$, e) $t^+ = 40$ and f) $t^+ = 60$.

the distance that the vortices travel before disappearing reduces. Plots for the $s_p^+ = 12.5$ and $s_p^+ = 20$ configuration are not presented as no starting vortices could be detected, with these configurations, the transition from individual jets to a uniform sheet of w velocity, and consequently the establishment of a sheet of negative vorticity, happens so quickly that a distinct vortex separate to the vorticity

present above each actuator does not occur.

Figure 4.21 shows that with the reduced displacement, the time taken from the point that the actuator is initiated until the starting vortex is dispelled decreases with time. For example in case of the $s_p^+ = 40$ configuration with strength $D_c = 40$ the vortex disappeared at $t^+ = 55$ this period reduces significantly to $t^+ = 17$, for the $s_p^+ = 20$ configuration with the same value of D_c . In each configuration an increase in plasma strength resulted in a reduction in the time taken for the vortex to diminish because both the spanwise velocity and the speed that which the vortex travels increases. A simple sketch of the evolution of the flow generated by multiple DBD actuators is shown in Figure 4.19

4.7 Discussion

A series of two dimensional simulations were run to provide an insight into the plasma model and the structures generated by both a solitary actuator and multiple actuators in different configurations. The model of a single actuator fits well with experimental observations. A wall jet is created that broadens and reduces in velocity with increased distance from the actuator. The formation of a starting vortex because of the initial rollup of the wall jet is also observed. A large entrainment of fluid towards the wall upstream of the actuator as a result of continuity is also present. The non-dimensionalised trajectory of the starting vortices scales with the time $t^{*0.67}$ and at an angle of 32° which compares well to recent experimental observations of $t^{*0.71}$ and an angle of 31° (Whalley, 2011). Allowing for the limited comparisons that can be made to experimental observations, the plasma model is considered to simulate the velocity profile and flow structures created by a typical DBD plasma actuator, therefore the model achieves its aim.

Alteration of the variables that define the plasma profile seem to have little effect on the overall flow model produced by an actuator with the exception of

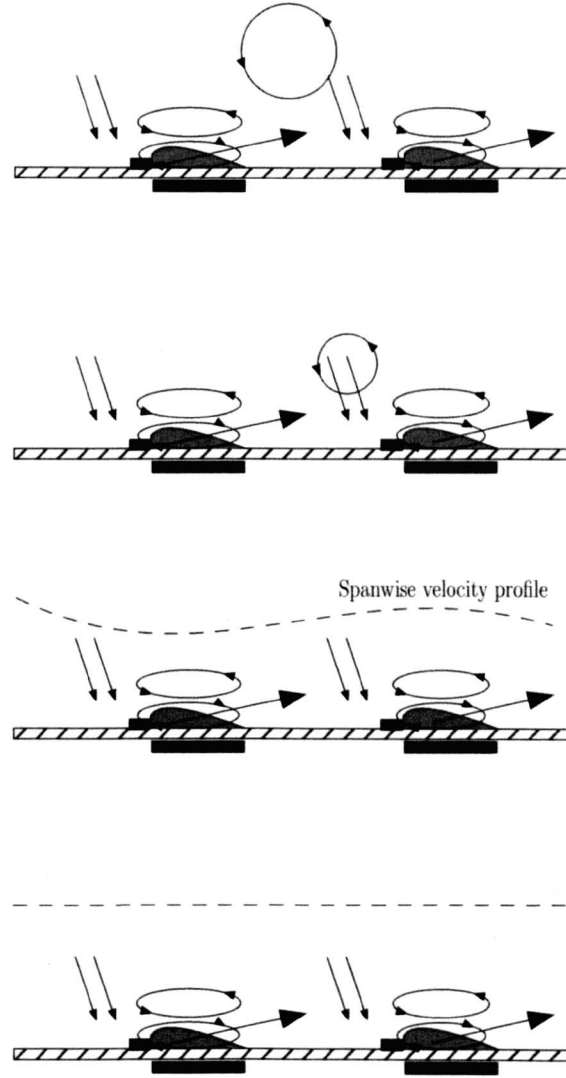


Figure 4.19: Sketch of the evolution of the flow created by multiple DBD plasma actuators.

the angle, where the entrainment of fluid relative to the wall jet velocity increased with increasing angle. The parameters for the plasma profile used in the turbulent simulations were set as $b^+ = 17.5$ and $\theta_p = 10^\circ$ after the parameter investigations. This was in order to keep the entrainment of fluid and the spacing between the actuators to a minimum.

In the case of multiple actuators the flow structure is initially seen to be

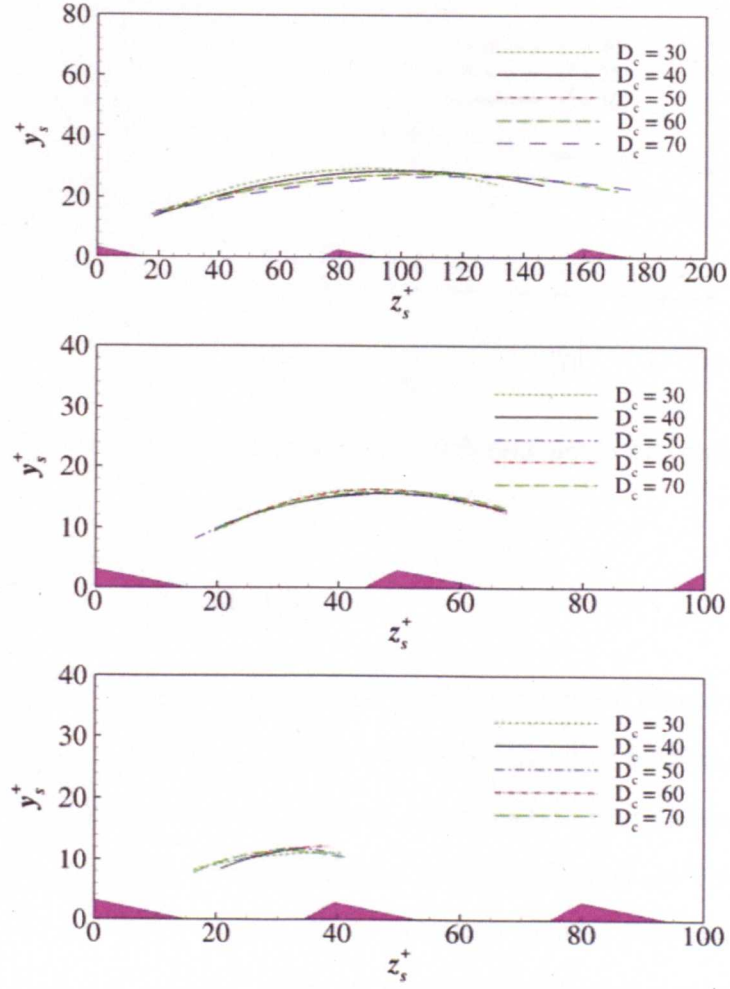


Figure 4.20: Vortex trajectory for various strengths D_c , (Purple triangle indicates location of plasma): a) $s_p^+ = 40$ configuration, b) $s_p^+ = 25$ configuration and c) $s_p^+ = 20$ configuration.

initially like that of a solitary actuator, but then begins to travel horizontally before disappearing, as the combined jets from the actuators produce a sheet of w velocity. The rate at which the vortex disperses, decreases with decreased spacing of the actuators. In configurations $s_p^+ = 10$ and $s_p^+ = 12.5$ no discernible vortices were generated.

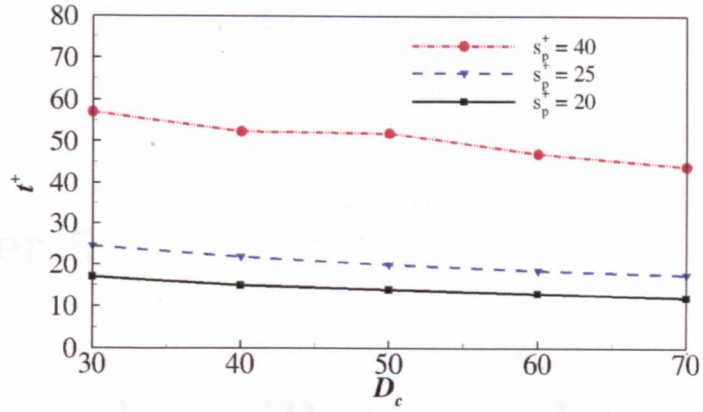


Figure 4.21: Time for vortex to disperse for different actuator configurations and strengths, d_c .

4.8 Chapter Summary

In this chapter the flow generated by a solitary DBD modelled actuator is compared to that from experimental observations. The resulting flow from the DBD model was found to closely follow that observed in experimental investigations. In addition the parameters that define the plasma model were investigated and conclusions were drawn as to the parameters to be used for the flow control simulations. The flow generated by multiple actuator configurations was also investigated and compared to that produced by a single actuator.

Chapter 5

Temporal oscillating plasma

5.1 Introduction

Spanwise wall oscillations have been reported to give large skin-friction reductions for certain parameters through suppression of the near-wall turbulence. The wall boundary condition for the spanwise component of velocity for this flow control method is:

$$w^+ = W_m^+ \sin\left(\frac{2\pi}{T^+} t^+\right). \quad (5.1)$$

As discussed in Section 2.3.2, Jukes et al. (2006b), conducted a series of experimental investigations into using opposing sets of DBD actuators to create oscillating spanwise wall motions in order to achieve a drag reduction. They used a series of actuator pairs orchestrated into two sets and orientated in a spanwise direction for several different actuator spacings, $s_p^+ = 20, 30$ and 50 . They reported a drag reduction with the smallest spacing using a square wave as an input signal to the actuator sets. Measuring the fluid velocity and skin-friction near DBD actuators is difficult because of the difficulty in placing a sensor in the area of plasma and the effect of the moderate temperature rise that occurs (Choi et al., 2011).

In this Chapter a series of simulations are run for various DBD actuator configurations. Each configuration is tested for various periods of temporal oscillation

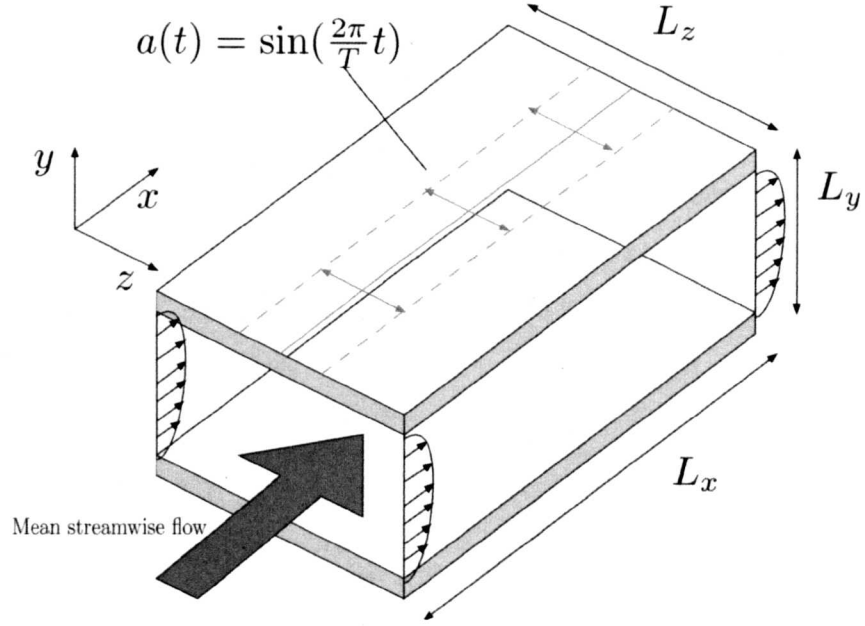


Figure 5.1: Schematic of the system for a turbulent channel flow with spanwise temporal oscillation, L_x , L_y and L_z are the dimensions of the computational domain.

to produce a spanwise oscillating flow near the wall. The results are tabulated and compared to the other configurations, and with spanwise wall oscillation results, to assess the performance of DBD actuators for turbulent skin-friction control.

5.2 Method

In the current simulations as described in more detail in Section 2.2, a sinusoidal force was used. The term $a(t)$ for a point in time is defined by the following equation:

$$a(t) = \sin\left(\frac{2\pi}{T}t\right), \quad (5.2)$$

the force term for the Navier-Stokes equations is then:

$$F_i = |a(t)|D_c E_i. \quad (5.3)$$

Figure 5.2 illustrates that a positive value of $a(t)$ results in activation of actuator Set 1 and deactivation of Set 2 (resulting in a positive spanwise velocity), while a negative value of $a(t)$ results in deactivation of Set 1 and activation of Set 2 (resulting in a negative spanwise velocity).

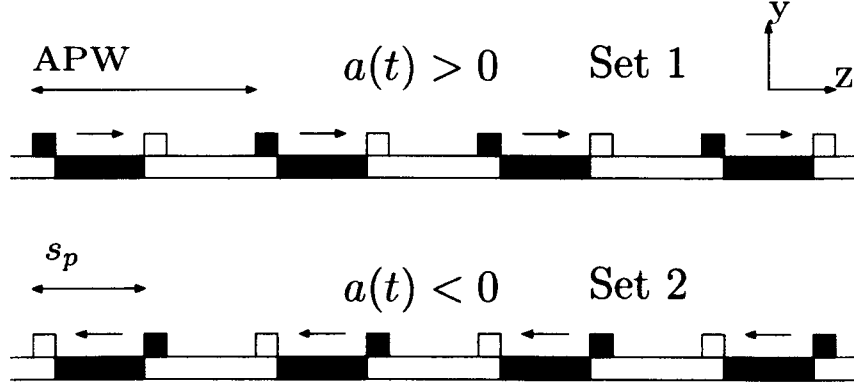


Figure 5.2: Schematic of the actuator sets and their activation in accordance with $a(t)$.

For this investigation the plasma actuators were defined for the entire length and width of the domain on both the top and bottom walls. Four configurations were tested, a uniform plasma configuration and three discrete configurations with the number of equally spaced actuator pairs, n , being $n = 40, 32$ and 20 (Table 5.1) producing an actuator spacing of $s_p^+ = 10, 12.5$ and 20 respectively.

n	L_z^+	s_p^+	b^+
20	800	20	17.5
32	800	12.5	17.5
40	800	10	17.5
∞	800	0	-

Table 5.1: DBD actuator configurations for simulations.

The uniform plasma configuration is referred to in graphs and tables by $s_p^+ = 0$. The plasma profile width for all the simulations including the uniform configuration is $b^+ = 17.5$ and $\theta_p = 10$. The explanations for these values and the exact configurations have been explained in Section 4.6. The intention of using different actuator configurations is to replicate as closely as possible spanwise wall oscillation with the uniform plasma configuration and then to digress to discrete actuator configurations, increasing the distance between each actuator to $s_p^+ = 20$. The latter case was found to be most effective by Jukes et al. (2006b) and the closest spacing achieved in their experiment.

5.2.1 Numerical procedure

The results were computed using the implicit method, described in Chapter 3. The Reynolds number for the simulations was $Re(\equiv U_m h / \nu) = 3150$. The Reynolds number based on the friction velocity u_{τ_0} of the no-control case was $Re_\tau = u_{\tau_0} h / \nu = 200$. The computational domain has dimensions $L_x = 18h$, $L_y = 2h$, $L_z = 4h$, and is discretised to a grid of $(360 \times 129 \times 320)$. The corresponding grid spacings were $\Delta x^+ = 10.0$, $\Delta y_{min}^+ = 0.1$, $\Delta y_{max}^+ = 9.0$ and $\Delta z^+ = 2.5$. Periodic boundary conditions were used in the spanwise and streamwise directions, while no-slip was applied to the top and bottom walls.

The simulations were run for a total time of $t_{tot} = 550$, $t_{tot}^+ = 7000$ ($t^+ = tu_{\tau_0}^2 / \nu$). This is longer than the time interval usually used for calculation of low-order turbulence statistics (Kim et al., 1987; Abe et al., 2001) but is of an order used in skin-friction parametric studies for spanwise wall oscillations (Quadrio and Ricco, 2004). Following time step tests the time step used was $\Delta t^+ \approx 0.1$.

The simulations were undertaken on a 3100 core cluster of 2.66 GHz Intel X5650 Westmere cores based on 2 sockets, 12 cores and 24GB of RAM per node. Each simulation required 3.5Gb of RAM and 600 CPU hours.

5.3 Results

Eleven different periods of oscillation were tested for each actuator configuration: $T^+ = 15, 30, 50, 75, 100, 125, 150, 200, 250, 300$ and 500 . The quantity of main interest in the simulations is the skin-friction drag coefficient:

$$C_f = \frac{2\tau_x}{\rho U_b^2}, \quad (5.4)$$

where ρ is the density of the fluid, τ_x is the longitudinal component of the shear stress at the wall, and U_b is the bulk velocity.

The simulations are all started from the same unperturbed flow as the initial condition and with the flow control starting at time $t = 0$. A time interval is required for the controlled flows to adapt to the new conditions and to reach a new quasi-equilibrium state. As observed with spanwise wall oscillations the duration of the transient is not monotonic and this transient time needs to be taken into account and discarded from the statistics. As used previously by Quadrio and Ricco (2004), a visual inspection of the time history of the skin-friction for each case was undertaken to select a point, t_i , which is noticeably after the transient and is where the time averaging of skin-friction data was initiated. For each case, the value t_i is given in Table 5.2 (Some examples of the time history of the skin-friction from $t^+ = 0$ to $t^+ = 3000$ are presented in Appendix B.1). Time averaged and phase averaged statistics for all other properties was initiated for all cases much further in time than the values of t_i at $t^+ = 4000$.

Table 5.2 presents the skin-friction results for the effect of change in the period of oscillation for the four actuator configurations. D_c was set to produce the maximum spanwise velocity or amplitude $W_m^+ \approx 12$. W_m^+ was found to increase if D_c was fixed and either T^+ increased or s_p^+ decreased. Initial tests had shown the phase averaged maximum spanwise velocity W_m^+ generated by the DBD turbulent simulations was identical to those generated by 2D simulations. Two dimensional

simulations were used to tailor the value of D_c so that $W_m^+ \approx 12$ for each case.

Case 0 in Table 5.2 is the no-control reference simulation, where $Re_\tau = 197.6$ and $C_f = 7.874 \times 10^{-3}$. The term DR is calculated as follows:

$$DR = \frac{U_b L_x L_z}{t_{tot} - t_i} \int_{t_i}^{t_{tot}} [(\tau_{x,0} - \tau_x)] dt, \quad (5.5)$$

the 0 subscript indicates the no-control case (Case 0). The drag reduction can be expressed as a percentage of the no-control skin-friction value, $DR\%$:

$$DR\% = 100 \times \frac{C_{f,0} - C_f}{C_{f,0}}, \quad (5.6)$$

hence a negative $DR\%$ value indicates a skin-friction increase.

A set of spanwise wall oscillations simulations for $W_m^+ = 12.0$ were run for comparison in analysis, and shown in Table 5.3, the results were comparable to those of previous studies (Quadrio and Ricco, 2004).

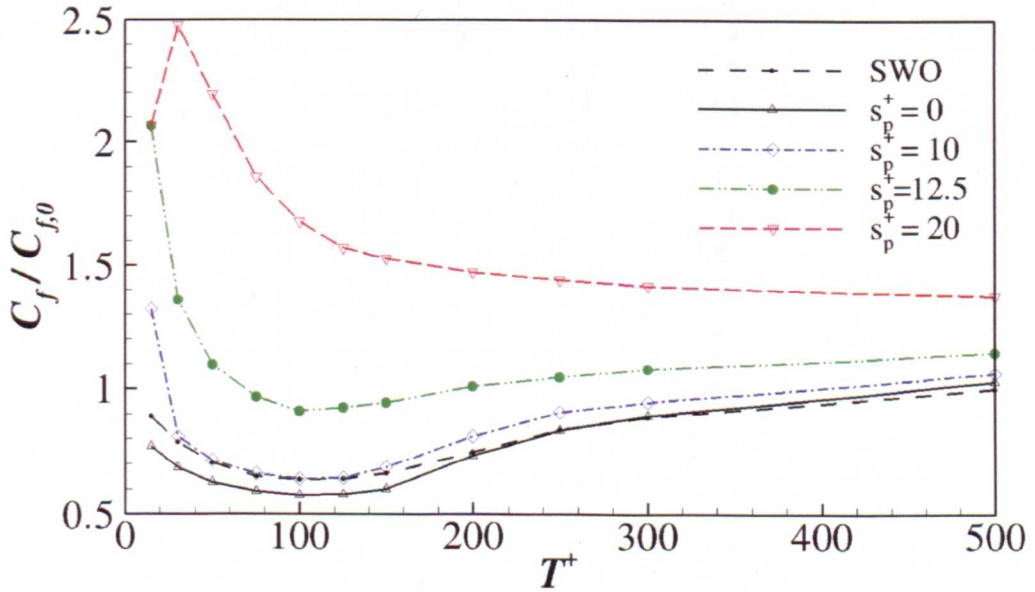


Figure 5.3: Time averaged coefficient of friction for different periods of oscillation T^+ for different plasma actuator configurations and spanwise wall oscillation (SWO) for $W_m^+ = 12$.

case	T^+	D_c	s_p^+	t_i	$C_f \times 10^{-3}$	$DR\%$
0	—	—	—	—	7.87	—
1	15.0	15.7	0	1000	5.99	24
2	30.0	12.0	0	1000	5.40	32
3	50.0	10.3	0	2000	4.94	37
4	75.0	9.4	0	2000	4.67	41
5	100.0	8.9	0	2000	4.54	42
6	125.0	8.7	0	3000	4.57	42
7	150.0	8.5	0	3000	4.75	40
8	200.0	8.2	0	2000	5.78	27
9	250.0	8.0	0	2000	6.56	17
10	300.0	7.9	0	2000	7.03	11
11	500.0	7.8	0	2000	8.10	-3
12	15.0	28.9	10	1500	10.39	-32
13	30.0	26.4	10	1500	6.38	19.0
14	50.0	23.9	10	2000	5.62	29
15	75.0	22.0	10	2000	5.22	34
16	100.0	21.0	10	2000	5.05	36
17	125.0	20.4	10	2000	5.08	37
18	150.0	20.0	10	2000	5.42	31
19	200.0	19.7	10	1500	6.37	19
20	250.0	18.9	10	1500	7.12	10
21	300.0	18.7	10	1500	7.44	6
22	500.0	17.7	10	1500	8.36	-6
23	15.0	32.6	12.5	1000	16.30	-110
24	30.0	31.7	12.5	1000	10.72	-36
25	50.0	27.4	12.5	1000	8.64	-10
26	75.0	25.5	12.5	1000	7.62	3
27	100.0	24.6	12.5	1500	7.16	9
28	125.0	24.0	12.5	1500	7.26	8
29	150.0	23.5	12.5	1500	7.42	6
30	200.0	23.0	12.5	1500	7.93	-1
31	250.0	22.4	12.5	1500	8.22	-4
32	300.0	22.2	12.5	1500	8.48	-8
33	500.0	21.3	12.5	1500	9.02	-15
34	15.0	35.6	20	1000	16.27	-110
35	30.0	34.8	20	1000	19.52	-150
36	50.0	32.7	20	1000	17.27	-120
37	75.0	32.4	20	1000	14.66	-86
38	100.0	31.5	20	1000	13.21	-68
39	125.0	30.9	20	1000	12.38	-57
40	150.0	29.7	20	1000	12.01	-53
41	200.0	28.9	20	1000	11.57	-47
42	250.0	28.6	20	1000	11.34	-44
43	300.0	28.1	20	1000	11.17	-42
44	500.0	27.5	20	1000	10.82	-37

Table 5.2: Data for different periods of oscillation and actuator configurations, $W_m^+ \approx 12$: period T^+ , actuator spacing s_p^+ , (case 0 refers to the no-control case configuration), t_i indicates the start of the time-averaging procedure for the calculation of the friction coefficient C_f , $DR\%$ indicates percentage drag reduction (negative number indicates drag increase).

case	T^+	t_i	$C_f \times 10^{-3}$	$DR\%$
s1	15	2000	6.82	11
s2	30	2000	6.20	21
s3	50	2000	5.56	29
s4	75	2000	5.14	34
s5	100	2000	5.02	36
s6	125	3000	5.05	36
s7	150	3000	5.23	34
s8	200	3000	5.87	25
s9	250	3000	6.59	16
s10	300	3000	6.98	11
s11	500	3000	7.95	1

Table 5.3: Data for spanwise wall oscillation for different periods of oscillation, $W_m^+ = 12.0$.

Figure 5.3 represents the coefficient of friction ratio, $C_f/C_{f,0}$, for the simulations presented in Tables 5.2 and 5.3, where $C_{f,0}$ is the coefficient of friction for no-control (case 0). Initial inspection of the coefficient of friction and the corresponding drag reduction shows several points of interest. The $DR\%$ obtained for the uniform plasma configuration is superior to that of the spanwise wall oscillation for $T^+ \leq 250$, for a comparable maximum spanwise velocity, W_m^+ . The greatest reduction was obtained at $T^+ = 100$, when a 44% drag reduction was produced as compared to a 36% drag reduction for spanwise wall oscillation. For $T^+ = 500$, uniform plasma produces a small drag increase of 3% as compared to a small decrease of 1% in the case of spanwise wall oscillation. Generally the trend in drag reduction with period of oscillation, T^+ , and a fixed W_m^+ is similar to that of spanwise wall oscillations. The drag reduction increases as T^+ increases from 0 to $T_{opt}^+ = 100 \sim 125$, then decreases beyond that point.

In the case of the discrete plasma configurations, the $s_p^+ = 10$ configuration provides a very good performance with the resulting drag reduction in most cases comparable to that achieved by uniform plasma and spanwise wall oscillation. However, a notable case is seen for the smallest period of oscillation $T^+ = 15$ (Case 12),

case	W_m^+	D_c	s_p^+	t_i	$C_f \times 10^{-3}$	$DR\%$
45	4.5	3.3	0	3000	5.81	26
46	6	4.4	0	3000	5.35	32
47	9	6.7	0	4000	4.77	39
5	12	8.7	0	4000	4.54	42
48	18	13.3	0	4000	4.39	44

Table 5.4: Data for one period of oscillation $T^+ = 100$, for uniform plasma configuration for various values of W_m^+ .

where the drag increase is large $DR = -32\%$, while in the case of uniform plasma, a drag reduction of $DR = 24\%$ is observed. The $s_p^+ = 12.5$ configuration shows a similar trend to both the $s_p^+ = 10$ and the uniform configurations, with an optimum period of oscillation at $T_{opt}^+ = 100 \sim 125$, although the achieved maximum drag reduction is far less with only a maximum reduction of $DR = 9\%$. There are drag increases for many periods of oscillation for $s_p^+ = 12.5$, in particular the shorter periods of oscillation $T^+ \leq 50$ with a drag increase of $DR = -110\%$ for $T^+ = 15$.

The $s_p^+ = 20$ configuration produced a large drag increase for every period of oscillation tested. Skin-friction increased rapidly with lower periods of oscillation from $T^+ < 125$ until at $T^+ = 30$ where the drag increase is $DR\% = -150$. The trend for the discrete configurations is for the skin-friction to increase with increased spacing and high drag increases are observed for the smaller periods of oscillation tested.

Further simulations were conducted for the uniform plasma configuration to determine the effect of increasing the strength, D_c and therefore W_m^+ , on the skin-friction for a fixed period of oscillation, $T^+ = 100$. Table 5.4, presents the data for the uniform plasma, and again the indication is that an increased drag reduction occurs compared to that obtained from spanwise wall oscillation for the same parameters (Quadrio and Ricco, 2004). For example a drag reduction of 44% for the $W_m^+ \approx 18$ case compared to 39% for that of spanwise wall oscillation for the same values of T^+ and W_m^+ taken from Quadrio and Ricco (2004). Increasing W_m^+ for uni-

case	W_m^+	D_c	s_p^+	t_i	$C_f \times 10^{-3}$	$DR\%$
16	12	21.0	10	2000	5.05	36
27	12	24.6	12.5	1500	7.16	9
38	12	31.5	20	1000	13.21	-68
49	4.5	7.9	10	3000	6.60	16
50	6	10.5	10	3000	6.01	24
51	9	15.8	10	3000	5.23	34
52	12	21.0	10	3000	4.82	39
53	18	31.5	10	3000	4.32	45
54	4.5	9.3	12.5	3000	9.19	-17
55	6	12.3	12.5	3000	8.59	-9
56	9	18.5	12.5	3000	7.74	2
57	12	24.6	12.5	3000	6.97	12
58	18	36.9	12.5	3000	6.09	23
59	4.5	11.8	20	3000	13.31	-69.0
60	6	15.8	20	3000	13.51	-72
61	9	23.7	20	3000	13.44	-71
62	12	31.5	20	3000	13.16	-67
63	18	47.3	20	3000	12.51	-59

Table 5.5: Data for one period of oscillation $T^+ = 100$, for discrete plasma configurations for various values of W_m^+ .

form plasma leads to an increase in $DR\%$, but the rate at which $DR\%$ increases with increasing W_m^+ decreases as seen with spanwise wall oscillations (Quadrio, 2011).

A set of simulations were conducted for the discrete configurations for a fixed period $T^+ = 100$, and a range of values for W_m^+ . To accommodate for these extra cases a smaller second computational domain was used with dimensions $L_x = 6$, $L_y = 2$, $L_z = 2$, and is discretised to a $(120 \times 129 \times 160)$ grid. The corresponding grid spacings were same as for the larger domain, $\Delta x^+ = 10.0$, $\Delta y_{min}^+ = 0.1$, $\Delta y_{max}^+ = 9.0$ and $\Delta z^+ = 2.5$. The time step used was $\Delta t^+ \approx 0.1$ apart from when $W_m^+ \approx 18$ (Cases 53, 58 and 63) where the time step was reduced to $\Delta t^+ \approx 0.05$.

Table 5.5 presents the data for the discrete plasma configurations obtained using the smaller domain. The larger domain simulations for $W_m^+ \approx 12.0$, from Table 5.2, are also shown and compared to the smaller domain simulations that used the same conditions. It is evident that there is a difference in C_f values

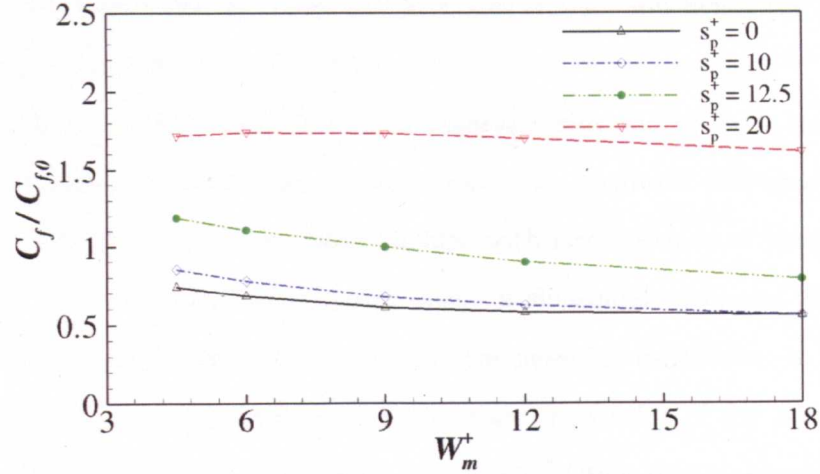


Figure 5.4: Time averaged coefficient of friction against maximum spanwise velocity W_m^+ for different plasma actuator configurations for $T^+ = 100$.

obtained between the different sized domains with lower skin-friction values for the smaller domain and with a difference of up to 5% for the $s_p^+ = 10$ case. However, the simulations using the smaller domain are still useful in displaying the trends e.g., for the $s_p^+ = 10$ configuration the drag reduction increases with increasing velocity to a maximum of $DR = 45\%$ for case 54. Interestingly for the $s_p^+ = 12.5$ configuration the lower values of W_m^+ lead to a drag increase with a drag reduction only observed as $W_m^+ \geq 9$, with a $DR = 23\%$ for $W_m^+ \approx 18$. In the $s_p^+ = 20$ case there is a large drag increase for every velocity tested and even for the $W_m^+ \approx 18$ there is still a large drag increase of $DR = -59\%$. The general indication is that as the actuator concentration is decreased the performance of the DBD actuators decreases to the point where it causes a drag increase. Increasing the strength of the actuation and hence the spanwise velocity achieved decreases the skin-friction.

From here on all the results presented are from simulations in Tables 5.2 and 5.3, where $W_m^+ \approx 12$.

Figure 5.5 is the plane and phase averaged skin-friction coefficient ratio for the different actuator configurations for four different periods of oscillation over one

cycle of oscillation. The activated actuator sets change and hence the polarity of the forcing changes at $t/T = 0$ and 0.5

A fairly constant skin-friction is observed with the $s_p^+ = 0$ configuration through the period of oscillation as in the case with spanwise wall oscillations. In both cases the skin-friction oscillates slightly with large periods of oscillation e.g., $T^+ = 500$. For example Figure 5.5(d) shows a sinusoidal oscillation in the skin-friction with a wave length equal to one half the period of oscillation. In the case of the discrete plasma configurations the temporal constitution of the skin-friction is significantly different with large 'spikes' in the skin-friction starting shortly after the polarity of the forcing changes at $t/T = 0.05$. For a specific period of oscillation the duration and height of the spike in skin-friction increases as the actuator spacing increases while the maximum skin-friction value reduces as the period of oscillation increases.

In the case of the $s_p^+ = 10$ configuration, the size of the spike is small in comparison to the other discrete cases and it returns to a value close to that of the minimum skin-friction coefficient obtained by the uniform plasma case. The minimum skin-friction coefficient ratio for the uniform and the $s_p^+ = 10$ configuration is $C_f/C_{f,0} < 0.6$ while for the $s_p^+ = 12.5$ configuration it is $C_f/C_{f,0} \approx 0.7$. The $s_p^+ = 20$ configuration shows extremely large drag increases as the force polarity changes, with $C_f/C_{f,0} > 2.0$ and does not reduce to a level lower than $C_{f,0}$ during the cycle.

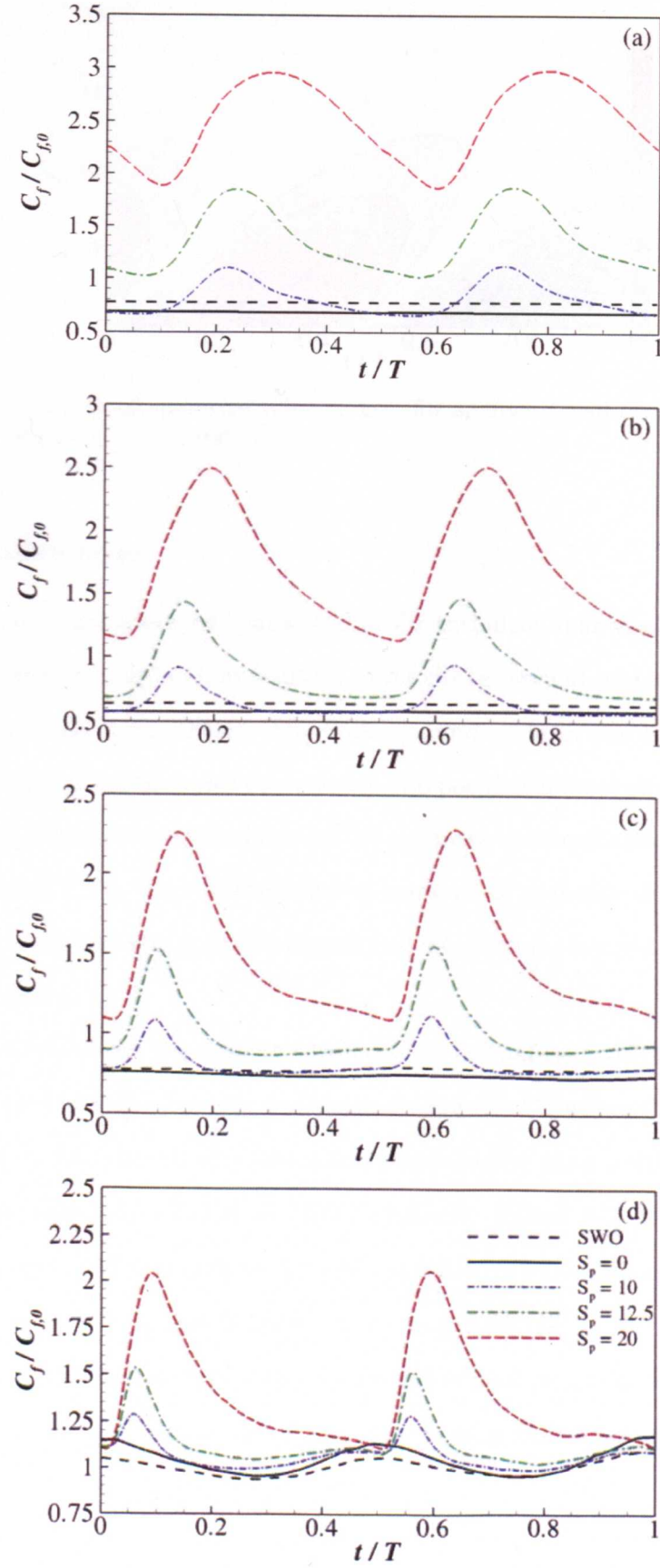


Figure 5.5: Skin-friction behaviour for different actuator configurations over one period of oscillation for $W_m^+ = 12$: a) $T^+ = 30$, b) $T^+ = 100$, c) $T^+ = 200$, and d) $T^+ = 500$.

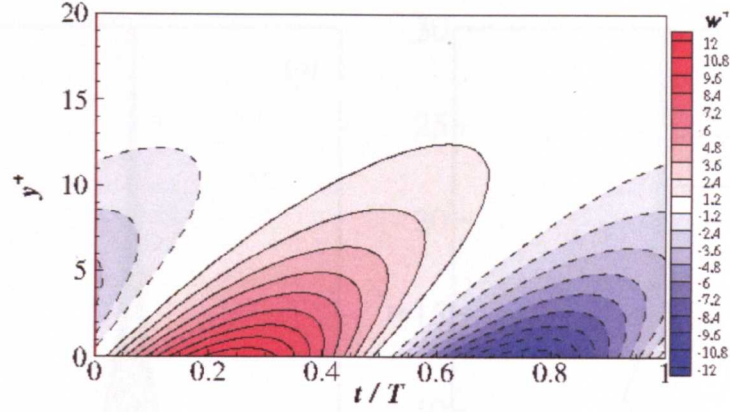


Figure 5.6: Contour of spanwise velocity w^+ , for spanwise wall oscillations for one period of oscillation, $T^+ = 100$.

5.3.1 Stokes layer

The turbulent space averaged spanwise flow for turbulent spanwise wall oscillation can be described by the laminar solution to the Stokes second problem (Choi et al., 2002; Quadrio and Ricco, 2004). The Stokes boundary layer can be split into two sections by segregating the spanwise velocity into positive and negative velocity. The phase averaged Stokes layer produced by 2D spanwise wall oscillation simulation for $W_m^+ = 12.0$ and $T^+ = 100$ is represented as contours of spanwise velocity in Figure 5.6, where the Stokes layer is clearly partitioned into sections of negative and positive spanwise velocity.

The Stokes layer penetration depth (not to be confused with the Stokes layer thickness), can be defined as the wall-normal distance, l^+ , where the amplitude of the oscillating spanwise velocity has a magnitude higher than a threshold velocity W_{th}^+ (see Equation 2.4). Choi et al. (2002) originally defined W_{th}^+ as a value typical of spanwise turbulent fluctuations. Quadrio and Ricco (2004) defined the threshold velocity as $W_{th}^+ = 1.2$ to best fit their scaling factor S^+ . $W_{th}^+ = 1.2$ is chosen to be used as the threshold velocity in this study and is used as the outer contour lines in Figure 5.6. From Equation 2.4, if the maximum spanwise velocity is fixed, the

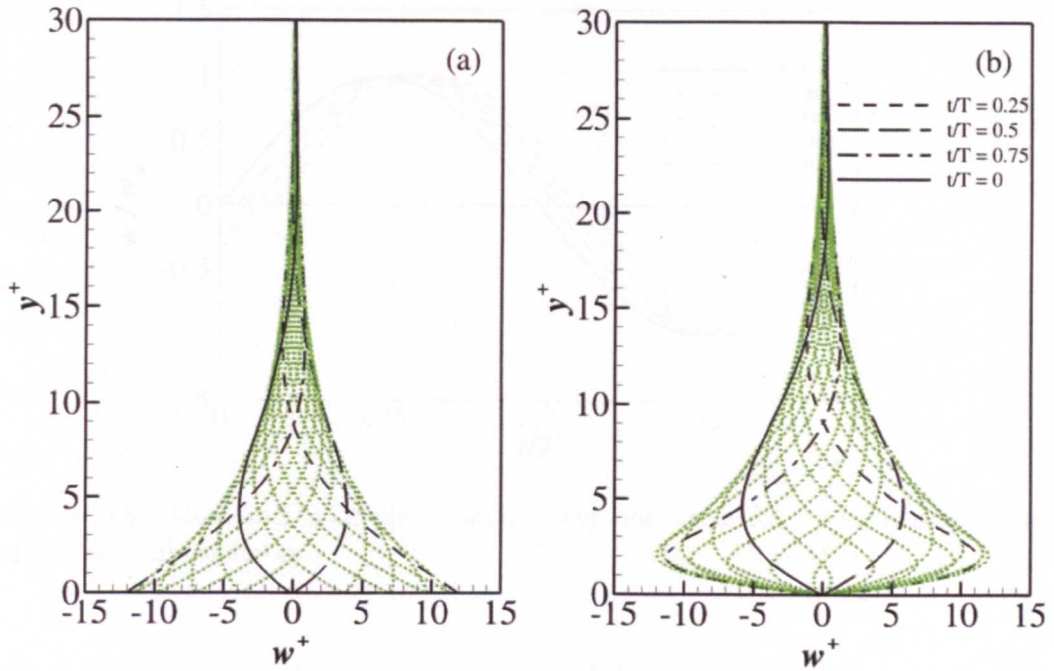


Figure 5.7: Spanwise velocity profile at various points in time for one period of oscillation, $T^+ = 100$: a) spanwise wall oscillation, b) uniform plasma.

penetration depth of the Stokes layer increases with increasing period of oscillation.

Figure 5.7 presents the phase averaged spanwise velocity profile for spanwise wall oscillation and for uniform plasma produced from 2D simulations for $T^+ = 100$ and $W_m^+ = 12$. There are two main differences between the two profiles, the first is that they are out of phase. Figure 5.8 presents the maximum spanwise velocity at time t for the spanwise wall oscillation and four periods of oscillation for uniform plasma over one cycle. For spanwise wall oscillation the polarity of the velocity changes at $t/T = 0.5$, but for the uniform configurations the force polarity changes at $t/T = 0.5$ and there is an interval until the polarity of the velocity changes. The phase difference between the spanwise and uniform plasma velocity profiles increases with decreasing T^+ , the phase difference ranging between $\phi = 0.05 \sim 0.1t/T$. The phase difference coincides with the start of the spikes seen in the skin-friction for the discrete plasma configurations indicating a possible connection between the skin-

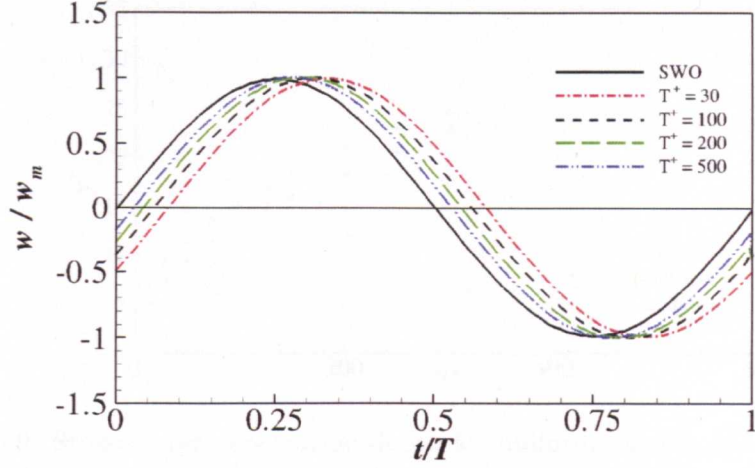


Figure 5.8: Maximum spanwise velocity over one cycle for uniform plasma and spanwise wall oscillation.

friction increases and the change in polarity of the wall-normal velocity.

The second difference between the two velocity profiles presented in Figure 5.7 is that the maximum velocity is at $y^+ \approx 2$ rather than at the wall. The maximum penetration depth of the plasma forcing is $\Delta^+ = 2$. Quadrio (2011) has suggested that for the same amplitude and oscillation if the penetration depth of a body force is small then the Stokes layer that is generated would be the same as that generated by a spanwise wall oscillation but just displaced from the wall. A similar observation of a displaced Stokes layer has been made for Lorentz forcing by Berger et al. (2000).

Figure 5.9 presents the Stokes layer penetration depth for spanwise wall oscillation and plasma simulations from 2D simulations for a range of oscillation periods $T^+ = 15 \sim 500$, at $W_m^+ = 12$ and is compared with the analytical solution for the Stokes layer penetration depth for spanwise wall oscillation derived from the laminar Stokes layer solution (Equation 2.4). The Stokes layer penetration depth for the spanwise wall oscillation simulations is very close to that of the analytical solution as observed previously by Choi et al. (2002). The Stokes layer penetration depth for the uniform plasma configuration for nearly all the periods of oscillation

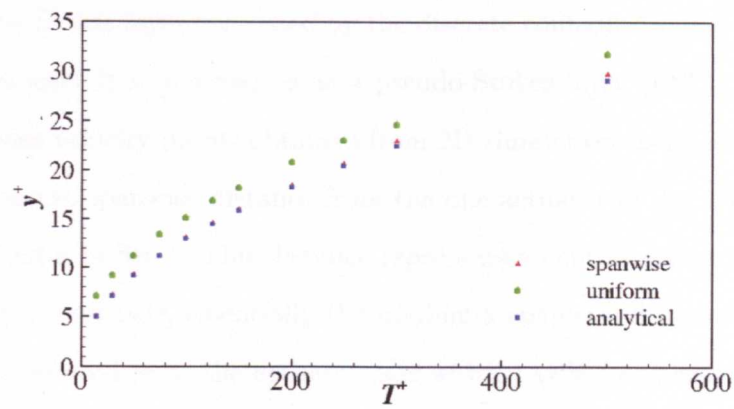


Figure 5.9: Stokes layer penetration depth for uniform plasma, spanwise wall oscillation and analytical result.

tested is approximately 2 wall units greater than that generated by spanwise wall oscillation (Figure 5.10).

Ricco and Quadrio (2008) suggested that the Stokes-layer penetration depth is the primary parameter for deducing the skin-friction reduction for spanwise wall oscillations if $T^+ < 150$. It may be that the higher drag reductions produced by uniform plasma for comparable parameters to wall oscillation occurs because of the displaced, and therefore increased, penetration depth from the wall of the Stokes layer.

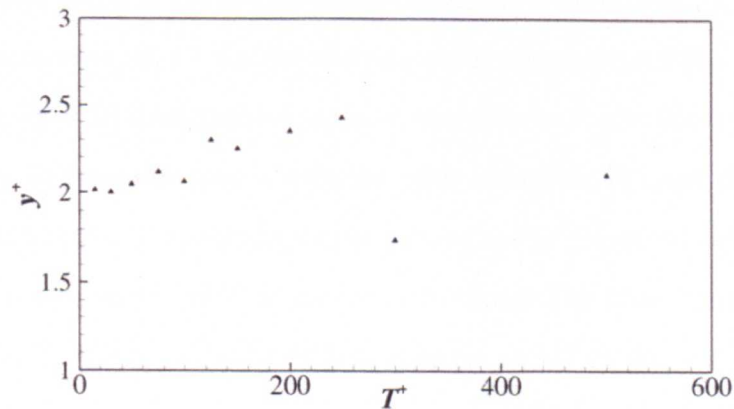


Figure 5.10: Stokes layer penetration depth difference between spanwise wall oscillation and uniform plasma simulations.

As the Stokes layer generated by the discrete configurations is not the result of a uniform force it is referred to as a pseudo-Stokes layer (PSL). The instantaneous spanwise velocity profile obtained from 2D simulations is phase and spatially averaged over the spanwise distance from the one actuator in Set 1 to the start of the next actuator in Set 1. This distance represents an entire actuator pair and the space until the next pair, essentially the minimum spanwise distance of force symmetry and is referred to as the actuator pair width (APW) as illustrated in Figure 5.2.

The phase averaged velocity field or PSL is not uniform over the APW. As an illustration Figures 5.11, 5.12, 5.13 and 5.14 portray the Stokes layer for uniform plasma and the minimum PSL for each discrete configuration for $T^+ = 30, 100, 200$ and 500 respectively. The minimum PSL is presented by the smallest magnitude of spanwise velocity over the length of the APW for each point in time during a cycle of operation.

For each plot (Figures 5.11 to 5.14) the outer contour represents the threshold velocity $W_{th}^+ = 1.2$, and the black contour lines are the contours for the uniform plasma configuration for that period of oscillation. The uniform plasma configurations clearly shows Stokes layers with a maximum spanwise velocity at $y^+ \approx 2$, with the penetration depth of the Stokes layers increasing with increasing T^+ .

For each value of T^+ for the discrete configurations the PSLs profiles, especially for the $s_p^+ = 10$ configuration, appear very alike to the uniform plasma Stokes layer profiles but become more dissimilar with increasing s_p^+ and decreasing T^+ . (For $s_p^+ = 20$ and $T^+ = 30$ a graph is not plotted as the threshold velocity W_{th} was not maintained along the APW at any point in time.) The PSLs however appear to become dissimilar from the uniform Stokes layers at $t/T \approx 0.1$, when the velocity changes polarity.

Figure 5.15 presents the cross-correlation coefficient $r_{w,w}(t)$ of the phase averaged spanwise velocity fields for 2D simulations for the discrete plasma config-

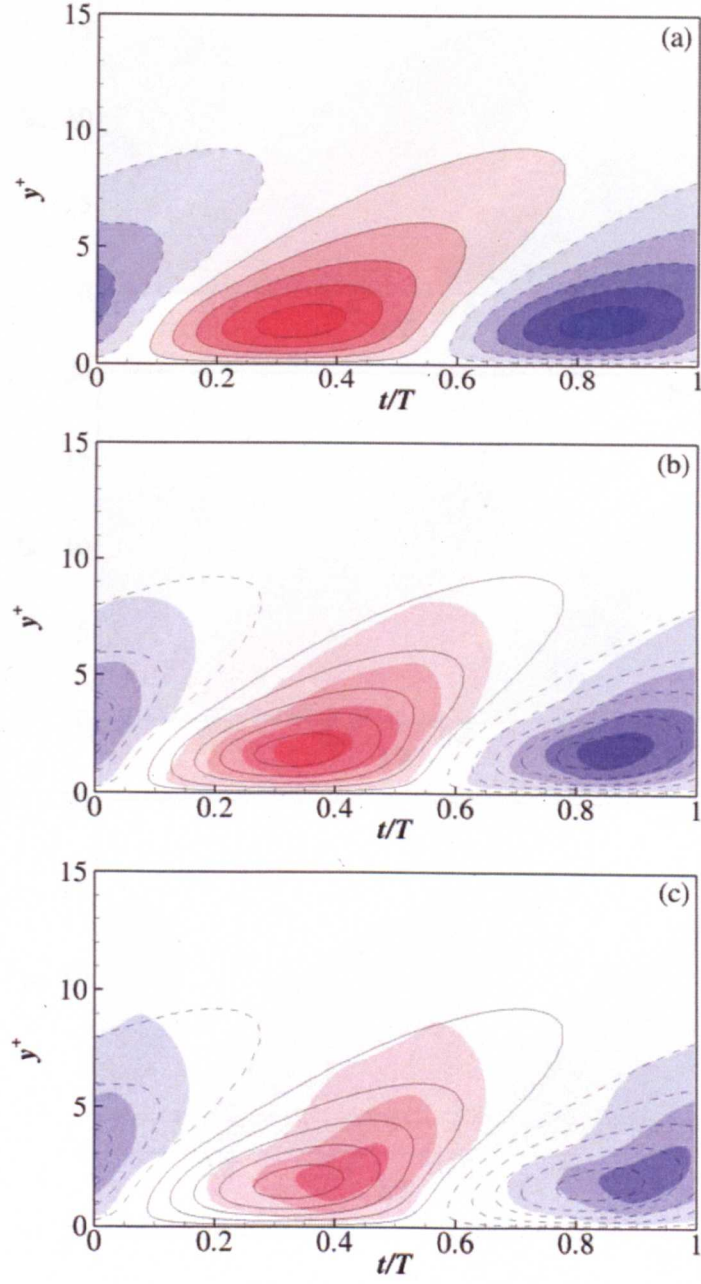


Figure 5.11: Contours of spanwise velocity for the minimum PSLs and uniform plasma Stokes layer over one period of oscillation, $T^+ = 30$: a) $s_p^+ = 0$, b) $s_p^+ = 10$, and c) $s_p^+ = 12.5$. (Contour lines start at $w^+ = W_{th}^+ = 1.2$ and increase by 2.4^+ . Blue contours and negative dash lines represent negative values)

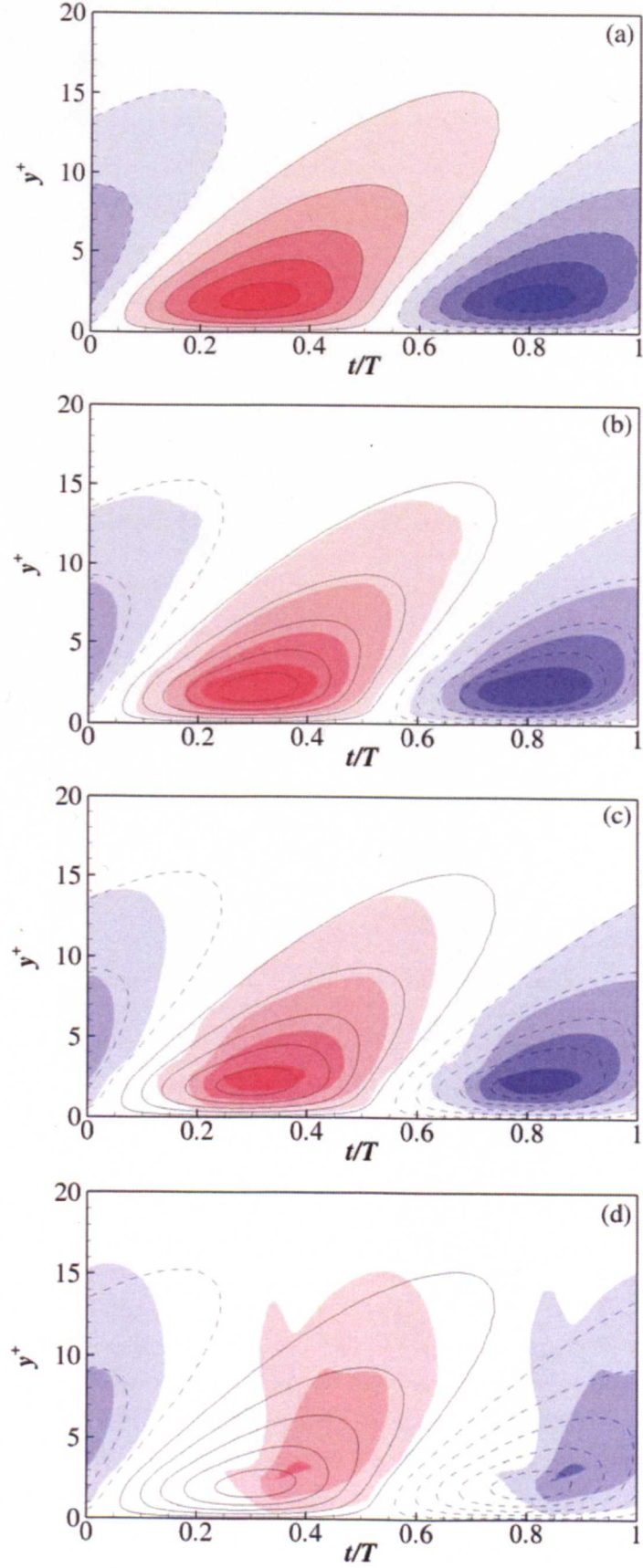


Figure 5.12: Contours of spanwise velocity for the minimum PSLs and uniform plasma Stokes layer over one period of oscillation, $T^+ = 100$: a) $s_p^+ = 0$, b) $s_p^+ = 10$, c) $s_p^+ = 12.5$ and d) $s_p^+ = 20$. (Contour lines start at $w^+ = W_{th}^+ = 1.2$ and increase by 2.4^+ . Blue contours and negative dash lines represent negative values)

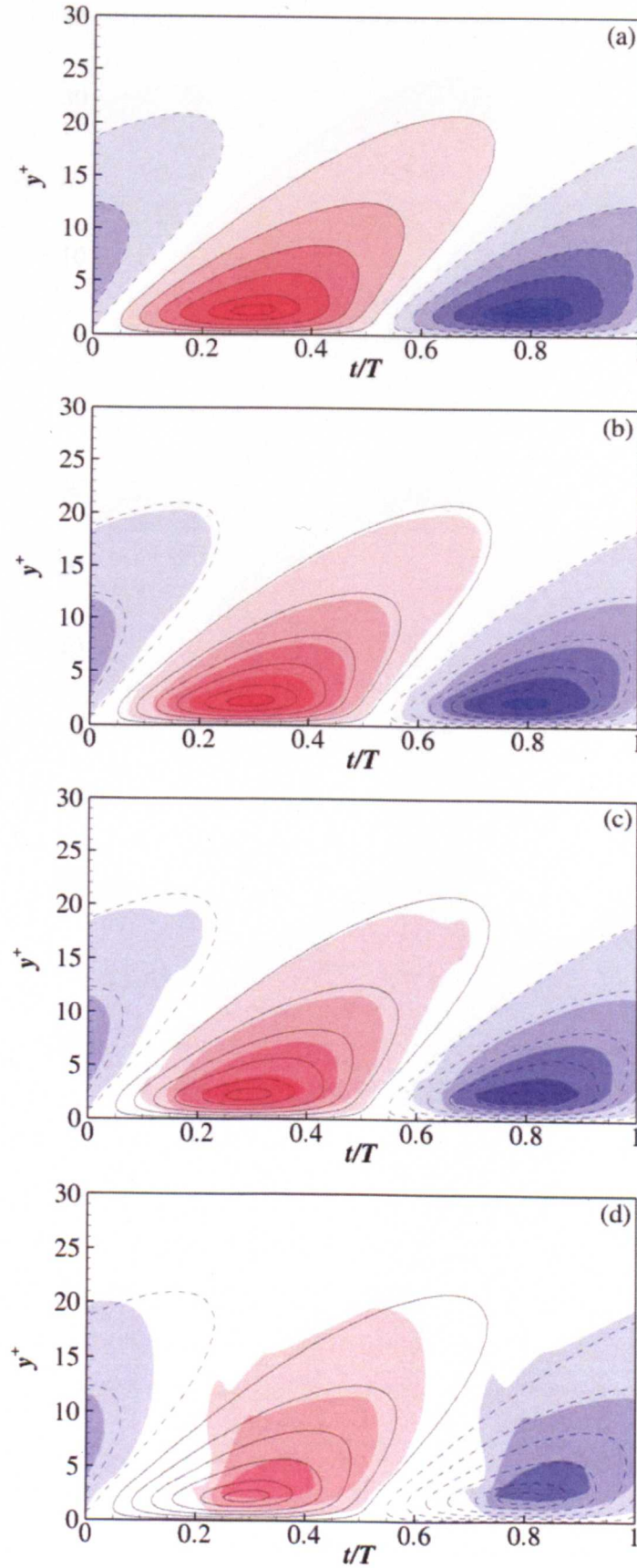


Figure 5.13: Contours of spanwise velocity for the minimum PSLs and uniform plasma Stokes layer over one period of oscillation, $T^+ = 200$: a) $s_p^+ = 0$, b) $s_p^+ = 10$, c) $s_p^+ = 12.5$ and d) $s_p^+ = 20$. (Contour lines start at $w^+ = W_{th}^+ = 1.2$ and increase by 2.4^+ . Blue contours and negative dash lines represent negative values)

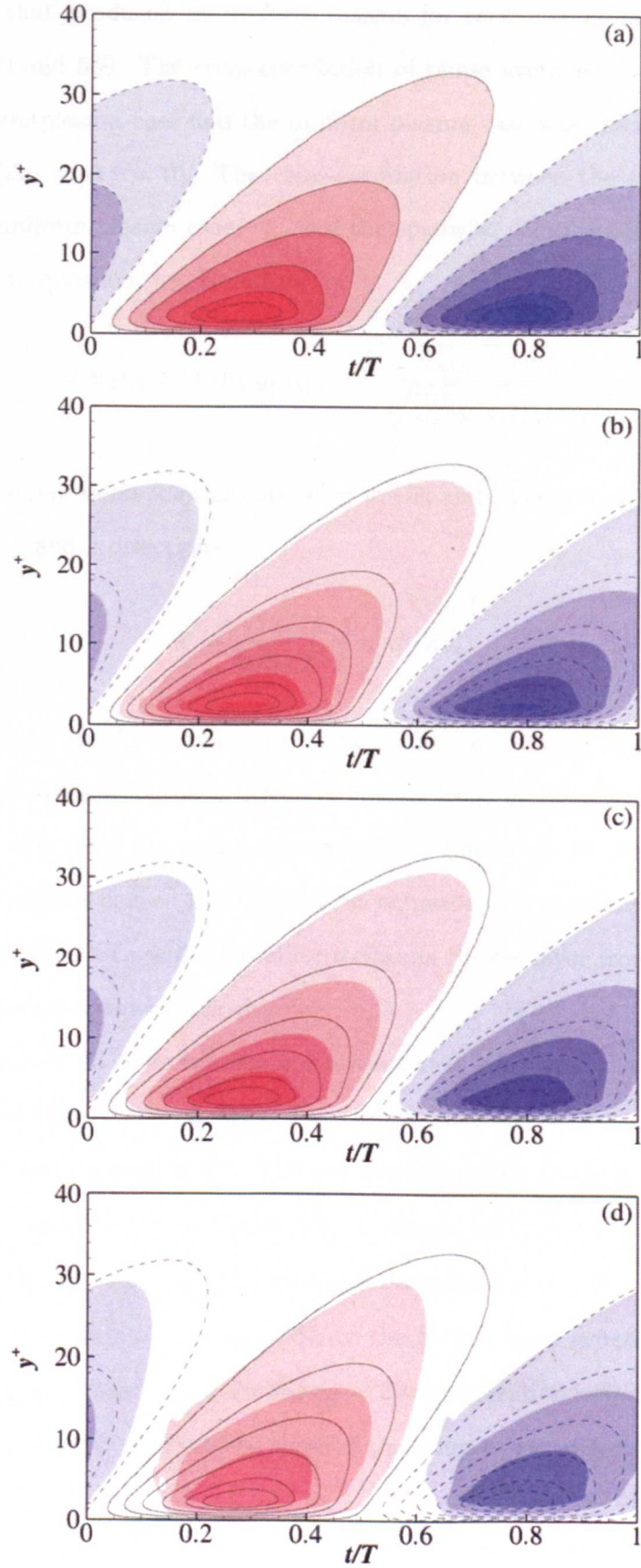


Figure 5.14: Contours of spanwise velocity for the minimum PSLs and uniform plasma Stokes layer over one period of oscillation, $T^+ = 500$: a) $s_p^+ = 0$, b) $s_p^+ = 10$, c) $s_p^+ = 12.5$ and d) $s_p^+ = 20$. (Contour lines start at $w^+ = W_{th}^+ = 1.2$ and increase by 2.4^+ . Blue contours and negative dash lines represent negative values)

urations to that produced by uniform plasma for each instant in time for $T^+ = 30, 100, 200$ and 500 . The cross-correlation of phase averaged spanwise velocities in the discrete plasma case and the uniform plasma case was calculated for a zero separation ($\Delta y = \Delta z = 0$). The cross-correlation between the spanwise velocity field of the uniform plasma case, w_1 , and the spanwise velocity field of the discrete plasma case in question, w_2 , is defined as:

$$r_{w,w}(t) = \langle w_1(y, z, t), w_2(y, z, t) \rangle = \frac{\overline{w'_1(y, z, t)w'_2(y, z, t)}}{\sqrt{\overline{w'^2_1(y, z, t)}}\sqrt{\overline{w'^2_2(y, z, t)}}}. \quad (5.7)$$

where a prime represents fluctuations, $w' = w - \overline{w}$, and $\overline{(\cdot)}$ denotes a two-dimensional average over y and z directions,

$$\overline{w} = \frac{1}{L_y L_z} \int \int w \, dy \, dz. \quad (5.8)$$

where L_y and L_z are the domain size in the y and z directions, respectively. Please note that the average in the y direction begins from $y_1^+ = 2$ and ends at $y_2^+ = L_y - 2$, and not from the walls, to remove the differences in near-wall spanwise velocity fluctuations caused by the different actuator configurations and to allow a comparison of the PSLs with the uniform plasma Stokes layer from the y -location of their maximum spanwise velocity.

In Figure 5.15 large troughs are present that start at $t/T \approx 0.5 - 0.1$ when the polarity of the velocity changes. The troughs increase in depth and width with increasing s_p^+ and decreasing T^+ . The troughs are similar to the spikes in the time history of the skin-friction in Figure 5.5. During a half period of oscillation after the troughs, the $s_p^+ = 10$ and 12.5 configurations show a tendency towards a near perfect positive correlation for the PSL to the Stokes layer generated by uniform plasma. The correlation $r_{w,w}(t)$ for the $s_p^+ = 20$ configuration improves between the troughs but is markedly reduced to those of the other two configurations for a given

period of oscillation.

Correlating $r_{w,w}(t)$ with the phase averaged skin-friction (Figure 5.5) for the same period of oscillation, produced strong negative correlations $r < -0.9$ for every case apart for the $s_p^+ = 20$ configuration at $T^+ = 30$, indicating a strong relationship between the skin-friction and the correlation of the PSLs to the Stokes layer generated by uniform plasma.

Figure 5.16 presents the cross-correlation coefficient $r_{w,w}$ of the phase averaged, spanwise velocity fields for the discrete plasma configurations to those produced by the uniform plasma configuration over the entire period of oscillation for all the periods of oscillation tested. The cross-correlation of phase averaged spanwise velocities in the discrete plasma case and the uniform plasma case was calculated for a zero separation ($\Delta y = \Delta z = \Delta t = 0$). Where the cross-correlation is defined as:

$$r_{w,w} = \langle w_1(y, z, t), w_2(y, z, t) \rangle = \frac{\overline{w'_1(y, z, t)w'_2(y, z, t)}}{\sqrt{\overline{w'^2_1(y, z, t)}}\sqrt{\overline{w'^2_2(y, z, t)}}}. \quad (5.9)$$

where a prime represents fluctuations, $w' = w - \overline{w}$, and $\overline{(\cdot)}$ denotes a three-dimensional average over y and z directions and time t ,

$$\overline{w} = \frac{1}{L_y L_z T} \int \int w \, dy \, dz \, dt. \quad (5.10)$$

where L_y and L_z are the domain size in the y and z directions and T is the period of oscillation, respectively. As with the calculation of $r_{w,w}(t)$, the average in the y direction begins from $y_1^+ = 2$ and ends at $y_2^+ = L_y - 2$.

The correlation between the velocity fields of the uniform plasma and the discrete configurations increases with increasing T^+ and decreasing s_p^+ . However with small periods of oscillation $T^+ \leq 50$, the correlation reduces substantially coinciding with the large increases in skin-friction present in Figure 5.3.

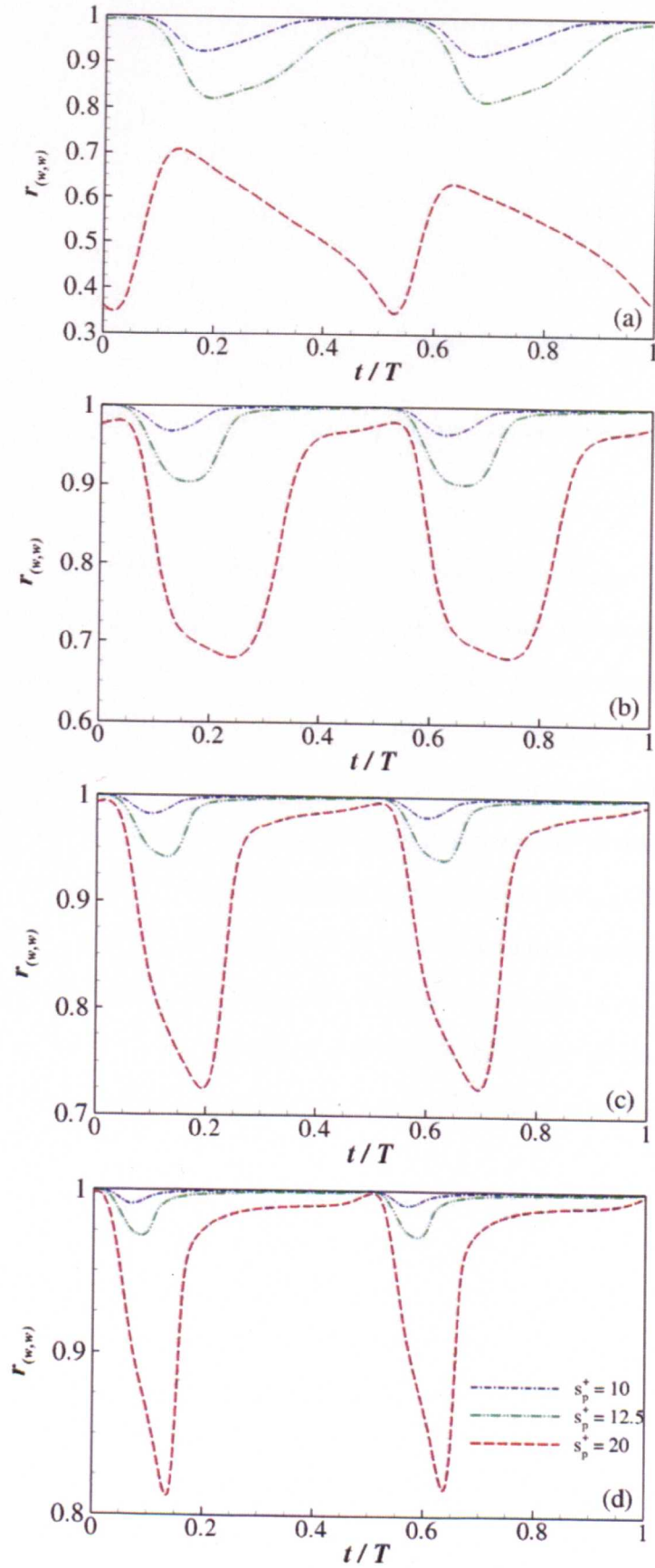


Figure 5.15: Correlation $r_{w,w}(t)$ for the discrete plasma actuator configurations: a) $T^+ = 30$, b) $T^+ = 100$, c) $T^+ = 200$, and d) $T^+ = 500$.

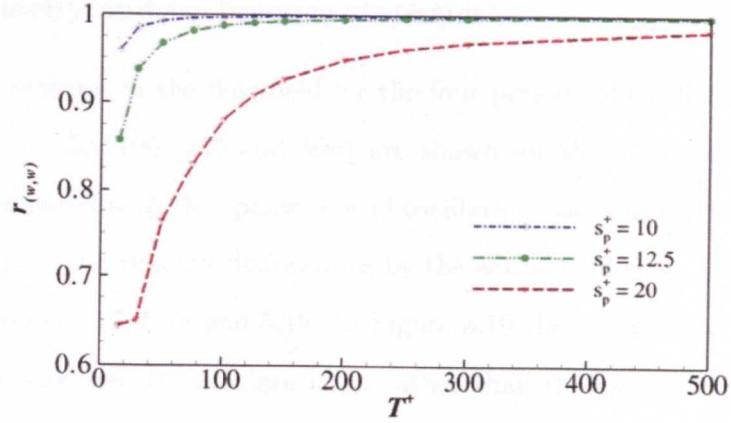


Figure 5.16: Correlation $r_{w,w}$ for the discrete plasma actuator configurations against T^+ .

The overall trend appears to be that the spanwise velocity fields, and therefore the PSLs above the near-wall area of discrete forcing, increase in similarity to those produced by uniform plasma with increasing T^+ and decreasing s_p^+ . However the PSLs differ markedly from the uniform plasma Stokes layers when the polarity of the spanwise velocity changes and coincides with large skin-friction increases. The time history of the skin-friction is strongly negatively correlated to the value of $r_{w,w}(t)$ during an oscillation and the depth of the troughs in $r_{w,w}(t)$ and the height of the spikes in $C_f(t)$ also increase with increasing actuator spacing and period of oscillation. The percentage of T^+ for the width of the trough in $r_{w,w}(t)$, and therefore for the PSL to become analogous with the Stokes layer produced by uniform plasma following a change in polarity of the force, increases with increasing s_p^+ and decreasing T^+ .

5.3.2 Velocity and turbulence statistics

Velocity fluctuations in the flow field for the four periods of oscillation of previous interest, ($T^+ = 50, 100, 200$ and 500) are shown for the four plasma configurations and compared with the spanwise wall oscillation case and the no-control case. Normalisation of the velocity fluctuations by the actual wall-shear velocity (u_{τ_m}) is shown in Figures 5.17, 5.18 and 5.19. In Figure 5.19 the instantaneous mean spanwise velocity was used to calculate w_{rms} rather than the canonical time-averaged mean to remove the effect of the mean instantaneous spanwise flow caused by the forcing. (Velocity fluctuations normalised by u_{τ_0} are presented in Appendix B)

For $T^+ = 30$ and $T^+ = 100$ there is an outward shift of u_{rms} for the spanwise wall oscillation, uniform plasma and $s_p^+ = 10$ configurations e.g., the y -location of maximum u_{rms} for $T^+ = 100$, shifts outwards from $y^+ \approx 12$ for the no-control flow to $y^+ \approx 20$ for spanwise wall oscillation and even further to $y^+ \approx 22$ for uniform plasma. This indicates an increased viscous sublayer but with similar flow characteristics to the no-control flow further from the wall. The $s_p^+ = 12.5$ and $s_p^+ = 20$ configurations show a more linear profile, reaching a plateau not far from the wall, indicating that the outer-flow is inherently different to that of the no-control case. With increasing T^+ , the u_{rms} profiles for the $s_p^+ = 12.5$ configuration become more akin to those for uniform plasma complying with the increasing correlation of the PSLs to the uniform plasma Stokes layer. In the $s_p^+ = 20$ configuration the u_{rms} profiles become more akin to those for the uniform plasma with increasing T^+ but remain distinct from the profiles of the other configurations.

The v_{rms} and w_{rms} profiles for the discrete configurations exhibit local maxima close to the wall because of the actuation (see Section 5.3.3). For $T^+ = 30$ and $T^+ = 100$ there is an attenuation in v_{rms} and w_{rms} for spanwise wall oscillation, uniform plasma and $s_p^+ = 10$ configuration but as $T^+ > T_{opt}^+$ the fluctuations increase over that of the no-control case. The v_{rms} and w_{rms} profiles for the $s_p^+ = 12.5$ and $s_p^+ = 20$ configurations are markedly higher but become more akin to the uniform

plasma and the $s_p^+ = 10$ configurations with increasing T^+ .

Phase averaging of the velocity fluctuations for the uniform plasma and the three discrete configurations normalised by the no-control wall-shear velocity (u_{τ_0}) is presented in Figures 5.20, 5.21 and 5.22. The mean instantaneous spanwise velocity is used as previously to calculate w_{rms} in Figure 5.22.

For Figures 5.20 to 5.22 the velocity fluctuations increase with increasing actuator spacing. In particular, regions of large fluctuations start at around $t/T \approx 0.1$ for the discrete configurations and the intensity and duration of these regions increases with increasing actuator spacing. A similar conclusion can be made for the vorticity fluctuations presented in Figures 5.24 and 5.25 which present wall-normal vorticity ($\omega'_{y_{rms}}$) and spanwise vorticity ($\omega'_{z_{rms}}$) respectively. In the case of the streamwise vorticity fluctuations presented in Figure 5.23, the forcing produces large values near the wall for all the configurations but, as with the other vorticity fluctuations, further from the wall $y^+ > 30$, $\omega'_{y_{rms}}$ increases with increasing actuator spacing.

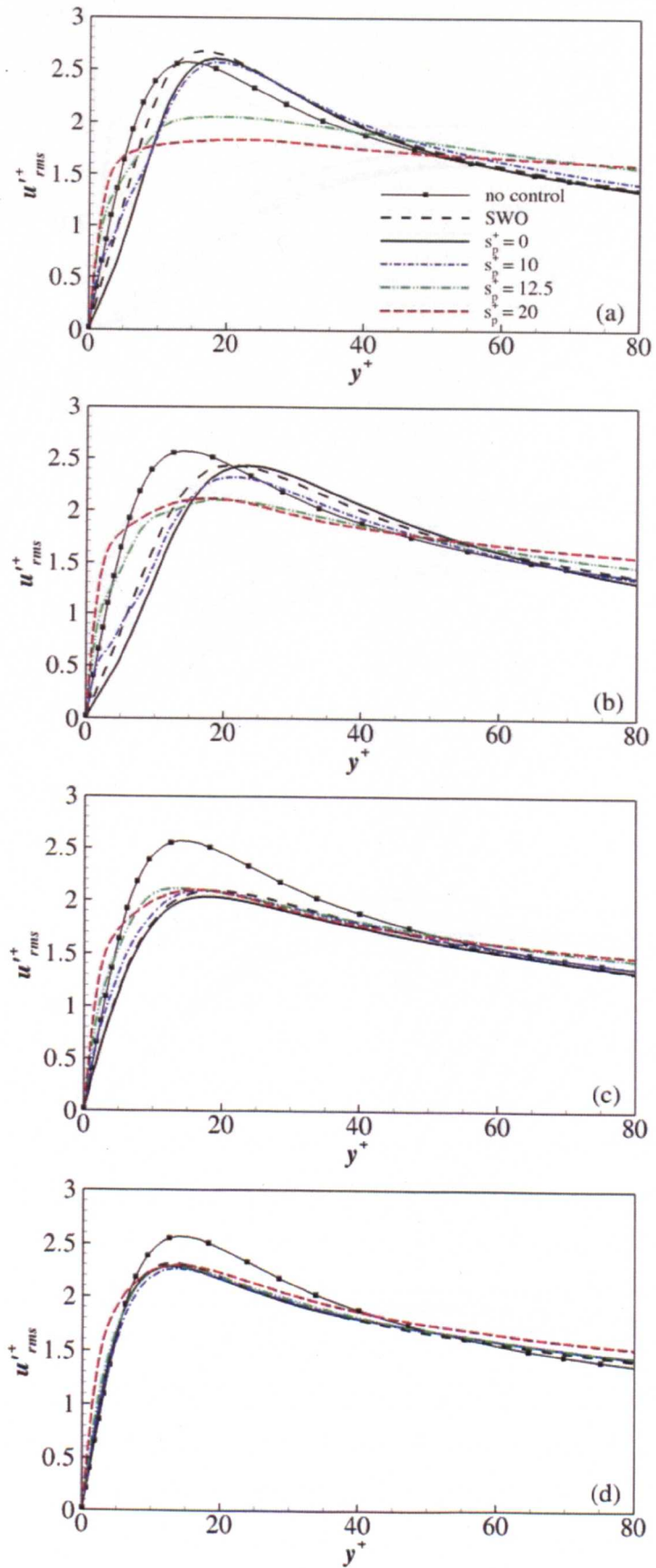


Figure 5.17: Root-mean-square streamwise velocity fluctuations, u_{rms} , normalised by the actual wall-shear velocity, u_{τ_m} : a) $T^+ = 30$, b) $T^+ = 100$, c) $T^+ = 200$ and d) $T^+ = 500$.

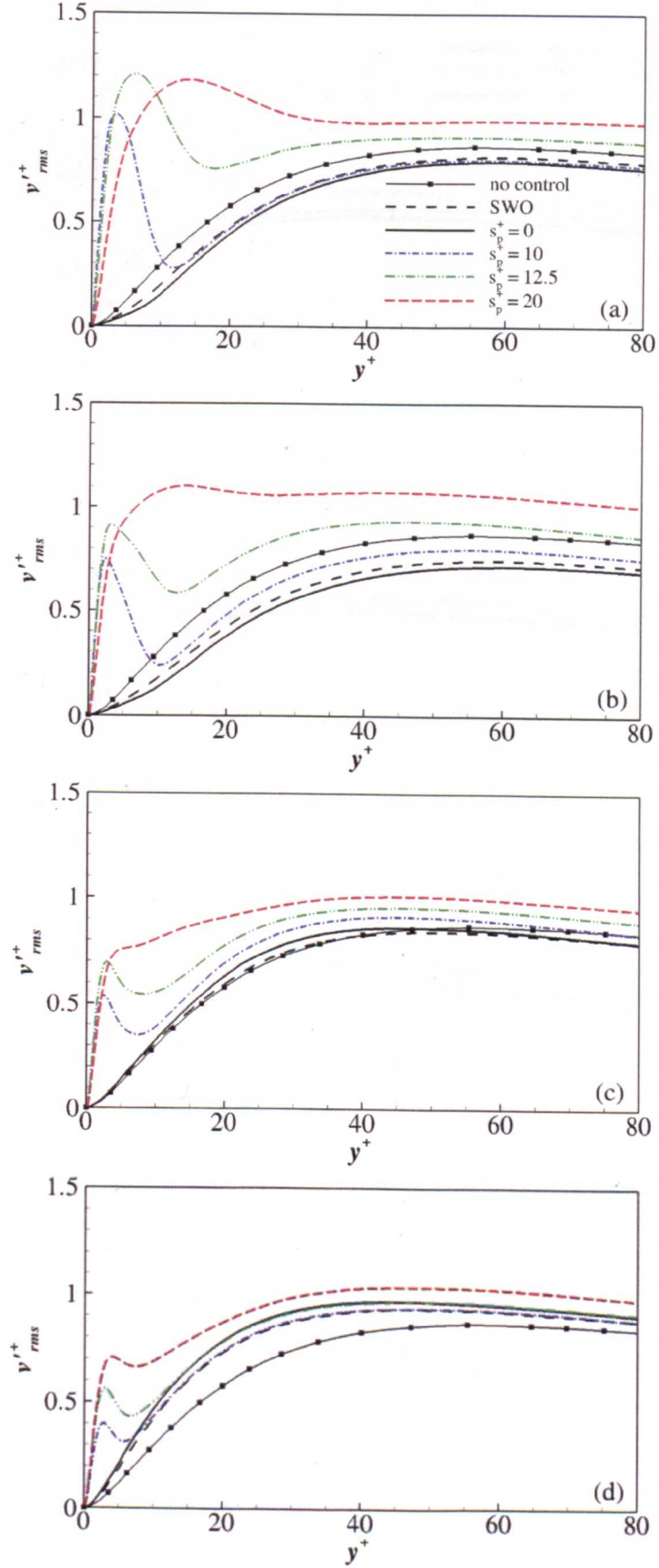


Figure 5.18: Root-mean-square wall-normal velocity fluctuations, v_{rms} , normalised by the actual wall-shear velocity, u_{τ_m} : a) $T^+ = 30$, b) $T^+ = 100$, c) $T^+ = 200$ and d) $T^+ = 500$.

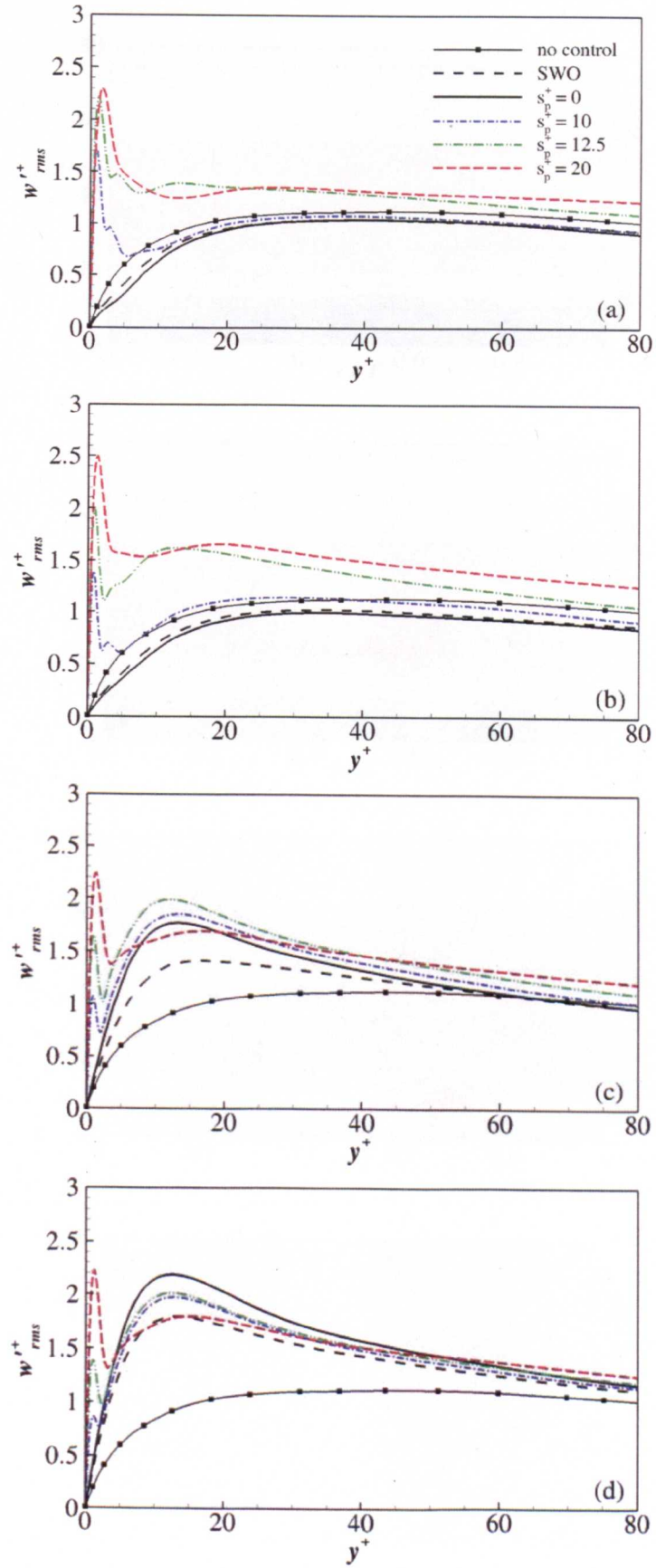


Figure 5.19: Root-mean-square spanwise velocity fluctuations, w_{rms} , normalised by the actual wall-shear velocity, $u_{\tau m}$: a) $T^+ = 30$, b) $T^+ = 100$, c) $T^+ = 200$ and d) $T^+ = 500$.

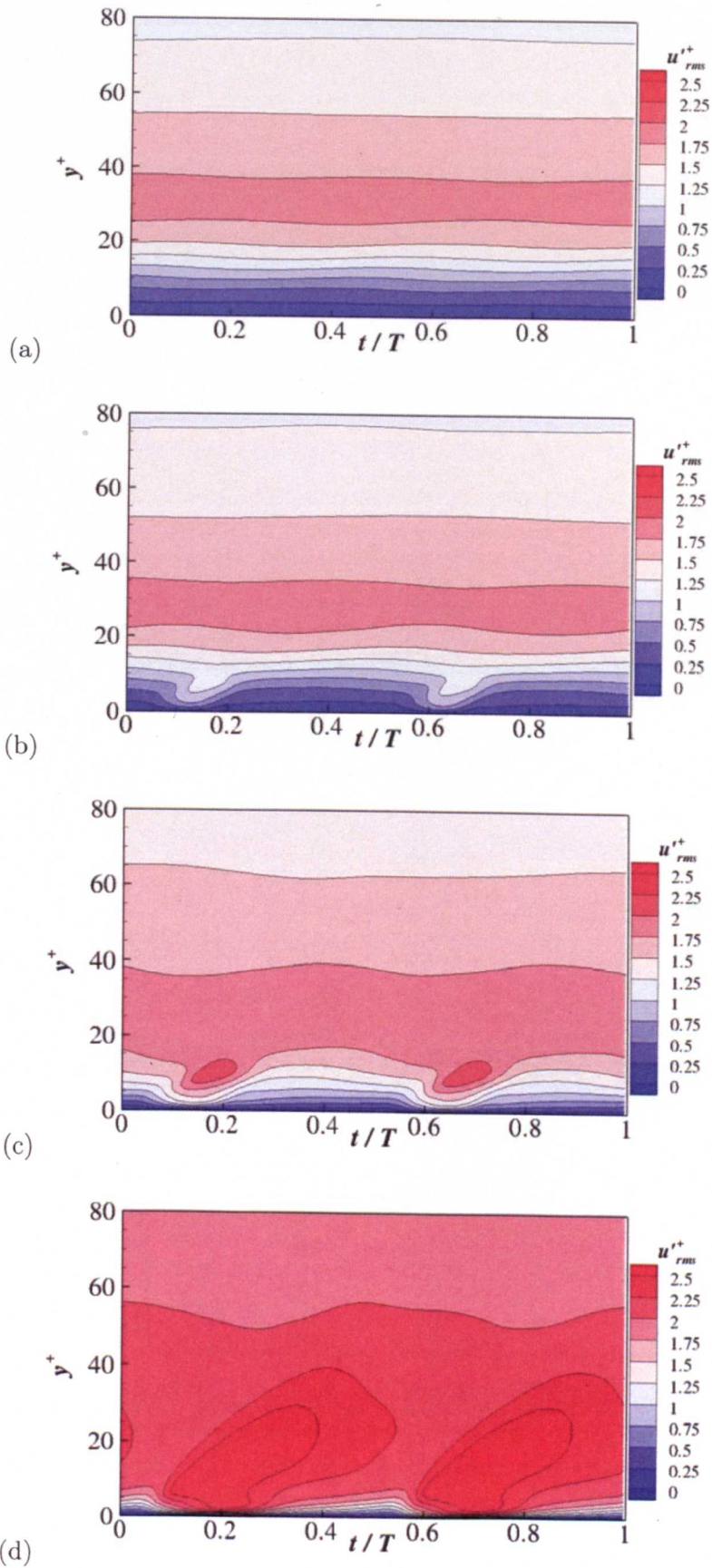


Figure 5.20: Phase averaged u_{rms} normalised by u_{τ_0} , contour plot for $T^+ = 100$: a) $s_p^+ = 0$, b) $s_p^+ = 10$, c) $s_p^+ = 12.5$ and d) $s_p^+ = 20$.

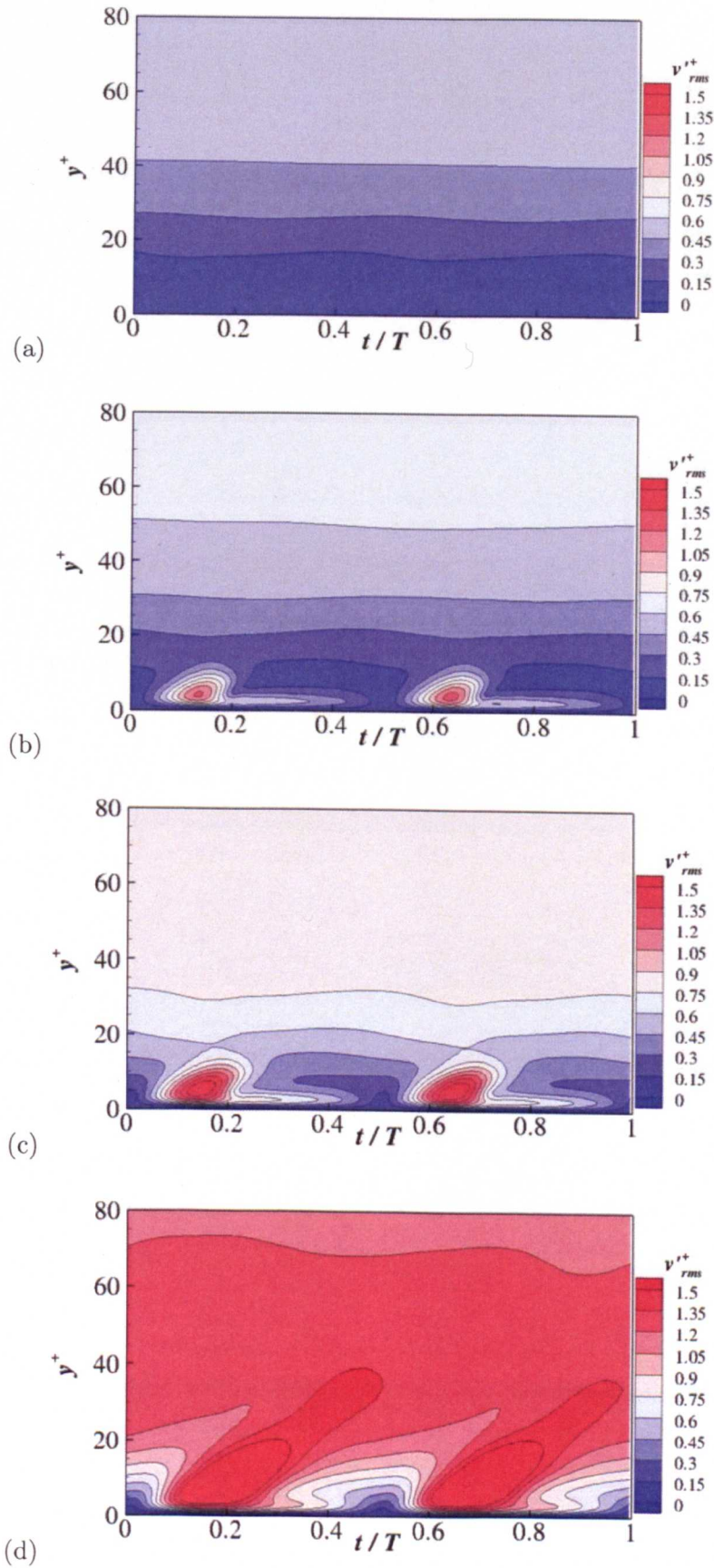


Figure 5.21: Phase averaged v_{rms} normalised by u_{τ_0} , contour plot for $T^+ = 100$: a) $s_p^+ = 0$, b) $s_p^+ = 10$, c) $s_p^+ = 12.5$ and d) $s_p^+ = 20$.

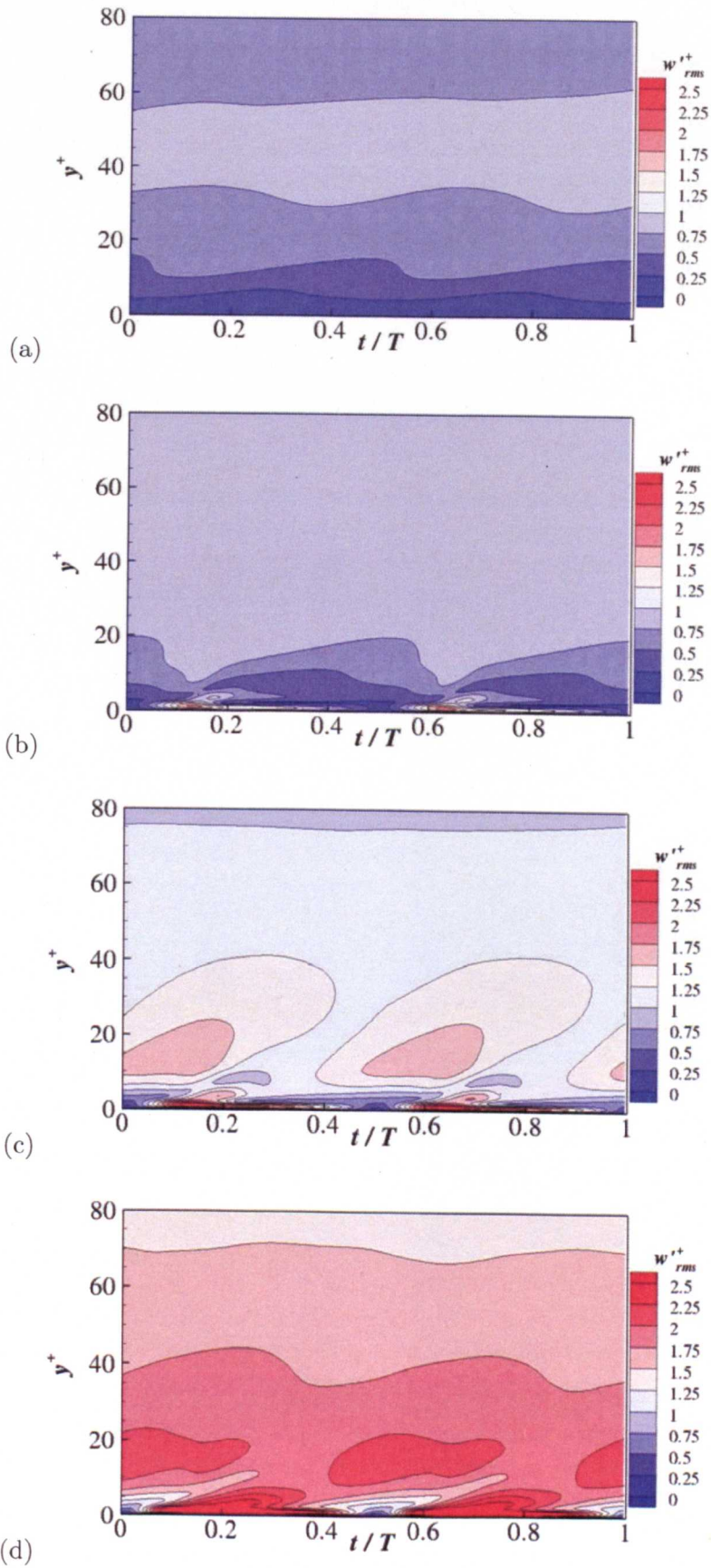


Figure 5.22: Phase averaged w_{rms} normalised by u_{τ_0} , contour plot for $T^+ = 100$: a) $s_p^+ = 0$, b) $s_p^+ = 10$, c) $s_p^+ = 12.5$ and d) $s_p^+ = 20$.

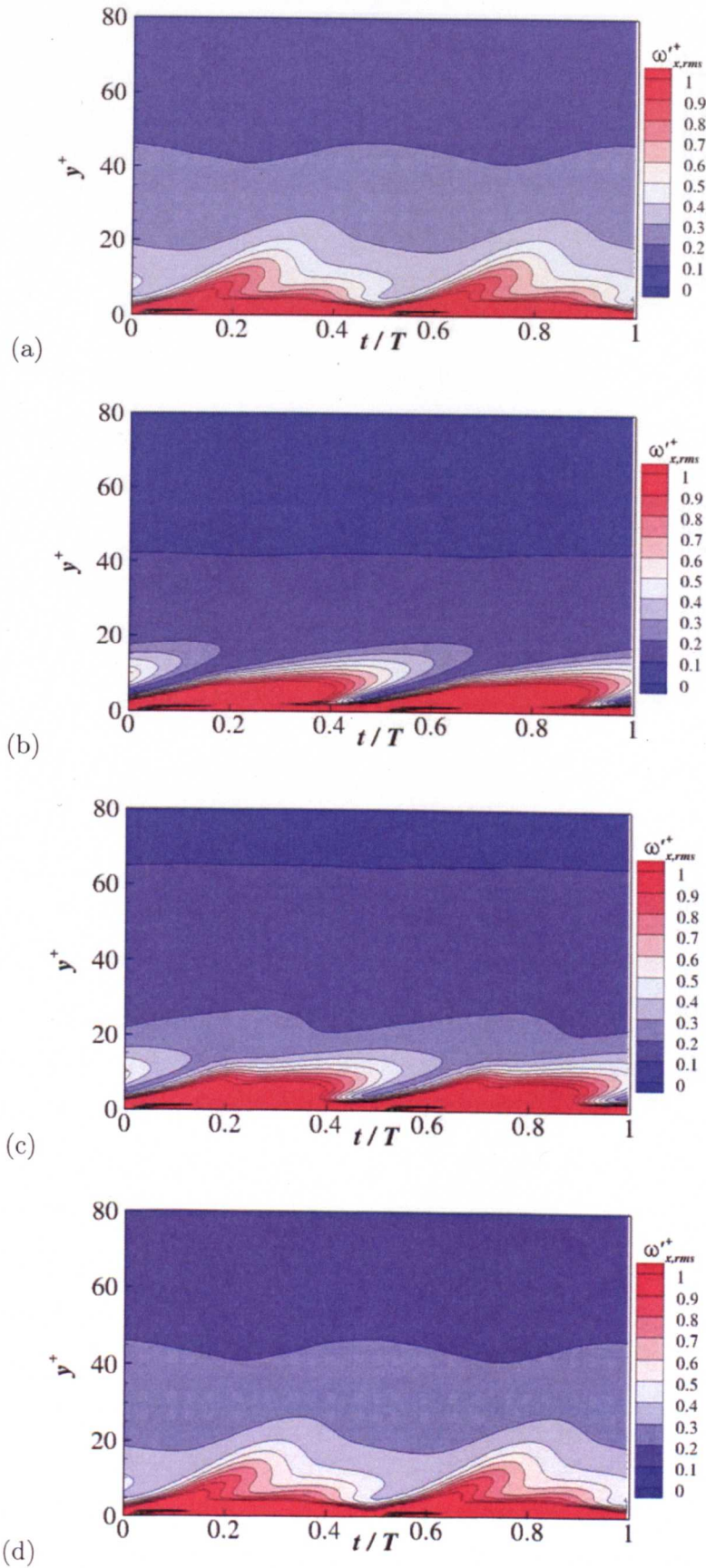


Figure 5.23: Phase averaged $\omega'_{x,rms}$ normalised by u_{τ_0} and h , contour plot for $T^+ = 100$: a) $s_p^+ = 0$, b) $s_p^+ = 10$, c) $s_p^+ = 12.5$ and d) $s_p^+ = 20$.

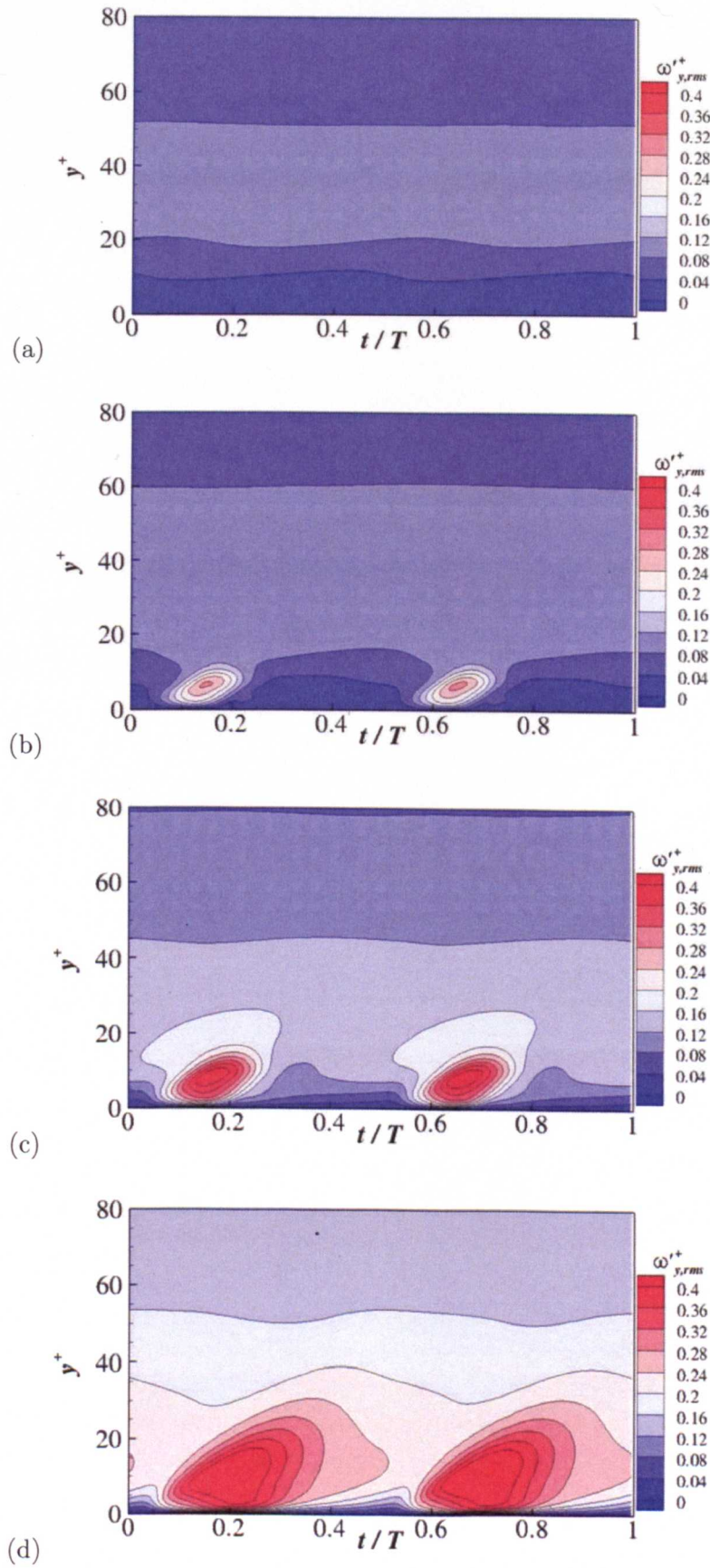


Figure 5.24: Phase averaged $\omega'_{x_{rms}}$ normalised by u_{τ_0} and h , contour plot for $T^+ = 100$: a) $s_p^+ = 0$, b) $s_p^+ = 10$, c) $s_p^+ = 12.5$ and d) $s_p^+ = 20$.

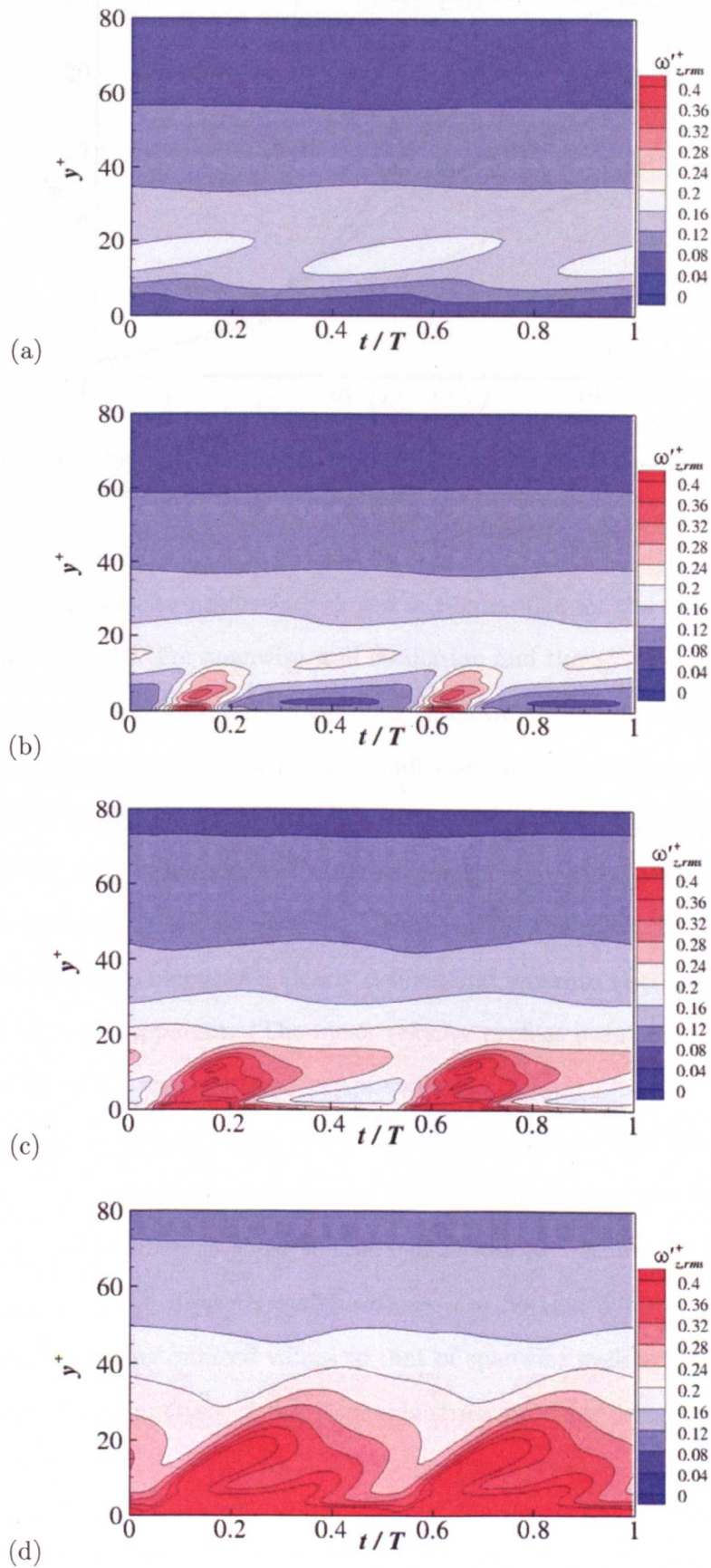


Figure 5.25: Phase averaged $\omega'_{x_{rms}}$ normalised by u_{τ_0} and h , contour plot for $T^+ = 100$: a) $s_p^+ = 0$, b) $s_p^+ = 10$, c) $s_p^+ = 12.5$ and d) $s_p^+ = 20$.

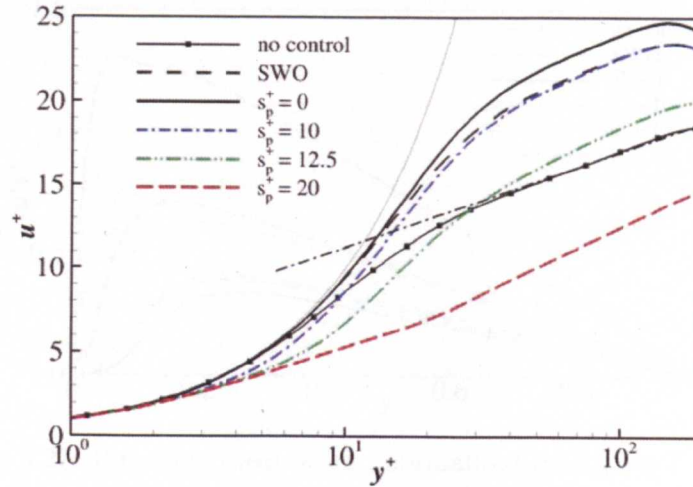


Figure 5.26: Mean velocity profiles normalised by actual wall-shear velocities, u_{τ_m} . (law of the wall $u^+ = y^+$, $u^+ = \frac{1}{\kappa} \ln y^+ + 5.5$)

The mean-velocity profiles are shown in Figure 5.26 for the different configurations for $T^+ = 100$. For spanwise wall oscillation and the $s_p^+ = 10$ configuration the point where the log-law intercepts $y^+ = u^+$ is elevated from $y^+ \approx 10$ to $y^+ \approx 15$, and for the uniform case to $y^+ \approx 17$. This indicates an increase in the viscous sublayer, which as is also shown in the shift in the streamwise velocity fluctuations. Although a 9% drag reduction was obtained for the $s_p^+ = 12.5$ configuration the shift in the intercept is not so apparent. However for the $s_p^+ = 20$ configuration where the skin-friction increases a clearly defined and separate viscous sublayer and log-law region is not apparent. (The mean-velocity profiles normalised by u_{τ_0} for a range of values of T^+ are presented in Appendix B.)

The Reynolds shear stress, $-\overline{u'v'}$, is shown in Figure 5.27 for $T^+ = 100$. All but the $s_p^+ = 20$ configuration show a reduction throughout the domain apart from near the wall where a local maxima is produced because of the entrainment/expulsion for the discrete configurations (see Section 5.3.3). The $s_p^+ = 0$ configuration displaying reduced values to that of spanwise wall oscillations.

The quadrant analysis of the Reynolds stress provides detail on the contri-

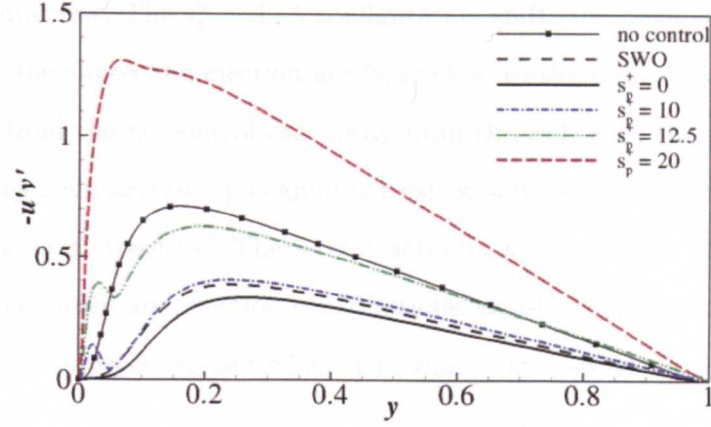
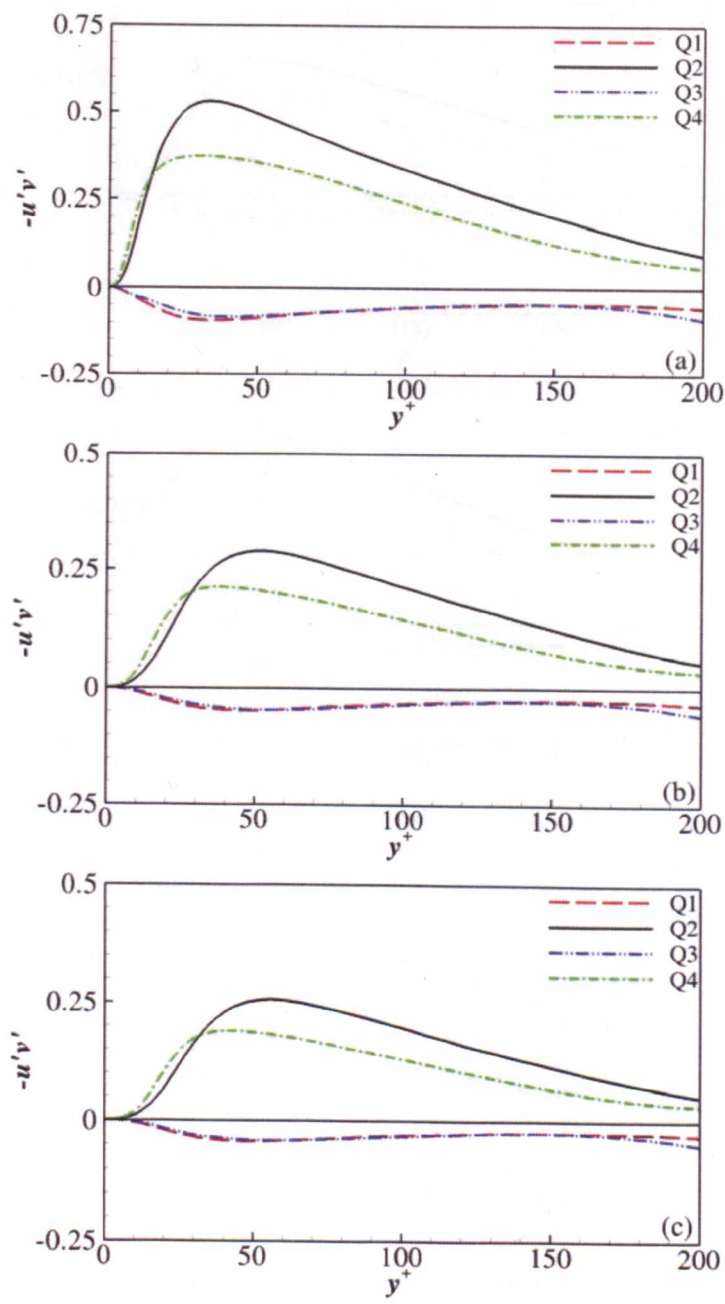


Figure 5.27: Reynolds shear stress, normalised by u_{τ_0} for $T^+ = 100$.

butions to the total turbulence production from events occurring in the flow. The second quadrant ($u_{rms} < 0$ and $v_{rms} > 0$; ejection) and fourth-quadrant ($u_{rms} > 0$ and $v_{rms} < 0$; sweep) events contribute to positive Reynolds shear stress and the first quadrant ($u_{rms} > 0$ and $v_{rms} > 0$) and third-quadrant ($u_{rms} < 0$ and $v_{rms} < 0$) events contribute to the negative Reynolds shear stress.

The contribution to the Reynolds shear stress is shown in Figure 5.27 for $T^+ = 100$, the sum of the four quadrants is equal to the local mean Reynolds shear stress. In the case of the no-control channel Figure 5.27(a) the ejection event is dominant away from the wall and the sweep event is dominant in the wall region and these contributions are approximately equal at $y^+ \approx 12$. Spanwise wall oscillation significantly reduces the ejection and sweep events and the point where their contributions are equal is shifted outwards to $y^+ \approx 30$. Uniform plasma shifts this point even further to $y^+ \approx 32$ and the fractional contributions from the sweep and ejection events are similar to that of the no-control case, implying that the outer-wall turbulence is attenuated and displaced but the structure remains similar. The $s_p^+ = 10$ configuration has a local maximum close to the wall. But the sweep and ejection events are then suppressed and shifted outwards with the y -location of equilibrium at $y^+ \approx 30$ and the fractional contributions of the events remain similar to the pre-

vious configurations. The $s_p^+ = 12.5$ configuration shifts the point of equilibrium to $y^+ \approx 23$ but the sweep and ejection are large close to the wall. There is only slight attenuation from the no-control case away from the wall with the percentage contribution of ejection and sweep beginning to show some similarity implying a subtle change to the flow structure. The largest actuator spacing, $s_p^+ = 20$ configuration, produces large sweep and ejection contributions, and their fractional contributions are very similar implying large turbulent mixing right through the domain.



(Caption overleaf.)

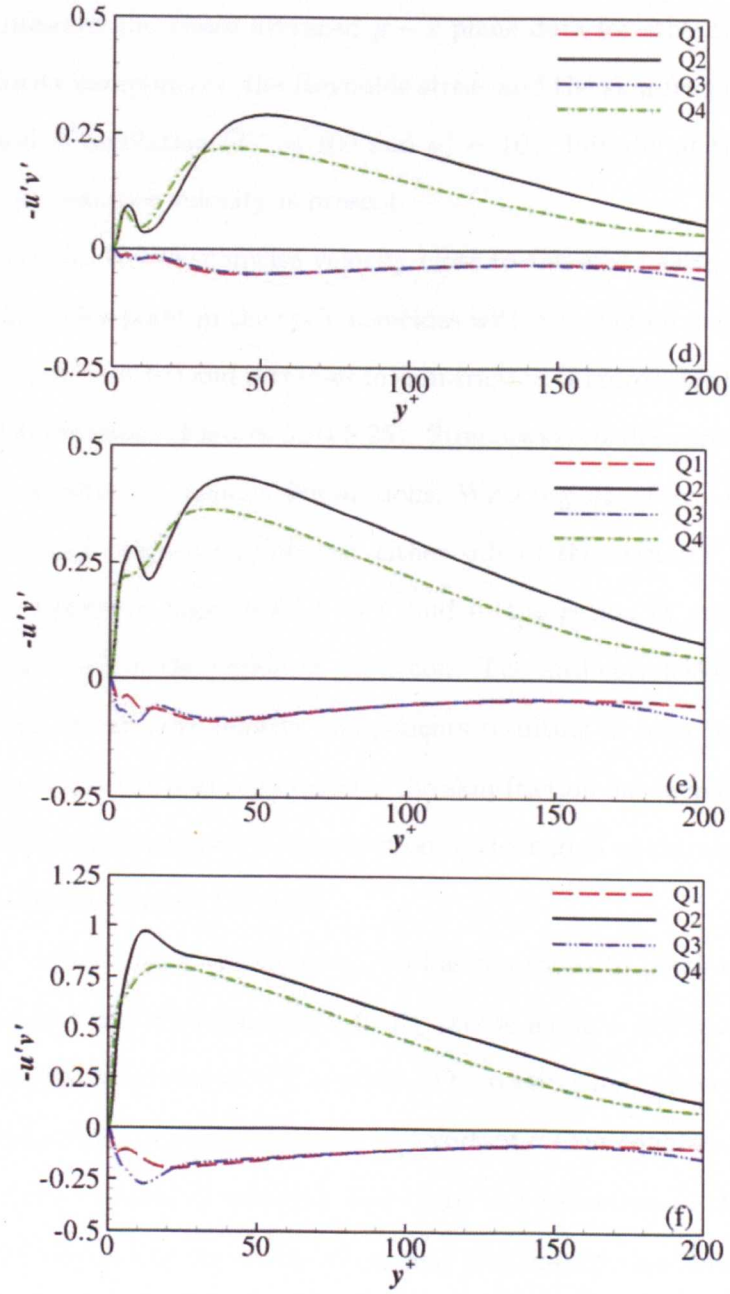


Figure 5.27: Reynolds shear stress from each quadrant. Reynolds shear stress from each quadrant normalised by the wall-shear velocity, u_{τ_0} , for $T^+ = 100$: a) No-control, b) Spanwise wall oscillation, c) $s_p^+ = 0$, d) $s_p^+ = 10$, e) $s_p^+ = 12.5$, f) $s_p^+ = 20$.

5.3.3 $Y - Z$ plane data

Figure 5.28 presents the phase averaged $y - z$ plane data for streamwise vorticity, the three velocity components, the Reynolds stress and the skin-friction profile over one half period of oscillation ($T^+ = 100$ and $s_p^+ = 10$). Initially at time $t/T = 0$ a strong negative spanwise velocity is present.

At $t/T = 0.125$ the spanwise velocity close to the wall has changed polarity and is irregular. This point in the cycle coincides with a reduction in the correlation $r_{w,w}(t)$ (see Figure 5.15(b)) and increases in skin-friction (Figure 5.5(b)), the velocity and vorticity fluctuations (Figures 5.20-5.25). Streamwise vortices are present above each actuator resulting in velocity fluctuations. With regions of expulsion (positive v) and entrainment (negative v) present either side of the actuator. The vortices also result in regions of high speed ($+u'$) fluid in the region of entrainment and low-speed fluid ($-u'$) in the region of expulsion. The anti-correlation between the wall-normal and streamwise velocity components resulting in high Reynolds stress increases close to the wall and consequently the skin-friction has increased from that at $t/T = 0$, with large increases in skin-friction in the region of entrainment as high speed fluid is drawn towards the wall.

By $t/T = 0.25$ the correlation $r_{w,w}(t)$ has improved to be close to a perfect positive correlation and the spanwise velocity profile along z in Figure 5.28(c) appears more uniform from that at $t/T = 0.125$. The vortices have reduced in strength and are forming a sheet of negative streamwise vorticity. Consequently the expulsion and ejection have reduced in strength and there is a reduction in the streamwise velocity fluctuations. The Reynolds stress and the skin-friction have attenuated. Further in time at $t/T = 0.375$ the velocity fluctuations have reduced further, and the skin-friction has reduced slightly more.

The $y - z$ plane data for the $s_p^+ = 12.5$ configuration is presented in Figure 5.29. As with the $s_p^+ = 10$ configuration a similar sequence of events occurs but the time taken for the streamwise vortices and the velocity fluctuations to attenuate

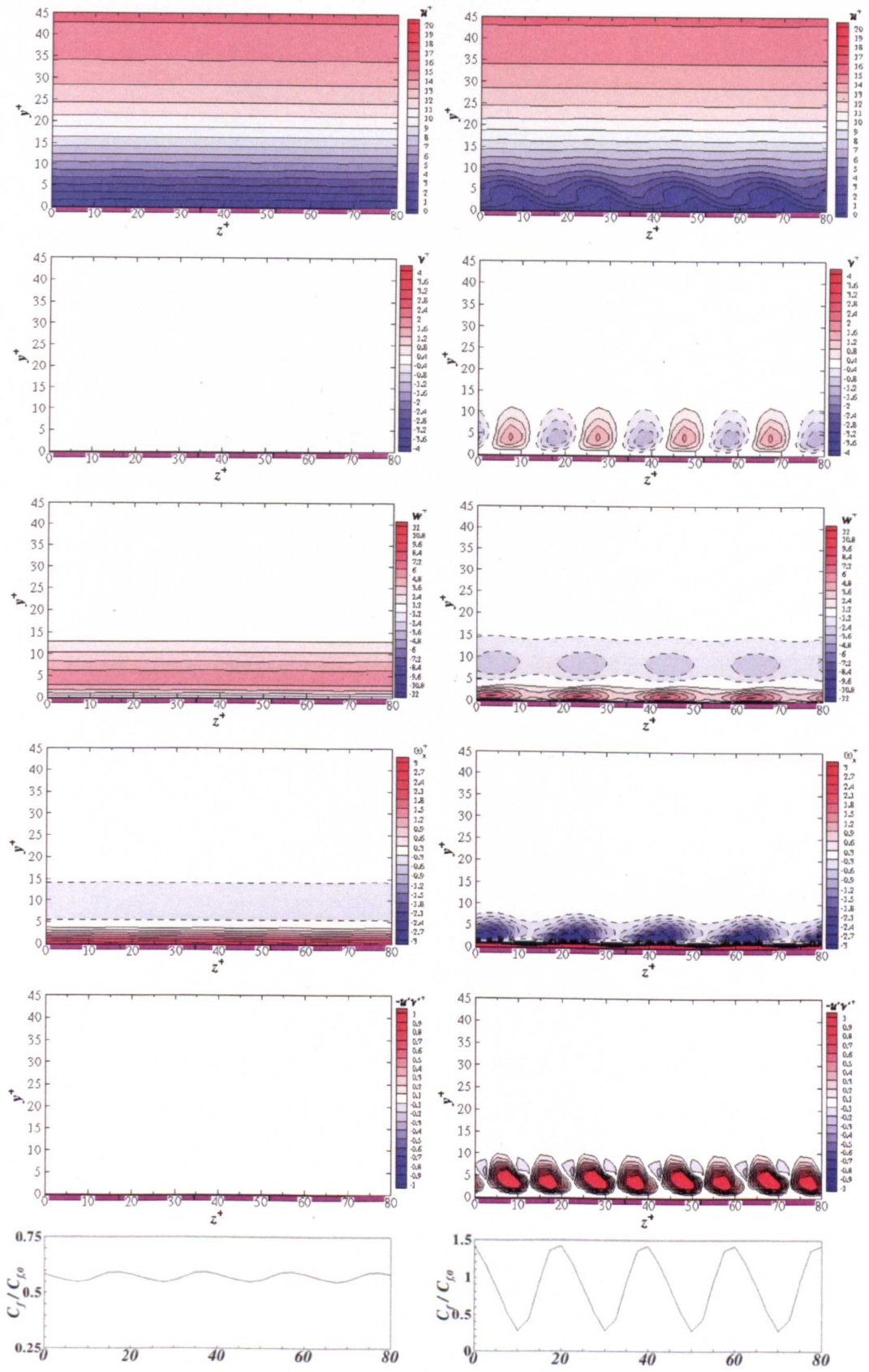
takes longer with stronger fluctuations and corresponding skin-friction increases prior to that observed for the $s_p^+ = 10$ configuration.

The data presented in Figure 5.30 presents a slightly different sequence of events for the $s_p^+ = 20$ configuration. The correlation $r_{w,w}(t)$ never approaches a close to perfect correlation $r_{w,w}(t) \approx 1$ in Figure 5.15(b) and the values of w_{rms} are large in Figure 5.22. This is evident from the non-uniform spanwise velocity profile along z with the distinct wall jets created by each actuator still clearly distinguishable by $t/T = 0.375$, unlike the two smaller actuator spacings where the jets had agglomerated into a sheet of uniform spanwise velocity not far from the wall. Consequently there are still areas of large streamwise vorticity rather than a uniform sheet of vorticity with starting vortices that have lifted away from the wall clearly evident at $t/T = 0.25$, unlike in the two smaller actuator spacings, a trend also seen for two dimensional quiescent simulations in Section 4.6. The expulsion/ejection is significantly larger in strength than in the two smaller actuator spacing configurations particularly at $t/T = 0.25$ and consequently large fluctuations in the streamwise velocity are present.

With the increased actuator spacing it is more apparent, that where there is entrainment the region of largest $-u'$ and $-v'$ is close to the wall $y^+ < 5$. While in the area of expulsion the area of highest $+u'$ and $+v'$ is further away from the wall, $y^+ \approx 10$, resulting in different y -locations for the Reynolds stress maxima. It is also more apparent that the local skin-friction is smaller in the area of expulsion and largest in the area of ejection where it is up to four times that of the time averaged no-control skin-friction at $t/T = 0.25$.

5.3.4 Flow visualisation

The λ_2 quantity introduced by Jeong and Hussain (1995) is frequently used to identify vortical structures. Iso-surfaces for values of $\lambda_2^+ = -0.0125$ based on the actual skin-friction velocity u_{τ_m} , which is the equivalent of the maximum xz plane averaged



(a)

(b)

(Caption overleaf.)

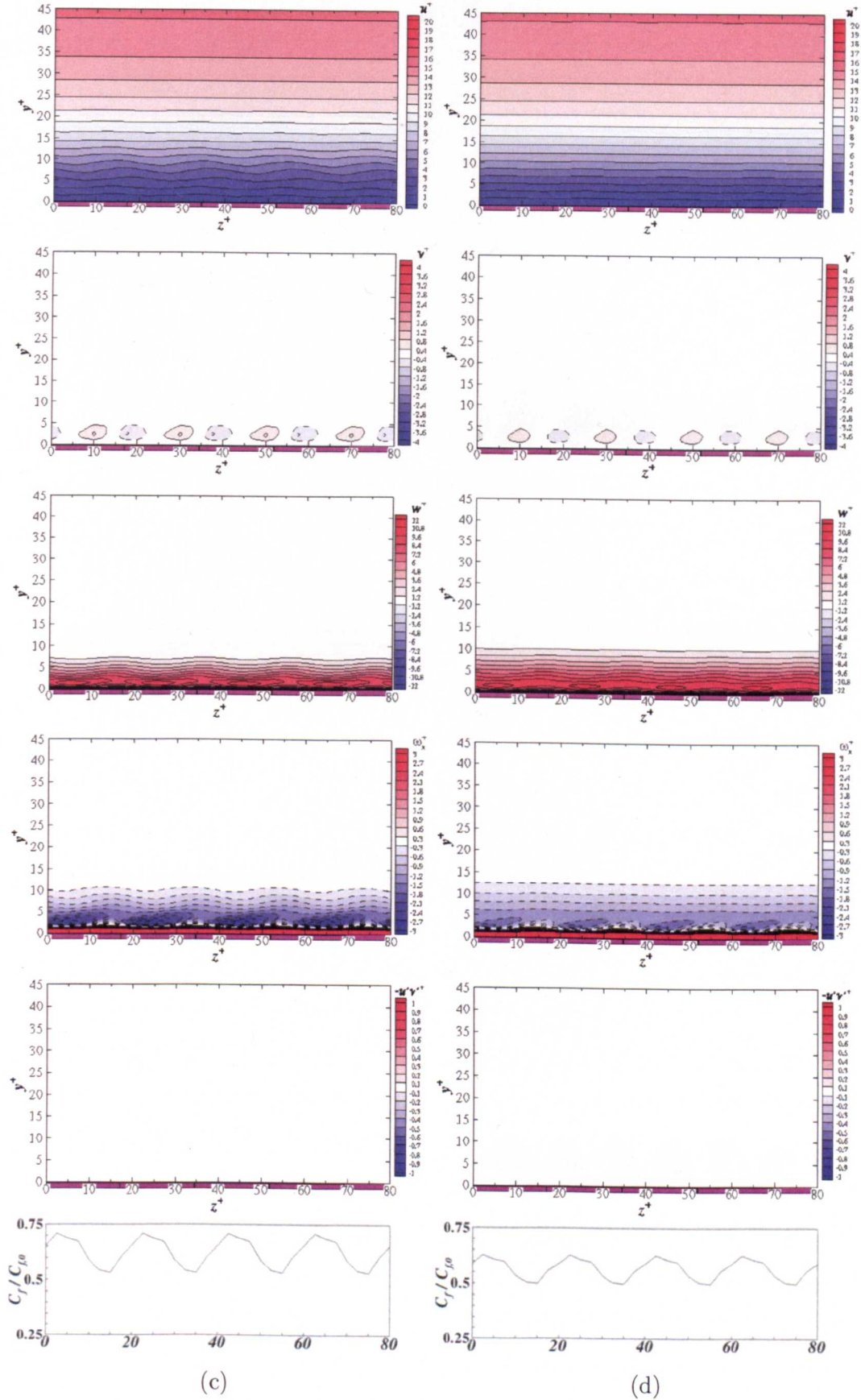
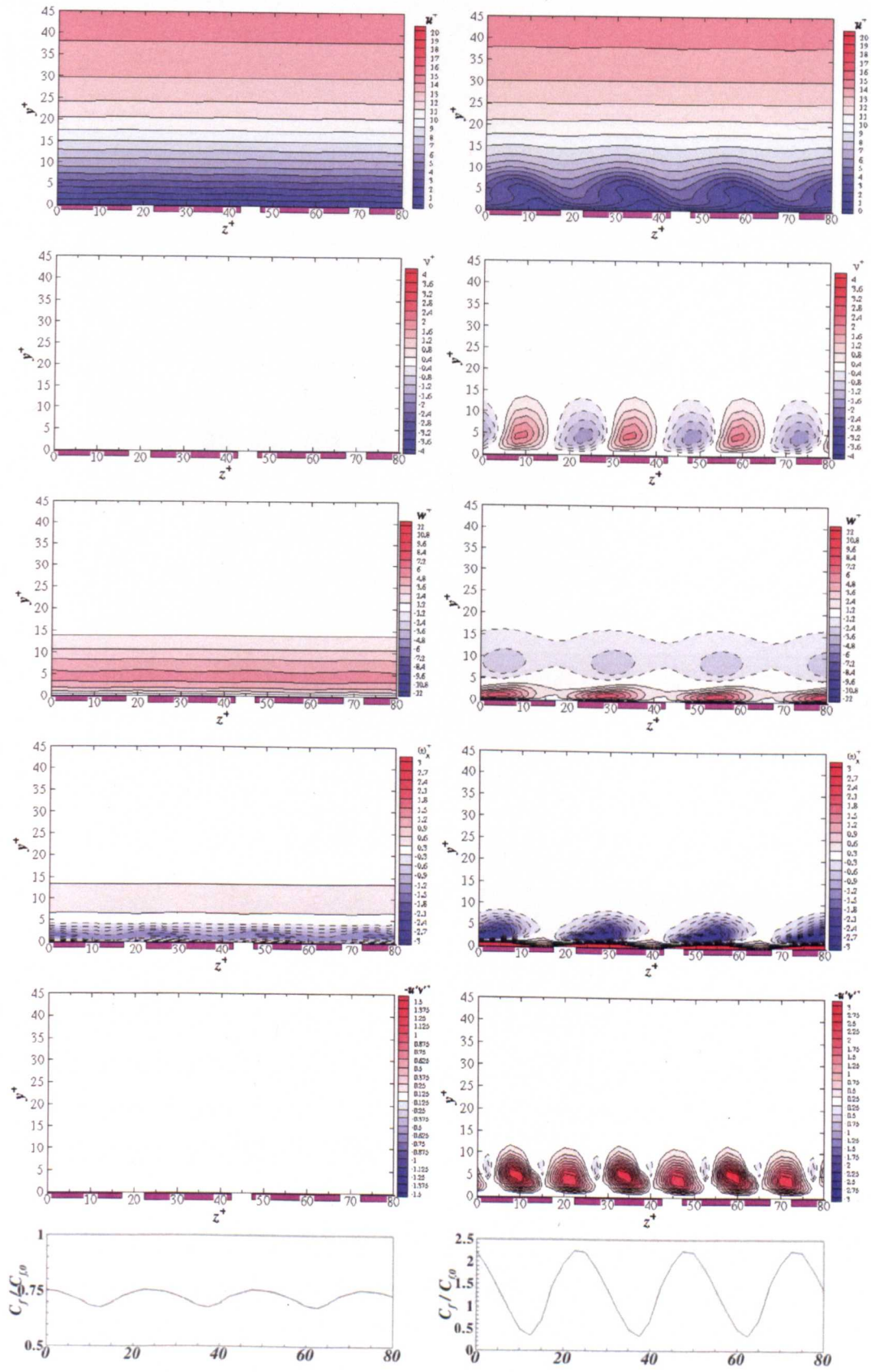


Figure 5.28: From top to bottom for each sub-figure: phase-averaged streamwise velocity u^+ , wall-normal velocity v^+ , spanwise velocity, w^+ , streamwise vorticity ω_x^+ , Reynolds stress $-u'v'^+$ contour plots with corresponding skin-friction ratio, $C_f/C_{f,0}$, for the $s_p^+ = 10$ configuration: a) $t/T = 0$, b) $t/T = 0.125$, c) $t/T = 0.25$ and d) $t/T = 0.375$.



(a)

(b)

(Caption overleaf.)

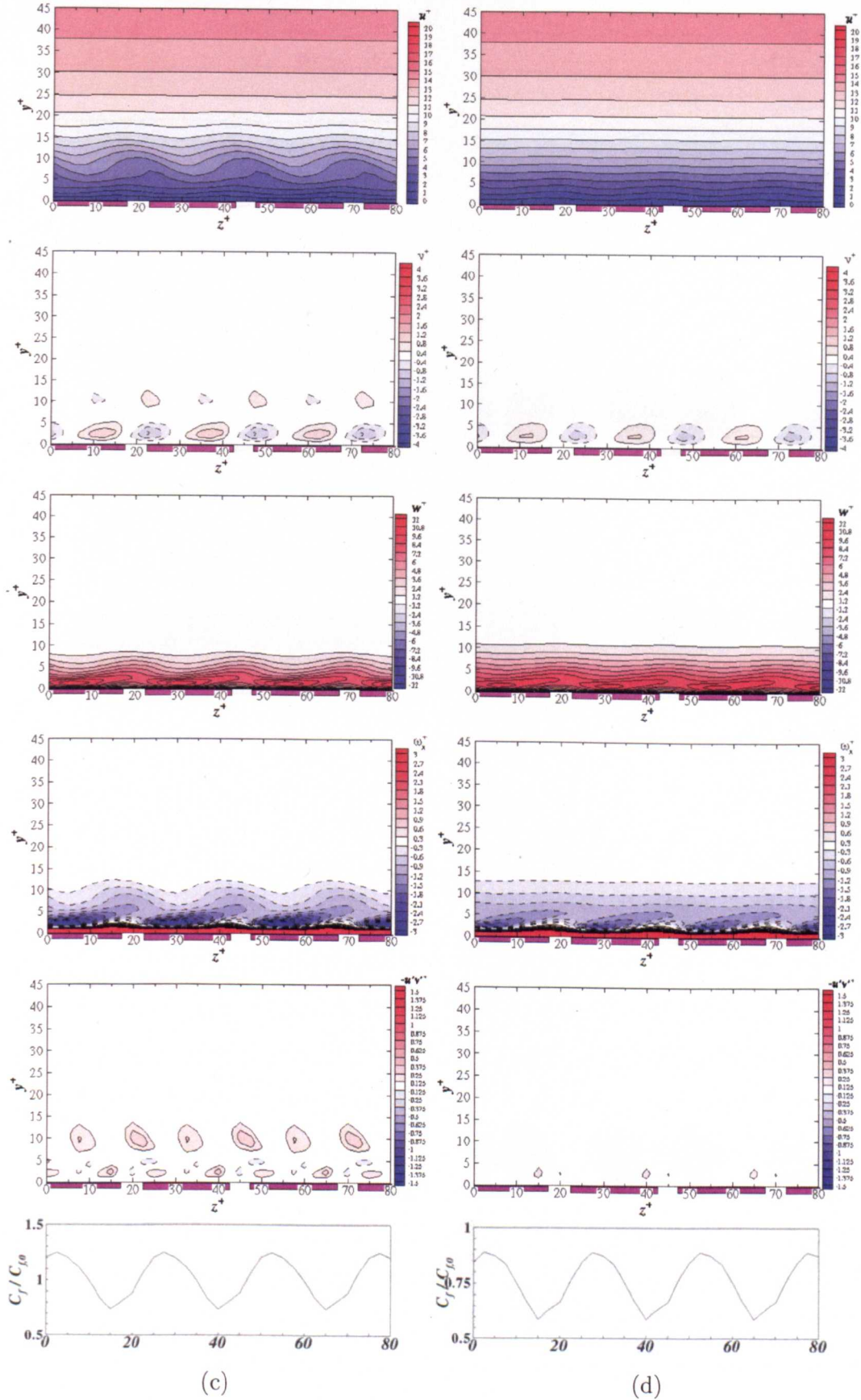
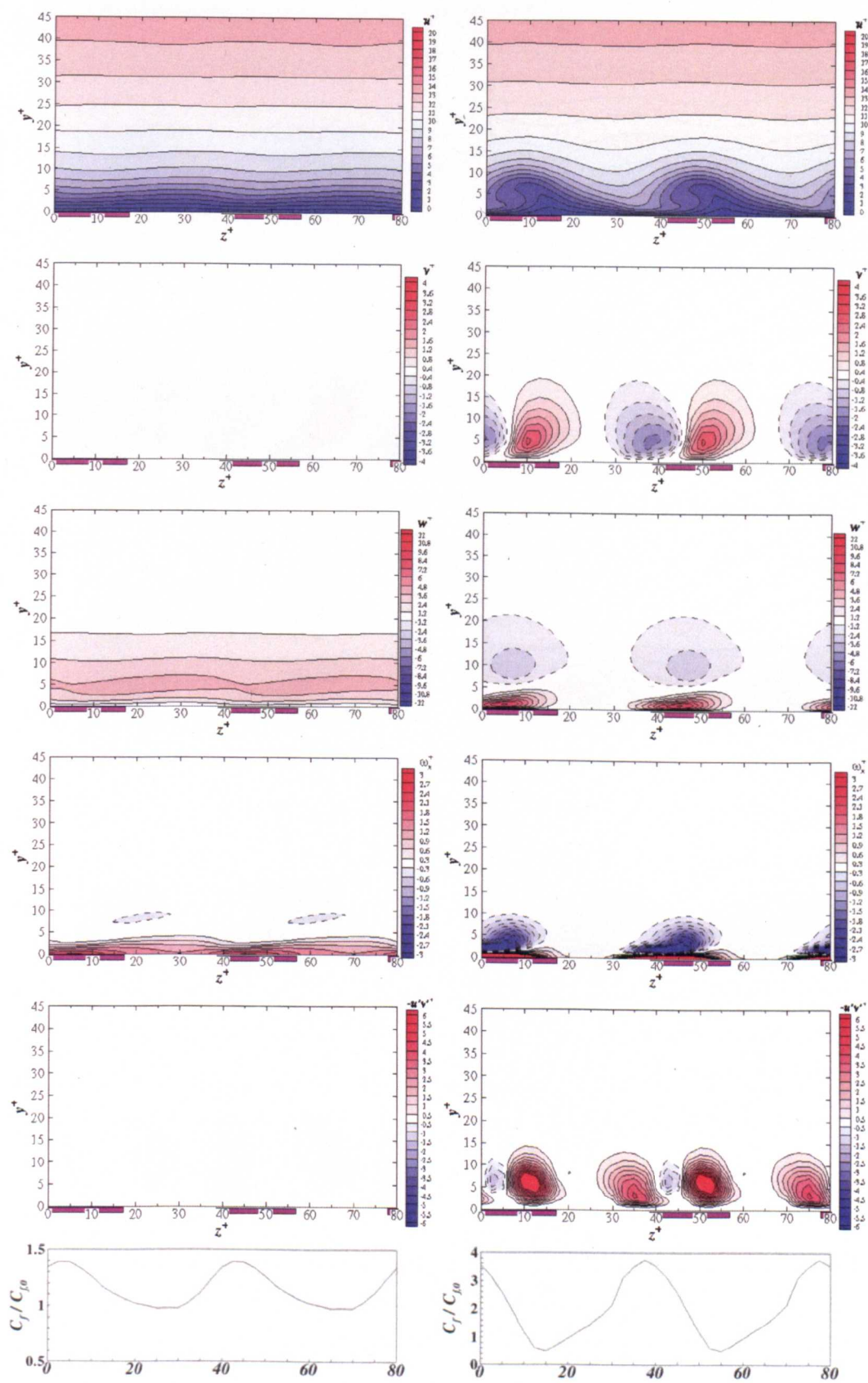


Figure 5.29: From top to bottom for each sub-figure: phase-averaged streamwise velocity u^+ , wall-normal velocity v^+ , spanwise velocity, w^+ , streamwise vorticity ω_x^+ , Reynolds stress $-u'v'^+$, contour plots with corresponding skin-friction ratio, $C_f/C_{f,0}$, for the $s_p^+ = 12.5$ configuration: a) $t/T = 0$, b) $t/T = 0.125$, c) $t/T = 0.25$ and d) $t/T = 0.375$.



(a)

(b)

(Caption overleaf.)

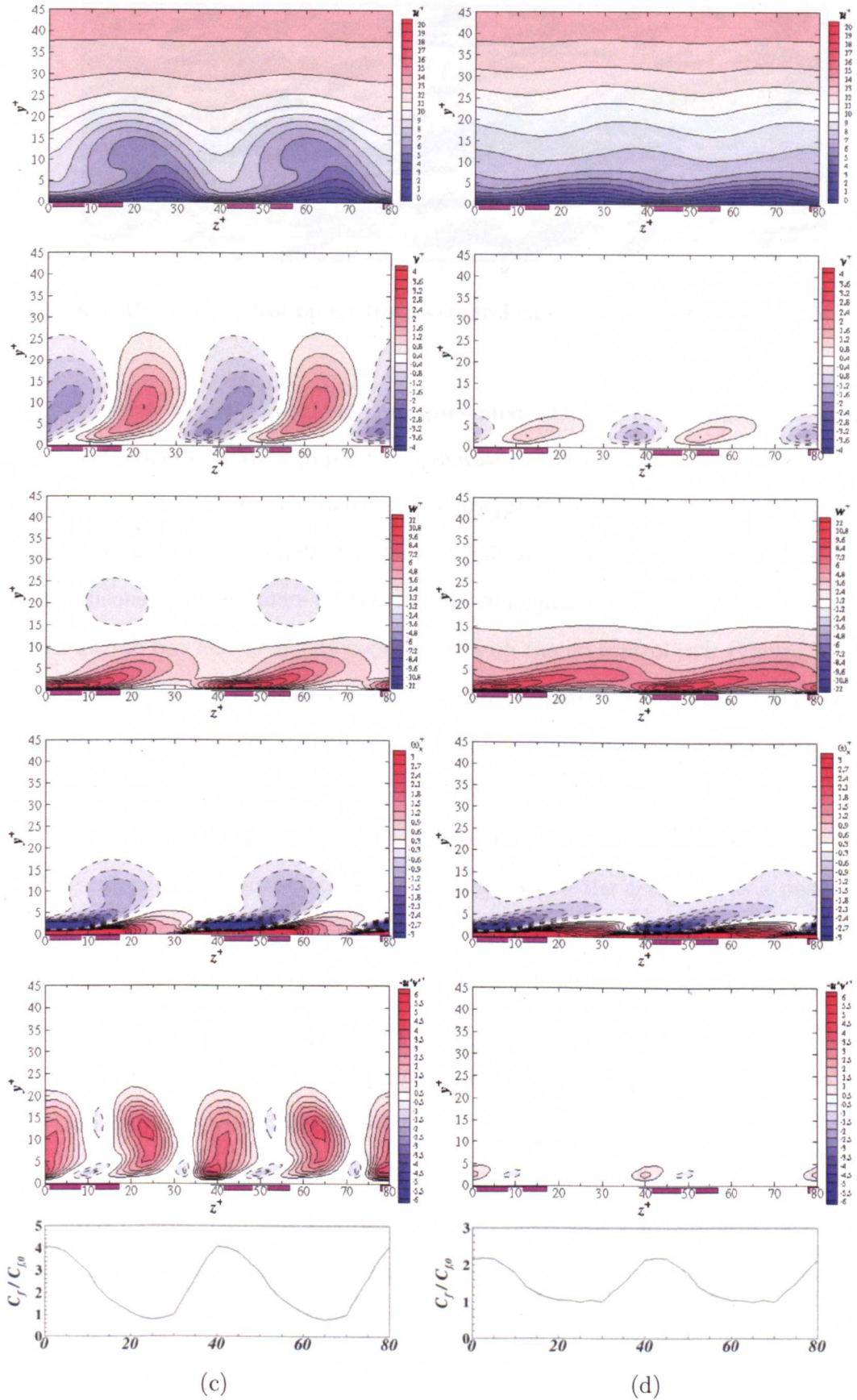


Figure 5.30: From top to bottom for each sub-figure: phase-averaged streamwise velocity u^+ , wall-normal velocity v^+ , spanwise velocity w^+ , streamwise vorticity ω_x^+ , Reynolds stress $-u'v'^+$, contour plots with corresponding skin-friction ratio, $C_f/C_{f,0}$, for the $s_p = 20$ configuration: a) $t/T = 0$, b) $t/T = 0.125$, c) $t/T = 0.25$ and d) $t/T = 0.375$.

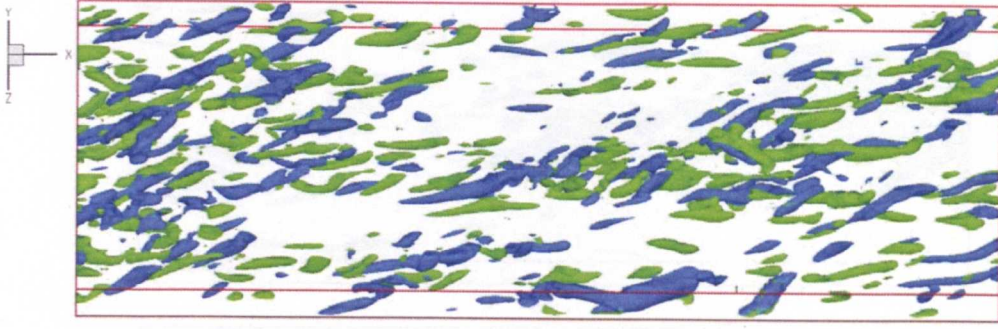


Figure 5.31: λ_2 visualisation for the no-control case $x = 0 - 9$, $\lambda_2^+ = -0.0125$.

$\lambda_{2_{rms}}$ value for the no-control case, are presented. The iso-surfaces are separated into structures associated with positive spanwise vorticity (blue contours) and negative spanwise vorticity (green contours) and are presented for the entire width of the domain but only longitudinally for the first half of the domain. Figure 5.32 is the instantaneous λ_2 iso-contours for the uniform configuration ($T^+ = 100$) at the mid-points for the two half-cycles. In comparison with the no-control case (Figure 5.31) the structures here are reduced in density and elongated in size. Elongation and reduction in frequency of structures has been previously witnessed with spanwise wall oscillation simulations (Viotti et al., 2009).

For the $s_p^+ = 10$ configuration the discrete plasma has been shown to introduce negative streamwise vorticity structures above the actuators as a positive spanwise force is generated and positive vorticity when a negative spanwise force is generated. These near-wall structures that run the length of the domain are clearly evident in Figure 5.33. Above them the turbulent structures are reduced and elongated, indicating a suppression and attenuation of the turbulence which is seen in the statistics presented in Section 5.3.2.

In the case of the $s_p^+ = 12.5$ configuration the outer-wall turbulent structures in Figure 5.34 appear to have increased and are smaller in size indicating an increase in the intensity of turbulence. The time averaged statistics indicates an increase in

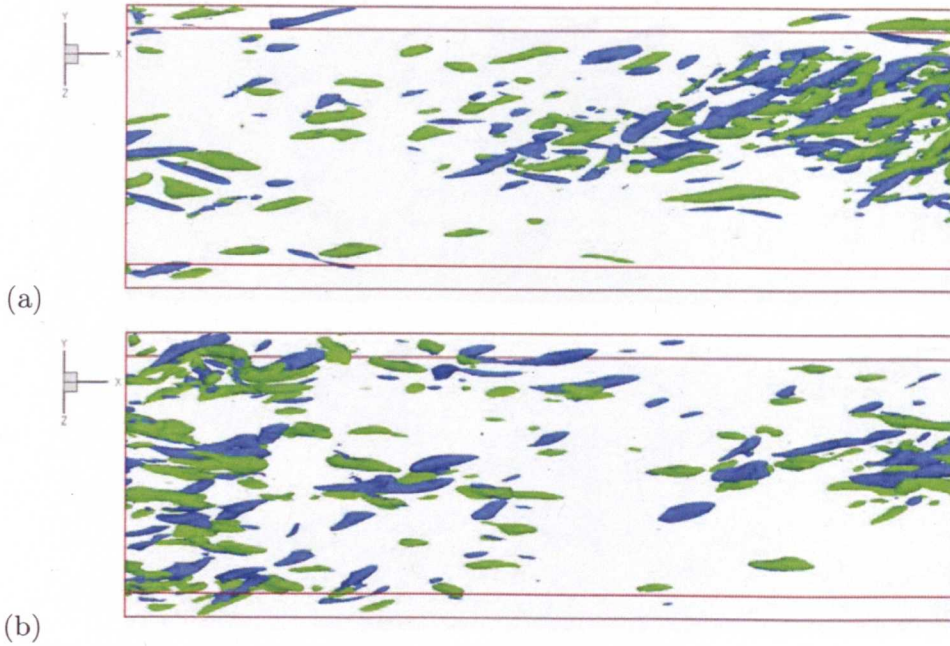


Figure 5.32: λ_2 visualisation for uniform plasma, $x = 0 - 9$, $\lambda_2^+ = -0.0125$: a) $t/T = 0.25$ and b) $t/T = 0.75$.

turbulence for the $s_p^+ = 20$ configuration and Figure 5.35 supports this as the whole domain is filled with numerous, densely packed, vortical structures.

5.4 Discussion

A series of simulations were run to investigate the possibility of using DBD plasma actuators for turbulent skin-friction control by generating temporally oscillating spanwise motions close to the wall. The intention was to go from spatially uniform, temporally oscillating spanwise wall oscillation, a technique known to provide large drag reductions and attenuate turbulence, and transform through a series of configurations to a final DBD configuration with an actuator spacing of $s_p^+ = 20$ in order to assess the effect on the drag reduction and turbulence for each configuration. A series of oscillation periods were used from $T^+ \doteq 15 \sim 500$ for each configuration. A large range was used for two reasons; the small periods were tested as Jukes et al.

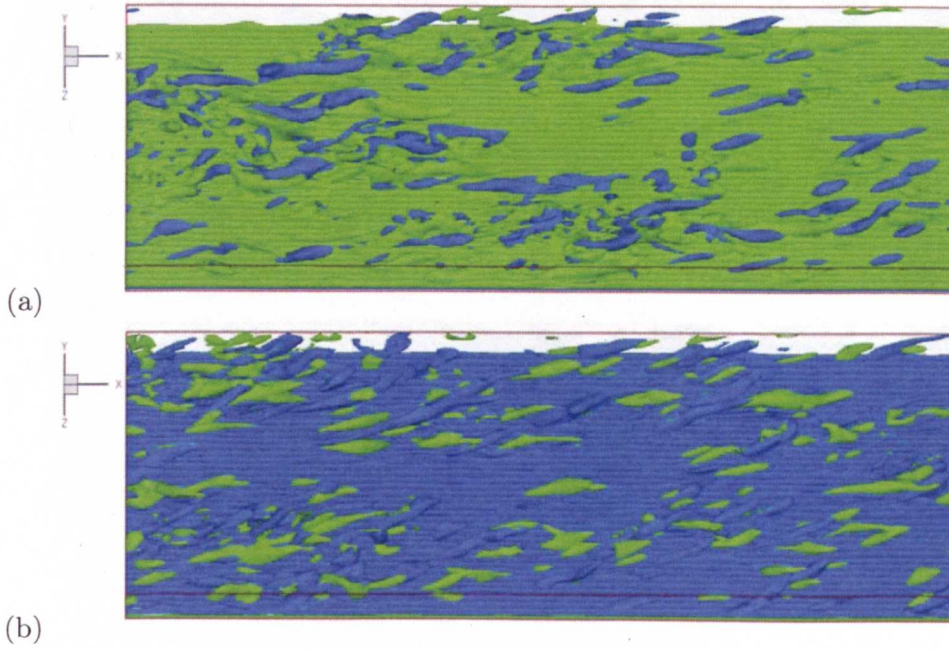


Figure 5.33: λ_2 visualisation for the $s_p^+ = 10$ configuration, $x = 0 - 9$, $\lambda_2^+ = -0.0125$: a) $t/T = 0.25$ and b) $t/T = 0.75$.

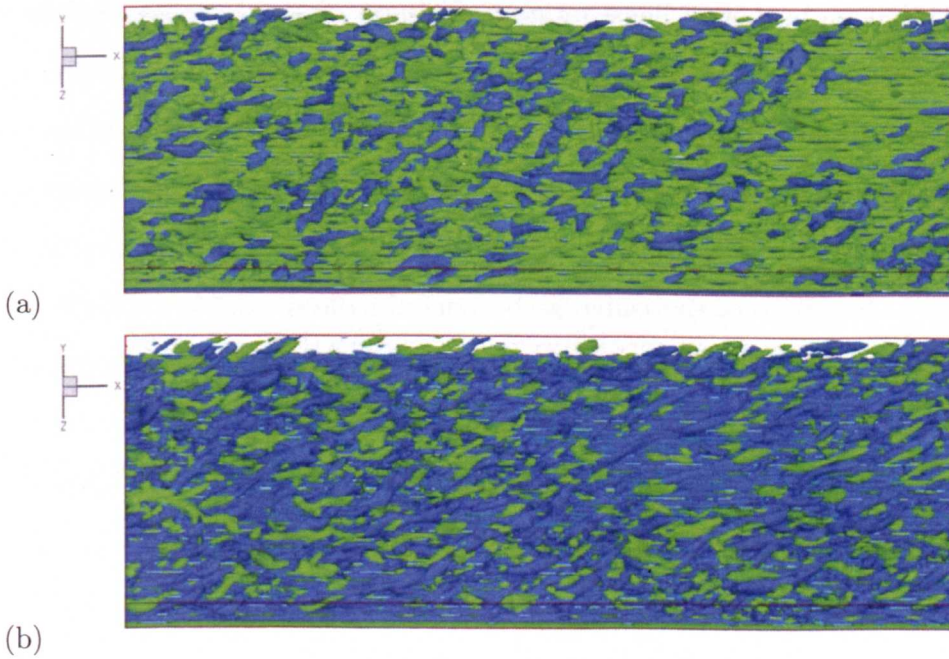


Figure 5.34: λ_2 visualisation for the $s_p^+ = 12.5$ configuration, $x = 0 - 9$, $\lambda_2^+ = -0.0125$: a) $t/T = 0.25$ and b) $t/T = 0.75$.

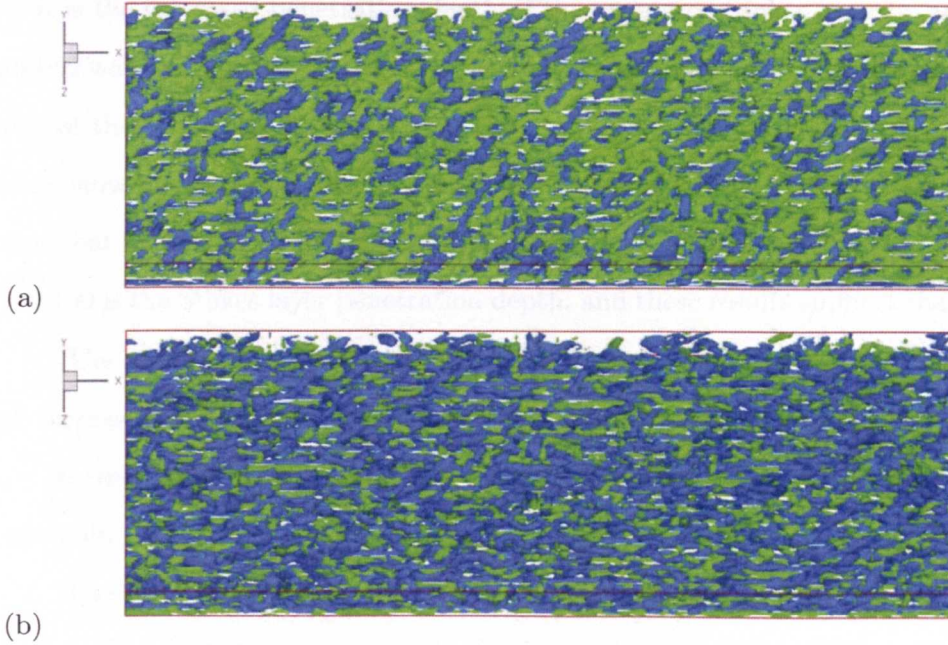


Figure 5.35: λ_2 visualisation for the $s_p^+ = 20$ configuration, $x = 0-9$, $\lambda_2^+ = -0.0125$: a) $t/T = 0.25$ and b) $t/T = 0.75$.

(2006b) had reported a large drag reduction for small periods of oscillations from their original experimental work and secondly large skin-friction increases had been observed in initial simulations as the forcing changed polarity. Thus it was decided to investigate whether, given increasing time, the more discrete configurations would mature between alternation of the forcing polarity into a drag reducing flow.

Uniform plasma resulted in larger drag reductions as compared to spanwise wall oscillations for the same maximum spanwise velocity, W_m^+ and period of oscillation, T^+ providing the latter was not too large, $T^+ < 300$. Compared to spanwise wall oscillation results the turbulence intensities and Reynolds shear stress are more attenuated and shifted further outwards from the wall. Visualisation of the flow shows a reduction in number and elongation of vortical structures. However, apart from an increased attenuation of turbulence over that of spanwise wall oscillations, the flow statistics appear to show the flow to be similar in nature and the drag reduction mechanism also appears to be similar. The reason for this improvement

in DR is the increased penetration depth of the generated Stokes layer by approximately 2 wall units for all the periods of oscillation tested. The increased penetration depth of the Stokes layer results from the displacement of the y -location of maximum spanwise velocity from the wall to $y^+ \approx 2$. Ricco and Quadrio (2008) have stated that for spanwise wall oscillations the critical measure for drag reduction if $T^+ < 150$ is the Stokes layer penetration depth, and these results support that view.

The uniform plasma was transformed through three discrete configurations with increasing spacing and therefore percentage of wall area without plasma. The $s_p^+ = 20$ configuration is the largest spacing tested and pertains to a 50% coverage of the wall.

The near-wall flow for the discrete configurations can be divided into two sections. The first stage starts as the forcing and consequently in time the near-wall spanwise velocity changes polarity. The velocity and vorticity perturbations that this produces lead to a large skin-friction increase. The second stage is the formation of a uniform PSL, the spanwise flow generated by the wall jets is seen to aggregate into a sheet of spanwise velocity. The PSL that this produces reduces the near-wall turbulence and skin-friction in the same manner as the Stokes layer for uniform plasma and spanwise wall oscillation.

Given sufficient time the PSL tends to increase its correlation to that of the Stokes layer generated by uniform plasma. The instantaneous correlation of the PSL to the uniform plasma Stokes layer appears to provide a good correlation ($r > -0.9$) to the skin-friction for that given moment in time. The time average skin-friction for the discrete configurations is therefore a trade off between the drag increasing first stage and the drag reducing second stage. The time for transition to the second stage and the magnitude of maximum skin-friction for the first stage, increases with increasing actuator spacing. In addition achievable skin-friction reduction starts to decrease as $T^+ > 125$ as the half period of oscillation becomes longer than the life time of the longest lived, and statistically important near-wall turbulent structures

becomes greater than the half period of oscillation.

There is a dramatic decline in the performance of DBD actuators for turbulent skin-friction control with increasing actuator spacing. The $s_p^+ = 10$ configuration produces large reductions of up to $DR = 37\%$. For the $s_p^+ = 12.5$ configuration with the introduction of a spanwise gap with no forcing of only 7.5 wall units the performance reduces markedly with a maximum $DR = 9\%$. This is more remarkable as the maximum spanwise velocity is $W_m^+ \approx 12$ which equates to 75% of the bulk mean velocity U_b . For the $s_p^+ = 20$ configuration the gap is widened to 20 wall units and consequently the drag reducing second stage never seems to occur and the generated flow is drag increasing for all the periods of oscillation tested.

One of the potential uses of the actuators would be for commercial aircraft. Calculating for a commercial aircraft flying at cruising altitude and speed (flight scales), a wall unit would be approximately $1.5\mu m$ in length. The scales are so small that the optimum frequency of oscillation for skin-friction control based on $T_{opt}^+ = 125$ would be approximately 50KHz. As previously mentioned the plasma profile was set at $b^+ = 17.5$ so that it is inline with a profile with of a few mm in low Reynolds numbers experiments. But at flight scales a value of $b^+ = 17.5$ would convert to a value of $b^* = 26.25\mu m$, much smaller than the few mm profile width of the plasma arc generated by current DBD actuators which would convert to a value of $b^+ > 2000$ at flight scales.

No investigation was made of various values of b^+ in this research. For even a small change in b^+ there could be a potential change in the results and there would certainly be changes in the results if the profile width was changed to hundreds or thousands of wall units in length.

5.5 Summary

The use of DBD actuators for turbulent skin-friction control by generation of a temporally sinusoidal, spanwise oscillating flow is investigated. Uniform plasma was found to produce larger skin-friction reductions than spanwise oscillation for a given period of oscillation, T^+ and maximum velocity, W_m^+ . The increased performance originates from the displacement of the Stokes layer by 2 wall units, with the maximum velocity at $y^+ \approx 2$ rather than at the wall. Progression was made from uniform plasma to an actuator spacing of $s_p^+ = 20$ through a series of increasing actuator spacing configurations. At these discrete configurations the change in polarity of the forcing and consequently the spanwise velocity, generates large velocity and vorticity perturbations resulting in an increase in the skin-friction. Over time the individual wall jets created by each DBD actuator aggregate to form a pseudo-Stokes layer and a drag reduction. The transitional period from the change in the spanwise velocity polarity until the PSL forms, increases with increased actuator spacing. The performance of the DBD actuators in obtaining a drag reduction declines rapidly with increasing actuator spacing and at a spacing of $s_p^+ = 20$ no drag reduction was achieved.

Chapter 6

Spatial oscillating plasma

6.1 Introduction

In Chapter 5, an investigation into the use of DBD plasma actuators to produce a spatially uniform temporally spanwise force close to wall to produce skin-friction reductions were carried out. One of the main conclusions from this work was that with discrete plasma configurations the ability of the DBD actuators to produce a skin-friction reduced dramatically with increased actuator spacing, in particular when the polarity of the spanwise velocity changed.

Viotti et al. (2009) and Berger et al. (2000) converted a spanwise wall oscillation and a spanwise Lorentz force respectively from a temporally oscillating wave into a longitudinally oscillating (referred to as spatial) wave. Using the natural convection velocity of near-wall turbulence, Viotti et al. (2009) converted temporal spanwise oscillations:

$$w(t) = W_m \sin \frac{2\pi}{T}t, \quad (6.1)$$

into a spatial counterpart, with a longitudinal sinusoidal distribution of spanwise velocity over a wavelength λ_x :

$$w(x) = W_m^+ \sin \left(\frac{2\pi}{\lambda_x}x \right), \quad (6.2)$$

where λ_x is the streamwise oscillation wavelength. There was an improvement in the energy budget for both the Lorentz forcing and the wall oscillation, and Viotti et al. (2009) reported skin-friction reductions that were 20-30% larger than those obtained with temporal forcing for a given amplitude. These findings suggested that a spatial arrangement of DBD actuators could lead to a reduction in the skin-friction values that had been previously recorded for the temporally oscillating arrangements.

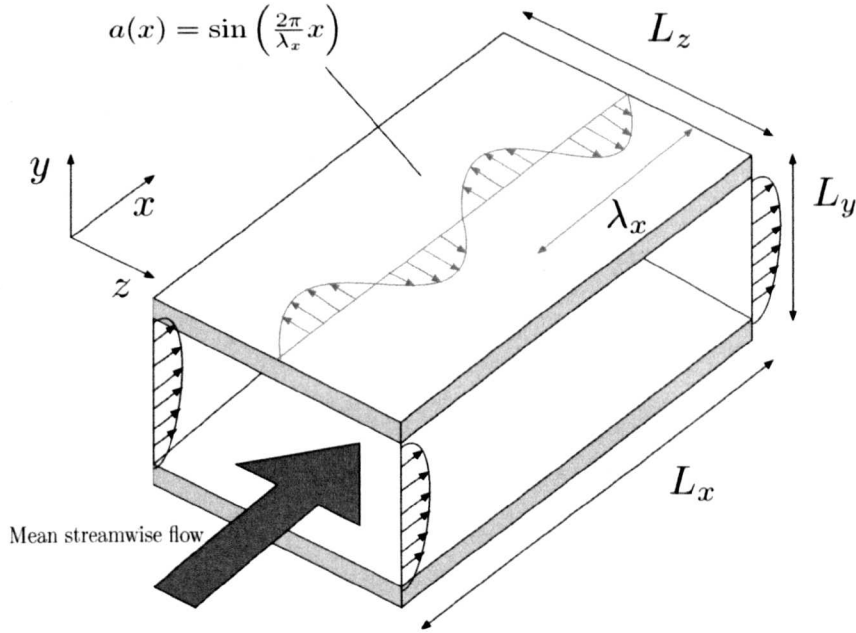


Figure 6.1: Schematic of the system for a turbulent channel flow with spatial wave of spanwise oscillation: L_x , L_y and L_z are the dimensions of the computational domain.

6.2 Method

The term $a(t)$ from Chapter 5 is converted into a spatial equivalent (see Figure 6.1):

$$a(x) = \sin\left(\frac{2\pi}{\lambda_x}x\right). \quad (6.3)$$

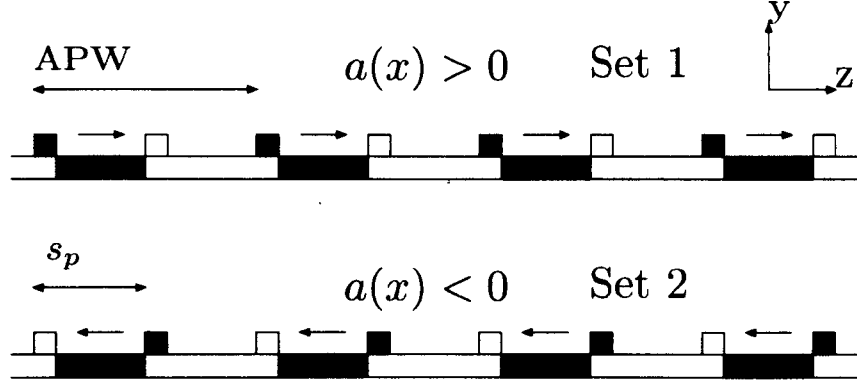


Figure 6.2: Schematic of the actuator sets and their activation in accordance with $a(x)$.

the force term for the Navier-Stokes equations is then:

$$F_i = |a(x)| D_c E_i, \quad (6.4)$$

Figure 6.2 shows a positive value of $a(x)$ resulting in activation of actuator Set 1 (the set that produces a positive spanwise velocity), while a negative value of $a(x)$ results in deactivation of Set 1 and activation of Set 2 (negative spanwise velocity). The actuators were prescribed for the entire width and length of both the top and bottom walls, so that the forcing is continuous in the streamwise direction. The four configurations in Chapter 5, $s_p^+ = 0, 10, 12.5$ and 20 were used, allowing a direct comparison with the results from Chapter 5.

The results were computed using the same domain and initial conditions as used for Chapter 5 i.e., $Re_\tau = 200$, $L_x = 18h$, $L_y = 2h$, $L_z = 4h$ ($\Delta x^+ = 10.0$, $\Delta y_{min}^+ = 0.1$, $\Delta y_{max}^+ = 9.0$ and $\Delta z^+ = 2.5$). The simulations were run for a total time of $t_{tot} = 550$, $t_{tot}^+ = 7000$, and the time step used was $\Delta t^+ \approx 0.1$.

6.3 Results

The periodic boundary conditions at the outlet and inlet of the domain limit the wavelengths to those that, when the domain length is divided by the wavelength, the quotient is an integer. The wavelengths used were $\lambda_x = 3.0, 4.5, 6.0, 9.0$ and 18.0 using u_{τ_0} , $\lambda_x^+ = 600, 900, 1200, 1800$ and 3600 . Using the convection velocity $C_w^+ = 10$ to compare the streamwise oscillating waves with that of the temporally oscillating ($\lambda_x^+ = C_w^+ T^+$) the values for λ_x^+ approximately equate to $T^+ = 60, 90, 120, 180$ and 360 respectively. Table 6.1 presents the skin-friction results for the five values of λ_x for the four actuator configurations with their respective maximum spanwise velocities W_m^+ . As the only method to ascertain what value of D_c was required to obtain a value of $W_m^+ = 12$ in each case was by the use 3D simulations, the values of D_c were estimated, and so there is a variation in W_m^+ .

A set of wall oscillation simulations were also undertaken for comparison and are presented in Table 6.2, the calculated skin-friction values are of similar magnitude to those reported by Viotti et al. (2009). Figure 6.3 represents the coefficient of friction ratio, for the simulations presented in Tables 6.1 and 6.2. The drag reductions obtained for the uniform plasma configuration, as found with the temporal oscillations in Chapter 5 were slightly higher to those found with spanwise wall oscillation for a comparable value of λ_x . The highest reduction was obtained at $\lambda_x^+ = 1200$, where a skin-friction reduction of $DR = 51\%$ was achieved as compared to a $DR = 47\%$ for spanwise wall oscillation. The optimum value of $\lambda_x^+ = 1200$ is close to the optimum value found by Viotti et al. (2009) of $\lambda_x^+ = 1250$, but this wavelength could not be tested in this work. This optimum value of $\lambda_x^+ = 1200$ equates to a temporal equivalent of $T^+ = 120$.

The $s_p^+ = 10$ configuration as it did with temporal oscillation provides a very good performance. The resulting drag reduction was comparable to that achieved

case	W_m^+	λ_x	D_c	t_i	s_p^+	$C_f \times 10^{-3}$	$DR\%$
0	—	—	—	—	7.87	—	—
101	12.1	3	8	3000	0	4.14	47
102	12.8	4.5	8	3000	0	3.95	50
103	13	6	8	3000	0	3.82	51
104	13.6	9	8	4000	0	3.97	50
105	13.7	18	8	3000	0	7.04	11
106	11.9	3	18.9	2000	10	4.36	44
107	12.2	4.5	18.9	2500	10	4.1	48
108	12.6	6	18.9	2500	10	4.04	48
109	12.8	9	18.9	2500	10	4.22	46
110	13	18	18.9	2000	10	6.99	11
111	12.1	3	22.4	2000	12.5	4.69	40
112	12.3	4.5	22.4	2000	12.5	4.4	44
113	12.5	6	22.4	3000	12.5	4.22	46
114	12.5	9	22.4	3000	12.5	4.77	39
115	12.5	18	22.4	2000	12.5	7.78	1
116	10.1	3	28.6	2000	20	12.13	-54
117	11.1	4.5	28.6	2000	20	10.64	-35
118	11.6	6	28.6	2000	20	10.13	-28
119	11.8	9	28.6	2000	20	9.87	-25
120	11.7	18	28.6	2000	20	10.01	-27

Table 6.1: Data for different wavelengths of oscillation and actuator configurations: wavelength λ_x^+ , actuator spacing s_p^+ , (case 0 refers to the no-control case), t_i indicates the start of the time-averaging procedure for the calculation of the friction coefficient C_f , $DR\%$ indicates percentage drag reduction (negative number indicates drag increase).

by uniform plasma and spanwise wall oscillation and therefore was an improvement on its temporally oscillating counterpart. The most notable difference from the results obtained with temporal oscillations was for the two larger actuation spacings. There is a substantial improvement in the skin-friction reduction for the $s_p^+ = 12.5$ configuration with drag reduction values close to those obtained for $s_p^+ = 10$ and uniform plasma. The highest skin-friction reduction was again seen at $\lambda_x^+ = 1200$ with a skin-friction reduction of $DR = 46\%$ was obtained. This is a substantial improvement over the 9% obtained for temporal oscillation indicating a significant change in the flow characteristics. The $s_p^+ = 20$ configuration produced an increase

case	λ_x	t_i	$C_f \times 10^{-3}$	DR%
s101	3	3000	4.48	43
s102	4.5	3000	4.23	46
s103	6	3000	4.12	47
s104	9	3000	4.15	47
s105	18	3000	6.82	13

Table 6.2: Data for spanwise wall oscillation for different wavelengths of oscillation, $W_m^+ = 12$.

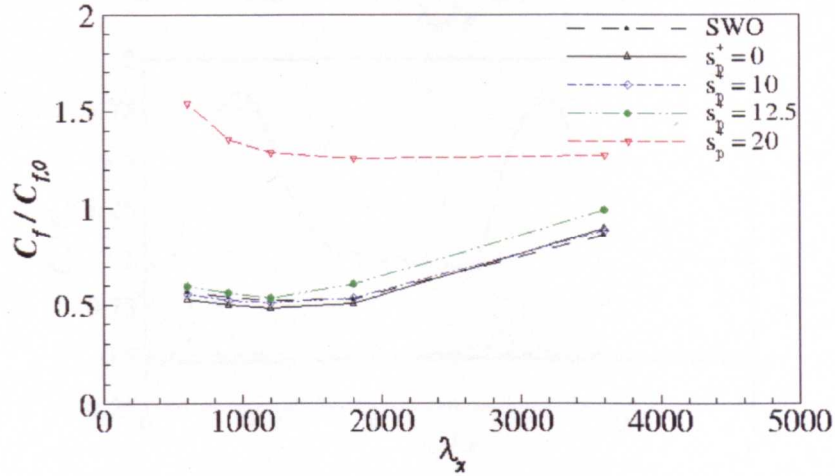


Figure 6.3: Time-averaged coefficient of friction for different wavelengths of oscillation λ_x^+ for different plasma actuator configurations and spanwise wall oscillation.

in skin-friction for every case tested but the increases were smaller than those obtained from their temporal counterparts.

Figure 6.4 is the time-averaged skin-friction coefficient ratio for three different wavelengths of oscillation over one wavelength of oscillation. To compare between temporal and spatial oscillating plasma the phase-averaged skin-friction coefficient ratio for $T^+ = 125$ (equivalent spatial wavelength, $\lambda_x^+ = 1250$), is plotted in Figure 6.5 and can be compared with the $\lambda_x^+ = 1200$ results in Figure 6.4(b). As found with temporal oscillations spikes in the skin-friction values occur as the polarity of the force and consequently the spanwise velocity changes for each discrete configuration.

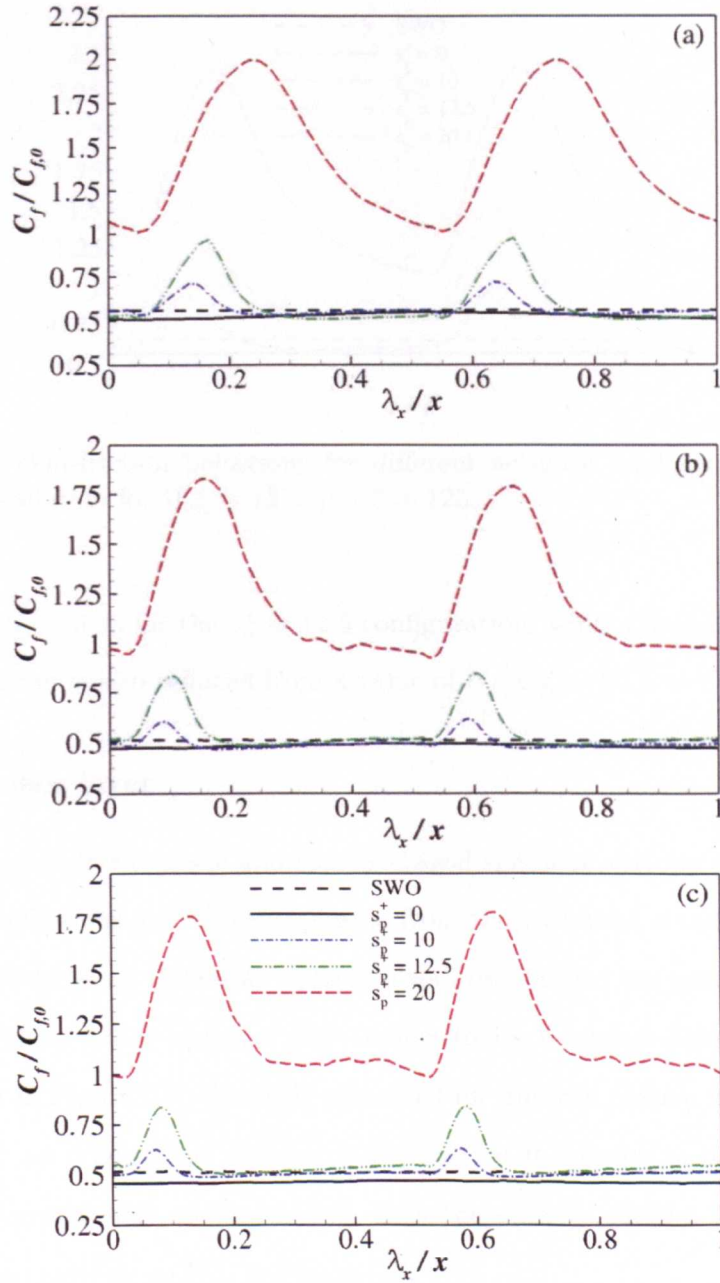


Figure 6.4: skin-friction behaviour for different actuator configurations over one wavelength of oscillation: a) $\lambda_x^+ = 600$, b) $\lambda_x^+ = 1200$ and c) $\lambda_x^+ = 1800$.

Comparison between Figures 6.4(b) and 6.5 shows that the height and width of the spikes for each configuration are noticeably reduced over those for temporal oscillation. For example, the maximum skin-friction ratio is reduced from $C_f/C_{f0} =$

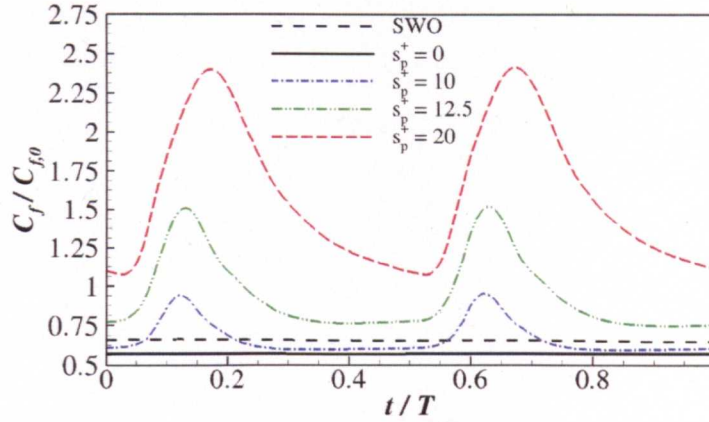


Figure 6.5: skin-friction behaviour for different actuator configurations over one period of oscillation for $W_m^+ = 12$ and $T^+ = 125$.

1.5 to $C_f/C_{f0} = 0.85$ for the $s_p^+ = 12.5$ configuration, while the minimum value for the skin-friction is also reduced from a value of $C_f/C_{f0} = 0.75$ to $C_f/C_{f0} = 0.5$.

6.3.1 Stokes layer

Figure 6.6 presents the space and time-averaged spanwise velocity profile for spanwise wall oscillations and uniform plasma from the turbulent simulations. As suggested by Viotti et al. (2009) for spanwise wall oscillations the spatial Stokes layer (SSL) in Figure 6.6(a) appears very similar to its temporal Stokes layer (TSL) counterpart in Figure 5.7. The SSL generated for uniform plasma has, like its TSL counterpart, an origin at $y^+ \approx 2$ but differs in that it appears to be more in phase with the spanwise wall oscillation SSL than the uniform plasma TSL is with the spanwise wall oscillation TSL in Figure 5.7.

Figure 6.7 presents the maximum spanwise velocity, taken from the time-averaged turbulent simulations for the spanwise wall oscillation, and three wavelengths of oscillation for uniform plasma over one cycle. In the spanwise wall oscillation the polarity of the spanwise velocity changes at $x/\lambda_x = 0.5$ and as with the TSL there is an interval until the spanwise velocity changes for the uniform plasma

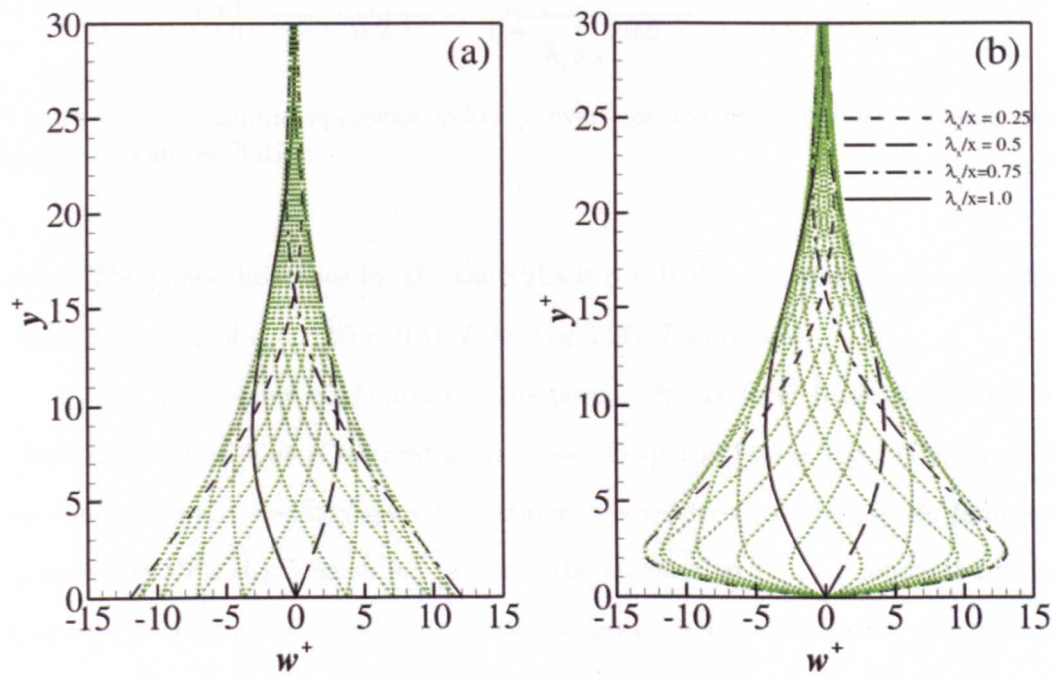


Figure 6.6: Spanwise velocity profile at various longitudinal locations for one period of oscillation, $\lambda_x^+ = 1200$: a) spanwise wall oscillation, b) uniform plasma.

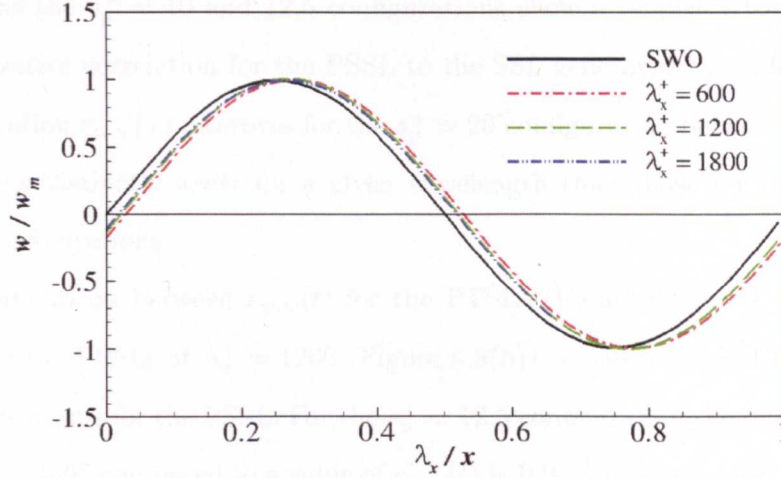


Figure 6.7: Maximum spanwise velocity over one cycle for uniform plasma and spanwise wall oscillation.

cases. The phase difference for the the SSLs is $\phi < 0.05 x/\lambda_x$ and is reduced to the phase difference of $\phi = 0.05 \sim 0.1t/T$ for the TSL (Figure 5.8).

For the discrete configurations the pseudo-Stokes layer from the spatial oscillating configurations is referred to as a pseudo spatial Stokes layer (PSSL) while for the temporally oscillating configurations it is referred to as a pseudo temporal Stokes layer (PTSL). Figure 6.8 presents the correlation $r_{w,w}(x)$ along the wavelength of oscillation of the time-averaged spanwise velocity fields for the discrete plasma configurations to that produced by uniform plasma for $\lambda_x^+ = 600, 1200$ and 1800. As in Chapter 5, for $r_{w,w}(t)$, the correlation was taken from $y^+ > 2$ to remove the differences in near-wall spanwise velocity fluctuations caused by the different actuator configurations and to allow a comparison of the PSSLs with the uniform plasma SSLs from the y -location of their origin.

In Figure 5.15 troughs are present in the correlation starting at $x/\lambda_x \approx 0 - 0.05$ when the polarity of the velocity changes. The troughs increase in depth and width with increasing s_p^+ and decreasing λ_x^+ , as seen with temporal oscillations for increasing s_p^+ and decreasing T^+ . During a half wavelength of oscillation after

the troughs the $s_p^+ = 10$ and 12.5 configurations show a tendency towards a near perfect positive correlation for the PSSL to the SSL generated by uniform plasma. The correlation $r_{w,w}(x)$ improves for the $s_p^+ = 20$ configuration between the troughs but remains distinctly lower for a given wavelength than those for the other two discrete configurations.

Comparison between $r_{w,w}(t)$ for the PTSs (Figure 6.9) at $T^+ = 125$ and $r_{w,w}(x)$ for the PSSs at $\lambda_x^+ = 1200$ (Figure 6.8(b)), shows a marked improvement in the correlations for the PSS. For the $s_p^+ = 12.5$ configuration the minimum value of $r_{w,w}(x) \approx 0.97$ compared to a value of $r_{w,w}(t) \approx 0.92$ for its temporally oscillating counterpart. An even bigger improvement in the correlation is seen for the $s_p^+ = 20$ configuration with a minimum value of $r_{w,w}(x) \approx 0.8$, a large improvement over $r_{w,w}(t) \approx 0.7$.

The spatial oscillating plasma arrangements appear very similar to the temporally oscillating cases in Chapter 5. The spanwise velocity fields, and therefore the PSSs, increase in similarity to those produced by uniform plasma with increasing λ_x^+ and decreasing s_p^+ . However, as seen with the PTSs, the PSSs differ markedly from the uniform plasma Stokes layers when the polarity of the spanwise velocity changes. The correlation $r_{w,w}(x)$ is markedly higher than the values obtained for $r_{w,w}(t)$ for the $s_p^+ = 12.5$ and $s_p^+ = 20$ configurations, indicating that with a spatial oscillating force the spanwise velocity profiles are more alike to those from uniform plasma than those as a result of a temporally oscillating wave. This improvement in the correlation results in the lower skin-friction profiles in Figure 6.4. Notwithstanding that spatial spanwise oscillations results in a larger $DR\%$ than does temporal oscillations, the three fold improvement in maximum $DR\%$ obtained with the $s_p^+ = 12.5$ configuration is mainly because of the improvement in $r_{w,w}(x)$.

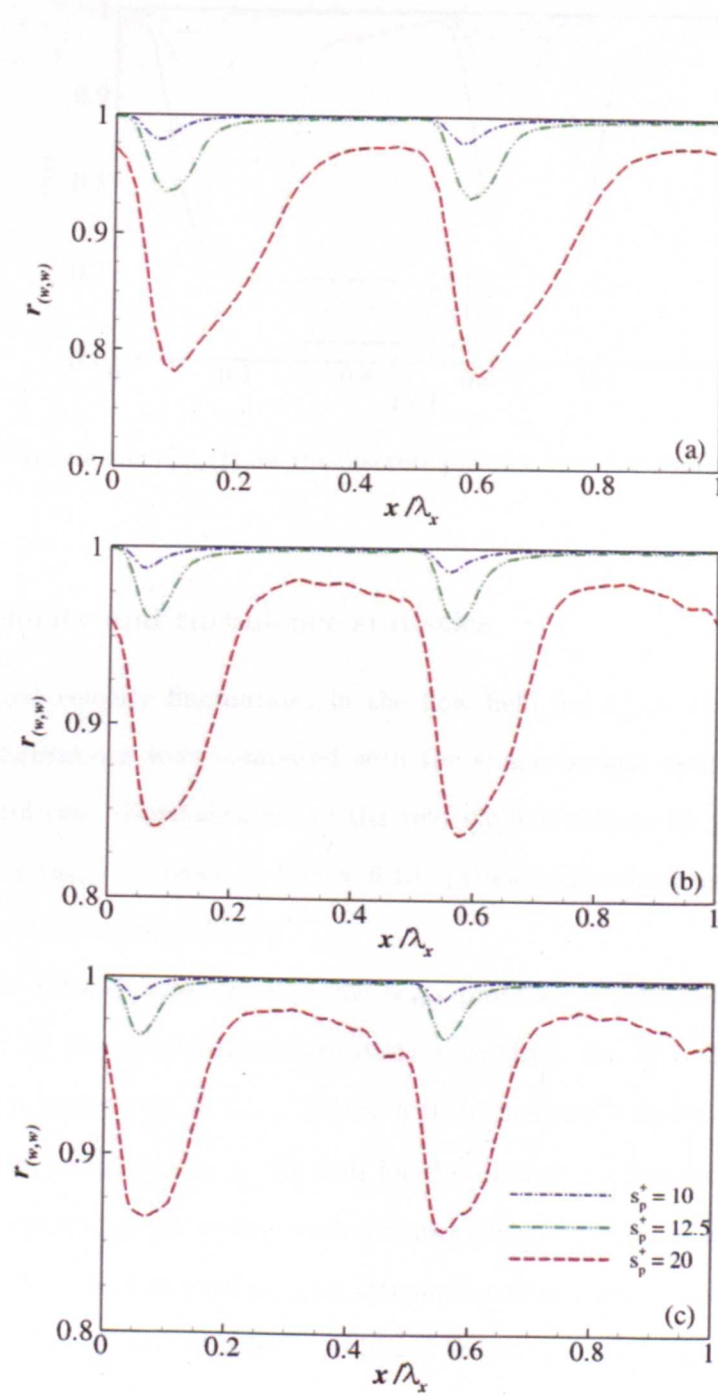


Figure 6.8: Correlation $r_{w,w}(x)$ for the discrete plasma actuator configurations: a) $\lambda_x^+ = 600$, b) $\lambda_x^+ = 1200$ and c) $\lambda_x^+ = 1800$.

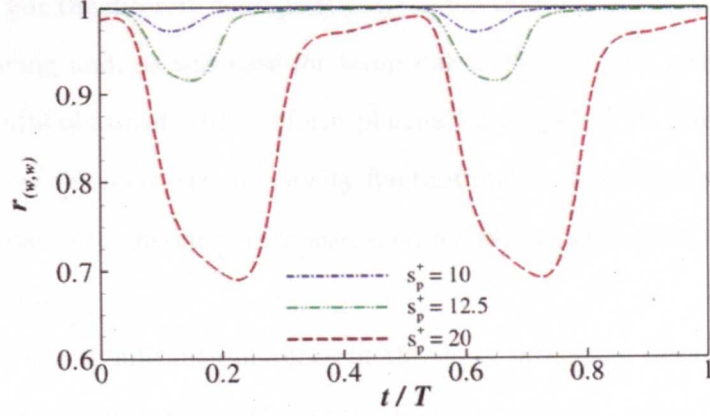


Figure 6.9: Correlation $r_{w,w}(t)$ for the discrete plasma actuator configurations, $T^+ = 125$.

6.3.2 Velocity and turbulence statistics

Time-averaged velocity fluctuations in the flow field for $\lambda_x^+ = 1200$ for the four plasma configurations were compared with the spanwise wall oscillation case and the no-control case. Normalisation of the velocity fluctuations by the actual wall-shear velocity (u_{τ_m}) is shown in Figure 6.10. (Velocity fluctuations normalised by u_{τ_0} are presented in Appendix C)

Figure 6.10(a) indicates that the u_{rms} profiles are attenuated and shifted outwards for all the controlled configurations apart from the $s_p^+ = 20$ configuration where there is an increase in u_{rms} . Figure 6.10(b) presents a similar trend for v_{rms} but with local maxima close to the wall for the discrete configurations because of the entrainment/expulsion around each actuator shown previously in Section 5.3.3. The w_{rms} profiles show as with u_{rms} an attenuation from the no-control case except for the $s_p^+ = 20$ configuration which are higher in the near wall region than of the no-control case.

The velocity fluctuations appear to be reduced and shifted from the wall as seen with temporal oscillations. The fluctuations are slightly more reduced for uniform plasma to that of spanwise wall oscillation as seen before with temporal

oscillations. For the discrete configurations the fluctuations increase with increasing actuator spacing and, as was case for temporal oscillation, the increases are small from the results obtained with uniform plasma for the $s_p^+ = 10$ configuration. The $s_p^+ = 12.5$ show the increases in velocity fluctuations from the uniform plasma case is small compared to the large increases seen for temporal oscillations (see Figures 5.17, 5.18 and 5.19).

There is a significant difference in the w_{rms} profiles of discrete plasma configurations for spatial waves to those generated by temporal waves. With temporal oscillations (see Figure 5.19) there are large near wall ($y^+ < 5$) local maxima which are not apparent for the spatial cases in particular the $s_p^+ = 10$ and $s_p^+ = 12.5$ cases show an attenuation from the no-control case in this region. This, with the reduced values in $\tau_{w,w}$ indicates that the spatial wave configurations reduce the inevitable fluctuations in spanwise velocity from discrete forcing over those generated by temporal oscillations.

The mean-velocity profiles normalised by the actual wall-shear velocities, u_{τ_m} , for the different configurations for $\lambda_x^+ = 1200$ are shown in Figure 6.11. The $s_p^+ = 10$, $s_p^+ = 12.5$ configurations and spanwise wall oscillations elevate the point where the log-law intercepts $y^+ = u^+$ from $y^+ \approx 10$ to $y^+ \approx 17$ while in the uniform case it is elevated further to $y^+ \approx 20$. This elevation indicates an increase in the viscous sublayer. The intercept point for the $s_p^+ = 10$ and spanwise wall oscillation has shifted slightly further from the wall to the y -location found for temporal oscillations of $y^+ \approx 15$ (see Figure 5.26). While the interception point has shifted from $y^+ \approx 17$ to $y^+ \approx 20$ for uniform plasma, the largest improvement is again for the $s_p^+ = 12.5$ configuration where the intercept has moved from $y^+ \approx 10$ to $y^+ \approx 15$.

The Reynolds shear stress, $-\overline{u'v'}$, is shown for $\lambda_x^+ = 1200$ in Figure 6.12. All but the $s_p^+ = 20$ configuration show a reduction throughout the domain apart from near the wall where local maxima are produced for the discrete configurations

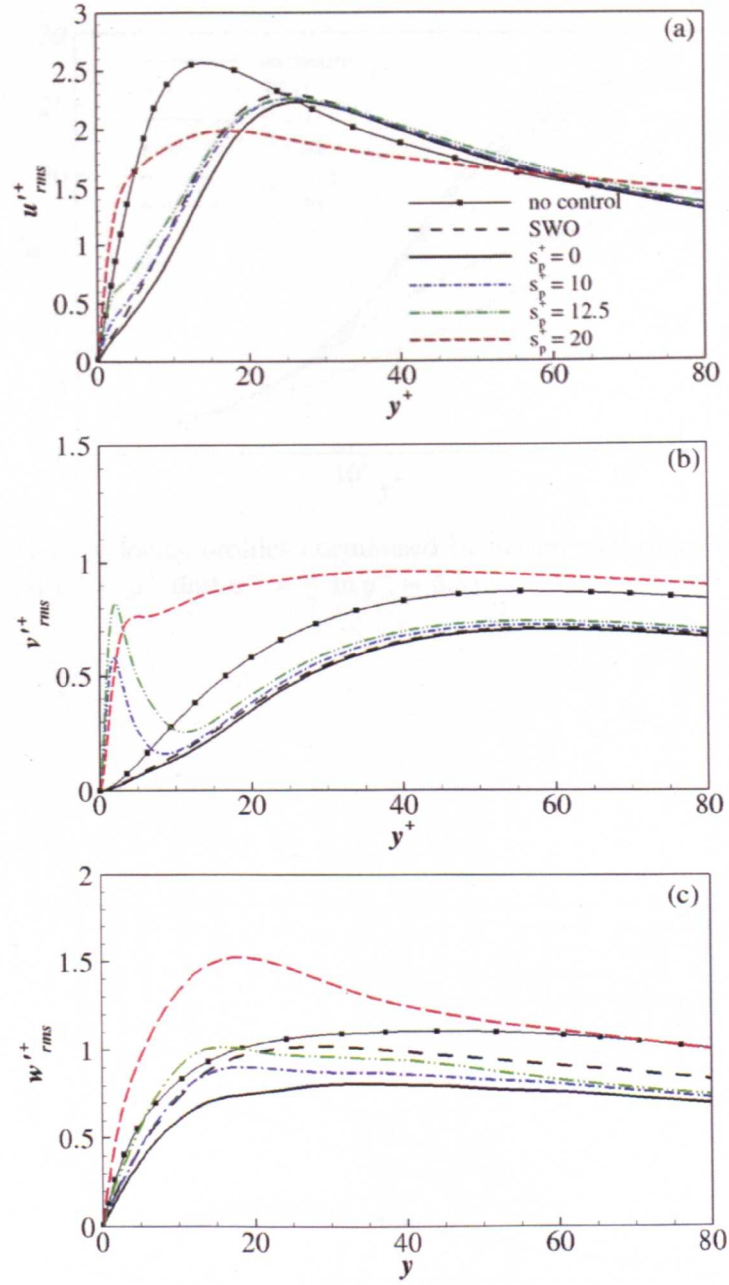


Figure 6.10: Root-mean-square velocity fluctuations, normalised by the actual wall-shear velocity, u_{τ_m} : a) u_{rms} , b) v_{rms} and c) w_{rms} .

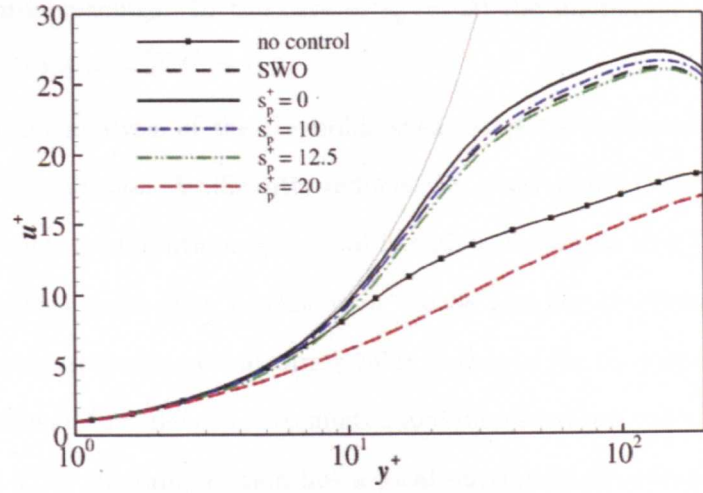


Figure 6.11: Mean velocity profiles normalised by actual wall-shear velocities, u_{τ_m} . (law of the wall $u^+ = y^+$ and $u^+ = \frac{1}{\kappa} \ln y^+ + 5.5$)

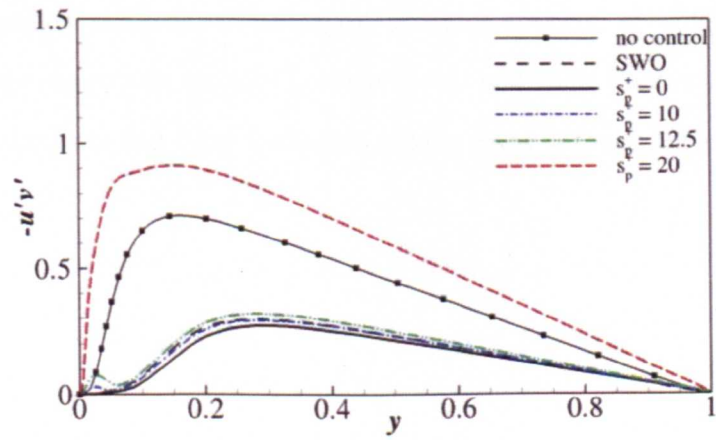
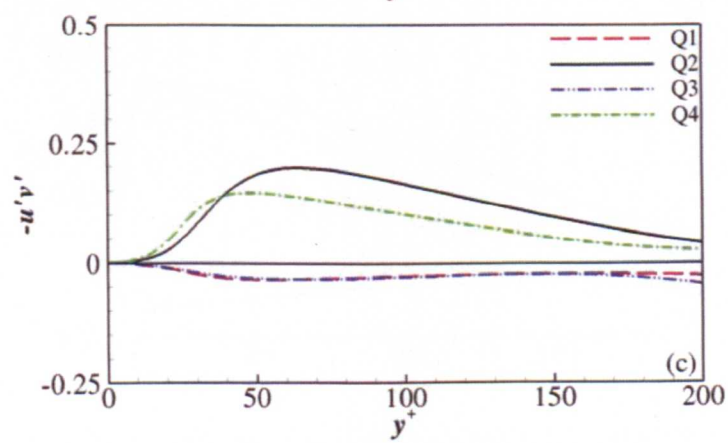
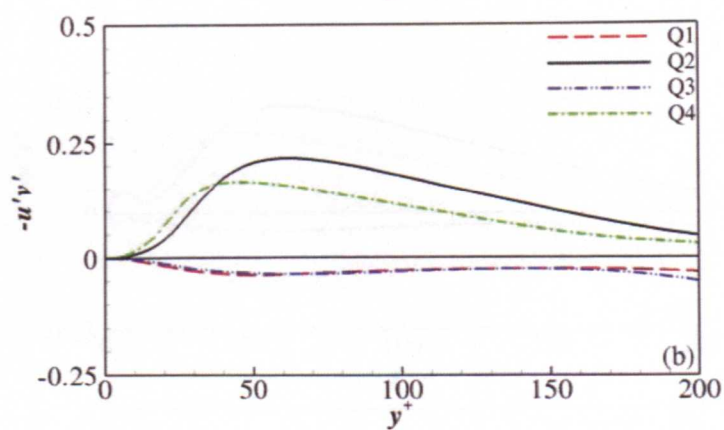
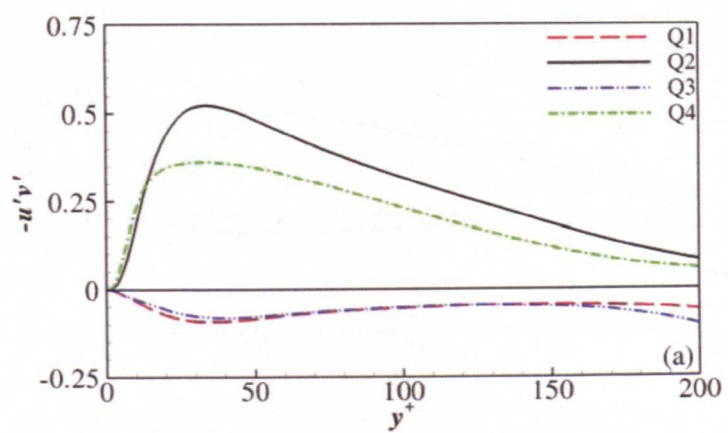


Figure 6.12: Reynolds shear stress, normalised by u_{τ_0} for $\lambda_x^+ = 1200$.

because of the entrainment/expulsion see Section 5.3.3). In comparison to temporal oscillations (see Figure 5.27) the Reynolds stress is reduced in especially for the two largest actuator spacings. In the case of $s_p^+ = 20$ the maximum value is reduced from $-\overline{u'v'}^+ \approx 1.4$ to $-\overline{u'v'}^+ \approx 0.9$.

Quadrant analysis of the Reynolds shear stress is presented in Figure 6.13. Spanwise wall oscillation significantly reduces the ejection and sweep events and the point where their contributions are equal is shifted outwards to $y^+ \approx 36$. Uniform plasma shifts this point even further to $y^+ \approx 38$ and the fractional contributions from the sweep and ejection events are similar to that of the no-control case implying that the outer-wall turbulence is attenuated and displaced but the structure remains similar. The $s_p^+ = 10$ configuration has a local maximum close to the wall however the sweep and ejection events are then suppressed and shifted outwards with the y -location of equilibrium at $y^+ \approx 35$ and the fractional contributions of the events remain unchanged. The $s_p^+ = 12.5$ configuration shifts the point of equilibrium to $y^+ \approx 35$ but the sweep and ejection are large close to the wall. There is only slight attenuation from the no-control case away from the wall with the percentage contribution of ejection and sweep beginning to show some similarity implying a subtle change to the flow structure. The largest actuator spacing, $s_p^+ = 20$ configuration, produces large sweep and ejection contributions, and their fractional contributions are very similar implying large turbulent mixing right through the domain.



(Caption overleaf.)

6.4 Discussion

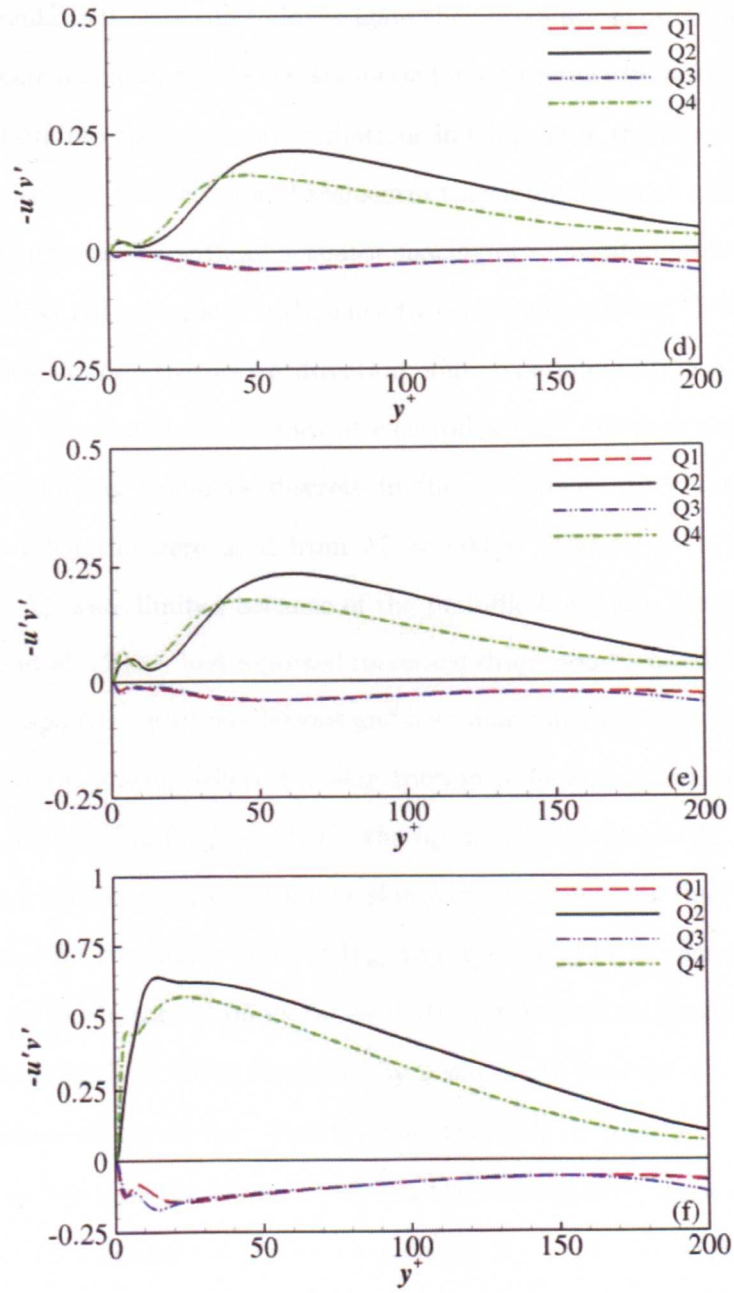


Figure 6.13: Reynolds shear stress from each quadrant normalised by the wall-shear velocity, u_{τ_0} for $\lambda_x^+ = 1200$. a) No-control, b) Spanwise wall oscillation, c) $s_p^+ = 0$, d) $s_p^+ = 10$, e) $s_p^+ = 12.5$, f) $s_p^+ = 20$

6.4 Discussion

A series of simulations were run to investigate the possibility of orientating DBD actuators to create a spatial oscillating spanwise force to reduce skin-friction. As with the investigation into the temporal oscillations in Chapter 5, the intention was to go from a spanwise wall oscillation and transform through a series of configurations to a final DBD configuration with an actuator spacing of $s_p^+ = 20$ in order to assess the effect on the drag reduction and turbulence by each configuration. The forcing used was continuous in the streamwise direction, but experimentally the spatial wave would have to be created by a series of electrodes with different signal strengths and hence the forcing would be discrete in the streamwise direction. A series of oscillation wavelengths were used from $\lambda_x^+ = 600 \sim 3600$ for each configuration. The values of λ_x^+ were limited because of the periodic boundary conditions.

Viotti et al. (2009) had reported increased drag reductions with longitudinal over temporal spanwise wall oscillations and a similar conclusion can be drawn from the use of uniform plasma where the skin-friction reduction increased from DR = 42% ($W_m^+ \approx 12$) to 52% ($W_m^+ \approx 13$) for the optimum wavelength $\lambda_x^+ = 1200$. The use of uniform plasma resulted in larger skin-friction reductions than did spanwise wall oscillations for the same values of W_m^+ and λ_x^+ as had been seen with temporal oscillations. As in the case of temporal oscillations this resulted from an increase in the penetration depth of the Stokes layer by 2 wall units because of a displacement of the y -location of maximum velocity from the wall to $y^+ = 2$. The increase in penetration depth of the Stokes layer and the consequent improvement in skin-friction reduction supports the previous conclusion in Chapter 5 and that of Quadrio (2011), of the Stokes layer penetration depth being the primary determinant of the skin-friction reduction providing the period or wavelength of oscillation is smaller than a value of $T_G^+ = 120$.

The three discrete configurations used in Chapter 5 were used. As in the

case of temporal oscillations, the near-wall flow for the discrete configurations can be divided into two sections. The first stage starts as the forcing, and consequently in time the near-wall spanwise velocity, changes polarity. The velocity and vorticity perturbations that this produces lead to an increase in the skin-friction. The second stage is the formation of a uniform PSSL, reducing the near-wall turbulence and skin-friction.

Comparison of the decrease in skin-friction from temporal to longitudinal oscillating waves was most dramatic for the larger actuator spacings. The maximum drag reduction for the $s_p^+ = 12.5$ configuration increasing from $DR = 9\%$ to $DR = 46\%$ for a spanwise velocity of $W_m^+ = 12$, with a dramatic increase in the suppression of velocity fluctuations in particular w_{rms} near the wall. The improvement in the correlation $r_{w,w}(x)$ over its temporal counterpart $r_{w,w}(t)$, implies that the PSSLs are generally more alike to the SSLs than are the PTSs to TSLs for a given set of oscillation parameters, particularly when the forcing, and consequently the spanwise velocity, changes polarity.

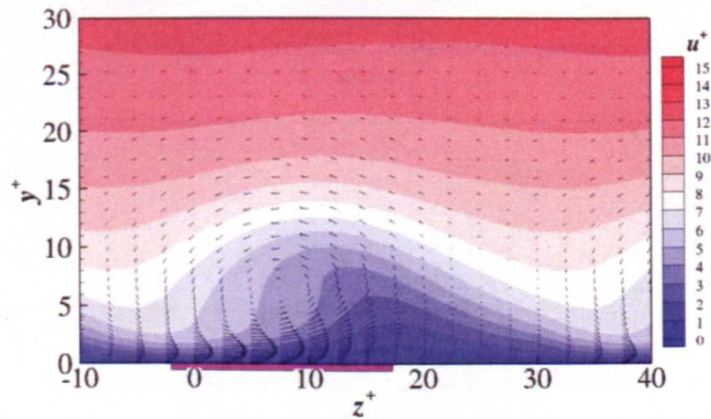


Figure 6.14: Contour plot of streamwise velocity at $x/\lambda_x = 0.1$ ($\lambda_x^+ = 1200$). Vectors generated from v and w .

In the case of temporal oscillations the fluid near the wall is subject to a forcing of a fixed period or wavelength, while in the case of spatial oscillations this

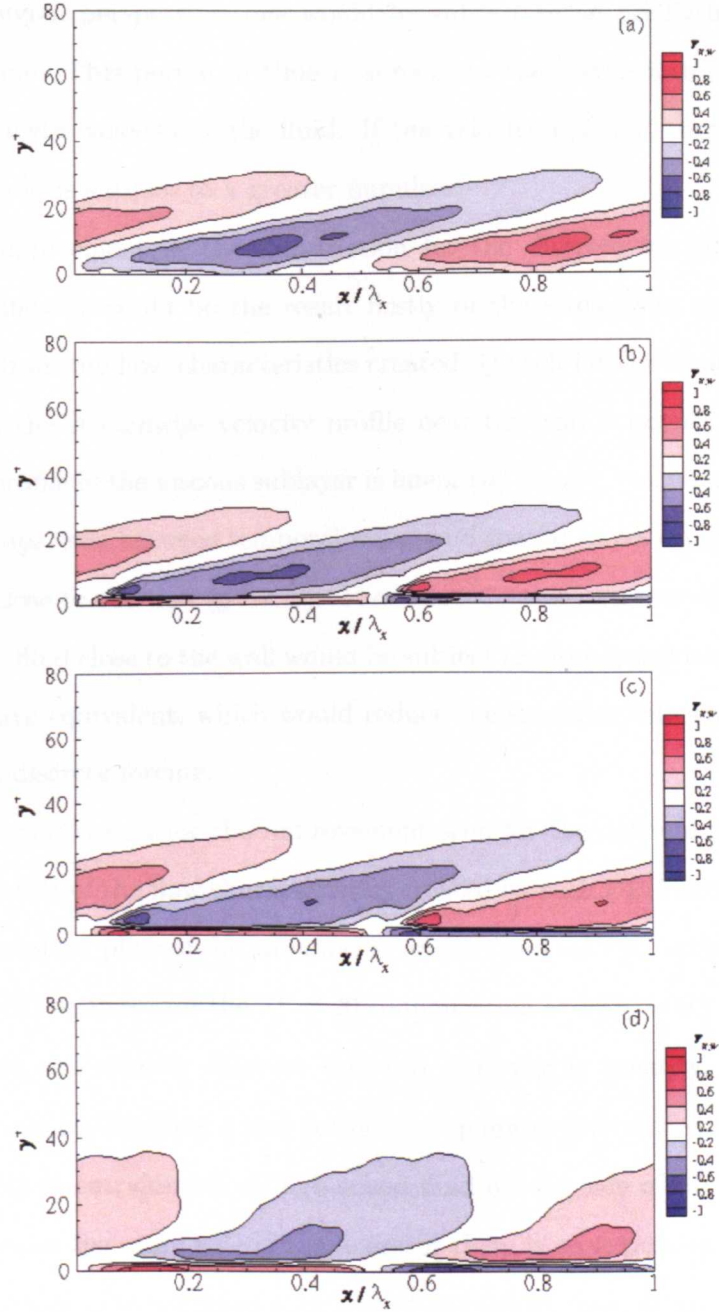


Figure 6.15: Contour plots of $r_{u,w}$ ($\lambda_x^+ = 1200$): a) $s_p^+ = 0$, b) $s_p^+ = 10$, c) $s_p^+ = 12.5$ and d) $s_p^+ = 20$.

period is not fixed. Spatial oscillation waves work on the principle that the velocity of the fluid transposes the spanwise force, so if one was to travel with the fluid, or

from a Lagrangian perspective, one would be subject to an oscillating force over a period of time. This period of time is subject to the wavelength of the forcing and the streamwise velocity of the fluid. If the velocity is lower, then over a fixed distance the fluid is subject to a greater impulse.

The improvement in the skin-friction for the discrete configurations over temporal oscillations could be the result firstly of the streamwise velocity profile and secondly from the flow characteristics created by each DBD actuator. The first reason is that the streamwise velocity profile near the wall is not $u^+ = C_w^+ = 10$. The velocity profile in the viscous sublayer is linear ($u^+ = y^+$), meaning that $u < C_w$ and that a comparison between temporal waves and spatial waves using $\lambda_x^+ = C_w T^+$ is subjective close to the wall ($y^+ < 5$). The reduced value in u near the wall would imply that the fluid close to the wall would be subject to more spanwise impulse than a temporal wave equivalent, which would reduce the spanwise velocity fluctuations caused by the discrete forcing.

The second reason for the improvement seen for the discrete configurations could be the result of the flow characteristics created by each DBD actuator. Figure 6.14 presents contour plots of the streamwise velocity and velocity vectors of v and w around one DBD actuator for the $s_p^+ = 20$ configuration at $x/\lambda_x = 0.1$ ($\lambda_x^+ = 1200$), a region where the velocity close to the wall is changing polarity. It has been previously shown in Chapters 4 and 5 that the spanwise jet created by each DBD actuator results in entrainment of high-speed fluid on one side of the actuator and as the jet slows on the other side of the actuator there is an expulsion of slow-speed fluid from the wall. From Figure 6.14 that it is evident there is an association of expulsion ($-u'$ and $+v$) with low spanwise velocity and of entrainment ($+u'$ and $-v$) with high spanwise velocity near the wall.

The cross-correlation coefficient $r_{u,w}$ of the streamwise velocity with the span-

wise velocity was calculated for a zero separation ($\Delta z = \Delta t = 0$):

$$r_{u,w}(x, y) = \overline{< u(x, y, z, t), w(x, y, z, t) >} = \frac{\overline{u'(x, y, z, t)w'(x, y, z, t)}}{\sqrt{\overline{u'^2(x, y, z, t)}}\sqrt{\overline{w'^2(x, y, z, t)}}}, \quad (6.5)$$

and is presented in Figure 6.15, where $\overline{(\cdot)}$ represents an average over z and time. Figure 6.15 shows that there is a high correlation or anti-correlation depending on the direction of the forcing near the wall that is not evident with uniform forcing (see Figure 6.15(a)). This suggests that fluid with low absolute spanwise velocity takes longer to travel the same distance as does fluid with high absolute spanwise velocity and is therefore subject to more impulse. Essentially the expulsion/ejection caused by each actuator could potentially help in distributing the spanwise velocity resulting in the improvements in the skin-friction for the discrete configurations over those produced by temporal oscillations, particularly when the forcing changes polarity.

Unfortunately although there is an improvement in the skin-friction reduction for discrete configurations, the skin-friction still increases as the actuator spacing increases. Although the $s_p^+ = 12.5$ configuration is with a spatial wave able to produce drag reductions of $DR > 40\%$, (levels that are only slightly less than that the $s_p^+ = 10$ and uniform plasma configurations), there is a decline to drag increasing flow for the $s_p^+ = 20$ configuration for all the wavelengths tested.

As with the temporal oscillations the plasma profile width was fixed at $b^+ = 17.5$ and the results could be significantly different if the value of b^+ was changed.

6.5 Chapter Summary

The use of DBD actuators for turbulent skin-friction control by the generation of a spatial sinusoidal spanwise oscillating flow is investigated. Spatial oscillations resulted in reduced skin-friction values to those produced from temporal oscilla-

tions for all the configurations tested. Uniform plasma was found to produce larger skin-friction reductions than spanwise wall oscillation for a given wavelength of oscillation, λ_x^+ , the increased performance again originating from the displacement of the Stokes layer by 2 wall units, with the maximum spanwise velocity at $y^+ \approx 2$ rather than at the wall. There was an increase for the discrete configurations in skin-friction as the polarity of the forcing and consequently the spanwise velocity changes, but this was significantly less to the increases produced by temporal oscillations. The maximum drag reduction for the $s_p^+ = 12.5$ configuration increasing from $DR = 9\%$ for temporal oscillation to $DR = 46\%$ for longitudinal oscillations. However the performance of DBD actuators in obtaining a drag reduction still declines with increasing actuator spacing as occurs with temporal oscillations and at a spacing of $s_p^+ = 20$ no drag reduction was achieved.

Chapter 7

Conclusions

7.1 Conclusions

DBD actuators provide a method of producing a spanwise oscillating near-wall force and potential skin-friction reductions, and offer the potential to reduce skin-friction. Experimental investigations of DBD actuators for turbulent skin-friction control have been hampered in recording near-wall measurements of velocity because of the difficulty in placing a sensor in the area of the plasma actuators. A numerical investigation was used as a means of gaining further insight into DBD actuators and their use for turbulent skin-friction control.

A modified DBD model developed from the Shyy et al. (2002) model was integrated into a DNS. The model and integration was devised so that a strength, D_c , was set to provide a desired maximum spanwise velocity, and not to calculate a velocity from a series of constituent variables such as the applied voltage and electrode width that would decide the output of the actuator.

A series of two-dimensional simulations, in initially quiescent flow, were undertaken and the results were found to compare well with experimental findings. A wall jet was produced by the actuator with a velocity profile similar to that of a laminar wall jet as found by Jukes et al. (2006a). The wall jet profile broadened and

slowed as the distance downstream of the actuator increased. A starting vortex was also observed that travels at 32° to the horizontal, reducing in strength over time. This is close to the 31° to the horizontal for the vortex observed by Whalley (2011). The growth rate of the starting vortex, was determined as being in the order of $t^{0.67}$ to a time and length scale based on the maximum wall jet velocity, w_j . This value is close to the $t^{0.71}$ and fits well with the experimental results by Whalley (2011) in experimental investigations. The close affinity of the results obtained from this DBD model with the experimental results confirms that the DBD model is satisfactory.

Plasma profile parameters were determined for the turbulent skin friction control simulations, the width of the profile was set at $b^+ = 17.5$ and the angle at $\theta_p = 10^\circ$. The use of DBD actuators for both the generation of a temporally and a spatial (longitudinal), spanwise oscillating flow was investigated. Three actuator spacings $s_p^+ = 10, 12.5$ and 20 were used. The $s_p^+ = 10$ configuration effectively resulted in no gap existing between the plasma profiles of the actuator in each set, thus resulting in a 100% coverage of the wall by plasma. Only the $s_p^+ = 20$ configuration resulted in a gap between each plasma profile that was larger than the plasma profile width itself. This resulted in plasma coverage of the wall that was less than 50%. The results obtained were compared to spanwise wall oscillations and a from a transversally uniform plasma force.

The uniform plasma configuration was found to produce larger skin-friction reductions than spanwise wall oscillation for both spatial and temporal waves. The largest reduction recorded was $DR = 51\%$ compared to a $DR = 47\%$ for a spanwise wall oscillation, both were obtained with a spatial wave at $W_m^+ = 12$ and $\lambda_x^+ = 1200$. The increased skin-friction reductions originated from the displacement of the Stokes layer by 2 wall units, with the maximum spanwise velocity at $y^+ \approx 2$ rather than at the wall as found with spanwise wall oscillations.

During a half-cycle of oscillation for the discrete configurations, the flow can be considered as having two separate stages. At the start of the half-cycle the

spanwise forcing, and consequently the velocity, changes polarity. This results in large velocity and vorticity perturbations that cause an increase in the skin-friction. Further into the half-cycle the individual wall jets created by each DBD actuator aggregate to form a pseudo-Stokes layer, and the perturbations are reduced and in some cases there is a skin-friction reduction. The spanwise velocity fields created by the discrete configurations were found to correlate well with those produced by the uniform plasma. The correlation improved with decreased actuator spacing and increased λ_x^+ or T^+ . For both the discrete configurations and the uniform plasma the optimum values of the wavelength was $\lambda_x^+ = 1200$ and $T^+ = 100 \sim 125$, which is the same as that previously observed for spanwise wall oscillations (Quadrio, 2011).

The spatial wave, as compared to a temporal wave, was found to produce increased skin-friction reduction for uniform plasma as had previously been seen for spanwise wall oscillations. The improvement was more dramatic for the discrete configurations where the drag increasing, first stage of the half period of oscillation was significantly attenuated from those produced by temporal oscillation. The $s_p^+ = 12.5$ configuration produced an average drag reduction of $DR = 9\%$ for temporal oscillation and this increased to $DR = 46\%$ for spatial waves. For both spatial and temporal waves the performance of the discrete configurations in producing an overall skin-friction reduction decreased with increasing actuator spacing. Using both temporal and spatial waves, the $s_p^+ = 20$ configuration, which is relatively small, did not produce a drag reduction for any case that was tested.

The investigation aimed to be similar to previous low Reynolds number experimental investigations and so the value of $b^+ = 17.5$ was set so that it was equivalent to a plasma profile width of a few mm, as is the case with the profile generated by current DBD actuators. However at flight scales a profile width of a few mm would equate to thousands of wall units and in the case of temporal oscillation the optimum frequency of oscillation would be approximately 50KHz while for spatial waves the optimum wavelength of oscillation would be less than 2mm in

length. A small change in the alteration of b^+ , and consequently the spacing of the actuators, could have an effect on the results and would certainly have an effect if the profile width is hundreds of wall units in length.

7.2 Recommendations

Actuator spacing appears to be crucial to the obtainment of a skin-friction reduction and it is suggested that further investigations are carried out to produce actuators that are capable of working in close proximity. Potentially the plasma profile width could have an effect if only changed by tens or even less wall units and an investigation of the effect of such a change is required. Unfortunately the model used in this investigation does not give guidance to the physical specifications of a required actuator such as the potential difference or electrode size and further development of a model that accurately simulates a force from such given parameters so as to aid experimental investigations would be of benefit.

Further investigation of the arrangement of actuators could also be done. Instead of a linear arrangement of actuators, an alternating checkerboard arrangement may lead to a reduction in perturbations and an increase in the regularity of the pseudo-Stokes layers, so minimising the effect of the increased actuator spacing.

This work involved simulations relevant to a DBD actuator while a sliding DBD actuator, as mentioned in Section 2.3, produces a large coverage and it may be feasible to utilise such actuators in a skin-friction control arrangement.

Appendix A

Helmholtz resonators

A.1 Introduction

One proposed method of flow control is active control using blowing and suction. Choi and Moin (1994) found that using control methods involving streamwise, span-wise and wall-normal velocities, that were determined by velocities in the buffer layer, they were able to achieve significant drag reductions. The main method of interest to these researchers was wall-normal velocity control. Suppression of the sweep and ejection events was achieved by applying blowing or suction on the channel walls exactly opposite to the wall-normal velocity at a prescribed y -location or detection plane.

For each point in time the boundary condition at the wall for $v(x, z)$ was dictated as:

$$v(x, 0, z; t) = -v(x, y_d, z; t), \quad (\text{A.1})$$

where $y_d(> 0)$ is the distance of the detection plane from the wall. The physical implication of this was that when high speed fluid moving towards the wall(sweep) was detected at y_d an equally strong blowing velocity was applied at the wall to nullify the sweep event. The contra-wise reaction occurred for an ejection event. This produced a virtual wall effect in the flow i.e., a wall-normal location where

the wall-normal velocity fluctuations are reduced to a minimum, roughly half way between the actual wall and the detection plane.

The y_d location has an effect on the performance of the control method. Choi and Moin (1994) found an optimum at $y_d^+ \approx 10$ with a smaller drag reduction at $y_d^+ \approx 5$ and a drag increase at $y_d^+ \approx 26$ at a Reynolds number of $Re_\tau = 180$. Later work revealed that a detection plane at $y_d^+ \approx 15$ was the optimum location (Hammond et al., 1998).

An investigation into the amplitude of the wall blowing and suction found that by reducing the amplitude of the blowing and suction from the value of $A = 1.0$ used previously,

$$v(x, 0, z; t) = -Av(x, y_d, z; t), \quad (\text{A.2})$$

a drag reduction for a detection plane between $5 \leq y_d \leq 30$ can be produced. It was also shown that the drag reduction increased linearly with the amplitude of the wall blowing and suction $0 < v_{rms}^+ < 0.15$ and that there was a maximum $v_{rms}^+ = 0.25$ above which drag reduction for all detection planes deteriorated (Chung and Talha, 2011).

Choi and Moin (1994) also found that with selective control, in the first case where blowing and suction was applied only when the magnitude of the wall-normal velocity at the sensor location exceeded that of v_{rms} of the wall-normal velocity at y_d ($|v(x, z)| > v_{rms}$), and in the second case twice that of v_{rms} , drag reduction of 20% and 15% respectively was achieved with only 25% and 5% respectively of the area being controlled. The small control area indicated that most of the drag reduction is achieved with the prevention of stronger events.

There are limitations to the practicality of this control method in that the input for the control scheme is the wall-normal velocity at a location inside the flow, and this is practically unfeasible. Choi and Moin (1994) investigated the correlation between various variables at the wall and the structures (wall-normal velocities)

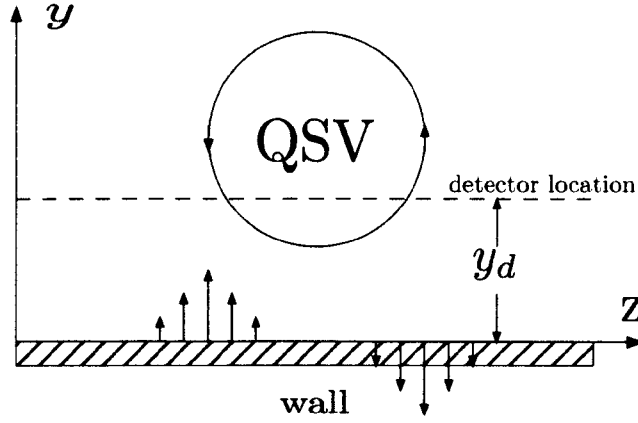


Figure A.1: Schematic diagram of opposition control.

above the wall, in an attempt to replicate the scheme by placing sensors at the wall. They investigated wall-pressure (p_w), streamwise velocity gradient ($\delta u' \delta y|_w$) and a variable derived from the Taylor series expansion and continuum equation of wall-normal velocity near the wall. They found that the first two showed little correlation, with the latter showing the most promise, yet only in the form of a modest 6% drag reduction. There has been much work since, into the practical application of such a scheme with the main focus on the sensing and control algorithms, for a wall based sensing scheme (Lee et al., 1997, 1988; Endo et al., 2000; Kang and Choi, 2000).

Research into micro-jets for flow control application found that the cavities of micro-jet actuators can produce a jet stream without being activated because of Helmholtz resonance occurring within the cavity of the actuator (Lockberby et al., 2007).

This investigation was made into Helmholtz resonating cavities, in a blowing and suction opposition control scheme. The advantages of this system is that it requires no energy and that any power savings made in reducing skin-friction would also be the net power saving of the system while absence of control or sensing elements make the system inherently simple.

A model for a resonator actuator is derived and then optimised using pre-

recorded turbulent channel flow data. A series of turbulent channel flow simulations were then run and the results analysed.

A.2 Resonator model

Using the equations derived for flow rate and rate of change of flow rate derived for a cavity by Lockberby et al. (2007) a model for a cavity can be derived. The

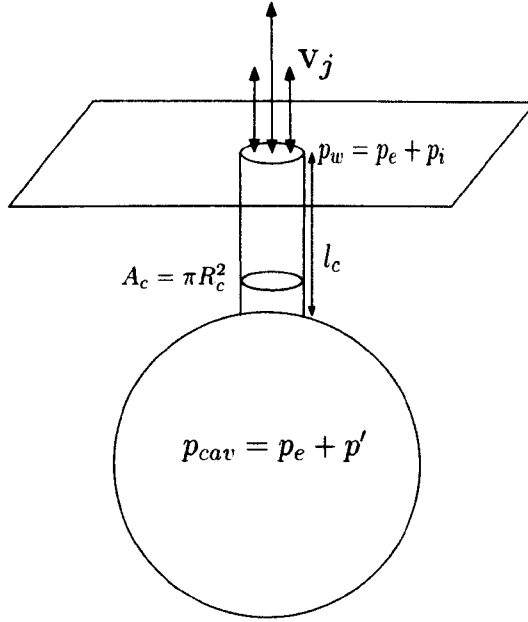


Figure A.2: Sketch of a cavity.

dimensions that define a cavity are: A_c , the cross-sectional area of the cavity orifice, R_c , the radius of the cavity orifice, l_c , the length of the cavity orifice and V_c , the volume of the cavity.

The dimensionalised equation for the instantaneous flow rate, Q , of air from the cavity is (Lockberby et al., 2007):

$$Q = A_c v_j = -\frac{V_c}{p_e} \frac{dp'}{dt}, \quad (\text{A.3})$$

where, p_c , is the time-mean pressure in the cavity, p' , is the fluctuating pres-

sure in the cavity, and v_j , is the bulk mean velocity of the jet. To non-dimensionalise Equation (A.3), the following dimensionless variables are used. Here, a superscript $< >^*$ represents dimensional variables, and a subscript $< >_{ref}$ represents reference variables.

$$V_c = \frac{V_C^*}{h_{ref}^3}, \quad t = \frac{t^*}{h_{ref}/u_{ref}}, \quad p' = \frac{p'^*}{p_{ref}}, \quad p_c = \frac{p_c^*}{p_{ref}}, \quad A_c = \frac{A_c^*}{h_{ref}^2}, \quad v_j = \frac{v_j^*}{u_{ref}}. \quad (\text{A.4})$$

Substituting them in and rearranging:

$$\frac{dp'}{dt} = -\frac{A_c}{V_c} p_c v_j. \quad (\text{A.5})$$

The flow momentum equation for fully developed flow is (Lockberby et al., 2007):

$$\rho_e \frac{dQ}{dt} = \eta \frac{p' - p_i}{l_c} \pi R_c^2 - 2\pi R_c \tau_w, \quad (\text{A.6})$$

where, ρ_e is the density of the fluid in the cavity, p_i , is the fluctuating pressure at the orifice exit, η is a factor due to assumption of a constant pressure gradient in the orifice. The wall-shear stress τ_w is:

$$\tau_w = \mu \frac{\partial v}{\partial r}. \quad (\text{A.7})$$

Assuming fully developed laminar pipe flow for the orifice:

$$\tau_w = 3\mu \frac{v_j}{R_c}. \quad (\text{A.8})$$

Then Equation (A.6) can be simplified to:

$$\rho_e \frac{dv_j}{dt} = \eta \frac{p' - p_i}{l_c} - 6\mu \frac{v}{R_c^2}. \quad (\text{A.9})$$

Non-dimensionalising Equation (A.9) using the terms from Equation (A.4):

$$\frac{dv_j}{dt} = \eta \frac{p_{ref}}{\rho_e \rho_{ref} u_{ref}^2 l_c} (p' - p_i) - \frac{6}{\rho_e Re R_c^2} v_j, \quad (\text{A.10})$$

where the Reynolds number Re is

$$Re = \frac{\rho_{ref} u_{ref} h_{ref}}{\mu}. \quad (\text{A.11})$$

A.2.1 Pressure term

The non-dimensionalised Equation (A.10) contains the term p_{ref} , the equations are therefore altered so that $p_{ref} = \rho_{ref} u_{ref}^2$ is used as the reference pressure:

$$\frac{dp'}{dt} = -\frac{A_c}{V_c} p_c v_j, \quad (\text{A.12})$$

$$\frac{dv_j}{dt} = \frac{\eta}{\rho_e l_c} (p' - p_i) - \frac{6}{\rho_e Re R_c^2} v_j. \quad (\text{A.13})$$

An issue with using u_{ref} and ρ_{ref} is that a value for p_c would have to be determined using the following equation:

$$p_c = \frac{p_{atm}}{\rho_{ref} u_{ref}^2}. \quad (\text{A.14})$$

The equation can be non-dimensionalised using speed of sound, c , Mach number, M , and the heat capacity ratio, γ :

$$c = \sqrt{\gamma \frac{P}{\rho}}, \quad (\text{A.15})$$

$$p_c = \frac{c^2}{\gamma u_{ref}^2}, \quad p_c = \frac{1}{\gamma M^2}. \quad (\text{A.16})$$

If the skin-friction velocity u_τ was used as the reference velocity for the model

so that $u_{\tau ef} = u_\tau$, then

$$\frac{dp'}{dt} = -\frac{A_c}{V_c} \frac{1}{\gamma M^2} v_j, \quad (\text{A.17})$$

$$\frac{dv_j}{dt} = \frac{\eta}{\rho_e l_c} (p' - p_i) - \frac{6}{\rho_e Re_\tau R_c^2} v_j. \quad (\text{A.18})$$

However, now that the reference variables are different for the resonator model and the channel flow simulation parameters, conversions between the two have to be made. With regards to the Mach number at flight conditions the friction velocity is typically 4% of the free stream velocity (Schlichting and Gersten, 1979):

$$Re_\tau = 0.04 Re. \quad (\text{A.19})$$

So, the Mach number based on the friction velocity can be calculated:

$$\frac{u_\tau}{U} = \frac{M_\tau}{M} = 0.04. \quad (\text{A.20})$$

So, for a typical flight Mach number of $M = 0.85$, $M_c = 0.0345$ and $\gamma = 1.4$. The atmospheric pressure at flight condition is:

$$p_e = \frac{1}{\gamma M_\tau^2} \approx 600, \quad (\text{A.21})$$

$$(\text{A.22})$$

A.3 Resonator optimisation

With a multitude of variables defining the resonator a method of optimisation was required. By combining the two first order ODE's, a second order ODE can be

formed. Re-arranging Equation (A.5) to make, v_j the subject of the equation:

$$v_j = -\frac{V_c}{A_c p_e} \frac{dp'}{dt}, \quad (\text{A.23})$$

and placing it twice into Equation (A.10) and rearranging the following second order ODE is produced:

$$\rho_e \frac{d^2 p'}{dt^2} + \frac{6}{Re_\tau R_c^2} \frac{dp'}{dt} + \frac{\eta A_c p_e}{l_c V_c} p' = \frac{\eta A_c p_e}{l_c V_c} p_i. \quad (\text{A.24})$$

Note that Equation (A.24) is very similar to the equation for a damped forced oscillating system:

$$m\ddot{x} + e\dot{x} + kx = J_m \sin \omega t, \quad (\text{A.25})$$

and, J , the driving force is defined as:

$$J = J_m \sin \omega t, \quad (\text{A.26})$$

and, ω , is the circular driving frequency and, C_c , the critical dampening coefficient is defined as:

$$C_c = 2m\sqrt{\frac{k}{m}} = 2m\omega_o, \quad (\text{A.27})$$

where, ω_o , is the natural frequency of oscillation of the resonator:

$$\omega_o = \sqrt{\frac{k}{m}} = \sqrt{\frac{\eta A_c p_e}{\rho_e l_c V_c}}. \quad (\text{A.28})$$

The closer $\frac{\omega}{\omega_o}$ is to 1, the greater the amplitude of response of the system and the lower the value of the dampening ratio ζ , the greater the response of the system, from Equation (A.10) :

$$\zeta = \frac{e}{C_c} = \frac{\frac{6}{Re_\tau R_c^2}}{2m\omega_o}, \quad (\text{A.29})$$

the radius of the orifice, R_c , can be determined as:

$$R = \sqrt{\frac{3}{\zeta \omega_o Re_\tau \rho_e}}. \quad (\text{A.30})$$

The temporal design frequency of the resonator, f_o , is therefore:

$$f_o = \frac{\omega_o}{2\pi} = \frac{3}{2\zeta \pi R_c^2 Re_\tau \rho_e}. \quad (\text{A.31})$$

or the design period of the resonator T_o :

$$T_o = \frac{2\pi}{\omega_o} \quad (\text{A.32})$$

and given that:

$$\sqrt{\frac{k}{m}} = J = \omega, \quad (\text{A.33})$$

$$l = \frac{\eta A_c p_e}{V_c \rho_e \omega_o^2}, V = \frac{\eta A_c p_e}{l \rho_e \omega_o^2}. \quad (\text{A.34})$$

The parameters that define the resonator can then be envisaged by two parameters ω_o , the natural frequency of oscillation of the resonator and, ζ , the coefficient of damping.

A.4 Method

The results were computed using the implicit method described in Chapter 3. The Reynolds number for the simulations was $Re(\equiv U_m h / \nu) = 3150$. The Reynolds number based on the skin-friction velocity u_{τ_0} of the no-control case, as in the plasma simulations, was $Re_\tau = u_{\tau_0} h / \nu = 200$. The computational domain has dimensions $L_x = 6h$, $L_y = 2h$, $L_z = 2h$ and is discretised to a grid of $(120 \times 129 \times 80)$. The corresponding grid spacings were $\Delta x^+ = 10.0$, $\Delta y_{min}^+ = 0.1$, $\Delta y_{max}^+ = 9.0$ and

$\Delta z^+ = 5.0$. The time step used was $\Delta t^+ (= \Delta t u_\tau^2 / \nu) = 0.1$. For the flow control the total time for sampling was $590h/U_m$. The simulation was run so that the opposite of the jet velocities produced by the resonator models was applied to the top wall of the channel so as to provide conservation of mass. Therefore only the flow of the bottom half of the channel is of interest.

A.5 Results

A.5.1 Wall-normal velocity and wall-pressure correlation

A no-control DNS with the wall-normal velocity, v , for the entire domain recorded for every time step along with the pressure fluctuations at the wall, p'_w , was run. The wall-pressure was correlated with the wall-normal velocity at $y^+ = 5, 10, 15$, to provide the value r_{pv} :

$$r_{pv}(\Delta y, \Delta z, \Delta t; y) = \langle p(x_0, 0, z, t), v(x_0 + \Delta x, y, z + \Delta z, t + \Delta t) \rangle. \quad (\text{A.35})$$

Figure A.3(a) shows that with r_{pv} at $\Delta t = 0$ at $y^+ = 10$ there is a negative correlation $r_{pv} \approx -0.35$ of limited strength, with the best correlation at $\Delta z = 0$ and $\Delta t = 0$. Figure A.3(b) represents the correlation r_{pv} for all three y -locations, $\Delta z = 0$, and shows that there is a correlation of $r_{pv} \approx -0.35$ at $\Delta x^+ = -30$ indicating that the pressure fluctuations at the wall are influenced in part by wall-normal events 30 viscous units upstream. This corresponds with observations that quasi-streamwise vortices, the structures that are suppressed by opposition control, have a similar influence on downstream wall-pressure (Kim et al., 2002a).

Further analysis with joint probability density functions of wall-pressure against wall-normal velocities, at $y^+ \approx 10$, (see Figure A.4) as with similar joint probability density functions produced by Choi and Moin (1994) indicate that wall-pressure has very little relation to the wall-normal velocity component. Although

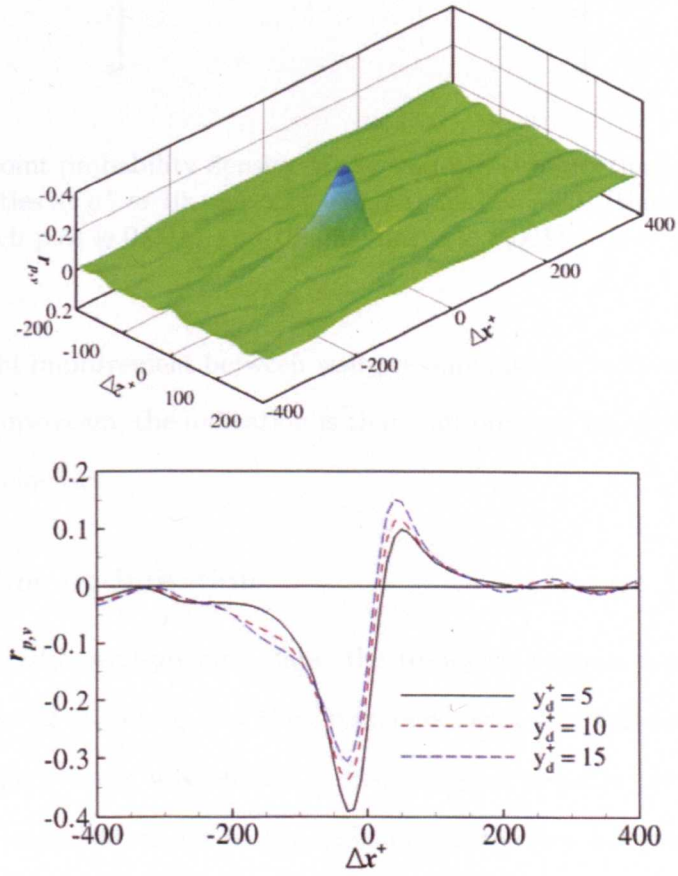


Figure A.3: (a) Surface plot of r_{pv} at $\Delta t^+ = 0$, $t = 0$ at $y^+ = 10$ and (b) r_{pv} at $\Delta t^+ = 0$, $t = 0$ at $\Delta z^+ = 10$.

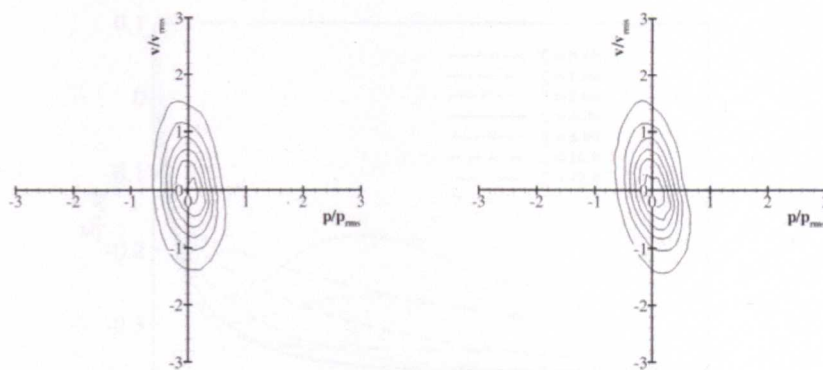


Figure A.4: Joint probability density of the wall-pressure fluctuations and the wall-normal velocities at $y^+ \approx 10$: (a) $\Delta x^+ = 0$, (b) $\Delta x^+ = -30$. (the value of the outer contour in each plot is 0.001, and the increment is 0.001).

there is a slight improvement between wall-pressure and the wall-normal velocity 30 viscous units upstream, the indication is that wall-pressure has little bearing on the wall-normal velocities.

A.5.2 Offline optimisation

Using the recorded wall-pressure data, the resonator outputs were calculated for different values of ω_o and ζ and then correlated with the wall-normal velocity at $y^+ = 10$. The process was offline, as pre-recorded pressure data was used and therefore the resonator output had no influence on the flow and hence the pressure. Results show that with a high wall-pressure fluctuation a negative wall-normal velocity was produced by the resonators, and a positive wall-normal velocity for a low wall-pressure fluctuation. This negative correlation between wall-pressure and resonator jet velocity, combined with the negative correlation between wall-normal velocity and wall-pressure, leads to a positive correlation between wall-normal velocity and resonator output velocity. This is opposite to the desired negative correlation required with blowing and suction drag reduction. Therefore the polarity of the res-

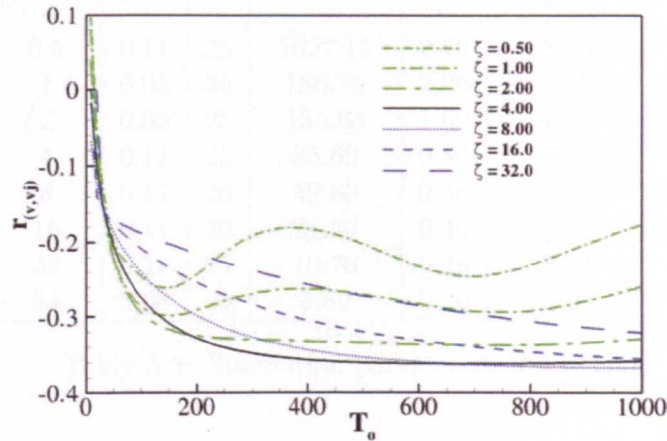


Figure A.5: Correlation of wall-normal velocity with the resonator output, R_{vv_j} , against design period of the resonator T_o for various values of dampening coefficient, ζ .

onators was reversed numerically to allow the desired negative correlation between the wall-normal velocity and the resonator output velocity.

Figure A.5 is a plot of the correlation of wall-normal velocity with the resonator output, R_{vv_j} , for values of T_o against ζ at $\Delta x = 0$ and $\Delta t = 0$ with $l_c^+ = 25$. It was found that by reducing η the strength of the resonator was reduced without effecting the correlation. Reducing l_c^+ would lead to an increase in the resonator strength, but it also affected the point of maximum correlation. Decreasing l_c^+ led to the resonator output having a greater correlation with wall-normal events upstream, inline with the pressure correlation r_{pv} , while increasing l_c^+ led to the optimum correlation being further downstream. With $l_c^+ = 25$ the optimum correlation was at $\Delta x^+ = 0$ i.e., the resonator output had its maximum correlation with the wall-normal velocity directly above it.

A.5.3 Controlled channel flows

A multitude of simulations were run, for various values of ω_o , ζ_o and l_c^+ . A resonator jet-velocity was calculated for every point on the wall, and the calculated resonator

$\zeta = \frac{c}{c_c}$	η	l^+	$V^+ \times 10^3$	R^+	$C_f \times 10^{-3}$	DR
—	—	—	—	—	7.84	0.0
0.5	0.11	25	1027.15	2.76	8.38	-7
1	0.03	25	186.76	2.26	7.82	0
2	0.05	25	155.63	1.60	7.74	1
4	0.11	25	85.60	0.80	7.58	3
8	0.11	25	42.80	0.56	7.73	1
16	0.11	25	21.40	0.40	7.91	-1
32	0.11	25	10.70	0.28	8.03	-2
64	0.08	25	3.89	0.20	7.99	-2

Table A.1: Simulation parameters, $T_o^+ = 800$.

velocities were used as the boundary condition of the DNS channel flow simulation. It was found that many simulations crashed, or led to large drag increases. Those simulations that failed initially showed a moderate output ($v_j^+ < 0.25$) but then steadily increased until, at some point, there was a sudden large increase in output ($v_j^+ > 10$). The large resonator outputs conflicted with the smaller outputs produced by the offline simulations for the same parameters, indicating that the resonators were altering the flow, so that the wall-pressure fluctuations were much higher than those formed with the uncontrolled flow resulting in higher velocity magnitudes from the resonators. If a simulation proved unstable the output of the resonators was reduced to provide stability, however reducing η led to low resonator outputs (see Table A.1), with a small influence on the flow and the statistics generated would naturally be only slightly different to that of the uncontrolled flow. A successful series of results was at $T_o^+ = 800$, for several dampening coefficients, (see Table A.1), for most values there was a drag increase, but there was a small drag decrease of $DR = 3\%$ with $\zeta = 4.0$, hereafter referred to as controlled case. This is compared to the no flow control case in the following.

Figure A.6 shows the time history of the skin-friction coefficient against the the time averaged skin-friction coefficient of the uncontrolled channel flow. The skin-friction fluctuations are of a similar magnitude to the uncontrolled flow, but on

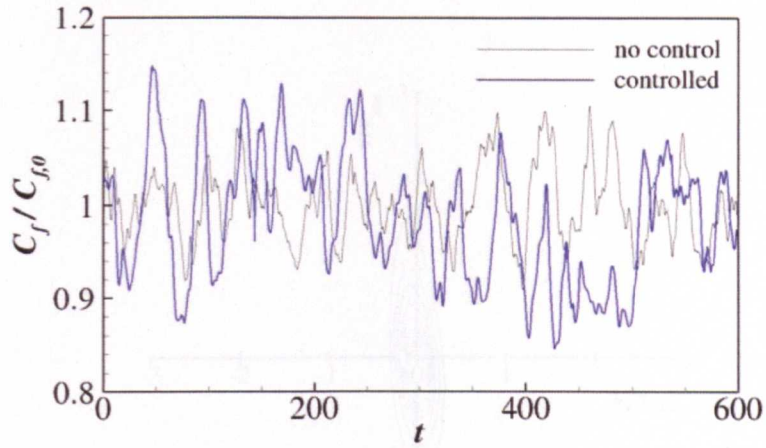


Figure A.6: Time history of the skin-friction coefficient.

average the skin-friction is lower than the uncontrolled case. Figure A.7 is a joint probability density function of v_j against wall-normal-velocity at $y^+ = 10$, there is a weak negative correlation with $r = -0.34$. This is far lower than the perfect negative correlation achieved with blowing and suction.

A.5.4 Mean properties

Some key features of the flow field for the $\zeta = 4.0$ case and the uncontrolled case are shown, so that the differences between them can be examined. All velocity and length scales are normalised by the channel half width, h , and unless otherwise stated with the uncontrolled wall-shear velocity u_{τ_0} .

The mean-velocity profiles normalised by the actual wall-shear velocities are shown in figure A.8 for both the uncontrolled and controlled channel. The mean velocity profiles are nearly the same, and so is the slope of the log-law. There is a slight increase in the point of interception of the log-law with $u^+ = y^+$ indicating an increase in the viscous sublayer, but the increase is slight as would be expected with such a small drag reduction.

Turbulence intensities are shown in Figure A.9, and are compared with the

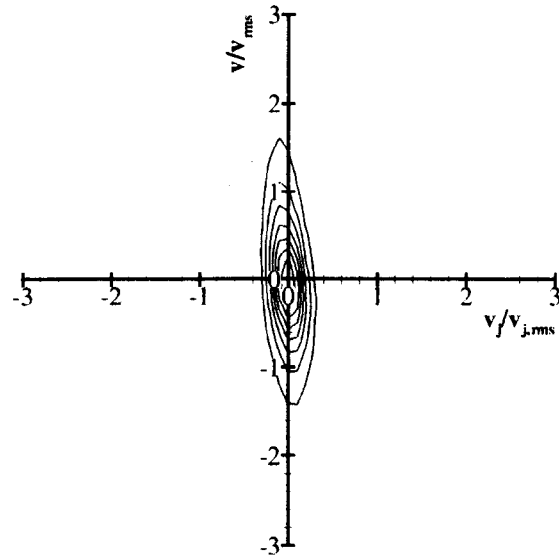


Figure A.7: Joint probability density of resonator output v_j and the wall-normal velocities at $y^+ \approx 10$ (the value of the outer contour in each plot is 0.001, and the increment is 0.001).

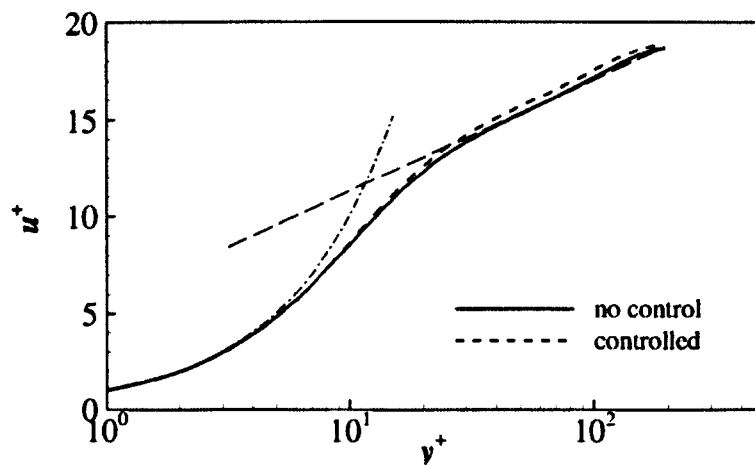


Figure A.8: Mean velocity profiles (law of the wall ($u^+ = y^+$ and $u^+ = \frac{1}{\kappa} \ln y^+ + 5.5$)).

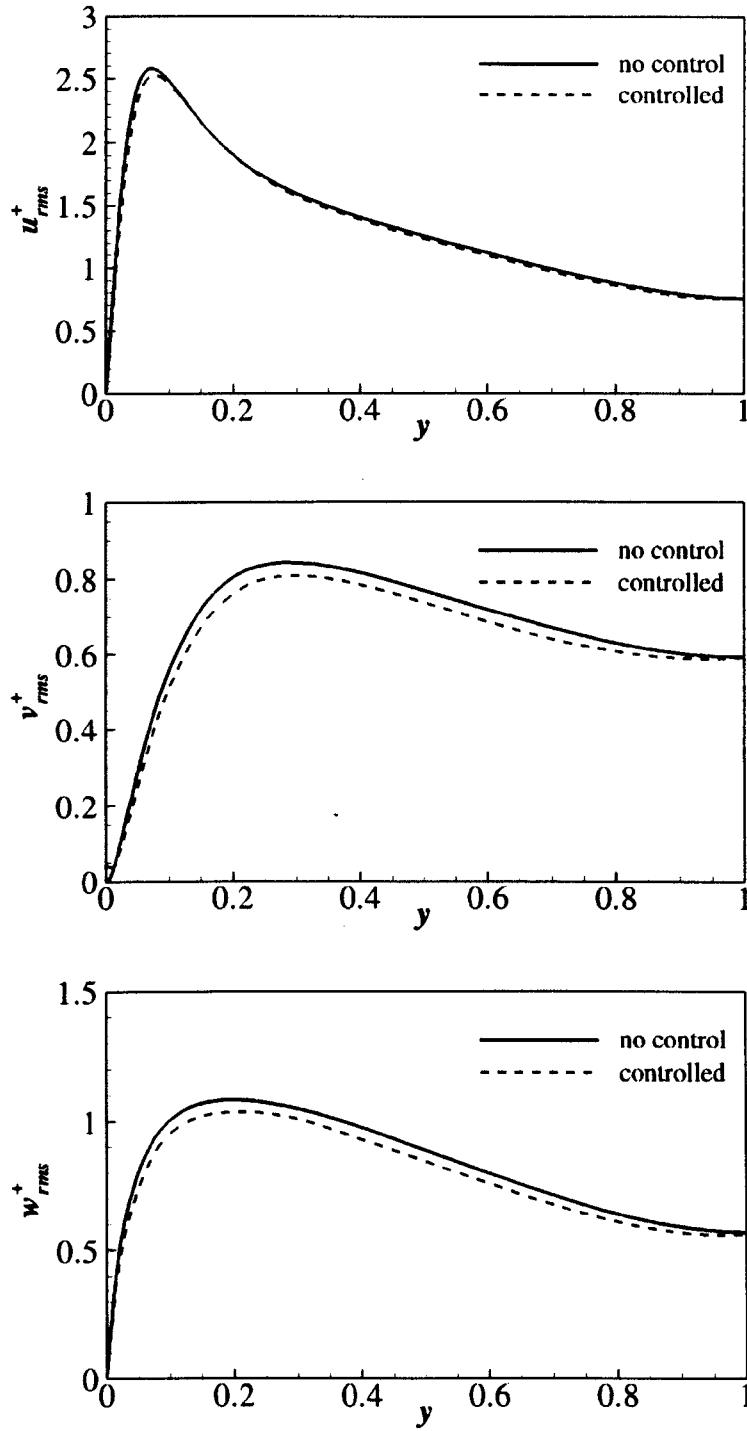


Figure A.9: Root-mean-square fluctuations normalised by the wall-shear velocity in global coordinates.

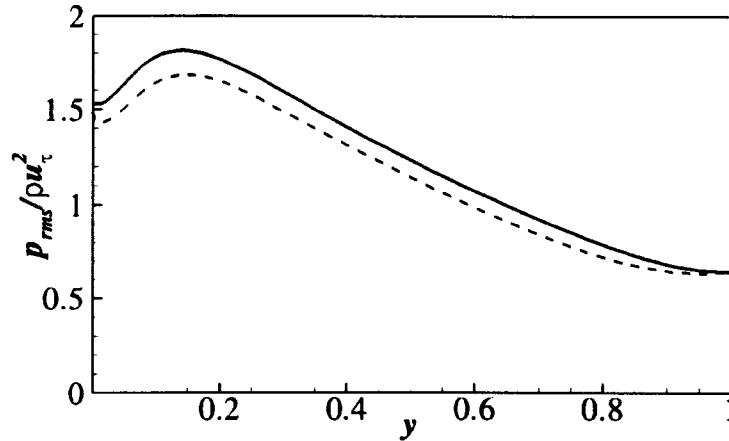


Figure A.10: Root-mean-square pressure fluctuations normalised by $u_{\tau 0}$. Dashed lines represent controlled case.

uncontrolled wall. Turbulence intensities are reduced throughout the channel, although there is an increase in v_{rms} near the wall, because of the resonator output and are in line with the observations made for blowing and suction.

The Reynolds shear stress $\overline{u'v'}$, is shown in Figure A.11, also shown is the total shear stress, $-\overline{uv} + (1/Re_{\tau} \frac{du}{dy})$. The slope of the total shear stress is a straight line as should be the case with fully developed turbulent flow. The shear stress and Reynolds stress is also reduced right through the profile. The contribution to the Reynolds shear stress from each quadrant is shown in Figure A.9. The sum of the values at each y -location from the four quadrants is equal to the local Reynolds shear stress. With uncontrolled channels, the ejection events are dominant away from the wall, and sweep events are dominant in the near wall region, while both equally contribute $y \approx 12$. In the the controlled channel, the Reynolds shear stress from the sweep and ejection events is reduced, although the fractional contributions remain the same. with the point where the sweep and ejection events are equal shifted slightly outwards by approximately 2 viscous units.

Root-mean square vorticity fluctuations are shown in Figure A.13. Wall-

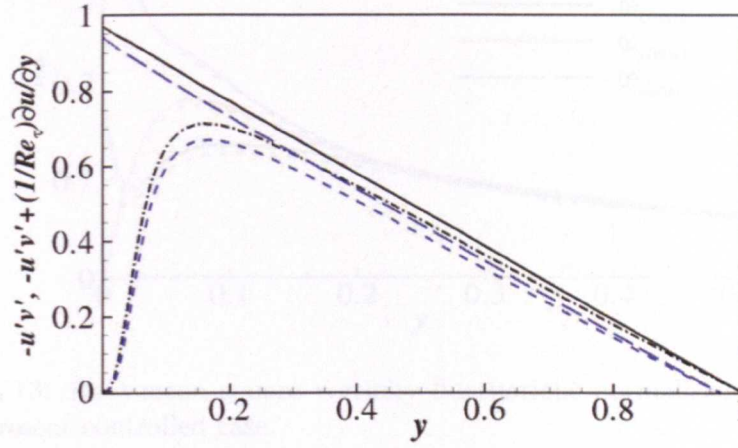


Figure A.11: Reynolds shear stress $(\overline{u'v'})$ and total shear stress $(-\overline{uv} + (1/Re_\tau) \frac{du}{dy})$ normalised by u_{τ_0} . Dashed lines represent controlled case.

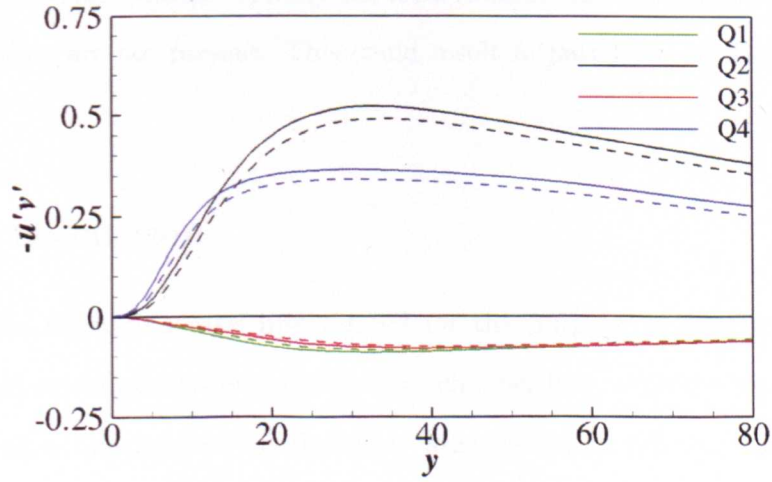


Figure A.12: Reynolds shear stress from each quadrant normalised by the wall-shear-shear velocity u_{τ_0} . Dashed lines represent controlled case.

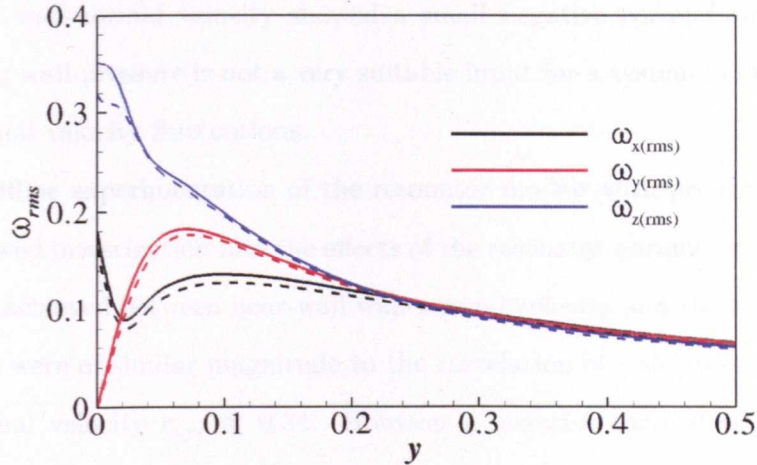


Figure A.13: Root-mean square vorticity fluctuations normalised by u_{τ_0} . Dashed lines represent controlled case.

normal and streamwise vorticity show a slight reduction through the channel, and a slight outward shift of the peaks which is more evident with wall-normal vorticity. There is a noticeable reduction in the spanwise vorticity close to the wall, which is to be expected with the reduced shear components. However, in both the case of spanwise and streamwise vorticity the local minima and maxima seen with blowing and suction, are not present. This could result in part from an incomplete virtual origin.

A.6 Discussion

Helmholtz resonators were investigated for the purpose of drag reduction, using direct numerical simulations of turbulent channel flow, with the intention of them mimicking a blowing and suction type drag reduction scheme. The advantages of such would be an easier real world implementation. A Resonator uses wall-pressure fluctuations as its input and produces a wall-normal jet-velocity. A model was derived for resonators that produced a wall-normal boundary condition for the DNS channel flow simulations. However analysis of wall-pressure correlations and

near-wall wall-normal velocity showed a small negative correlation $r_{pv} \approx -0.35$, indicating wall-pressure is not a very suitable input for a system in order to counter wall-normal velocity fluctuations.

Offline experimentation of the resonator models with pre-recorded pressure data allowed investigation into the effects of the resonator parameters. The best correlations achieved between near-wall wall-normal velocity and the resonator output velocities were of similar magnitude to the correlation of wall pressure to near-wall wall-normal velocity $r_{vv_j} \approx 0.34$. However a negative correlation was to be desired in order to achieve a similar drag reduction mechanism to that obtained from blowing and suction. Therefore to achieve a desired drag reduction the polarity of the resonator output from the resonator model was reversed before being used as boundary condition and this removing an element of the physical basis of the model and simulation.

The highest drag reduction achieved with the configurations tested was a modest 3% drag reduction which was achieved with $l_c^+ = 25$, $\zeta = 4$ and $t_o^+ = 800$, and $\eta = 0.11$, with the entire bottom wall having its wall-normal boundary condition prescribed by the resonator model. This fits well with the maximum 6% drag reduction achieved by (Choi and Moin, 1994) using information at the wall. Most of the simulations conducted either crashed or led to drag increases with working simulations usually having a small response.

The statistics of the best controlled channel case was compared with the uncontrolled channel flow, with uncontrolled and controlled simulations starting with the same initial conditions. There was a slight upward shift in the log-law and viscous-sublayer thickness, although the shift was slight which is expected with such a small drag reduction. Velocity, vorticity and pressure fluctuations and the Reynolds shear stress were reduced throughout the channels although the reductions obtained were small. As the response from the actuators were so weak, the differences between the controlled flow and uncontrolled flow are slight. The drag

reduction scheme is thought to be the same as that with blowing and suction. However, as expected with the small strength of the resonators and the low correlation between the near wall wall-normal velocity and the resonator output, the virtual origin is only slightly displaced and furthermore it is incomplete.

A.7 Summary

Helmholtz resonators were investigated for use in turbulent skin-friction control, a model was derived. The variable that determines the output of a resonator is the wall pressure fluctuations and it was found that there was a weak negative correlation between the wall pressure and the wall-normal velocity at $y^+ \approx 10$. A maximum 3% skin-friction reduction was obtained, but only when the polarity of the actuator model was reversed. It was therefore concluded that, for the configurations tested, the Helmholtz resonators offered only a minimum and variable effect in skin-friction control.

Appendix B

Temporal oscillating plasma results

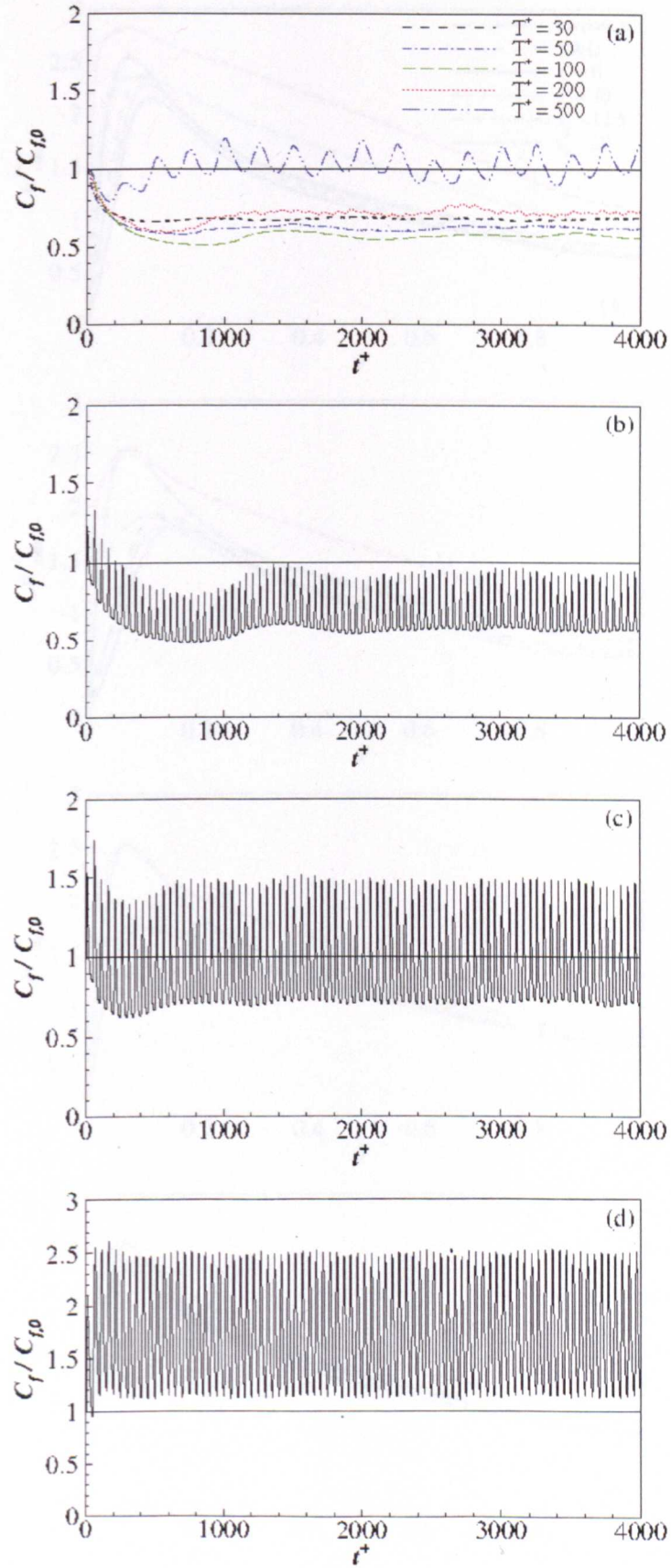


Figure B.1: Time history of the skin-friction coefficient for different actuator configurations: a) $s_p^+ = 0$, b) $s_p^+ = 10$ and $T^+ = 100$, c) $s_p^+ = 12.5$ and $T^+ = 100$, d) $s_p^+ = 20$ and $T^+ = 100$.

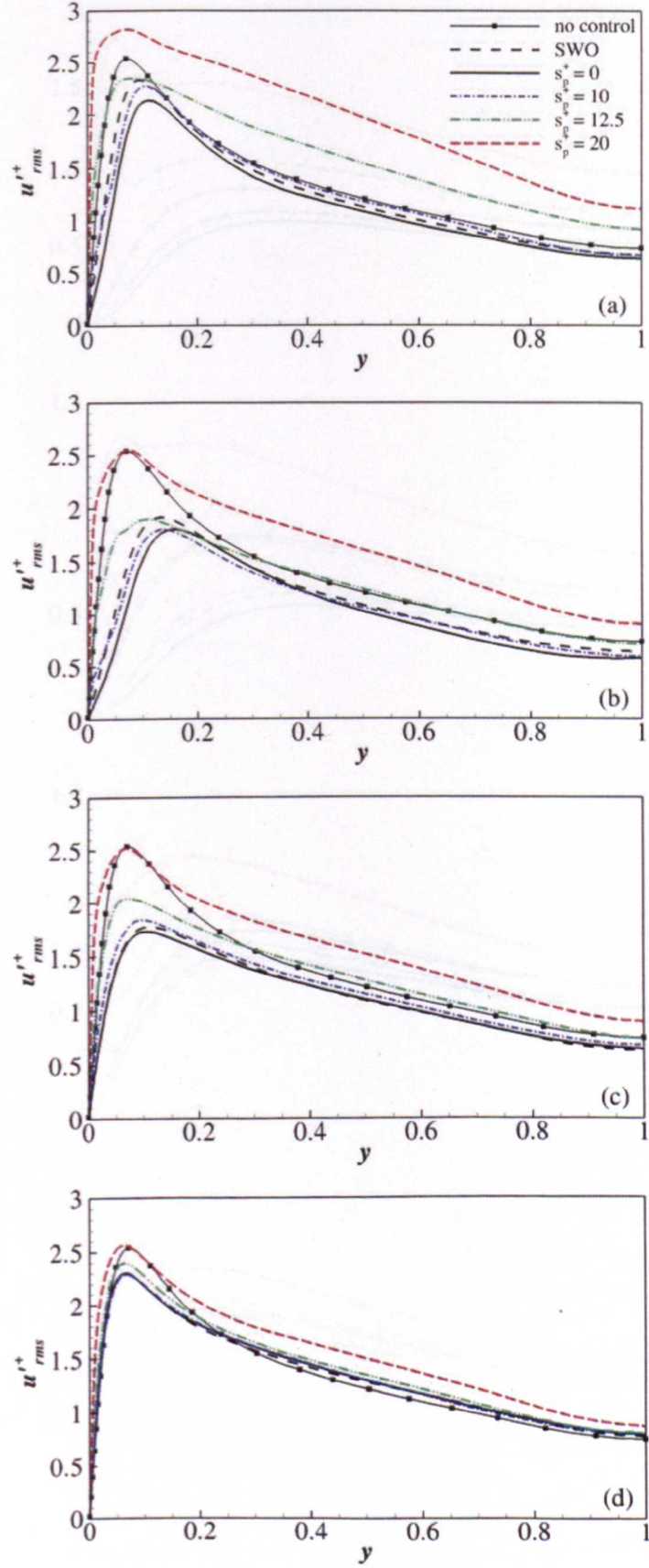


Figure B.2: Time history of the skin-friction coefficient Root-mean-square stream-wise velocity fluctuations, u_{rms} , normalised by the no-control wall-shear velocity, u_{τ_0} in global coordinates: a) $T^+ = 30$, b) $T^+ = 100$, c) $T^+ = 200$, d) $T^+ = 500$.

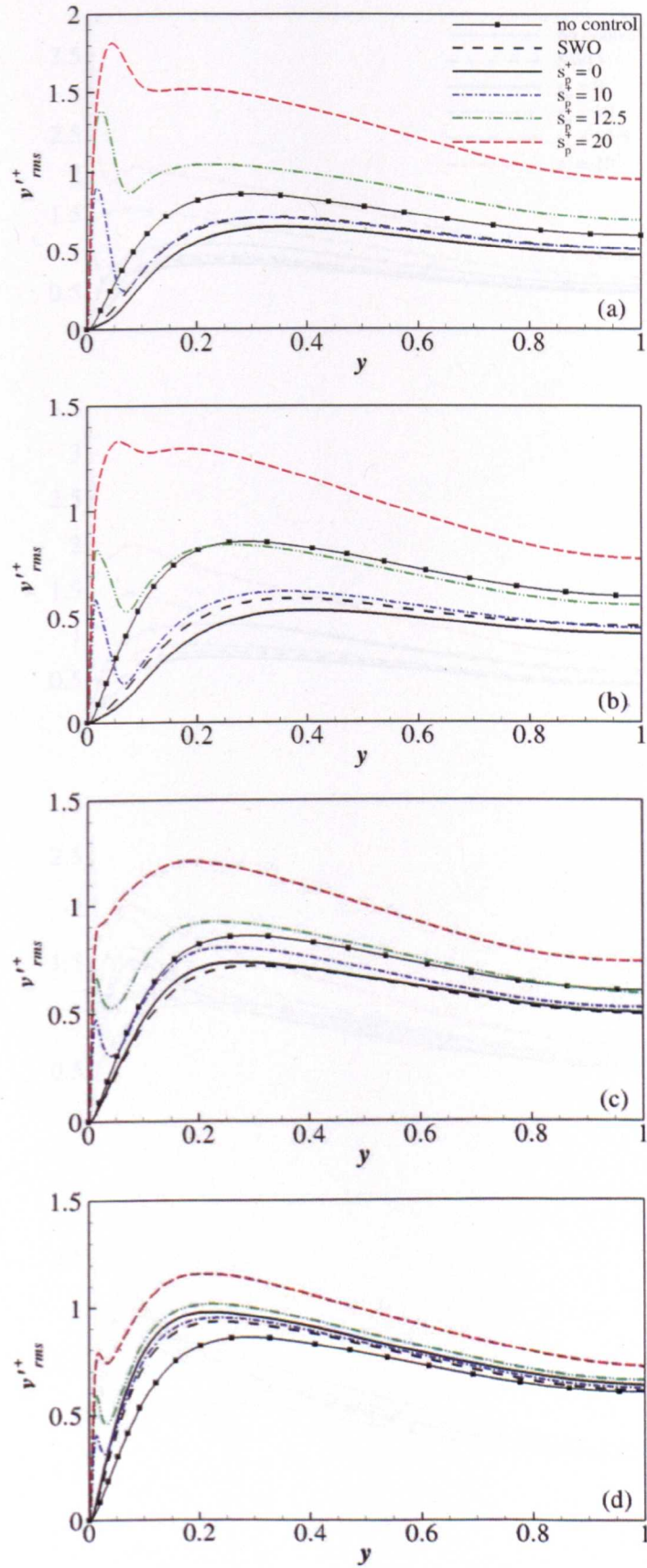


Figure B.3: Root-mean-square wall-normal velocity fluctuations, v_{rms} , normalised by the no-control wall-shear velocity, u_{τ_0} in global coordinates: a) $T^+ = 30$, b) $T^+ = 100$, c) $T^+ = 200$, d) $T^+ = 500$.

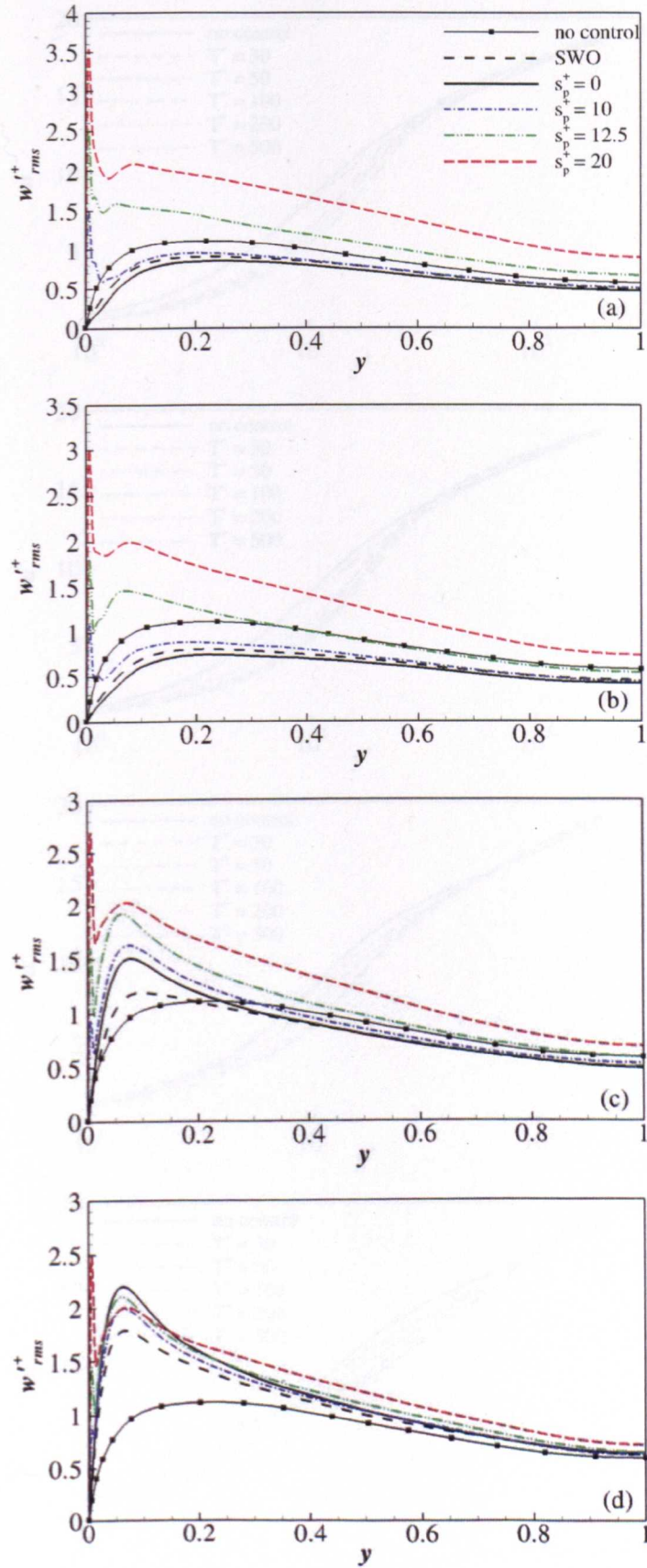


Figure B.4: Root-mean-square spanwise velocity fluctuations, w_{rms} , normalised by the no-control wall-shear velocity, u_{τ_0} in global coordinates: a) $T^+ = 30$, b) $T^+ = 100$, c) $T^+ = 200$, d) $T^+ = 500$.

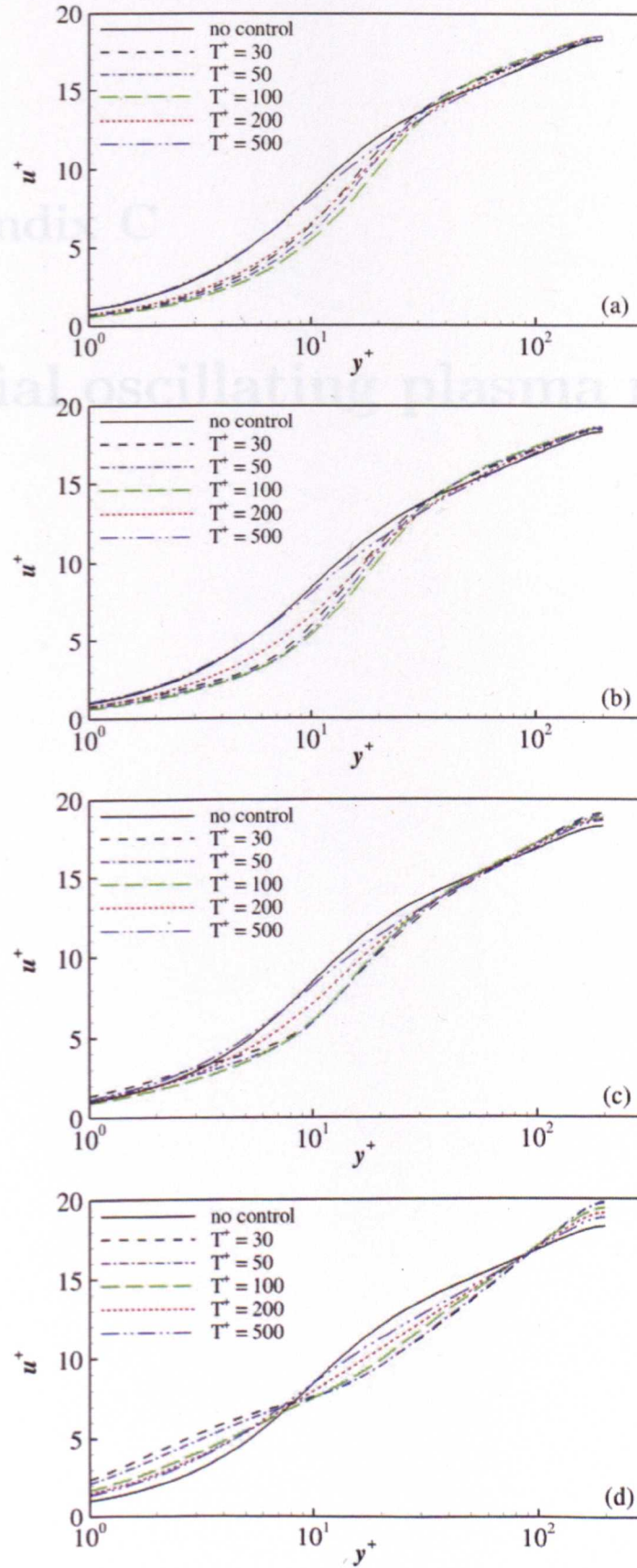


Figure B.5: Mean-velocity profiles normalised by $u_{\tau 0}$: a) $s_p^+ = 0$, b) $s_p^+ = 10$, c) $s_p^+ = 12.5$, d) $s_p^+ = 20$.

Appendix C

Spatial oscillating plasma results

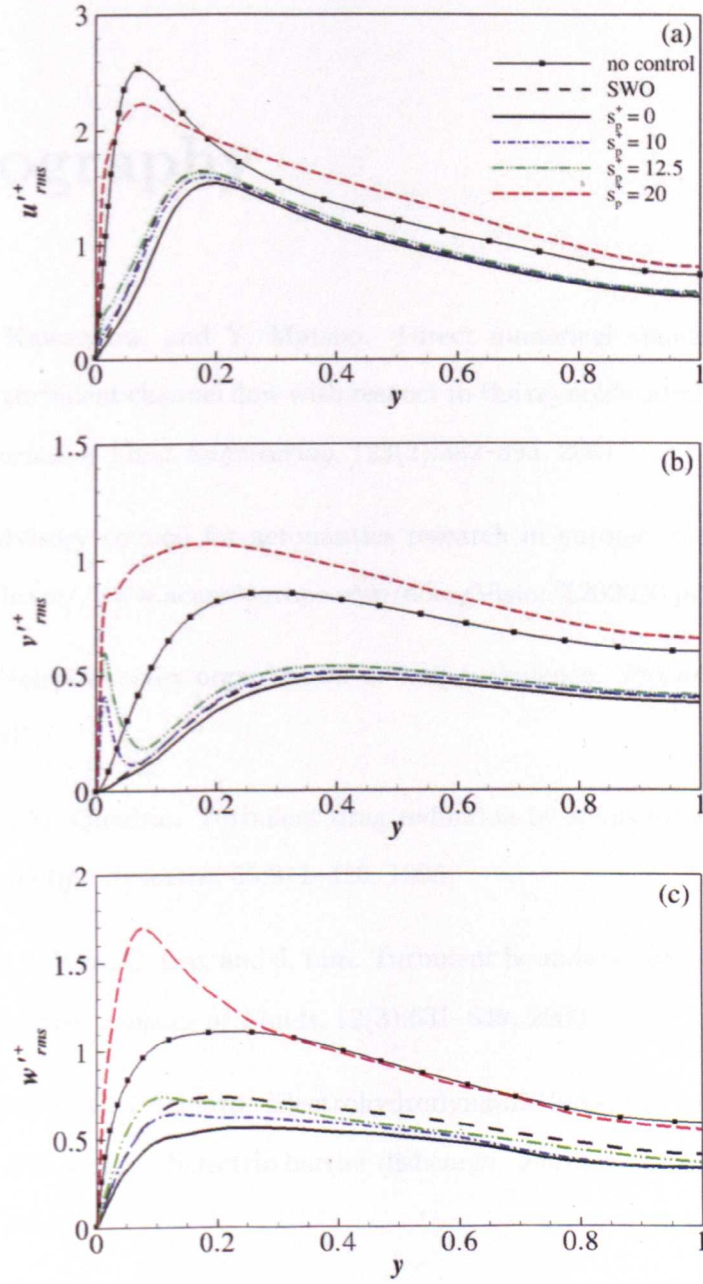


Figure C.1: Root-mean-square velocity fluctuations, normalised by, u_{τ_0} : a) u_{rms} , b) v_{rms} and c) w_{rms} .

Bibliography

- H. Abe, H. Kawamura, and Y. Matsuo. Direct numerical simulation of a fully developed turbulent channel flow with respect to the reynolds number dependence. *ASME Journal of Fluid Engineering*, 123(2):382–393, 2001.
- ACARE. Advisory council for aeronautics research in europe: a vision for 2020, 2001. See <http://www.acare4europe.com/docs/Vision%202020.pdf>.
- R. Adrian. Hairpin vortex organisation in wall turbulence. *Physics of Fluids*, 19: 041301, 2007.
- A. Baron and M. Quadrio. Turbulent drag reduction by spanwise wall oscillations. *Applied Scientific Research*, 55:311–326, 1996.
- T. W. Berger, J. Kim, C. Lee, and J. Lim. Turbulent boundary layer control utilizing the lorentz force. *Physics of Fluids*, 12(3):631–649, 2000.
- J. P. Boeuf and L. C. Pitchford. Electrohydrodynamic force and aerodynamic flow acceleration in surface dielectric barrier dishcharge. *Journal of Applied Physics*, 97 (103307), 2005.
- J. P. Boeuf, Y. Lagmich, Th. Unfer, Th. Callegari, and L. C. Pitchford. Electrohydrodynamic force in dielectric barrier discharge plasma actuators. *Journal of Applied Physics*, 40:652–662, 2007.

- P. W. Carpenter, C. Davies, and Lucey A. D. Hydrodynamics and compliant walls: Does the dolphin have a secret? *AIAA Journal*, 79(6):758–765, 2000.
- L. N. III Cattafesta and M. Sheplak. Actuators for active flow control. *Annual Review of Fluid Mechanics*, 43:247–72, 2011.
- H. Choi and P. Moin. Effects of the computational time step on numerical solutions of turbulent flow. *Journal of Computational Physics*, 113:1–4, 1994.
- H. Choi, P. Moin, and J. Kim. Direct numerical simulation of turbulent flow over riblets. *Journal of Fluid Mechanics*, 255:503–539, 1993.
- H. Choi, P. Moin, and J. Kim. Active turbulence control for drag reduction in wall-bounded flows. *Journal of Fluid Mechanics*, 262:75–110, 1994.
- J. I. Choi, C. X. Xu, and H. J. Sung. Drag reduction by spanwise wall oscillation in wall-bounded turbulent flows. *AIAA Journal*, 40(5):842–850, 2002.
- K. S. Choi and B. R. Clayton. The mechanism of turbulent drag reduction with wall oscillation. *AIAA Journal*, 22:1–9, 2001.
- K. S. Choi and M. Graham. Drag reduction of turbulent pipe flows by circular-wall oscillation. *Journal of Computational Physics*, 10(1):7–9, 1998.
- K. S. Choi, J. R. DeBisschop, and B. R. Clayton. Turbulent boundary layer control by means of spanwise-wall oscillation. *AIAA Journal*, 36:1157–63, 1998.
- K. S. Choi, T. Jukes, and R. Whalley. Turbulent boundary-layer control with plasma actuators. *Philosophical Transactions of the Royal Society*, 369(1940):1443–1458, 2011.
- Y. M. Chung and T. Talha. Effectiveness of active flow control for turbulent skin friction drag reduction. *Physics of Fluids*, 23(2):025102, 2011.

- T. C. Corke, M. Post, and D. M. Orlov. Sdbd plasma enhanced aerodynamic: concepts, optimization and applications. *Progress in Aerospace Science*, 43: 193–217, 2007.
- T. C. Corke, C. L. Enloe, and S. P. Wilkinson. Dielectric barrier discharge plasma actuators for flow control. *Annual Review of Fluid Mechanics*, 42:505–529, 2010.
- T. C. Corke, P. O. Bowles, H. E. Chuan, and E. H. Matlis. Sensing and control of flow separation using plasma actuators. *Philosophical Transactions of the Royal Society*, 369(1940):1459–1475, 2011.
- M. R. Dhanak and C. Si. On reduction of turbulent wall friction through spanwise oscillations. *Journal of Fluid Mechanics*, 383:175–95, 2000.
- Y. Du and G. E. Karniadakis. Suppressing wall turbulence-turbulence via a transverse travelling wave. *Science*, 288:1230–34, 2000.
- Y. Du, V. Symeonidis, and G. E. Karniadakis. Drag reduction in wall-bounded turbulence via a transverse travelling wave. *Journal of Fluid Mechanics*, 457: 1–34, 2002.
- T. Endo, N. Kasagi, and Y. Suzuki. Feedback control of wall turbulence with wall deformation. *Journal of Computational Physics*, 21:568, 2000.
- C. L. Enloe, R. D. McLaughlin, R. D. Vandyken, K. D. Kachner, E. J. Jumper, and T. C. Corke. Mechanisms and responses of a single dielectric barrier plasma actuator: Plasma morphology. *AIAA Journal*, 42(3), 2004a.
- C. L. Enloe, R. D. McLaughlin, R. D. Vandyken, K. D. Kachner, E. J. Jumper, and T. C. Corke. Mechanisms and responses of a single dielectric barrier plasma actuator: Geometric effects. *AIAA Journal*, 42(3), 2004b.
- C. L. Enloe, M. G. McHarg, and T. E. McLaughlin. Time-correlated force production

- measurements of the dielectric barrier discharge plasma aerodynamic actuator. *Journal of Applied Physics*, 103:073302, 2008.
- M. Forte, J. Jolibois, J. Pons, E. Moreau, G. Touchard, and M. Cazalens. Optimization of dielectric barrier discharge plasma actuator by stationary and non-stationary measurements of the induced flow velocity: application to airflow control. *Experiments in Fluids*, 43:917–928, 2007.
- M. Gad-el Hak. Modern developments in flow control. *Applied Mechanics Review*, 49(7):365–379, 1996.
- M. Gad-el Hak. *Flow control: Passive, Active and Reactive Flow Management*. Cambridge University Press, 2000.
- D. V. Gaitonde, M. R. Visbal, and S. Roy. Control of flow past a wing section with plasma-based body forces. In *AIAA Paper 2005-5302, 36th AIAA Plasmadynamics and Lasers Conference, Toronto, Ontario*, 2005.
- R. Garcia-Mayoral and J. Jimenez. Drag reduction by riblets. *Philosophical Transactions of the Royal Society*, 369:1412–1427, 2011.
- M. B. Glauert. The wall jet. *Journal of Fluid Mechanics*, 1:625–643, 1956.
- E. P. Hammond, T. R. Bewley, and P. Moin. Observed mechanisms for turbulence attenuation and enhancement in opposition-controlled wall-bounded flows. *Physics of Fluids*, 10(9):2421–2423, 1998.
- J. Huang. *Separation control over low pressure turbine blades using plasma actuators*. PhD thesis, Notre Dame University, U.S.A., 2005.
- X. Huang and X. Zhang. Streamwise and spanwise plasma actuators for flow-induced noise control. *Physics of Fluids*, 20:037101, 2008.
- W. P. Jeon and R. F. Blackwater. Perturbations in the wall region using flush mounted piezoceramic actuators. *Experiments in fluids*. 28:485–496, 2000.

- J. Jeong and F. Hussain. On the identification of a vortex. *Journal of Fluid Mechanics*, 285:69–94, 1995.
- J. Jimenez and A. Pinelli. The autonomous cycle of near-wall turbulence. *JFM*, 389:335–359, 1999.
- D. R. Joslin, Thomas H. T., and Choudhari M. M. Synergism of flow and noise control technologies. *Progress in Aerospace Science*, 41:363–417, 2005.
- T. N. Jukes. *Turbulent drag reduction using surface plasma*. PhD thesis, University of Nottingham, 2007.
- T. N. Jukes and K. S. Choi. Long lasting modification to vortex shedding using a short plasma excitation. *Physical Review Letters*, 102:254501, 2009a.
- T. N. Jukes and K. S. Choi. Flow control around a circular cylinder using a pulsed dielectric discharge surface plasma. *Physics of Fluids*, 21(8):084103, 2009b.
- T. N. Jukes, K. S. Choi, G. A. Johnson, and S. J. Scott. Characterization of surface plasma-induced wall flows through velocity and temperature measurements. *AIAA Journal*, 44(4):764–771, 2006a.
- T. N. Jukes, K. S. Choi, G. A. Johnson, and S. J. Scott. Turbulent drag reduction by surface plasma through spanwise flow oscillation. In *AIAA Paper 2006-3693, 3rd AIAA Flow Control Conference, San Francisco, CA*, 2006b.
- T. N. Jukes, K. S. Choi, T. Segawa, and H. Yoshida. Jet flow induced by a surface plasma actuator. *Journal of Systems and Control engineering*, 222:347–356, 2008.
- W. J. Jung, N. Mangiavacchi, and R. Akhavan. Suppression of turbulence in wall-bounded flows by high-frequency spanwise oscillations. *Physics of Fluids A*, 4(8):1605–1607, 1992.
- S. Kang and H. Choi. Active wall motions for skin-friction drag reduction. *Physics of Fluids*. 12:3301, 2000.

- G. E. Karniadakis and K.-S. Choi. Mechanisms on transverse motions in turbulent wall flows. *Annual Review of Fluid Mechanics*, 35:45–62, 2003.
- J. Kim. Physics and control of near wall turbulence for drag reduction. *Philosophical Transactions of the Royal Society*, 369(1940):1396–1411, 2011.
- J. Kim and F. Hussain. Propagation velocity of perturbations in turbulent channel flow. *Physics of Fluids A*, 5(3):695–706, 1993.
- J. Kim, P. Moin, and R. Moser. Turbulence statistics in fully developed channel flow at low reynolds number. *Journal of Fluid Mechanics*, 177:133–166, 1987.
- J. Kim, J.-I. Choi, and H. J. Sung. Relationship between wall pressure fluctuations and streamwise vortices in a turbulent boundary layer. *Physics of Fluids*, 14: 898–892, 2002a.
- J. Kim, D. Kim, and H. C. Choi. On the role of oxygen in dielectric barrier discharge actuation of aerodynamic flows. *Applied Physics Letters*, 91:181501–3, 2007.
- K. Kim, S.-J. Baek, and H. J. Sung. An implicit velocity decoupling procedure for the incompressible navier-stokes equations. *International Journal for Numerical Methods in Fluids*, 38:125, 2002b.
- A. G. Kravchenko, H. Choi, and P. Moin. On the relation of near-wall streamwise vortices to wall skin friction in turbulent boundary layers. *Physics of Fluids A*, 5 (12):3307–3309, 1993.
- F. Laadhari, L. Skandaji, and R. Morel. Turbulence reduction in a boundary layer by a local spanwise oscillating surface. *Physics of Fluids*, 6(10):3218–3220, 1994.
- C. Lee, J. Kim, and H. Choi. Suboptimal control of turbulent channel flow for drag reduction. *Journal of Fluid Mechanics*, 358:245–258, 1988.
- C. Lee, J. Kim, D. Babcock, and R. Goodman. Application of neural networks to turbulence control for drag reduction. *Physics of Fluids*, 9(6):1740–1747, 1997.

- M. A. Leschziner, H. Choi, and K. S. Choi. Flow-control approaches to drag reduction in aerodynamics: progress and prospects. *Philosophical Transactions of the Royal Society*, 369(1940):1349–1351, 2011.
- Y. Li, X. Zhang, and X. Huang. The use of plasma actuators for bluff body broadband noise control. *Experiments in Fluids*, pages DOI 10.1007/s00348-009-0806-3, 2009.
- D. A. Lockberby, P. W. Carpenter, and C. D. Christopher. Is helmholtz resonance a problem for micro-jet actuators? *Flow, Turbulence and Combustion*, 78:205–222, 2007.
- I. Marusic, P. A. Mckeen, H. M. Monkewitz, H. M. Nagib, A. J. Smits, and Sreenivasan K. R. Wall-bounded turbulent flows at high reynolds numbers: Recent advances and key issues.
- B. E. Mertz and T. C. Corke. Single-dielectric barrier discharge plasma actuator modelling and validation. *Journal of Fluid Mechanics*, 669(17):557–583, 2011.
- P. Moin, Shih D., D. Driver, and N. Mansour. Direct numerical simulation of a three-dimensional turbulent boundary layer. *Physics of Fluids A*, 2:1846–1853, 1990.
- E. Moreau. Airflow control by non-thermal plasma actuators. *Journal of Physics D: Applied Physics*, 40:605–636, 2007.
- E. Moreau, C. Louste, and G. Touchard. Electric wind induced by sliding discharge in air at atmospheric pressure. *Journal of Electrostatics*, 66:107–114, 2007.
- T. C. Nelson, R. C. Corke, H. He, C. Othman, and T. Matsuno. Modification of the flow structure over a uav wing for roll control. In *AIAA Paper 2007-0877, 45th AIAA Aerospace Sciences Meeting and Exhibit, Reno, NV, JAN 2007*.

- D. M. Orlov. *Modelling and simulation of single dielectric barrier discharge plasma actuators*. PhD thesis, University of Notre Dame, 2006.
- D. M. Orlov, T. Apker, C. He, H. Othman, and T. C. Corke. Modelling and experiment of leading edge separation control using sdbd plasma actuators. In *AIAA Paper 2007-0877, 45th AIAA Aerospace Sciences Meeting and Exhibit, Reno, NV, JAN 2007*.
- D. Palmeiro and P. Lavoie. Comparative analysis on single dielectric barrier discharge plasma actuator models. In *Seventh international sympos on turbulence and shear flow phenomena*, 2011.
- J. Pons, E. Moreau, and G. Touchard. Assymetric surface barrier discharge in air at atmospheric pressure: electric properties and induced airflow characteristics. *Journal of Physics D: Applied Physics*, 38:3635–3642, 2005.
- M. Quadrio. Drag reduction in turbulent boundary layers by in-plane wall motion. *Journal of Fluid Mechanics*, 369(1940):1428–1442, 2011.
- M. Quadrio and P. Ricco. Critical assessment of turbulent drag reduction through spanwise wall oscillations. *Journal of Fluid Mechanics*, 521:251–271, 2004.
- M. Quadrio, P. Ricco, and C. Viotti. Streamwise-travelling waves of spanwise velocity for turbulent drag reduction. *Journal of Fluid Mechanics*, 627(161-178), 2009.
- P. Ricco and M. Quadrio. Wall-oscillation conditions for drag reduction in turbulent channel flow. *International Journal of Heat and Flow*, 29(4):891–902, 2008.
- P. Ricco and M. Quadrio. The laminar generalised stokes layer and turbulent drag reduction. *JFM*, In press, 2010.
- D. P. Rizetta and M. R. Visbal. Large eddy simulation of plasma-based control strategies for bluff body flow. *AIAA Journal*. 47(3):717–729, 2009.

- S. K. Robinson. Coherent motions in the turbulent boundary layer. *Annual Review of Fluid Mechanics*, 23:601, 1991.
- J. R. Roth, D. M. Sherman, and S. P. Wilkinson. Electrohydrodynamic flow control with a flow-dishcharge surface plasma. *AIAA Journal*, 38(7):1166–1172, 2000.
- H. Schlichting and K. Gersten. *Boundary layer theory*, page 715. Springer-Verlag, eighth edition, 1979.
- W. Shyy, B. Jayaraman, and A. Andersson. Modelling of glow discharge-induced fluid dynamics. *Journal of Applied Physics*, 92(11):6434–6443, 2002.
- K. P. Singh, S. Roy, and D. V. Gaitonde. Modeling of dielectric barrier discharge plasma actuator with atmospheric air chemistry. In *AIAA Paper 2006-3381, AIAA 37th Plasmadynamics and Lasers Conference, San Francisco, CA, JUN 2006*.
- Y. B. Suzen, P. G. Huang, and D. E. Ashpis. Numerical simulations of flow separation control in low-pressure turbines using plasma actuators. In *AIAA Paper 2007-937, 45th AIAA Aerospace Sciences Meeting and Exhibit, Reno, NV, JAN 2007*.
- T. Talha. *A numerical investigation of three dimensional unsteady turbulent channel flow subjected to temporal acceleration*. PhD thesis, School of Engineering, University of Warwick, U.K., 2011.
- F. O. Thomas, A. Kozlov, and T. C. Corke. Plasma actuators for cylinder flow control and noise reduction. *AIAA Journal*, 46(8):1921–1931, 2008.
- F. O. Thomas, T. C. Corke, M. Iqbal, A. Kozlow, and Schatzman D. Optimization of dielectric barrier discharge plasma actuators for active aerodynamic flow control. *AIAA Journal*, 47:2169–2178, 2009.

- C. Viotti, M. Quadrio, and P. Luchini. Streamwise oscillation of spanwise velocity at the wall of a channel for turbulent drag reduction. *Physics of Fluids*, 21(115109), 2009.
- R. D. Whalley. *Turbulent boundary-layer control with DBD plasma actuators using spanwise travelling-wave technique*. PhD thesis, University of Nottingham, 2011.
- P. Wilkinson. Investigation of an oscillating surface plasma for turbulent drag reduction. In *AIAA Paper 2003-1023, 41st Aerospace science meeting and exhibit, Reno, NV.*, 2003.
- H. Zhao, J. Z. Wu, and J. S Luo. Turbulent drag reduction by traveling wave of flexible wall.